Terms and Conditions of Use of Digitised Theses from Trinity College Library Dublin

Copyright statement

All material supplied by Trinity College Library is protected by copyright (under the Copyright and Related Rights Act, 2000 as amended) and other relevant Intellectual Property Rights. By accessing and using a Digitised Thesis from Trinity College Library you acknowledge that all Intellectual Property Rights in any Works supplied are the sole and exclusive property of the copyright and/or other IPR holder. Specific copyright holders may not be explicitly identified. Use of materials from other sources within a thesis should not be construed as a claim over them.

A non-exclusive, non-transferable licence is hereby granted to those using or reproducing, in whole or in part, the material for valid purposes, providing the copyright owners are acknowledged using the normal conventions. Where specific permission to use material is required, this is identified and such permission must be sought from the copyright holder or agency cited.

Liability statement

By using a Digitised Thesis, I accept that Trinity College Dublin bears no legal responsibility for the accuracy, legality or comprehensiveness of materials contained within the thesis, and that Trinity College Dublin accepts no liability for indirect, consequential, or incidental, damages or losses arising from use of the thesis for whatever reason. Information located in a thesis may be subject to specific use constraints, details of which may not be explicitly described. It is the responsibility of potential and actual users to be aware of such constraints and to abide by them. By making use of material from a digitised thesis, you accept these copyright and disclaimer provisions. Where it is brought to the attention of Trinity College Library that there may be a breach of copyright or other restraint, it is the policy to withdraw or take down access to a thesis while the issue is being resolved.

Access Agreement

By using a Digitised Thesis from Trinity College Library you are bound by the following Terms & Conditions. Please read them carefully.

I have read and I understand the following statement: All material supplied via a Digitised Thesis from Trinity College Library is protected by copyright and other intellectual property rights, and duplication or sale of all or part of any of a thesis is not permitted, except that material may be duplicated by you for your research use or for educational purposes in electronic or print form providing the copyright owners are acknowledged using the normal conventions. You must obtain permission for any other use. Electronic or print copies may not be offered, whether for sale or otherwise to anyone. This copy has been supplied on the understanding that it is copyright material and that no quotation from the thesis may be published without proper acknowledgement.
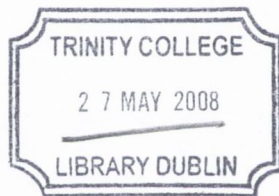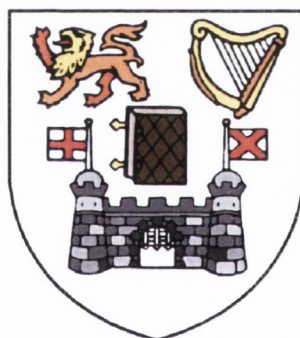
Characterisation of n-ferrocenyl Alkanethiol Self-Assembled Monolayers

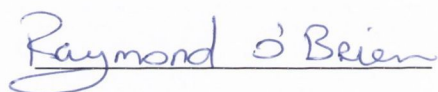Raymond O' Brien

B.A. (Chem.)

A thesis submitted to the University of Dublin for the degree of

Doctor of Philosophy.

Department of Chemistry

University of Dublin

2007

Declaration

This thesis has not been submitted as an exercise for a degree at any other University. Except where otherwise indicated, the work described herein has been carried out by the author alone. I, the undersigned, do also give permission to the Libraries of Trinity College, Dublin, to copy this thesis in whole or in part without further reference to me.

Raymond O Brien

DECLARATION

This thesis has not been submitted as an exercise for a degree at any other university. Except where stated, the work described therein was carried out by me alone.

I give permission for the Library to lend or copy this thesis upon request.

Signed: *Raymond O'Brien*

Summary

The study of self-assembled monolayers and their applications in chemistry and materials science have been of interest since the early 1980's. Due to their stable and dense structure self-assembled monolayers have been investigated for uses in many applications including biosensors and electronics. Many other areas of academic research have been guided towards the understanding of fundamental relationships between structure and interfacial monolayer properties due to the vastness of potential applications. Research in polymer and electronics industries have highlighted the utilization of self-assembly in thin film technologies. The facility to modify the functionality of the constituent molecules makes self-assembled monolayers ideal for the investigations of fundamental principles governing molecular substrate interactions, intermolecular forces (van der Waal's interactions, hydrogen bonding, π-π interactions), and molecule-solvent interactions that affect interfacial properties such as corrosion, lubrication, adhesion, growth and wetting.

The eventual goal of the majority of self-assembled monolayer research is to achieve an understanding of the structure-property relationships and especially, to determine which structural factors enable rational but wide ranging control over the properties of existing self-assembled monolayers. To this purpose my Ph. D has concentrated on the characterisation of redox active self assembled monolayers, the complete understanding of which is essential to the development of these SAMs as usable applications

There are three main areas in this work. The first deals with the integrity of self-assembled monolayers investigations of unsubstituted alkanethiol monolayers. In initial work conducted to optimize monolayer deposition protocol and quality, the corresponding non redox active C_{12} ferrocenyl alkanethiol monolayer was fabricated. The electron transfer properties of these non redox active monolayers were investigated using cyclic voltammetry and electrochemical impedance spectroscopy. The effect of an external magnetic field (0.5 T) on the growth of the unsubstituted alkanethiol was also

investigated. Finally, in this section the application of a potential to the bare gold electrode during alkanethiol adsorption was investigated.

In the second section the properties of redox active SAM films of varying chain lengths (n=8, 10 and 12) formed under potential control are examined in detail largely using cyclic voltammetry and compared with similar films formed via passive deposition. In particular, characteristic voltammetric parameters such as anodic/cathodic peak separation, standard potential, peak widths at half maximum and surface coverages are examined for ferrocenyl alkanethiol films as a function of electrolyte nature, concentration and experimental time scale.

A comparison of potentially assisted deposition versus the normal method of 48 h passive deposition was undertaken by analysing similar parameters as in the above section. Finally, in order to examine the quality of the 2 h potential assisted deposition method a comparison of this method versus a 2 h passive deposition was carried out.

The last section investigated the effects of an external magnetic field on the electron transport properties of the redox active self assembled monolayers. Significantly reduced currents were observed during the SAM redox processes under the influence of a magnetic field. We also observed a reduction in the surface coverage values of the redox active monolayers on application of the external magnetic field. The current transient data provided by chronoamperometry showed a decrease in electron transfer rates through the monolayer as a result of the application of the magnetic field.

For my parents, Maeve and Brian.

Acknowledgements

First and foremost, I would like to thank Dr. Michael E.G. Lyons for providing me with the opportunity to work within his research group and for his supervision over the course of this study. I thank the Higher Education Authority and the PRTLI for financial assistance throughout this endeavour.

I would like to thank Dr. Noelle Scully for her guidance in the synthesis of the n-ferrocenyl alkanethiols. I thank Dr. John O'Brien for running the many NMR studies. I am also indebted to the other academic, technical and secretarial staff within the Chemistry Department of Trinity College for their help over the past three and half years.

A big thank you must go to the members of the Lyons group, past and present (Michael Brandon, Michael Kinsella, Gareth Keeley, Deirdre Kelleher and Conchuir MacGloinn) for their help with my Ph.D and the great laughs we had in the lab. Most of all I would like to thank Johnny for all the laughs and the help from day one. I would also thank all of the other postgraduate students within the department. Thanks to all of my friends in both Dublin and Kerry for all the good times over the years. Very special thanks must go to Aisling for all her support.

All members of my family, both immediate and extended, receive great thanks. To my brother, Dave, I say 'cheers' for all his support and keeping me in the loop with all the news at home. Finally, the biggest thank you must go to my parents to whom this thesis is dedicated. They have always supported me and have ensured that I have been able to take every opportunity in life, for which I will be eternally grateful. Thank You.

Table of Contents

3. Synthesis of n-Ferrocenyl Alkanethiols

4. Characterisation of Non-Redox Active Alkanethiol SAMs

5. Polarisation of Redox Active Alkanethiol SAMs

7. General Conclusions and Future Recommendations

Appendix:NMR Characterisation of 12-Ferrocenyl Alkanethiol SAM

Abbreviations

A	Area
C	Concentration
CA	Chronamperometry
C_{dif}	Diffuse layer capacitance
C_{DL}	Double Layer Capacitance
C_H	Reciprocal capacitance
CV	Cyclic voltammetry
D	Diffusion co-efficient
e	Electronic Charge
ET	Electron transfer
F_{ad}	Force of adhesion
i_c	Double layer charging current
i_F	Faradaic current
k_{ad}	Adsorption rate constants
PAD	Potential Assisted Deposition
PD	Passive Deposition
PET	Plane of electron transfer
R	Gas Constant
R_{CT}	charge transfer resistance
R_S	Solution resistance
SAM	Self-Assembled Monolayer
STM	Scanning Tunneling Microscopy
T	Temperature
t	Time
Ts	Surface Temperature
V	Voltage
V_{AB}	Electronic coupling factors
x	Mole fraction

Z	Impedance
Z_W	Warburg impedance
α	Transfer Coefficient
β	Adsorbate chain length
Γ	Surface Coverage
ΔE_{ads}	Adsorption energy
ΔE_{corr}	Corregation of substrate potential experienced by molecule
ΔE_{fwhm}	Peak half-width
ΔE_g	Energy of gauche defect
ΔEh_{yd}	Van der Waals interaction of (hydrocarbon) tails
ΔE_p	Peak potential separation
ε	Dielectric constant
ε_o	Permittivity of free space
θ	Surface fraction
θ_t	Tilt of molecular axis
λ	Reorganizational energy
ν	Scan Rate
φ_{PET}	Electrostatic potential at the PET
χ_H	Interpolate spacing
χt	Tilt direction
ψ	Twist angle
n	Number of electrons transferred
F	Faradays Constant
Q	Charge
E	Potential
E^0	Standard potential
I	Current
Ψ	Normalised Current
ξ	Normalised potential
f_c	Net Flux

CHAPTER 1

Introduction to Organosulfur Self Assembled Monolayers

1 Introduction

1.1 Introduction to Self-Assembled Monolayers

The study of self-assembled monolayers and their applications in chemistry and materials science have been of interest since the early 1980's[1-3]. Self-assembled monolayers have been investigated for use in biosensors[4-6] and chemical technology[7,8], lubrication[9], non-linear optical films[10-13], adhesion[14-16], prevention of corrosion[17-22], electronics[23] and many other areas due to their stable and dense structure.

Academic research had been guided towards the understanding of fundamental relationships between structure and interfacial monolayer properties due to the vastness of potential applications. Research in the polymer and electronics industries have highlighted the use of self-assembly in thin film technologies[24-30]. The facility to modify the functionality of the constituent molecules makes self-assembled monolayers ideal for the investigations of fundamental principles governing molecular substrate interactions, intermolecular forces (van der Waal's interactions, hydrogen bonding, π-π interactions), and molecule-solvent interactions that affect interfacial properties such as corrosion[18, 22, 31], lubrication[32,33], adhesion[34-36], growth[37-39], ordering[32,40] and wetting[41-44].

The eventual goal of the majority of self-assembled monolayer research is to achieve an understanding of the structure-property relationships and especially, to determine which structural factors enable rational but wide ranging control over the properties of existing self-assembled monolayers.

1.2 Definition of Self-Assembled Monolayer

It is important to define what the term "self assembled monolayer" means. An organized Self-Assembled Monolayer (SAM) is a single layer of molecules on a substrate in which the molecules exhibit a high degree of orientation, order and molecular packing[45]. A classic picture of an organized monolayer consists of molecules with identifiable head and tail groups, aligned perfectly on a smooth surface [46]. (Figure 1.1)
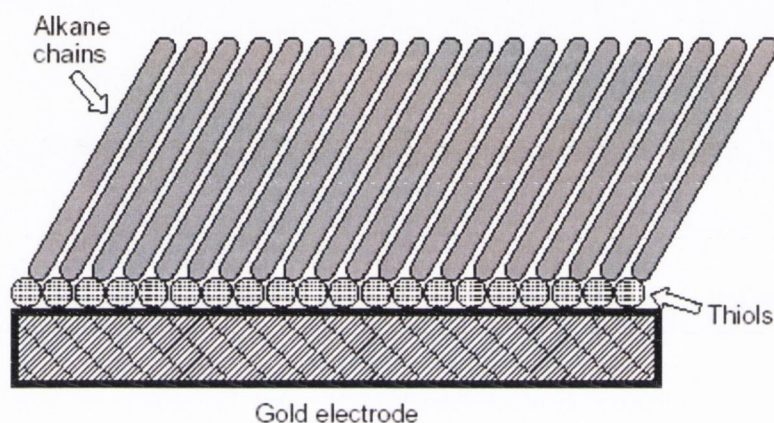
Figure 1.1: *An organized monolayer on a substrate (electrode). The monolayer can be deposited by the LB method or by self-assembly[46].*

In more specific terms, this definition means that certain conditions must be accorded to before an adsorbed layer of material can be classified as a self-assembled monolayer:

- The adsorbed layer must only be one molecule in thickness
- The adsorbed layer must be continuous across surface
- The adsorbed material must be bound to the surface via chemical bonds
- Formation of the adsorbed layer must be self-limiting in the presence of excess solvent
- The adsorbed layer must be well ordered

The first condition is self-explanatory, if the layer is to be described as a monolayer it can only be one molecule in thickness. Similarly, if the adsorbed layer is not continuous, but rather only present in islands or clumps, then it can not be identifiable

as a monolayer. In order for self-assembly to work, a strong bond between the substrate, and an atom or moiety in the molecule and an additional lateral interaction between molecules in the monolayer is needed. The monolayer resists solvent rinse due to the sufficient stability produced by the strength of the head group-substrate bond, the density of the packing and the lateral interactions. Figure 1.2 represents a schematic, illustrating the components of a SAM.
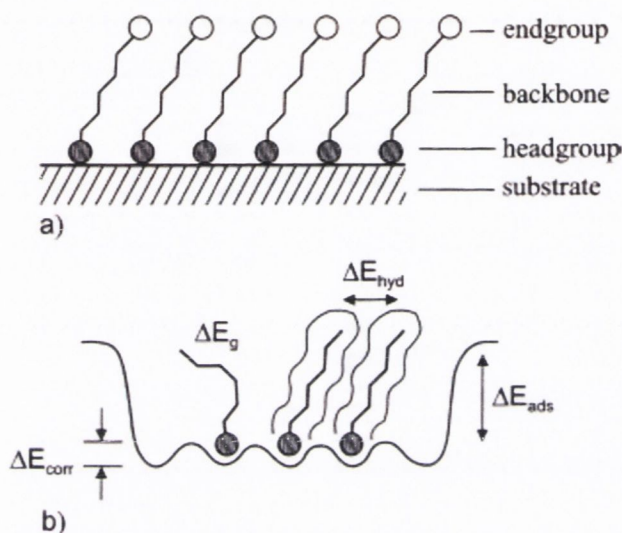
Figure 1.2: *(a) Schematic of SAM. Shaded circle indicates chemisorbing headgroup and open circle endgroup, which can be chosen from variety of chemical functionalities. (b) Schematic of different energies. ΔE_{ads} stands for adsorption energy, ΔE_{corr} corrugation of substrate potential experienced by molecule, ΔEh_{yd} van der Waals interaction of (hydrocarbon) tails, and ΔE_g energy of gauche defect (or, generally, deviation from fully stretched backbone)[45].*

Another important condition is that the formation of a SAM should be self-limiting. The deposition of adsorbate to structure surface should cease when the structure attains a dense state i.e. on formation of a single layer. This is a universal characteristic of all self-assembled monolayers. It results from the detail that the chemical interaction between adsorbate to substrate is the driving force for self-assembly. It is then obvious that no more molecules will attach to the monolayer when the adsorbate is out of contact to react with the substrate surface.

The Langmuir-Blodgett Method and the Self-Assembly Method are the two common methods for depositing a monolayer. The Langmuir-Blodgett Method consists of spreading amphiphilic molecules on the air-water interface; the molecules

are compressed laterally. Transfer to the substrate takes place by either touching the substrate to the interface or by dipping the substrate through the interface[2]. The Self-Assembly method consists of a monolayer forming spontaneously upon exposure to the substrate from a homogeneous solution. Often the Self-Assembly process is accompanied by a striking change in the wetting properties of the substrate; the substrate emerges dry from the deposition solution.
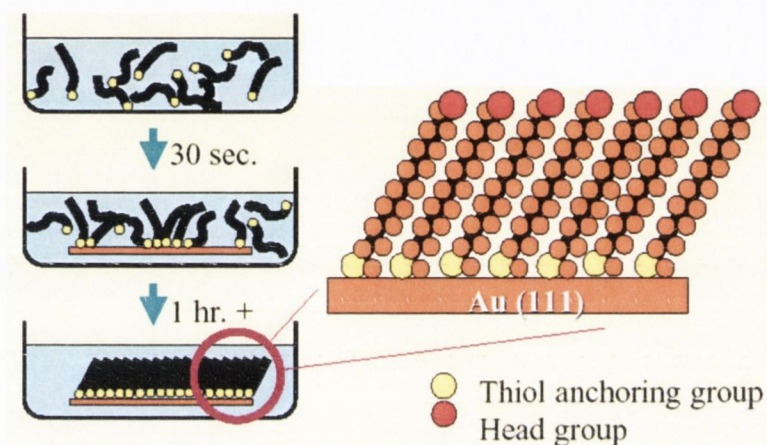
Figure 1.3: *Picture presenting the self-assembly method of alkanethiols onto a surface.*

The overall self-assembly process can be summarized as follows (figure 1.3): The sticking coefficient for alkanethiols on Au (111) is near unity at low temperature, and decreases with increasing temperature (starting when the surface temperature (T_s) is ~50 K below the desorption temperature). The initial stage of adsorption is reported to start with a physisorbed state, with the molecules lying almost parallel to the surface. Following the physisorption, alkanethiolates are dissociatively chemisorbed to the gold surface via the sulfur atom after cleavage of the S–H bonds. In the low coverage regime or ''lying-down'' phase, the molecular axis of the chemisorbed molecules has been reported to be parallel stretched along the molecular axis. Increased coverage results in formation of ordered structures, where the hydrocarbon chains have a smaller tilt angle. Different structural phases are observed as coverage increases. At full coverage (full coverage defined as ($\theta=1$) to mean saturation coverage, one thiol molecule per three gold surface atoms), the SAM structure is highly ordered.

1.3 Self-Assembled Monolayer History

Organic thin films have been studied expansively for many years, even dating back more then 200 years ago when Franklin[47] observed the calming influence of oil on water. He spread a spoonful of oil on a pond and observed that the oil spontaneously spread to cover the pond's surface. His explanation was that the amphiphilic oil molecules had reorganized themselves to maximize the contact of their polar functionalities with the polar water molecules of the pond water. In the 19th Century Pockels and Lord Rayleigh[48] prepared monolayers at the air-water interface. Their experiments established methods for reproducibly generating these films and provided evidence of a layered structure that was only a single molecule in thickness.

Langmuir[49] was the first to provide an understanding of their structure (e.g. orientation of the adsorbates) at the molecular level. Later, Langmuir and Blodgett[50] reported that the adsorbates in a Langmuir monolayer could be transferred to a solid support to generate a physisorbed monolayer. This monolayer became known as a Langmuir-Blodgett film. The development of these films was significant as it demonstrated that the interfacial properties of solid surfaces could be influenced by merely adsorbing a thin organic film.

In the 1940's Zisman[51] conducted the first studies of self-assembled monolayers on solid substrates. These were formed by the dipping of a metal or metal oxide surface into an adsorbate solution, such as alkyl amines. The resulting films were autophobic i.e. films were unwet by the solvent used in monolayer formation and the interfacial properties were similar to these of Langmuir-Blodgett films. The feature which differentiated " self-assembled " films from Langmuir-Blodgett films was shown by Zisman[51] to be that the driving forces involved in self-assembly were ligating chemical interactions between the polar functional groups of the adsorbates and the metal or metal oxide atoms, whereas in Langmuir-Blodgett films, the adsorbate-substrate interactions were primarily of a physical nature.

In the 1950's and 1960's, Zisman[52, 53] examined the properties of SAMs. The most significant result obtained was that the interfacial properties could be controlled by altering the identity of the terminal functional groups. For example it was shown that the interfacial free energy could be decreased by substitution of terminal methyl

groups by trifluoro methyl groups. Zisman used this result to examine the relationship between the interfacial energetics of the organic thin films and the physical and chemical properties. However, Zisman's films suffered from only modest stabilities due to low energies of adsorption between adsorbates and substrates. As a result, work on self-assembly stalled and remained an unpopular method for monolayer film construction.

We may enquire for what reason did self-assembly become such a popular subject to investigate once more? There seems to be several favourable factors which were responsible for the re-ignition of the popularity of research in the area. The first factor was an increase in the demand for smaller electronic devices which led to research being initiated to examine molecular materials for electronic applications. A second reason was that sensor technology became a major industrial target and interfacial science was the only method available to successfully produce small, versatile and inexpensive sensors. Finally, the recent increased activity in molecular biology research has made workers investigate the behaviour of biological molecules at interfaces. It was a combination of these activities that created a demand for investigations of the solid-liquid and solid-gas interfaces at the molecular level. The production of commercially available analytical devices which were sensitive enough to characterize single layers of molecules also aided and encouraged investigations.

Sagiv[54-57] revived interest in SAMs when he published a series of papers which demonstrated that alkyl silanes could be used to form very stable monolayers on aluminium oxide and glass. In 1983, Bell Laboratories based researchers working on SAMs discovered that long-chain thiols and disulfides form stable and well-packed monolayers on gold. The high affinity of the metals (Au, Pt) towards sulfur adsorption allows a diverse range of functional groups to be incorporated into the SAM or onto the exposed surface of the SAM. Recognition of this novel approach can be credited to Allara and Nuzzo[58]. This work served as a launch pad for the exploration of SAM systems based on sulfur-metal interactions.

However, it was a series of papers by various groups, including Finklea et al.[59] in 1987 and Whitesides et al.[60] in 1988 that resulted in an explosion of research on self-assembled monolayers. Initially, Finklea[59] looked at octadecyltrichlorosilane

SAMs and found that monolayers formed from alkyl mercaptans are remarkably stable as electrode coatings. Finklea associated the increased stability with the high affinity of sulfur for gold. Furthermore, he saw that these alkyl mercaptans formed sufficiently compact monolayers with barrier properties that suppressed electrochemical processes, including gold oxidation and interfacial electron transfer with long range redox molecules located in the solution phase. From this he concluded that it was possible to investigate electron transfer via electrochemical techniques across the monolayer film. Soon afterwards, it was discovered that other organosulfur compounds such as alkanethiols and alkyl sulfides also coordinated to the surfaces of metals such as gold, silver and copper to form compact well defined SAMs.

Whitesides et al.[60] studied the co-ordination of long chain hydroxy alkanethiols to gold surfaces via the sulfur atom. These produced ordered hydrophilic monolayers, the outer surface of which had exposed hydroxyl groups. They also studied mixed monolayer systems consisting of two hydroxy alkanethiols of differing chain length, n. They found that this mixed monolayer system was formed by co-adsorption and resulted in the generation of a monolayer which had a disordered surface region that was less hydrophilic when compared with the homogeneous hydoxylic surface film formed from either of the pure hydroxy alkanethiol compounds. It was also shown that the degree of order in the hydrophilicity could be controlled simultaneously by controlling the composition of the monolayer.

1.4 Types of Self-Assembled Monolayers on Electrodes

With the exception of carbon, SAMs have been formed on every common electrode material. SAMs containing sulfur compounds, especially thiols, disulfides, and sulfides have all been coated onto the common metal materials. Gold, silver, platinum and mercury being those most commonly used metals. Gold is the best substrate due to the affinity of sulfur to the gold. The most common SAMs are those containing varying lengths of alkane chains. Syntheses for sulfur compounds containing C_{5-14} chain lengths have been produced. These carbon chain lengths form the best SAMs due to their flexibility and non-negligible chain-chain interactions. Short carbon chain

lengths (n<5) are less common due to the different balance of the interactions (chain-chain) and are unable to form ordered monolayers. SAMs based on the adsorption of isonitriles are less common[61,62].

1.5 Advantages of Self-Assembled Monolayers Based on Thiols and Related Molecules

The first advantage is the ease of formation of the SAMs upon exposure of gold, platinum and other metals to thiols and related sulfur compounds dissolved in a suitable organic solvent. Deposition of a thiol monolayer upon a metal occurs in a matter of seconds to minutes. In practice, exposure of the metal to the thiol solution is usually overnight. This ensures a densely packed and highly oriented monolayer. The high degree of orientation is due to van der Waals forces between the methylene groups. Anaerobic or anhydrous conditions are not a necessity for the self-assembly method. Neither is a vacuum needed. Solvent choice is not a major factor in SAM formation. Displacement of weakly adsorbed impurities by the assembling layer is as a result of the high affinity of sulfur to the metal. Also, accessibility of the metal surface does not seem to be an important factor since; the range of substrate areas can vary from submicroscopic to macroscopic. These substrates can be either porous or smooth.

The strength of the bond formed and the affinity of sulfur for the metal is a further advantage. Disruption of the self-assembly process or destabilization of the SAM will not occur even if there is a wide range of functional groups in the adsorbing molecule. In the case of the substituted alkanethiols used in this course of work, the terminal substituent can be an alkane (linear, branched) alkene, alkyne, aromatic, halide or nitrile.[43,63] Heteroatoms[64,65] and aromatic compounds[66] can be contained in the 'body' of the molecule. A single functional group will be exposed on the external surface if the SAM is densely packed and uniform in composition.

1.6 Introduction to Ferrocene Alkanethiol SAMs

Chidsey et al,[67] carried out much of the earliest work on ferrocene alkanethiols around the late 1980's. Chidsey formed a co-adsorption of ferrocene-terminated alkanethiols with corresponding unsubstituted *n*-alkanethiols on evaporated gold films, yielding a stable electroactive SAM. Figure 1.4 illustrates this system of co-adsorption.
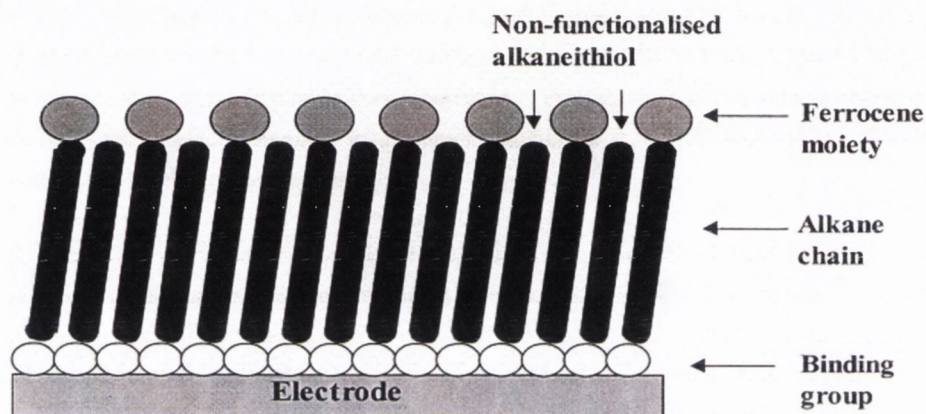
Figure 1.4: *Representation of an electroactive ferrocene complex adsorbed onto an electrode separated by a diluent alkane chain[46].*

Employing electrochemical techniques, namely Cyclic Voltammetry (CV) and limited study employing ellipsometry, Chidsey found that mixed monolayers with low mole fractions of alkanethiols linked to ferrocene by a polar ester group. These monolayers showed ideal surface electrochemistry in 1 M $HClO_4$ i.e. the ferrocene oxidation and ferricenium reduction peaks are symmetric with $\Delta E_{fwhm}= 90$ mV and $\Delta E_p= 0$ mV. This indicates that the ferrocene groups are homogeneous and non-interacting. Chidsey also showed that higher surface loadings or use of alkanethiols linked to a non-polar ferrocene group lead to a widening of electrochemical features, indicating the operation of interactions amongst the surface bound ferrocene groups or the presence of inhomogeneous adsorption sites. He found that longer chain lengths and lower ferrocene surface concentrations resulted in slower electron transfer kinetics between the substrate metal and the ferrocene groups. Finally, Chidsey found that exchange of ferrocene-terminated alkanethiols for unsubstituted alkanethiols proved to be useful as a measure of defects and also as a means of avoiding the

influence of defects on the kinetics of electron transfer to the remaining ferrocene sites.

Collard and Fox[68] continued this trend by examining the treatment of mixed monolayers of hexadecanethiol and 16-(ferrocenylcabonyloxy)hexadecanethiol on gold with solutions of alkanethiols. They found that this resulted in the replacement of approximately one third of the electroactive thiol's original surface coverage. Collard and Fox monitored this exchange by integration of the cyclic voltammetric wave. A mechanism of interchange between the defect-site and the crystalline-domain alkanethiol was suggested (figure 1.5).

Scheme I

crystalline domain site $\xleftrightarrow{slow}$ defect site

RSH $\downarrow$ $\downarrow$ RSH

slow exchange   fast exchange
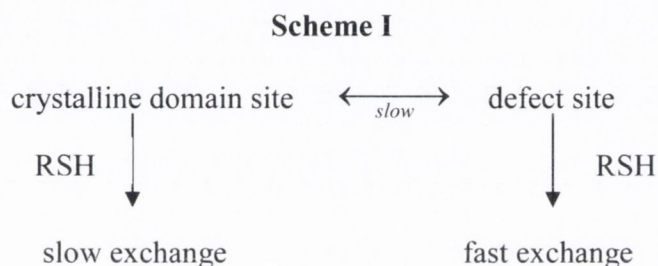
Figure 1.5: *Mechanism of interchange between the defect-site and the crystalline-domain alkanethiol[68].*

Although it is assumed that diffusion of alkanethiols within the two-dimensional crystal-like monolayer is slow, defects at the crystalline domain boundaries can diffuse across the surface by conformational changes in the alkyl chain. Defect site and crystalline-domain alkanethiols could be interchanged in this manner. Alkanethiols adsorbed during an exchange enter the monolayer at a fast exchanging site (i.e., a defect) and most of it can then be re-exchanged, indicating that the exchangeable and non-exchangeable sites are not in rapid equilibrium. The inability to re-exchange all of the alkanethiol adsorbed in the first exchange indicates that there is a process whereby exchangeable (i.e., defect-localized) alkanethiol eventually equilibrates with non-exchangeable (i.e., crystalline-domain) alkanethiol.

Creager and Rowe[69], studied self-assembled mixed monolayers composed of ferrocenylhexadecanethiol and n-alkanethiols which were prepared on polycrystalline gold electrodes. They found that as the n-alkanethiol chain-length increases for

monolayers containing ferrocenylalkanethiols and n-alkanethiols from 4 to 12 carbons long, the amount of adsorbed ferrocene decreased. It was established that the redox potential shifted in a positive direction as the chain length of n-alkanethiol increased. Creager and Rowe explained this shift in terms of the progressively more alkane like environment created by the co-adsorbed alkanethiols which stabilizes ferrocenium relative to ferrocene. The positive shift is a measure of the energy that is required to force the electrogenerated ferricenium ion to reside in the non-polar poorly solvated environment. Following oxidation, the monolayer was found to be more permeable to electrolyte ions and solvent. The proof of this was that the capacitive charging current was always found to be larger at potentials more positive than the ferrocene redox potential.

In other work Creager and Rowe[70] also studied mixed monolayers of N-(7-mercaptoheptyl)-ferrocenecarboxamide coadsorbed onto gold electrodes with n-alkanethiol derivatives of variable chain-length and terminal functionality. This system was more advantageous than the first system[72] in that the redox active ferrocene derivative is slightly soluble in water. This permitted direct comparison of formal potentials for the adsorbed species with those for the identical species in bulk solution. It also allowed quantitative interpretation of the observed shift in formal potentials in terms of specific physical models for the electrode/monolayer/solution interface. Creager and Rowe considered two such models, to explain the difference in formal potential[69]. The first model was based on the difference in the spatial distribution of ions in the interfacial region and its effect on the formal potential for the adsorbed species. This was representative of a double layer effect on the apparent formal potential in the monolayer. The second model was based on differences in ion solvation energies in the interfacial region relative to the bulk solvent. This model was representative of a solvent effect on the apparent formal potential in the monolayer. They carried out experiments that focused on the variations in electrolyte type and concentration, differences in ferrocene surface coverage, and differences in solvent. From their studies Creager and Rowe concluded that both ion solvation and ion spatial distribution effects are important and it is necessary to consider both to explain the data.

Creager and Weber[71], have used CV and chronoamperometry to extract rate constants and reorganization energies for surface attached ferrocene moieties on the alkanethiols. They presented a treatment of linear sweep voltammetry for redox active groups irreversibly adsorbed on electrodes. They carried out voltammetric experiments over wide range of scan rates for ferrocene oxidation/reduction in self-assembled monolayers of N-(15-mercaptopentadecyl)ferrocenecarboxyamide coadsorbed with mercaptohexadecanol onto gold. Creager and Rowe predicted that broader voltammograms and greater shifts in peak potentials with increasing scan rate would occur and this was borne out in their results (Figure 1.6). They also calculated values of 7 s^{-1} and 6.6 s^{-1} for k^o from two different data sets. These results parallel Chidsey's results which were obtained using potential step amperometry whereas Creager and Weber employed voltammetry instead.
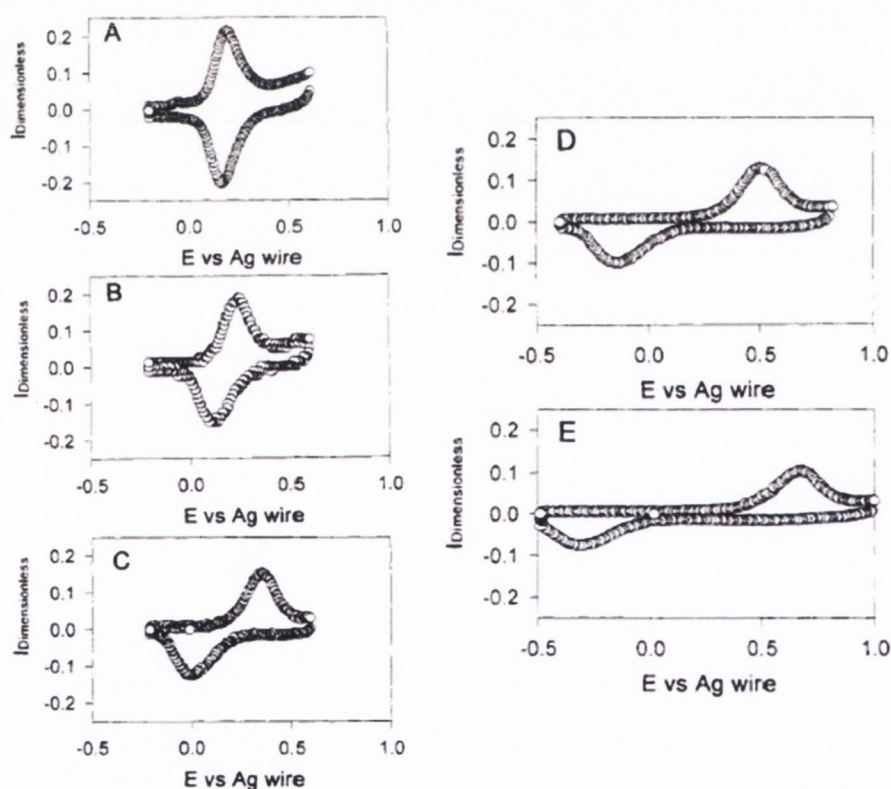
Figure 1.6: *Effect of sweep rate on voltammetry of a mixed FcCONH-C$_{15}$SH/HO-C$_{16}$SH monolayer (Γ_{Fc} = 9.5 X 10^{-11} molcm^{-2}) in aqueous 1 M HClO$_4$ at room temperature. Currents have been normalized by the factor vQF/RT, where v is the sweep rate and Q the charge under the voltammetric wave. Sweep rates were (A) 0.1, (B) 1.0. (C) 10.0,(D) 100.0, and (E) 1000.0 V s^{-1}.[71]*

Murray et al. [72] studied temperature and distance dependence of electron transfer kinetics of self-assembled mixed monolayers of the ferrocene alkanethiol $(CpFeCpCO_2(CH_2)_nSH)$ (Cp=cyclopentadienyl) and n-alkanethiol $CH_3(CH_2)_nSH$ coadsorbed on gold electrodes for n= 8,12 and 16 at low temperatures (120-140 K). The determination of the manner in which the electron transfer kinetics varies with distance, provides information on the extent of coupling between the attached redox site and the electrode and is of interest both for fundamental mechanistic reasons and for optimizing the level of control of interfacial electron transfer rates in the nanostructured systems. The low temperature investigations of ferrocene alkanethiol monolayers revealed that k^o varies among the self-assembled monolayer ferrocene site populations, i.e., k^o exhibits a kinetic dispersion. Figure 1.7 shows that the oxidation-reduction peak potential separation ΔE_P between oxidation and reduction peak potentials in $CpFcCpCO_2(CH_2)_{16}SH/(CH_2)_{15}SH$ mixed monolayer voltammetry increases as the electron transfer rate is thermally quenched by lowering temperatures.
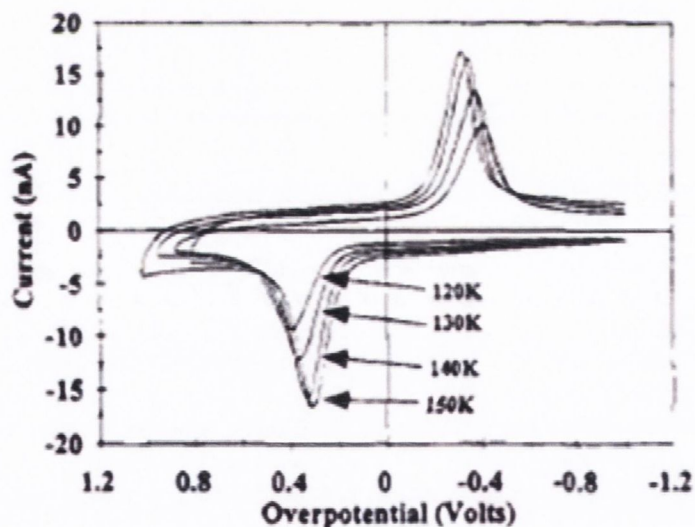
Figure 1.7: *Temperature-dependent cyclic voltammetry (100 mVs^{-1}) of a mixed monolayer of $CpFcCpCO_2(CH_2)_{16}SH/(CH_2)_{15}SH/bulk.$ In contact with 2:1 (v/v) chloroethane:butyronitrile/0.075 M Bu_4NPF_6.* [72]

Cyclic voltammograms at high temperatures for n = 8, 12 and 16 ferrocene self-assembled monolayers exhibit ΔE_P that increase systematically (i.e. smaller k^o) with

increasing alkane chain length. From these ΔE_{PEAK} values k^o can obtained using a Marcus theory formulation. This involves generating working curves of ΔE_{PEAK} vs $\log(\upsilon/k^o)$ by using digitally simulating voltammograms with Marcus-density of states theory. From these working curves the k^o values derived are not strongly sensitive to the value of ET barrier reorganizational energy (λ) assumed in the working curve. Murray's results showed that the low-temperature k^o values vary exponentially with alkane chain length even though the monolayers are kinetically polydisperse (Table 1.1).

T/K^a	υ (V/s)	ΔE_{PEAK} (mV)	k^o (s^{-1})
120	0.01	647	2.0×10^{-6}
$\Gamma = 1.15 \times 10^{-10}$ mol/cm^2	0.1	810	2.5×10^{-6}
	1.0	1045	2.0×10^{-6}
130	0.01	586	1.1×10^{-5}
$\Gamma = 1.22 \times 10^{-10}$ mol/cm^2	0.1	742	1.3×10^{-5}
	1.0	950	1.4×10^{-5}
140	0.01	527	3.5×10^{-5}
$\Gamma = 1.44 \times 10^{-10}$ mol/cm^2	0.1	679	3.7×10^{-5}
	1.0	857	4.0×10^{-5}
150	0.01	476	1.1×10^{-4}
$\Gamma = 1.5 \times 10^{-10}$ mol/cm^2	0.1	630	1.4×10^{-4}
	1.0	805	1.5×10^{-4}

Table 1.1: *Cyclic Voltammetry Peak Potential Separations (ΔE_{PEAK}) and Marcus-DOS Derived Rate Constants for a $CpFeCpCO_2(CH_2)_{16}SH/CH_3(CH_2)_{15}SH$ SAM in Contact with 2: 1 (v/v) Chloroethane:Butyronitrile/0.075 M Bu_4NPF_6.*[72]

Smalley and Chidsey[73] looked at the characterisation of the distance dependence of the electron transfer rate constant for an alkanethiol tethered ferrocene system for shorter chain n-alkanethiols ($n \leq 8$). It was found that the rate constant was too fast to be measured by conventional electrochemical methods (e.g. chronoamperometry). Instead, they employed the indirect laser induced temperature (ILIT) method to characterize the rates of electron transfer between ferrocenium/ferrocene redox couple for $5 \leq n \leq 9$. The objective of the ILIT method is to effect a rapid (<5 ns) and small (<5 K) change in the temperature at an electrode/electrolyte interface using a pulsed Nd:YAG laser. This laser heats the "back" side of a thin metal film electrode whose "front" side with attached monolayer contacts the electrolyte. Some laser energy is adsorbed by the metal film and is degraded to heat which rapidly diffuses

across the electrode raising the temperature of the electrode/electrolyte interface. This temperature increase effects a change in the open-circuit potential. This circuit potential is a function of the dissipation of the thermal perturbation and of the rate of electron transfer between the electrode and the redox moieties. From these studies, it has been established that longer alkyl chains (usually with 11 or more CH_2 groups) adsorb preferentially and in more ordered structure than their equivalent shorter ones, due to the Van der Waals interactions between the alkyl chains.

Uosaki et al.[74] studied the effects of acyl and alkyl group introduction into the ferrocene ring on the redox potential and the adsorption behaviour of ferrocene derivative self assembled alkanethiol monolayers. Uosaki studied the electrochemical characteristics of gold electrodes modified with six ferrocenylalkane thiol and disulfide derivatives. On introduction of the acyl group into the ferrocene ring of the ferrocenylalkane thiols, the redox potentials of the modified electrodes in 0.1 M $HClO_4$ were found to shift positively by around 300 mV per acyl group[74]. The reason for this shift is the electron-withdrawing effect of the carbonyl group and was in agreement with work carried out by Mann and Barnes[75].

Mann and Barnes reported that the redox potentials of ferrocene derivatives dissolved in solutions became more positive as the number of carbonyl groups introduded to the ferrocene derivative increases. On introducing the akyl group (butyl) into the ferrocene ring, the redox potentials shifted by about 15 mV in a positive direction. The reason for this movement was due to steric hindrance of counter-ion movement i.e. the excess energy is required for ion-pair formation between the ferrocenium cation in the butyl ferrocenyl derivative and the counter-ion, because the butyl chain of the butyl ferrocenyl derivative prevents the counter-ion from approaching the ferrocene moiety. The surface concentration of these ferrocene derivatives was estimated from the redox charge of the ferrocene moieties[74]. Both the maximum surface concentration (Γ_{max}) and the adsorption rate constants (k_{ad}) on gold decreased as the number of the acyl groups increased. The effect of the butyl group on Γ_{max} and k_{ad} was smaller. The reason for Γ_{max} decrease as the number of carbonyl group increases seems to be due to the decrease in the adsorbate-adsorbate interaction on the introduction of a carbonyl group. This was found to be reasonable as the

attractive hydrophobic interaction between methylene chains is important in the formation of ordered monolayer of the alkanethiol on gold, and the carbonyl group introduction causes a hindrance to this interaction. The k_{ad} decrease with increasing carbonyl group is as a result of the steric effect of the carbonyl group.

Murray et al.[76] measured electron transfer kinetics between a surface-immobilised redox monolayer and a high temperature superconductor (HTSC) electrode at temperatures above and below the superconductor transition temperature (T_c, 119 K). Murray et al. coated a $Tl_2Ba_2CaCu_2O_8$ (Tl_{2212}) with an ultrathin Au film onto which redox monolayers of ferroceneoctanethiol with octanethiol diluent are co-chemisorbed by self-assembly. An alkane chain tunneling barrier separates the ferrocene redox moiety from the metal film/HTSC (figure 1.8).
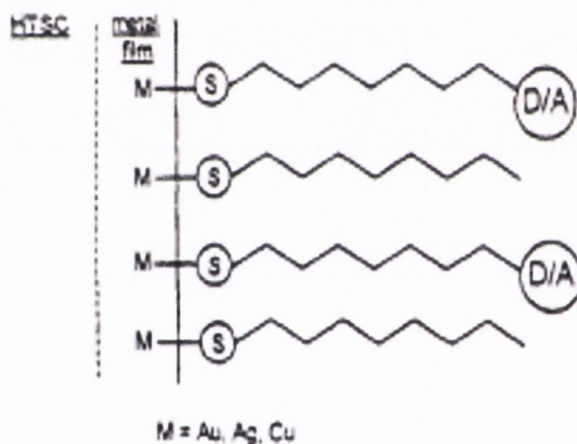
Figure 1.8: *Presents a strategy for tethering electron donor/acceptor species to the surfaces of HTSC electrodes involving chemisorption of self-assembled monolayer of D/A-alkanethiol, diluted with alkanethiol, to the thin Ag or Au film that coats the HTSC.*[76]

Murray et al. showed that the ferrocene monolayers display well defined voltammetry down to 105 K. The electron transfer rate measurements gave only estimated values for the electron transfer rate constant. The estimates at the temperatures employed were k^o= 0.35 s^{-1} (140 K); 0.025 s^{-1} (124 K); 0.007 s^{-1} (121 K) and 0.0008 s^{-1} (118 K). The values for voltammetry and rate measurements were the first of their kind for a molecular monolayer on an electrode in the superconducting state. These results guided adjustment of the alkane chain tunneling barrier to a length appropriate for slower and more accurate electron transfer measurements, even at applied

overpotentials large enough to reduce the electron transfer barrier to values smaller than the electron-pairing energy.

Porter et al.[77] employed an adhesion-based atomic force microscopic characterisation to look at real time monitoring of the electrochemical transformation of a surface bound ferrocene-terminated alkanethiolate monolayer at a gold surface. The measurements were conducted using a monolayer formed by the chemisorption of 11-mercaptoundecyl ferrocenecarboxylate at a Au electrode and a methyl-terminated (octadecanethiolate) monolayer modified gold-coated probe tip. These formed the tip-sample combination, which was used so that changes in the force of adhesion (F_{ad}) could be correlated with the redox transformation of the ferrocenyl group. From their results, Porter found that the one-electron oxidation of the ferrocenyl group of the 11-mercaptoundecyl ferrocenecarboxylate resulted in a decrease in the observed force of adhesion at the microcontact formed by the two different surfaces. Surface tension arguments were used to attribute this change to the decrease in the effective miscibility at the microcontact as a consequence of the oxidation of the ferrocenyl group to the ferrocenium ion.

Creager and Weber et al.[78] employed high-speed CV (0.1 V s^{-1} to 10,000 V s^{-1}) to study the oxidation/reduction kinetics of several ferrocene containing monolayers on gold electrodes. These monolayers were formed by coadsorption of N-(mercaptoalkyl)ferrocenecarboxamide, $[(C_5H_5)Fe(C_5H_4)CONH(CH_2)_nSH$, where n = 7-10, and 15 with mercapto alcohol ($HO(CH_2)_{n+1}SH$ where n = 7-10, and 15]. From these experiments the standard electron-transfer rate constants were obtained as a function of chain length and a value of $k^o = 6.6$ s^{-1} was obtained for n=15. This value being quite close to those reported in earlier work by the authors[71]. From these rate constants a value describing the exponential decay of rate with adsorbate chain length (β) was calculated. Electronic coupling factors, $|V_{AB}|$, describing the bridge-mediated long range coupling between adsorbed ferrocene groups and the underlying gold surface were quantitatively estimated from the rate data. From Creager's results electronic coupling factors varied from a high of 6.5 cm^{-1} for the short chain monolayer (10 bonds in pathway linking ferrocene to the electrode) to a low of 0.06 cm^{-1} for the long chain monolayer (18 bonds linking ferrocene to the electrode).

These factors are in good agreement with work carried out by Closs and Miller[79], who found a value of 6.2 cm^{-1} for an electronic coupling factor in a donor-acceptor molecule in which the bridge is a saturated hydrocarbon (a steroid) with 10 molecules linking the donor and the acceptor.

Ellis et al.[80] employed cyclic voltammetry and X-ray Photoelectron Spectroscopy (XPS) to examine the influence of different chemical pretreatments on the formation and electrochemistry of 11-(ferrocenylcarbonyloxy)undecanethiol and n-decanethiol self-assembled mixed monolayers. Ellis et al. employed two different pre-treatment methods, one was a "hot-etched" treatment which involved the soaking of the substrate in a dilute boiling piranha solution for 1 min, rinsing thoroughly with water, hydrogen peroxide, water, followed by drying in a jet of nitrogen. The second pretreatment was called a "cold-etched" treatment and consisted of sonicating the gold surface in a boiling solution of 50:50 ethanol/chloroform for 5 min, drying in a jet of nitrogen, covering with a room temperature piranha solution for 1 min, rinsing thoroughly with deionised water, hydrogen peroxide, and water, and followed by further drying in a jet of nitrogen. Ellis concluded from the results that the "hot-etched" pretreated substrate provides mixed monolayers of higher surface coverages of the electroactive ferrocene thiol than a "cold-etched" substrate (figure 1.9).
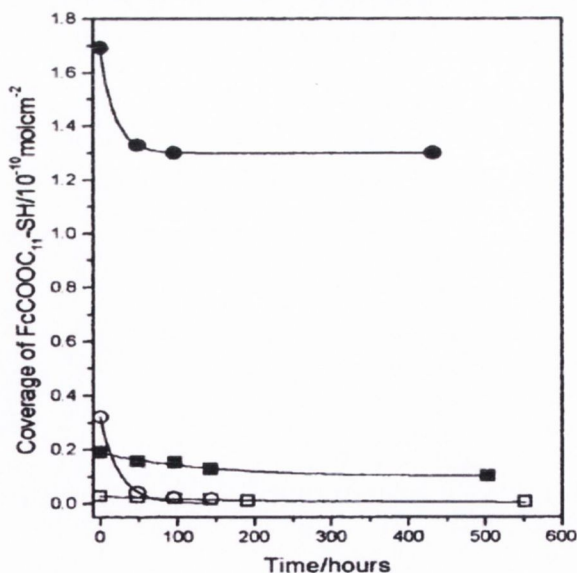
Figure 1.9: *Surface coverage of FcCOOC$_{11}$-SH as a function of immersion time in ethanol for monolayers (48 h adsorption time) formed from 1 μM(1.0/0.0) solution on cold-etched surface (O) and on hot-etched surface (●) and from 1 μM(0.5/0.5) solution on "cold -etched" surface (□) and on hot-etched surface (■) (the solid lines are exponential fits of the data)[80].*

The reason put forward for the "hot-etched" substrate is that it presents a greater percentage of higher binding sites than the "cold-etched" substrate. The higher stability of these binding sites for the ferrocenylalkanethiolate was confirmed by desorption experiments in ethanol. From charging current measurements in cyclic voltammograms comparison of the monolayers on the two pre-treated surfaces suggested that the monolayers formed on the hot-etched surfaces are less permeable than those formed on the cold-etched surfaces (Figure 1.10).
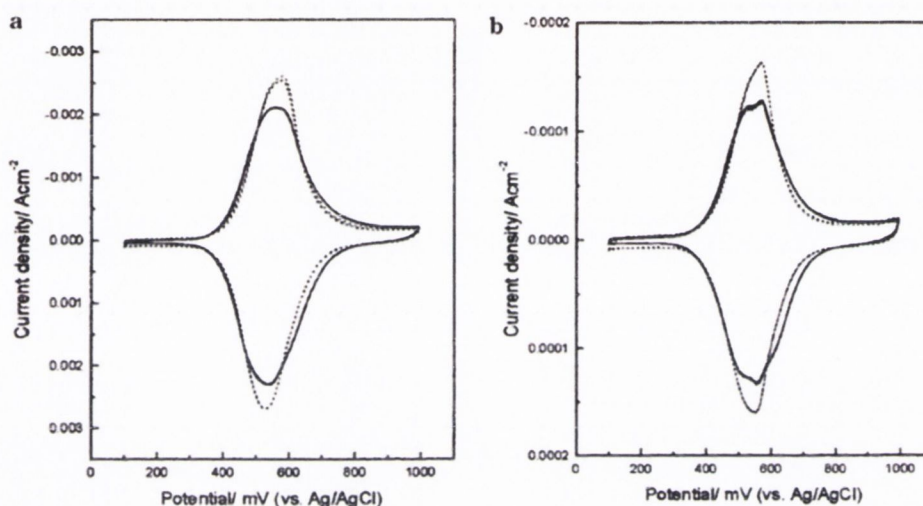
Figure 1.10: *Cyclic voltammograms for a cold-etched surface (dotted line) and a hot-etched surface (solid line) immersed in a 1 mM (1.0/0.0 FcCOOC$_{11}$-SH/C$_{10}$-SH) solution. The scan rate is (a) 10 V/s and (b) 500 mVs^{-1}* [80].

From figure 1.10(a) it is seen that similar ferrocene surface coverages are obtained, however the oxidation/reduction peaks for monolayers formed at the hot-etched surface are broader than the corresponding cold-etched peaks. This is indicative of a greater extent of inhomogeneities of the microenvironment of the ferrocene groups at the former surface. In figure 1.10(b), at a lower scan rate the difference is more marked, where a splitting in the oxidation/reduction peaks is observed in the cyclic voltammogram of the hot-etched surface.

Chung and Lee[81] investigated the reorientation of a ferrocene terminated undecanethiol induced by the coadsorption of dodecanethiol. Chung formed self-assembled monolayers of 11-sulfidoundecyl ferrocenecarboxylate (FcCOO(CH$_2$)$_{11}$SH) and carried out FT-IR external reflection spectroscopy with p-

polarised light on this monolayer. The monolayer was then immersed in a solution of dodecanethiol and further FT-IR was employed. Figure 1.11 presents the infrared spectrum of the monolayer before and after the coadsorption of dodecanethiol.
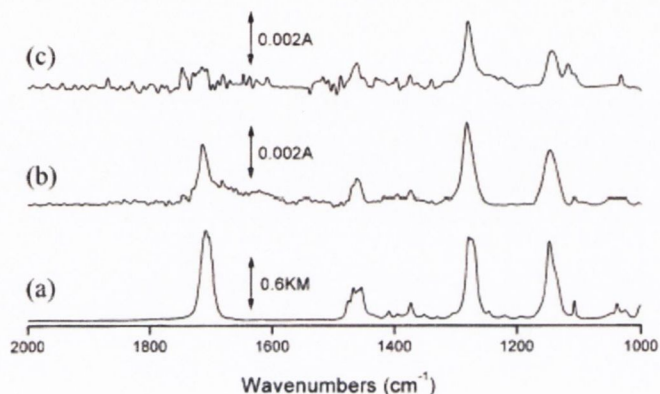
Figure 1.11: *Comparison of the FT-IR spectra of FcCOO(CH$_2$)$_{11}$SH powder dispersed in KCl(DRIFTS) (a), the monolayer of FcCOO (CH$_2$)$_{11}$S on gold (b), and the monolayer of FcCOO(CH$_2$)$_{11}$S on gold treated with CH$_3$(CH$_2$)$_{11}$SH (c).*[81]

Chung reported that presence of reorientation of the monolayer could be inferred by the disappearance of the carbonyl stretching peak. The peak at 1713 cm^{-1} is attributed to the v(C=O) and was intense on the spectrum in figure 1.11(b). On immersion of the monolayer into the dodecanethiol, the intensity of the carbonyl peak decreased (Figure 1.11(c)). Chung implied that the carbonyl group was removed completely or reorientated parallel to the surface. However, C-O stretching peaks at 1282 cm^{-1} [v(C(C=O)-O)] and 1146 cm^{-1} [v(C-C-O)] remained at the same intensity. Chung implied that the incoming dodecanethiol molecules did not replace many of the FcCOO(CH$_2$)$_{11}$SH molecules but rather induced the reorientation of the structure. Chung and Lee postulated that this behaviour was dependent on the relative chain lengths of ferrocene terminated thiol and unsubstituted alkanethiol (Figure 1.12).

Figure 1.12(a) depicts the structure of the monolayer before the coadsorption of dodecanethiol. The addition of dodecanethiol on the monolayer results in C-O single bond on the carbonyl side of the ester being rotated. This meant that the coadsorbed dodecanethiol molecules on gold caused the ferrocenyl group to be pushed upwards in order to make more room for themselves. The resulting structure is shown in figure 1.12(b).
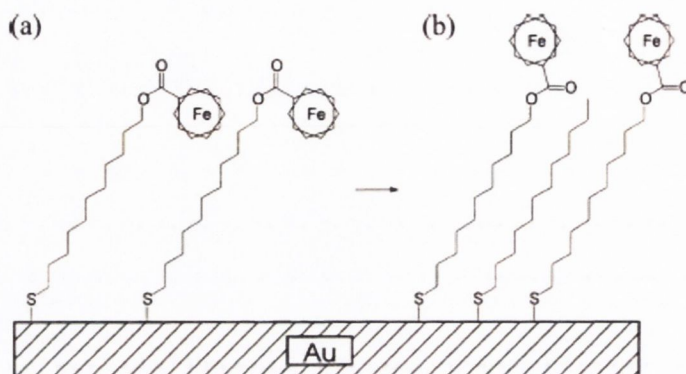
Figure 1.12: *A schematic representation for the reorientation of the FcCOO(CH$_2$)$_{11}$S monolayer self-assembled on gold before the coadsorption of CH$_3$(CH$_2$)$_{11}$S (a) and after the coadsorption of CH$_3$(CH$_2$)$_{11}$S (b).*[81]

Sumner et al.[82] studied the electrochemistry two different series of monolayers, one series has ferrocene groups linked to gold substrate by simple alkane chains and the second series where the two methylene groups in the bridge adjacent to the ferrocene group were replaced by a carboxamide group. The monolayer structures are shown in figure 1.13.

(n = 7,8,9,10)
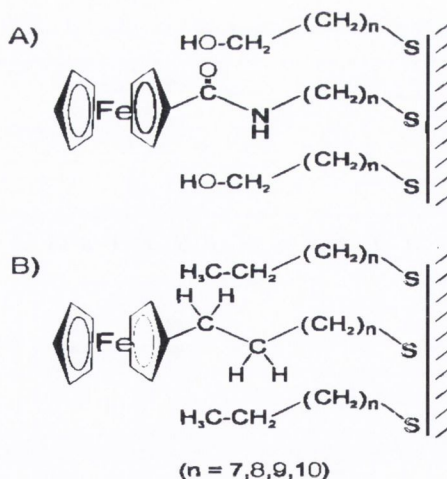
Figure 1.13: *Illustrative structures of (A) mixed monolayers of N-(ω-mercaptoalkyl) ferrocenecarboxamides with ω-mercapto-alkanols, and (B) mixed monolayers of ω-mercapto-alkylferrocenes with alkanethiols on gold*[82].

The standard electron-transfer rate constants for oxidation/reduction kinetics of the ferrocene groups were investigated using a novel ac voltammetry method developed

by Creager and Wooster[83]. Sumner et al. found that the rate constants in both series decreased exponentially as polymethylene chain lengths increased (Table 2). They also found that the rate constants are very similar in the two series when they are compared according to the number of individual bonds in the direct pathway linking the ferrocene group to the gold electrode[10].

Monolayer Components	E_{PEAK} (V)	k_0 (s^{-1})
$Fc-CO-NH- (CH_2)_7 -SH/HO-(CH_2)_8-SH$	+0.572	1.1×10^5
$Fc-CO-NH- (CH_2)_8 -SH/HO-(CH_2)_9-SH$	+0.55	1.5×10^4
$Fc-CO-NH- (CH_2)_9 -SH/HO-(CH_2)_{10}-SH$	+0.563	6.9×10^3
$Fc-CO-NH- (CH_2)_{10} -SH/HO-(CH_2)_{11}-SH$	+0.568	1.3×10^3
$Fc-(CH_2)_9 -SH/CH_3-(CH_2)_8-SH$	+0.362	9.0×10^4
$Fc-(CH_2)_{10} -SH/CH_3-(CH_2)_9-SH$	+0.365	4.0×10^4
$Fc-(CH_2)_{11} -SH/CH_3-(CH_2)_{10}-SH$	+0.362	4.7×10^3
$Fc-(CH_2)_{12} -SH/CH_3-(CH_2)_{11}-SH$	+0.341	1.8×10^3

Table 1.2: *Table of the standard electron-transfer rate constants for ferrocene monolayers[82].*

Sumner suggested from this that the contribution of the carboxamide group to the overall bridge-mediated electronic coupling is not very different from that of a pair of methylene groups i.e. the replacement of a pair of methylene groups with the carboxamide group had only a minimal effect on the rate.

Kalaji and co.[84], presented work that described an *in situ* spectroelectrochemical study of a series of short chain ferrocene derivatives with a carbonyl functionality [$FcCO(CH_2)_n$ SH, with n≤9]. *In situ* subtractively normalized interfacial FTIR spectroscopy (SNIFTIRS) was used to probe structural and orientational changes occurring in the short chain monolayers induced by the redox activity of the ferrocene end group. This technique involves recording difference IR/FTIR spectra at different potentials. By computing (normalized) difference spectra, spectra essentially free of bulk contributions are obtained. Only adsorbed or desorbed species remain present in the differential spectra, usually seen as negative and positive going bands respectively. Figure 1.14 shows the SNIFTIRS spectra obtained from a $(C_5H_5)Fe(C_5H_4)CO(CH_2)_5SH$ monolayer (FcC6) on a Au (111) surface in $HClO_4$.
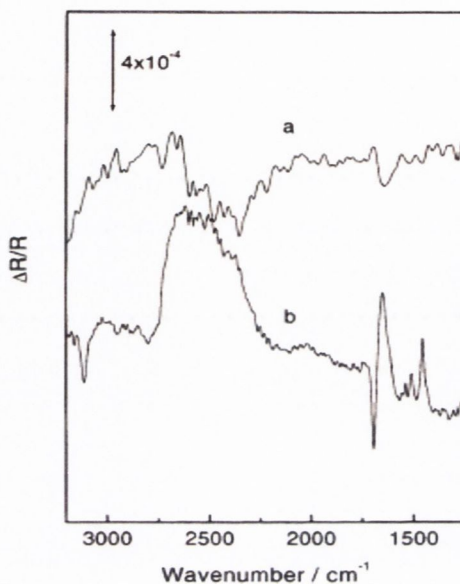
Figure 1.14: *Normalised difference spectra of a Au (111) disc electrode modified with FcC6. The spectra were recorded at (a) 400 mV and (b) 650 mV using p-polarised radiation, in $HClO_4$ (0.5 mol dm^3) in D_2O electrolyte solution. The reference spectrum was recorded at 200 mV.[84]*

The reference spectra were recorded at 200 mV as this is the potential where ferrocene appears in its reduced form. From the spectra it is seen that the oxidation process produces differences in the IR spectra of the monolayer. Kalaji's results showed that the oxidation of the ferrocene groups in the FcC6 monolayer is accompanied by a rotation of the ferrocene groups towards a position where the plane of the cyclopentadienyl rings switches to a position normal to the surface of the electrode. The ferrocene moiety was seen to be the only component of the FcC6 monolayer to move. The movement was a simple rotation around the Fc-C bond. Figure 1.15 depicts the rotation of the ferrocene group around the Fc-C bond as oxidation occurs. Figure 1.15 (c) shows that rotated molecule B and it can be clearly seen that the plane of the cyclopentadienyl rinds was perpendicular to the surface in the oxidised state.
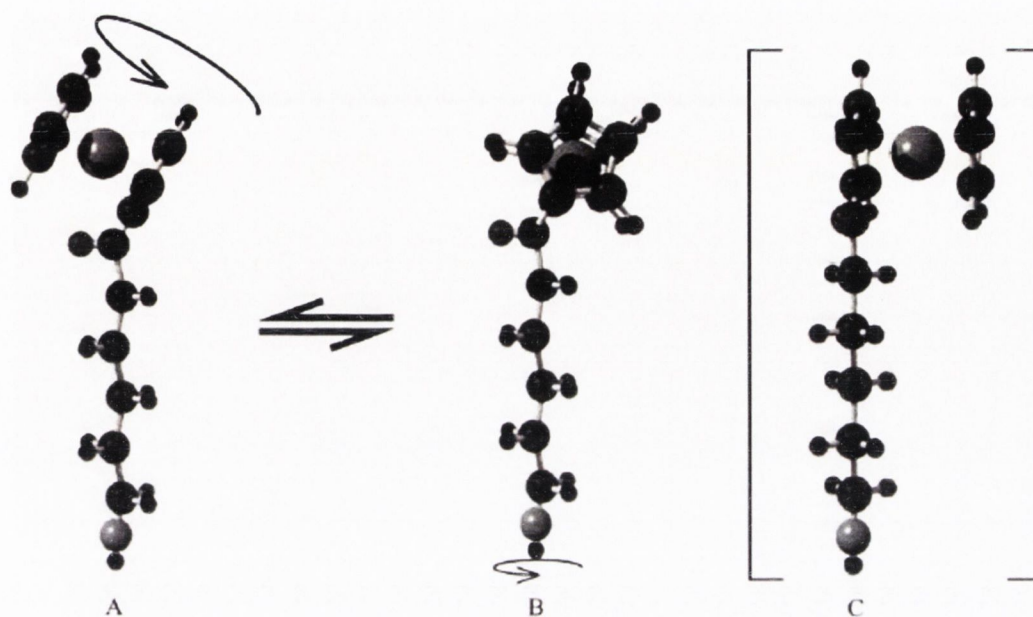
Figure 1.15: *A model showing the rotation of the ferrocene group upon oxidation (A→B) and a view of B after rotation of the whole molecule (B→C).*[84]

Napper et al.[85] employed cyclic voltammetry to measure ferrocene self-assembled mixed monolayer electron transfer rate constants. The mixed monolayers were formed by coadsorption of a redox-active ferrocene based alkanethiol $[(\eta^5C_5H_5)Fe(\eta^5C_5H_4)\text{-}CO_2(CH_2)_5X(CH_2)_6SH$, where X = -CH$_2$- or –O-]$_2$ and a diluent alkanethiol $[CH_3(CH_2)_4Y(CH_2)_6SH$, where Y = -CH$_2$- or –O-]. Napper et al. found that the replacement of a single methylene group by an ether link in the electroactive thiol causes a marked decrease in the rate constant. This result arose from a decrease in the electronic coupling between the gold surface and the ferrocene redox couple. The decrease in coupling arose from the exchange interaction and energetic changes in the ether-linked molecule. The introduction of an ether linkage into the electroactive thiol chain led Napper to the observation of a reduced rate constant. It was seen that the rate constant for the ether diluent was reduced by approximately 4.2 times in value, from 35 s^{-1} to 8.4 s^{-1}. The rate constant for the alkane diluent decreased from 55 s^{-1} to 12 s^{-1}, a reduction of 4.6 times in value. This result was suggestive of the importance of intermolecular interactions when determining the electronic coupling through compact films.

Sumner and Creager[86] investigated the redox chemistry of ferrocene groups in alkanethiolate-based monolayer films on gold electrodes using ac voltammetry. However, they deviated from normal self-assembled monolayer structuring by positioning the ferrocene groups within the interior of the monolayer. Sumner and Creager considered the redox kinetics for the ferrocene groups where the groups were exposed to the electrolyte solution at the monolayer-solution interface, the usual self-assembled method, where a monolayer is formed with ferrocene-capped and nonferrocene-capped alkanethiol chains of the same length. In the case where the ferrocene groups are "buried" within the monolayer interior by forming the monolayer from the same ferrocene-capped alkanethiols as exposed monolayers, but with nonferrocene-capped coadsorbates with much longer alkane chains. Figure 1.16 illustrates the two methods and the monolayers in question.
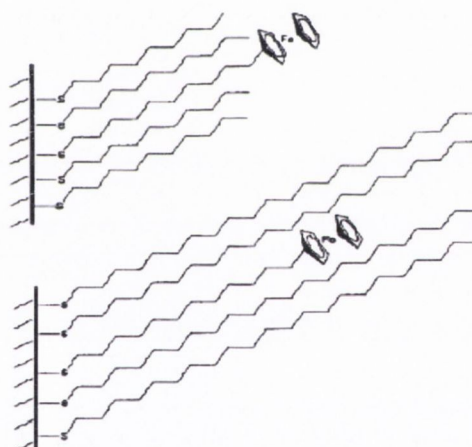
Figure 1.16: *Illustrative structures of ferrocene-containing alkanethiolate monolayers: (top) Fc-$C_{10}H_{20}$-SH/$C_{10}H_{21}$-SH; and (bottom) Fc-$C_{10}H_{24}$-SH/$C_{20}H_{41}$-SH.*[86]

Sumner and Creager results showed that ferrocene groups that were buried in the monolayer displayed oxidation-reduction potentials that were strongly shifted in a positive direction relative to potentials obtained for monolayers where the ferrocene groups were exposed to the electrolyte solution. However, their main finding was that the redox kinetics associated with ferrocene oxidation/reduction was far more sluggish when the ferrocene groups were buried within the monolayer in comparison to monolayer where the ferrocene groups were exposed. It was observed that $k =$

40,000 s^{-1}, for ferrocene oxidation/reduction in a ferrocenyl-decanethiol coadsorbed with decanethiol monolayer, whereas $k = 200$ s^{-1} for a monolayer of ferrocenyl-decanethiol coadsorbed with 1-mercaptoeicosane ($C_{20}H_{41}SH$). Sumner and Creager found that the differences in behavior for "buried" and "exposed" ferrocene groups depended critically upon the electrolyte anion size, i.e., ferrocene oxidation/ reduction was almost completely inhibited when sodium poly(p-styrene sulfonate) was used as the electrolyte. These results were interpreted in terms of a reaction which involved a coupled electron-transfer and ion-transfer. This meant that electron transfer from ferrocene to the electrode must occur alongside anion transfer from the electrolyte to the oxidized ferricenium site in the monolayer, and the rate of electron transfer can depend critically upon the rate of ion transfer into the monolayer.

Shimazu and co-workers[87], examined mixed monolayers of ferrocenyloctanethiol (FcC$_8$SH) and alkanethiols of various chain lengths, which were constructed after predetermining the surface composition by the initial coverage of Pb underpotentially deposited on a bare gold electrode during first step of the preparation. Single waves observed in the reductive desorption voltammograms show no formation of single component domains.
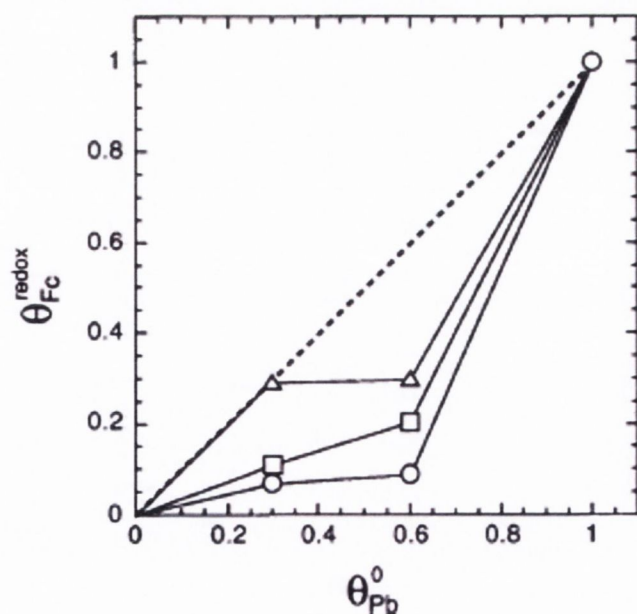
Figure 1.17: *The fraction of the electroactive FcC8SH as a function of the initial Pb coverage. Alkanethiols: C8SH (triangle), C12SH (square) and C18SH (circle). The dotted line represents the surface coverage of Fcc8SH expected.[87]*

Comparison of the desorption charges and oxidation charges of the FcC_8SH monolayer, which were similar at 55.1 μC cm^{-2} and 44.5 μC cm^{-2} respectively indicated that in the single component molecules all FcC_8SH molecules were electroactive. Shimazu then integrated the current during the redox reaction of the mixed monolayers to obtain the redox charges, Q_{redox}. The surface fraction of the electroactive FcC8SH ($\theta^{redox}{}_{Fc}$) is plotted as a function of the initial Pb coverage. The surface fraction is defined as $\theta^{redox}{}_{Fc} = Q_{redox}/ Q_{redox}{}^0$ where $Q_{redox}{}^0$ is the charge due to the redox reaction of the single-component FcC8SH monolayer (figure 1.17). The surface fraction of the electroactive FcC_8SH was found to be smaller than expected. These results indicated that monolayers showed a considerable amount of the ferrocene moieties which were not electroactive. Shimazu also showed that the mass change during the redox reaction of the ferrocene was greater than that expected from the simple association of the ferrocenium cation with the electrolyte anion, and in addition was greater than that for the mixed monolayers prepared from mixed solutions of the precursor thiols. The mass per electron (mpe) for the single-component FcC_8SH was found to be 157 g mol^{-1}. For the mixed $FcC_8SH/C_{18}SH$ monolayers a value of 449 g mol^{-1} is obtained. Shimazu interpreted that the mass change was due to the incorporation of the anion and water upon oxidation, into the "pocket" surrounded by alkanethiol ($C_{18}SH$) molecules and a FcC_8SH molecule at the bottom.

Smalley et al.[88] investigated the standard heterogeneous electron-transfer rate constants between substrate gold electrodes and ferrocene redox couples attached to the electrode surface by various chain lengths of an alkanethiol bridge as a constituent of a mixed self-assembled monolayers which were measured by as a function of temperature. The ferrocene was directly attached to either the alkanethiol bridge or through an ester (CO_2) linkage. The rate constants for long bridge lengths (containing 11 or more methylene groups) were measured using either chronoamperometry or cyclic voltammetry; the rate constants for shorter bridges were measured using the indirect laser induced temperature jump technique. Analysis of the distance (bridge length) dependence on the preexponential factors obtained from the Arrhenius analysis of the rate constant versus temperature data demonstrates a clear limiting

behaviour at a surprisingly small value of this preexponential factor. This limiting behaviour is independent of both the identity of the redox couples and the nature of the linkage of the couple to the bridge. The possible explanations for this behaviour include the possible effects of bridge conformational flexibility upon the electron transfer kinetics.

In recent years, the study of ferrocenyl alkanethiols has progressed towards the study of biferrocene and its corresponding alkanethiols. Dong et al. was one of the first groups to undertake this area of study. Dong et al.[89] studied the spectroscopic and electrochemical characterisation of chemisorbed biferrocenyl alkanethiols on Au (111) surface. Figure 1.18 illustrates the biferrocene derivatives employed in the study. The characterisation of several other techniques including, TEM, UV-vis, and NMR were also included.

Figure 1.18: *Illustration of the biferrocene derivatives employed.*

The biferrocenyl alkanethiol monolayers were formed using the same self-assembly method as employed for the single ferrocenyl alkanethiol self assembled monolayers. The thiol monolayers were prepared by soaking Au(111) electrodes in ethanol solutions of a biferrocene-terminated thiol (1a-c) and unsubstituted thiol at 1mM total thiol concentration. Dong et al. observed two successive reversible one-electron redox waves for the biferrocenyl alkanethiol Au nanoclusters and the biferrocenyl alkanethiol monolayers on Au (111) (figure 1.19).

From the graph it can be seen that the positive and negative current peaks for each redox wave occur at almost the same potential, and the peak current increases almost linearly with the scan rate. Dong also reported that repeated cyclic voltammetry scanning does not alter the voltammograms, demonstrating that these biferrocenyl alkanethiol self assembled monolayers are stable to electrochemical

cycling. The surface coverages of the biferrocenyl alkanethiol self assembled monolayers were also calculated from the voltammograms. For the monolayers of $BiFc(CH_2)_5SH$ a surface coverage of 2.05×10^{-14} mol cm^{-2} when the mole fraction of biferrocene ($x_{Bifc} = 1$) and $(C_5H_{11})BiFc(CH_2)_5SH$ has a surface coverage of 3.27×10^{-14} mol cm^{-2} when the $x_{Bifc} = 1$. However as the x_{Bifc} decreases so too does the surface coverage. The standard electron transfer rate constant (k_s) was calculated from the splitting between the oxidation and reduction peaks. Dong discovered that the k_s of the second redox wave is always larger then the k_s for the first wave. Dong reasoned that in the existence of the stronger Fe-Fe interaction, the oxidation potential of the second wave shifted to a higher voltage and the reduction voltage of the second wave shifts to a lower voltage, when the charge density of the biferrocenyl moiety caused by the oxidization of one of the ferrocenyl moieties increases i.e. the intermolecular electron hopping mechanism may play a role in determining the magnitude of the k_s value.
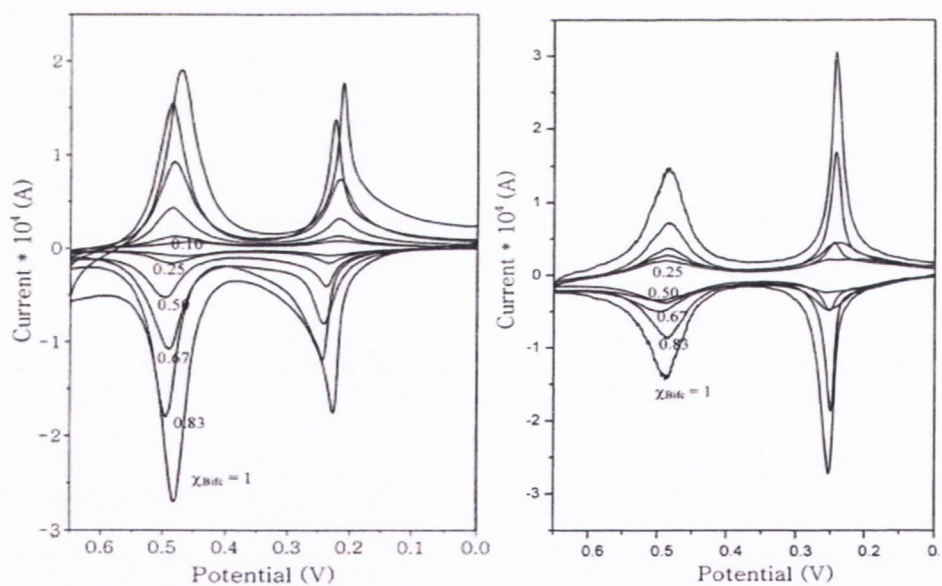
Figure 1.19: *Cyclic voltammograms in 1 M HClO$_4$ of mixed monolayers of BiFc(CH$_2$)$_5$SH and 1-pentanethiol (left) and mixed monolayers of (C$_5$H$_{11}$)BiFc(CH$_2$)$_5$SH and 1-pentanethiol (right). Both sets of monolayers are formed from ethanol solutions containing various mole fractions (x$_{Bifc}$) of BiFc(CH$_2$)$_5$SH. Scan rate = 100 mVs^{-1}.*[89]

However, in the last year the use of ferrocene alkanethiols has switched again, this time towards developing methods to probe the nature and structure of nanoscale

environments. The behaviour of ferrocene-containing monolayers can be used to probe nanoscale organization and was investigated by Chambers et al[90]. This group reported a cyclic voltammetry investigation of the internal, hydrogen-bond-driven phase separation of amide-containing thiols and alkanethiols. Chambers investigated amide-containing thiols with a terminal ferrocene carboxylate functional group in two binary monolayers, one homogeneously mixed and the other phase separated. They found that for homogeneously mixed self-assembled monolayers, the current-voltage behaviour was nearly ideal at low ferrocene coverage. In addition, the ferrocene concentration on the surface was found to be directly proportional to the amount of ferrocene-terminated thiol in the soaking solution. The phase-separated monolayers at low ferrocene coverage, in comparison, exhibited broader oxidation and reduction peaks, and the ferrocene adsorbate concentration in the soaking solution. The data when taken together demonstrate that the electrochemical response of tethered redox probes can be used to detect internal hydrogen-bond-driven nanoscale phase separation of amide-containing thiols and alkanethiols.

1.7 Structure of SAMs

SAMs have been formed using different systems. The "pair" of the chemisorbing headgroup of the molecule and the substrate is the defining feature. As a result of this, the "chemisorption pair" is used to classify the specific system used in this body of work. The forces that conspire to determine the structure of alkanethiol monolayers can be grouped into three classes, interactions between thiol head groups, corrugated dispersion forces between alkyl chains and interactions between alkanethiol endgroups. The balance of these forces determines the specific molecular packing habit. The SAM system discussed here is that of thiols on Au (111), which is one of the most popular SAM systems. Some other frequently systems in use are shown in figure 1.20 [46].

Figure 1.20: *Some frequently used compounds for SAMs. For purpose of illustration, chain length is specified to n = 10. (1) n-alkanethiol: HS-$(CH_2)_{n-1}$-CH_3; (2) α,ω-alkanedithiol: HS-$(CH_2)_n$-SH; (3) ω -mercaptoalkanol: HS-$(CH_2)_n$-OH; (4) ω-mercaptoalkane carboxylic acid: HS-$(CH2)_{n-1}$-COOH;* [46]

Thiols on Au (111) are used to depict the different features characterizing the SAMs structure. The structure of the molecular backbone can be illustrated (Figure 1.21). This backbone includes a possible tilt angle with respect to the surface normal, the tilt direction and the tilt angle. The molecular backbone does not necessarily need to be extended fully, in principle. This is due to the possibility that alkane chains might be bent or exhibit gauche effects. Also, different backbones have different degrees of freedom to describe their conformational state.
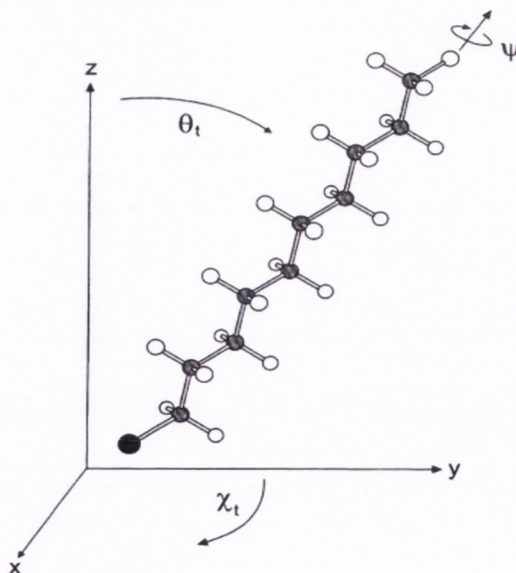
Figure 1.21: *Schematic of angular degrees of freedom of alkanethiol (bound to substrate via thiol group, with alkyl chain fully stretched). Angle θ_t refers to tilt of molecular axis with respect to substrate surface normal. χt defines tilt direction, i.e., it is derived from projection of molecule in substrate plane. χ_t is undefined for θ_t = 0. Twist angle, ψ, describes rotation about axis of molecule.* [46]

1.7.1 Alkanethiols on Au (111)

Alkanethiols on Au (111) have become a SAMs model system for a number of reasons. Firstly, Au is relatively inert and easy to clean. Secondly, the Au (111) surface is the lowest energy surface as reflected in the tendency of thin film growth to propagate in the (111) direction. Thirdly, the Au-S interaction is very strong and the monolayer formed will be stable. Therefore, since evaporated Au films are easy to prepare and because technological applications are more likely to be rely on thin films than single-crystals, the Au (111) surface is the optimal surface.

1.7.2 Alkanethiols as the archetypal case

N-alkanethiols are considered the simplest case among the thiols on Au(111) because they are relatively simple compounds, from a chemical view and are fully saturated. These n-alkanethiols exhibit all necessary features and degrees of freedom typical for SAMs.

1.7.3 Alkanethiol Molecular Lattice

For many years the structure of alkanethiol SAMs grown on Au (111) surfaces has been the source of much research. This section traces this research from its initial investigations in the late 1980's to the present day. The Au (111) surface is also described below.

1.7.3.1 Au(111) Surface- Herringbone Reconstruction

A (111) lattice plane within the face centred cubic (fcc) Au crystal is a hexagonal array of atoms all in equivalent positions. Gold's lowest energy surface is Au (111), as seen in the tendency of thin film-growth to propagate in the (111) direction[91] . If Au retained this surface; the flat terraces between atomic steps would appear featureless. Instead, the surface of the Au reconstructs i.e. it shortens its nearest neighbour distances to compensate for the smaller number of neighbours. Au is the only fcc metal whose (111) surface reconstructs. The reconstruction of Au(111) surface is not a conventional one; but is a complex system consisting of both short range and long range structure termed the herringbone pattern. This herringbone

reconstruction offers strikingly ordered adsorption and nucleation sites on the surface. On analyzing an Scanning Tunneling Microscopy (STM) image of the Au surface, it is seen that, for the reconstructed Au(111) short range surface, 23 gold surface atoms are packed on 22 bulk lattice sites along the direction in a unit cell resulting in uniaxial contraction of 4.4% relative to bulk layers[92].
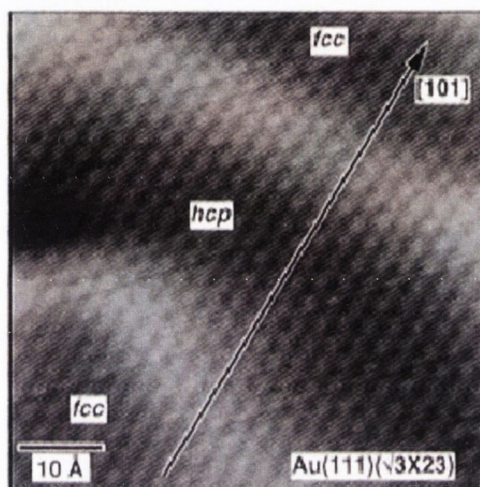
Figure 1.22: *Constant-current STM topograph of bare Au(111) herringbone-reconstructed surface showing quasihexagonal arrangement of Au atoms and bright ridges due to variations in registry between surface and subsurface layers. Atomic rows deviate from linearity due to partial stacking fault in hcp regions (ABA stacking).*[93]

This contraction causes variations in registry between the surface and subsurface atomic layers such that the stacking arrangement alternates between normal, unfaulted ABC stacking (face centred cubic) and faulted ABA (hexagonal closed packed), with faulted and unfaulted regions delineated by rows of bridging Au atoms, shown in figure 1.22[93]. These bridging rows are manifest in STM as elevated ridges aligned with substrate (121) directions[94]. They pair forming a ($\sqrt{3}$ x 23) surface unit cell that can adopt 1 of 3 orientational registries. Figure 1.23 shows a constant-current UHV STM topograph of the same herringbone-reconstructed surface. It also includes a ball model of the single ($\sqrt{3}$ x 23) surface unit cell.
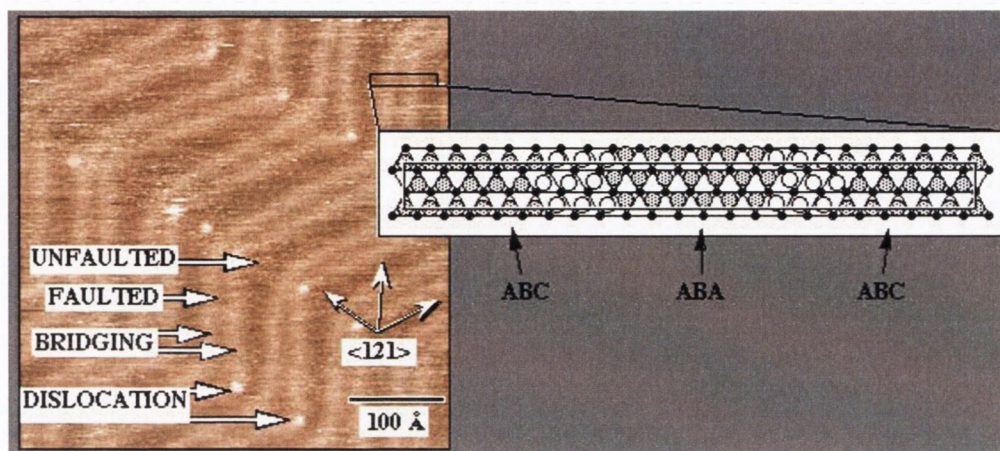
Figure 1.23: *Constant-current UHV STM topograph of bare Au(111) herringbone-reconstructed surface. Enlarged area shows ball model of a single (√3x 23) surface unit cell. Surface layer is 4.4% uniaxially compressed. Compression causes surface-to-subsurface atomic registry to vary from unfaulted (ABC) stacking, to bridging, to faulted (ABA) stacking, to bridging, and back to unfaulted stacking. Bridging rows adopt alternating 60E bends, half of which contain surface-confined dislocation.[94]*

1.7.3.2 Early Molecular Structure Studies

The forces that conspire to determine the structure of alkanethiol monolayers can be placed into three classifications: Firstly, interactions between thiol groups and the corrugated Au lattice. Secondly, dispersion forces between the alkyl chains, and, finally interactions alkanethiol endgroups. It is the balance of these forces that will determine the specific molecular packing habit. Electron Diffraction was employed to carry out early structural studies. These studies reported an incommensurate (7 x 7) molecular overlayer for $AuC_{21}CH_3$[95]. Later studies reported that the correct interpretation of the Bragg reflections indicates a commensurate (√3 x √3)R30° structure (figure 1.24).

The adsorption is said to be commensurate as the molecules adsorb in a pattern that is in exact correspondence with the surface atoms. When the alkanethiol molecules adsorb on the Au (111) surface they are in the 3-fold hollow sites. However, they are too large to fit every vacant site, so they seem to be spaced into every other site as suggested in figure 1.24. Simple geometry indicates that the distance between adjacent adsorbate alkanethiol molecules is √3 times the Au to Au

spacing. Also, a row of adsorbate molecules is at an angle of 30° with respect to a row of Au atoms in the underlayer[96].
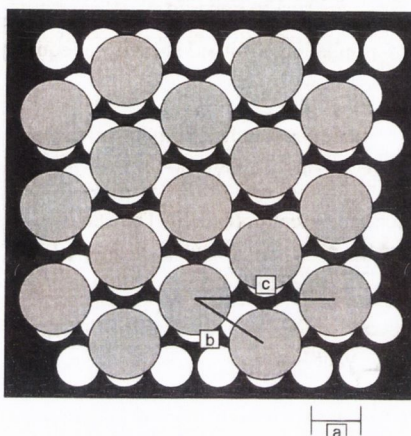
Figure 1.24: *Schematic representation of a adsorbed layer with a (√3 x √3)R30° structure on a Au (111) surface* [96]

This is a 30° rotation of the incommensurate (7 x 7)[97]. Infrared (IR) adsorption studies have confirmed that alkanethiol monolayers are dense and solid like. IR also highlighted that the thiols are tilted ~30° off of the surface normal and that the planes defined by the all-transhydrocarbon backbone exist in 2 dissimilar twist azimuths[40]. These structural analysis tools are all spatially averaging and have, therefore, left unanswered questions about, number, nature and structure of surface defects. Scanning probe microscopy studies on alkanethiols have been used to answer these questions pertaining to local structural features. Porter et al. were among the pioneering groups in this area. Porter observed the hexagonal (√3 x √3)R30° lattice structure for chains with n = 2, 4 – 17 using both atomic force microscopy (AFM)[98]and scanning tunneling microscopy (STM)[99]. Dubois employed low energy electron diffraction (LEED)[100] and observed the same structure for n < 3 whereas for 4 < n < 12 they reported larger unit cells [(m√3 x √3)R30°, where m is an integer between 4 and 6 depending on length of chain]. Both Porter and Dubois assigned the threefold hollow site as the preferred adsorption site. Poirier and Tarlov have also performed STM measurements that clearly show that the surface of these monolayers

exhibit a repeating pattern of bright and dark spots that correspond to a c(4 x 2) superlattice of a basic (√3 x √3)R30° overlayer[101]. This is shown in figure 1.25.
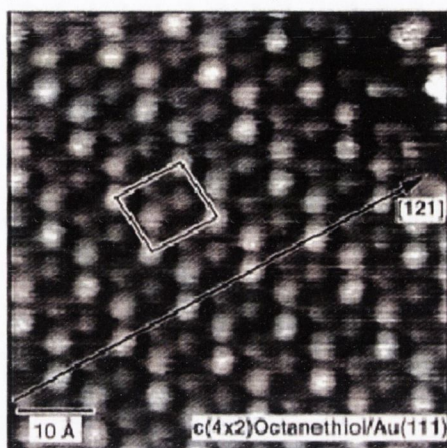
Figure 1.25: *Constant-current STM topograph of octanethiol monolayer on Au(111). Au reconstruction is lifted and alkanethiols adopt commensurate crystalline lattice characteriized by a c(4x2) superlattice of a (√3 x √3)R30°.[101]*

Employing low energy atom diffraction (LEAD), with He as the atom, Camillone et al.[102] suggested an orthorhombic unit cell that comprises of four thiols arranged as two like pairs, this is consistant with IR data. Camillone's orthorhombic primitive unit cell has dimensions of 3a x 2√3a [a = 2.884Å, the Au lattice constant] and can be equally described as a c(4 x 2) superlattice of a (√3 x √3)R30° hexagonal lattice. The structure was subsequently confirmed by grazing incidence X-Ray diffraction (GIXD)[103]. Interestingly the c(4 x 2) superlattice was not reported in the initial STM study[99]. However, it was seen in the later studies which used high impedance tunneling junctions[101].

Figure 1.25 represents an image with molecular resolution of an octanethiol monolayer on Au(111) with the rectangular primitive cell outlined. Each bright spot indicates an individual thiol molecule. The modulation in intensity is reflective of the presence of 2 discrete thiol conformations and their spatial arrangements agree with the previous He diffraction and X-Ray diffraction measurements.

In addition to the spatial arrangement highlighted in figure 1.25, it has been proposed by Delamarche et al.[104] using STM that several molecular conformations co-exist in SAMs at room temperature. They found that some conformations are similar are similar to bulk alkanes; others confirm the model provided on H-scattering

and X-Ray diffraction by Camillone. Delamarche showed that the exact determination of the surface corrugation allowed the identification of two new variants of the c(4x2) superlattice and one characterized by a ($\sqrt{3}$ x $\sqrt{3}$)R30° primitive unit cell and their explanation with molecular models.

This suggestion of polymorphism, however is contradicted by the absence in GIXD of certain reflections that are forbidden by the c(4x2) symmetry shown in figure 1.25, but are allowed by the proposed symmetries shown by Fenter[105,106]. Interpretation of the internal structure of the unit cell is complicated by morphological limitations of STM[107]. "Convolution" of a cylindrically asymmetric tip with the various orientational and tilt domain can give the untrue impression of disparate internal structure.

The two discrete molecular features comprising the unit cell were originally attributed to an alternation of the plane define by the all-trans hydrocarbon backbones, a model consistent with the IR data (figure 1.26)[40,108,-110].
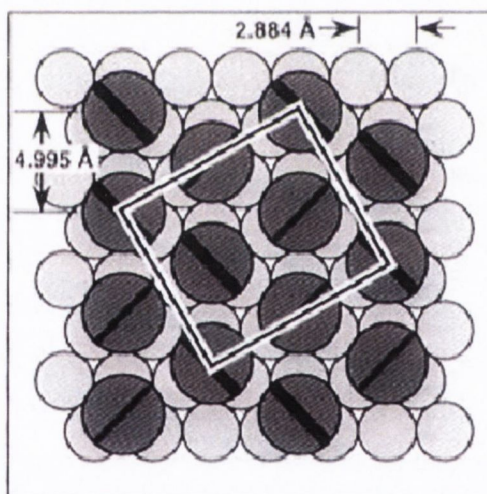
Figure 1.26: *Model of commensuration condition between alkanethiol monolayer (large circles) and bulk terminated Au surface (small circles). Diagonal slash in large circles represents azimuthal orientation of plane defined by all-trans hydrocarbon chain.*

Fenter[111] proposed that the origin of the superstructure could be attributed to head group- substrate interactions and proposed a unit cell with two pairs of non equivalent sulfur atoms, each pair had one atom on the threefold hollow site and one on the bridge site, at relatively short distances from each other. Fenter also looked at the

effect of chain length on 2-Dimensional packing structure for chains of n between 10 and 30. The group obtained two different systems for n<14 and for n>16. The difference was distinguished by the tilt angle of the chains, caused by the balance between the interactions of the interchain and the substrate-headgroup. Fenter did however, observe the ($\sqrt{3}$ x 2$\sqrt{3}$) superstructure for all the alkanethiols measured in their studies.

Other studies using microscopy techniques on shorter chains (n < 6) have reported several striped phases. Dishner et al.[112] observed in addition to a ($\sqrt{3}$ x 2$\sqrt{3}$) structure, a (2$\sqrt{3}$ x $\sqrt{3}$)R30° striped phase for methanethiol SAMs. Voets[113] looked at the observation of (p x $\sqrt{3}$) structures and evidence for dimerised sulfurs on the substrate. The structure seemed to question the ($\sqrt{3}$ x $\sqrt{3}$)R30° structure. Using STM, Voets imaged alkanethiols on Au for (4≤n≤8). He discovered (p x $\sqrt{3}$) structures for n≤6 and the ($\sqrt{3}$ x $\sqrt{3}$)R30° for n≥7 both for high densities of (22 ± 2)Å^2 per molecule indicating a dependence of structure on chain length. They reported striped phases for the n=4 -6 with unit cells (p x $\sqrt{3}$) [p=3 for n=4,5 and p=4 for n=6] on Au(111).

More recent studies have been computational studies. Yourdshahyan et al.[114] performed first-principles calculations based on density–functional theory (DFT) to study adsorption of n-alkyl thiolates on the Au(111) surface. They showed that thiol molecules adsorbed on the Au(111) surface with different coverages and chain lengths chemisorb on the *fcc* threefold hollow site and not the *hcp* site as previously reported.

Using a similar method, Grönbeck et al.[115] also reported that the fcc threefold hollow site was the most stable configuration. It was also shown that there is a difference between fcc and hcp hollow sites, which is not easily detected in calculations based on a limited number of Au atoms used for the substrate.

However, Hayashi et al.[116] and Vargas et al.[117] reported the bridge site as the most stable adsorption site. Vargas et al. studied the coverage dependence of the adsorption energy for different adsorption sites. The group identified a ($\sqrt{3}$ x 2$\sqrt{3}$) superlattice with the sulfur atoms sitting on two inequivalent bridge sites. This ($\sqrt{3}$ x 2$\sqrt{3}$) was energetically indistinguishable from the ($\sqrt{3}$ x $\sqrt{3}$)R30° hexagonal lattice at full coverage.

Fischer et al.[118] focused attention on decanethiols in Au (111) (where long chains were described with classical potentials, which are coupled to quantum description of the headgroup-substrate interaction) and discovered bridge and bridge-like sites for the sulfurs, resulting in the c(4 x 2) structure. Franzen[119], addressed the issue of the chain length dependence and discovered that methylthiol differs from the longer chain thiols, but that ethanethiol would be a reasonable model.

Hammer and Molina[120] investigated an altogether different model, involving vacancies on the Au surface. However, work by Kondoh[121] ruled this theory out by his experimental data on methylthiols. It is noted that the model is also inconsistent with the experimental data on decanethiols, in specific terms the scans of the "specular rod" (a significant number of vacancies would result in differing data on the "specular rod"), irrespective of the model employed for thiol structure.
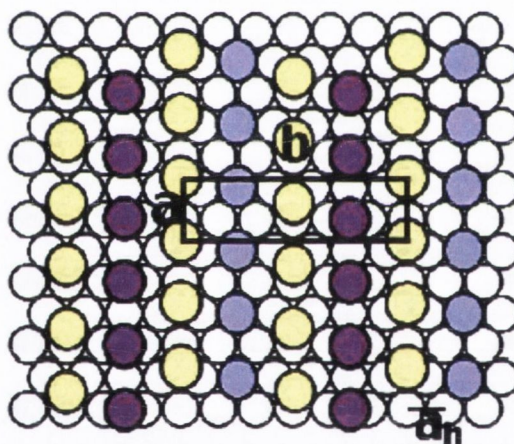
Figure 1.27: *Schematic model describing a new 6x√3 superlattice observed after phase transitions from the c(4 x 2) phase. The rectangular unit mesh is composed of four alkanethiol molecules, and the lattice constants of the unit cell are a = √3a_h = 4.9 Å, b = 6ah = 17.5 Å, where a_h = 2.89 Å and denotes the interatomic spacing of the Au(111) lattice. White circles represent Au atoms, and colored circles represent alkanethiol molecules adsorbed on Au(111).*[122]

In very recent studies, Noh and Hara[122] using STM investigated the time-dependant phase transitions of closely packed alkanethiol self assembled monolayers on Au (111). They reported phase transitions from the c(4 x 2) phase to a new (6 x √3) phase after long term storage of alkanethiol SAMs at room temperature. This new phase is shown in figure 1.27. They found that c(4 x 2) phase is still in non-

equilibrium state, though earlier studies regarded the c(4 x 2) phase to be in equilibrium state.

Liu et al.[123] reported on STM [under ultrahigh vacuum (UHV) conditions] investigations of structures and phase transitions of annealed decanethiol monolayers on Au (111) surfaces. They found that for freshly prepared decanethiol SAMs at saturation coverage's, that the highest density phase, the ($\sqrt{3}$ x $\sqrt{3}$)R30° phase and the c(4$\sqrt{3}$ x 2$\sqrt{3}$)R30° superlattice are the only stable ordered structures below the melting temperature. They also reported that mild annealing below the melting temperature results in an increase in the size of crystalline domains and disappearance of vacancy islands.

O' Dwyer et al.[124] performed studies of self assembled monolayers of 1-nonanethiol on sputtered Au surfaces using AFM and STM. They showed by STM that the c(4 x 2) superlattice reverts back to the (3 x 2$\sqrt{3}$) structure when imaged under non-contact AFM conditions. The reason for this is twofold; firstly, the chance in the twist of the alkyl chains induced by the attractive force interaction varies the surface topography. Second, an alteration in the force interaction between the tip and the surface depending on the tip-surface distances induces the apparent structural change.
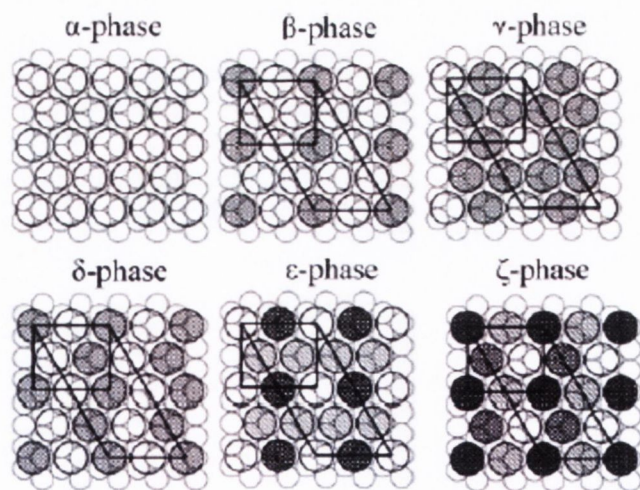
Figure 1.28: *($\sqrt{3}$x $\sqrt{3}$) structure (á phase) and different phases of c(4 x 2) of C12 SAMs. Higher molecules are shaded dark. The phase observed here is denoted as the ζ phase.[126]*

Godin et al.[125] investigated SAMs grown on large-grained gold by employing STM. This imaging revealed the c(4 x 2) superstructure of the ($\sqrt{3}$ x $\sqrt{3}$)R30° lattice, which is consistant with a crystalline dodecanetiol SAM in the vertical standing up phase.

Lussem et al.[126] looked at self assembled monolayers of dodecanethiol grown onto (111) oriented gold by vacuum phase deposition. Using ultrahigh vacuum STM, they showed that the monolayer films consist of domains that exhibit the c(4x2) overstructure of the hexagonal ($\sqrt{3}$ x $\sqrt{3}$)R30° of alkanethiols on gold. However, by looking at higher resolution scans they discovered a new phase c(4 x 2) structure consisting of four inequivalent molecules that display different heights in the STM images. Figure 1.28 depicts the different arrangements of apparently higher and lower molecules. The α-phase is the normal ($\sqrt{3}$ x $\sqrt{3}$)R30° structure without any superlattice, the β,γ and δ phases consist of molecules with two different heights. In high-resolution images, the c(4 x 2) reconstruction can be resolved, and are shown in figure 1.29 and 1.30.
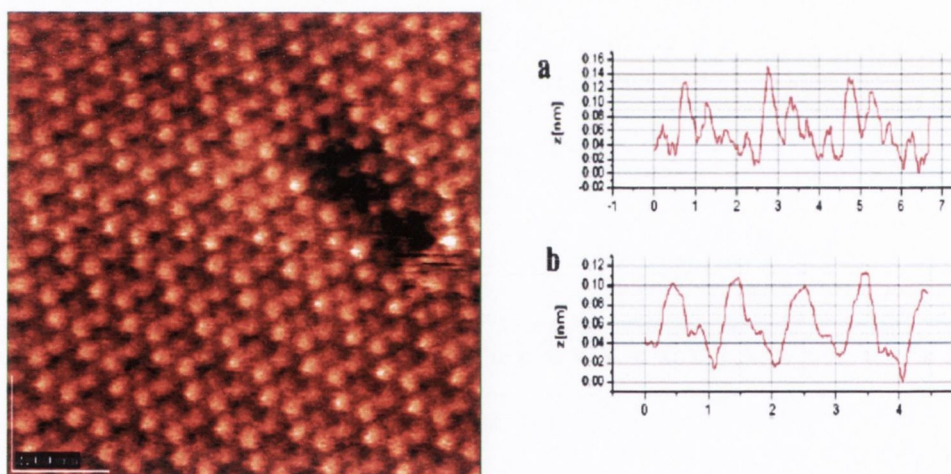
Figure 1.29: *phase of the c(4 x 2) structure of the C12 SAM. The film is grown at an exposure of 27 000 Langmuir. V_t = 1.59 V, I_t = 50 pA; image size, 9.7 x 9.7 nm$_2$.*

Two different phases of c(4 x 2) can be identified; the normal δ-phase with two different heights (Figure 1.29) above and a new phase with four different heights (Figure 1.30) below.
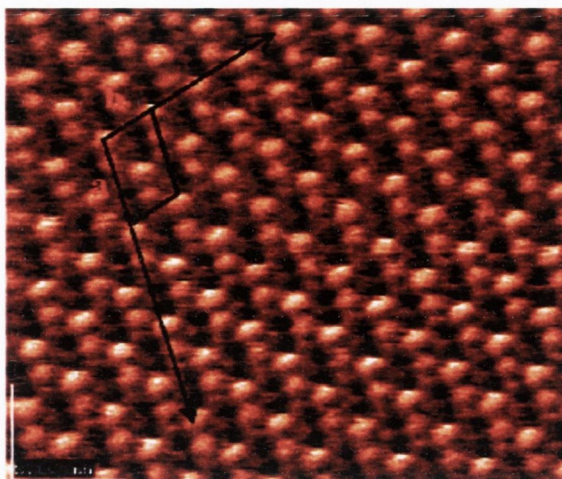
Figure 1.30: *New c(4 x 2) structure with four inequivalent molecules. The film is grown at an exposure of 27 000 Langmuir. $V_t = 1.55$ V, $I_t = 45$ pA. Image size: 10 x 10 nm^2.*

The height differences are shown in the cross-sections a. and b. along cross-section b, one high molecule and one low molecule alternate. This pattern leads to the ζ-phase shown in figure 1.28. The new ζ-phase can be based on the disulfide model of Fenter et al.[111], the twisting of molecules or a combination of both.

Another model has recently been proposed for the c(4 x 2) superstructure by Torrelles et al., on the basis of GIXD data, in which the S atoms are located in adjacent *fcc* and *hcp* hollow sites, with no evidence of dimmer formation or pairing[127]. However, there is evidence of substrate reconstruction, and while the lateral and normal relaxations of the Au atoms are small, this effect plays an important role for the c(4 x 2) superstructure.

In conclusion, although many research groups over the last two decades have attempted to look at the structure of alkanethiols, the results for the energetically most favourable structure remains inconsistent.

1.8 Electrochemical Characterisation of Alkanethiol SAMs

1.8.1 Double Layer and Capacitance

Electrolyte/electrode interfaces exhibit a capacitance whose magnitude reflects the distribution of ions on the solution side of the interface. In the simplest model the electrode/electrolyte interface consists of two layers - an inner layer termed the Helmholtz layer, which consists of a layer of ions and solvent in physical contact with the electrode, and an outer diffuse layer, consisting of a layer of ions near the electrode whose concentration deviates from bulk concentration (Figure 1.31).
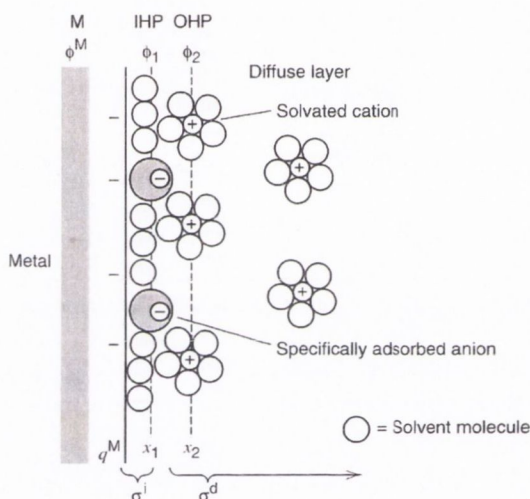
Figure 1.31: *Proposed model of the double layer region under conditions where anions are specifically adsorbed.*[96]

1.8.1.1 The Helmholtz Layer

The Helmholtz layer is the simplest representation of the metal/solution interface. The locus of the electrical centers of the specifically adsorbed ions is called the inner Helmholtz layer (I.H.P.) The locus of centers of the solvated ions is called the outer Helmholtz level (O.H.P). The interaction of the solvated ions with the charged metal involves only long-range electrostatic forces, so that their interaction is essentially independent of the chemical properties of the ions. These ions are called nonspecifically adsorbed ions. He proposed that the counter-charge in solution also resides at the surface i.e. there would be two sheets of charge, having opposite polarity, separated by a distance of molecular order. Such a structure is equivalent to

a parallel-plate capacitor. The simple parallel-plate capacitor model predicts that the reciprocal capacitance (C_H) increases linearly with the thickness of the dielectric layer:

$$C_H = \frac{\varepsilon_o \varepsilon_r}{\chi_H} \qquad (1.1)$$

where ε is the dielectric constant of the medium and ε_o is the permittivity of free space and χ_H is the distance between plate capacitors (interpolate spacing). This capacitance can be interpreted as a equivalent circuit. The figure 1.32 shows a simple Randles equivalent circuit representation of electrode/solution interface region.
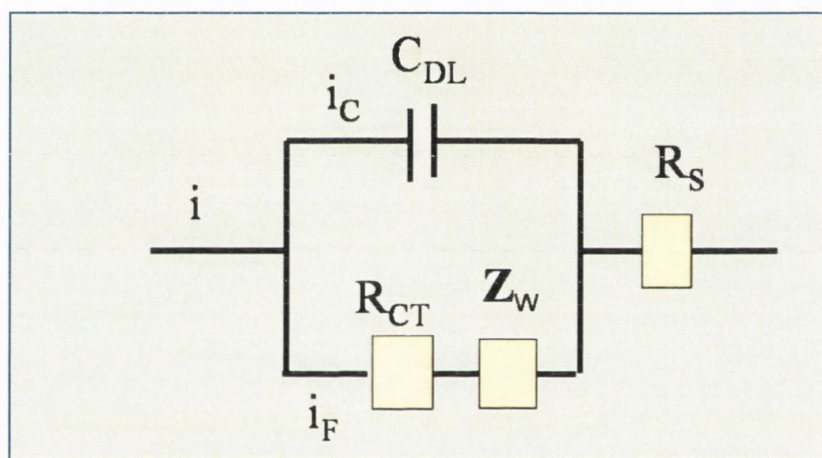
Figure 1.32: *Schematic of the modified Randles equivalent circuit for a SAM coated metal.*

From the figure, i_c represents the double layer charging current, i_F is the Faradaic current, R_S is the solution resistance and R_{CT} is the charge transfer resistance. Z_W is the Warburg impedance.

In electrolytes with high concentrations, the interfacial capacitance is dominated by the capacitance of the Helmholtz layer. Typical Helmholtz capacitances are about 10-100 $\mu F\ cm^{-2}$ for most metals. These capacitances are dependant on potential.

When self-assembly of a long chain alkanethiol occurs on a metal electrode, the Helmholtz layer alters from a mixture of ions and solvent with a high dielectric constant (ε_r) to an ion-free hydrocarbon layer with a low dielectric constant. As a

result, the interfacial capacitance is greatly reduced and becomes potential independent.

Measurements of interfacial capacitances are often obtained from the charging current in a cyclic voltammogram. Capacitance behaviour can be studied in detail using AC (alternating current) impedance spectroscopy or AC voltammetry. Figure 1.33 presents an alkanethiol SAM film modeled as a simple parallel-plate capacitor.
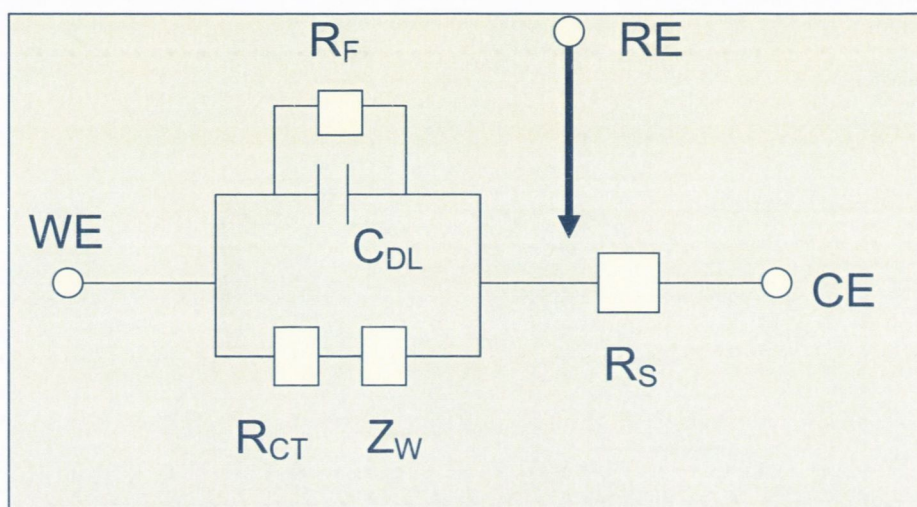
Figure 1.33: *Schematic of the modified Randles equivalent circuit for a SAM coated metal.*

WE denotes the working electrode, CE is the counter electrode, RE represents the reference electrode. The SAM film resistance is R_F and R_S is the solution resistance and R_{CT} is the charge transfer resistance. Z_W is the Warburg impedance.

1.8.1.2 The Diffuse Layer

The diffuse layer is a three-dimensional region which extends from the OHP into the bulk of the solution. It is in this diffuse layer that the nonspecifically adsorbed ions are distributed. The thickness of the diffuse layer depends on the total ionic concentration in a solution. The idea of the diffuse layer was proposed by Gouy and Chapman.

The greatest concentration of excess charge is adjacent to the electrode surface, where electrostatic forces are most able to overcome thermal processes, while progressively lesser concentrations would be found at greater distances as those

forces become weaker. Thus an average distance of charge separation replaces χ_h in the capacitance expression (eqn. 1.1) It can be expected that average distance shows dependences on potential and electrolyte concentration. As the electrode becomes more highly charged, the diffuse layer should become more compact and C_d should rise. As the electrolyte concentration rises, there should be a similar compression of the diffuse layer and a consequent rise in capacitance.

$$C_D = (\frac{2z^2e^2\varepsilon\,\varepsilon_0 n^0}{kT})^{1/2}\cosh\left(\frac{ze\phi_0}{2kT}\right)$$ (1.2)

The schematic representation of the Guoy-Chapman model is shown below:
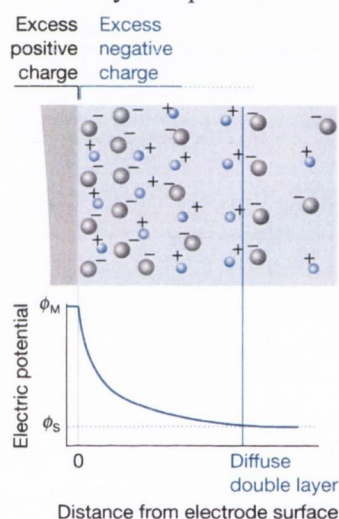
Figure 1.34: Representation of the *Gouy-Chapman Model*

1.8.1.3 Stern Model

Neither the Helmholtz compact layer model nor the Guoy-Chapman diffuse layer model is totally satisfactory. As seen, in the Guoy-Chapman model the solvated ions are modeled as point charges. However, the neglection of the ion size is unrealistic. In reality the solvated ion can only approach the electrode surface to a distance equal to its solvated radius. Stern combined the features of the Helmholtz and Guoy-Chapman models. A schematic of this model is shown in figure 1.35.
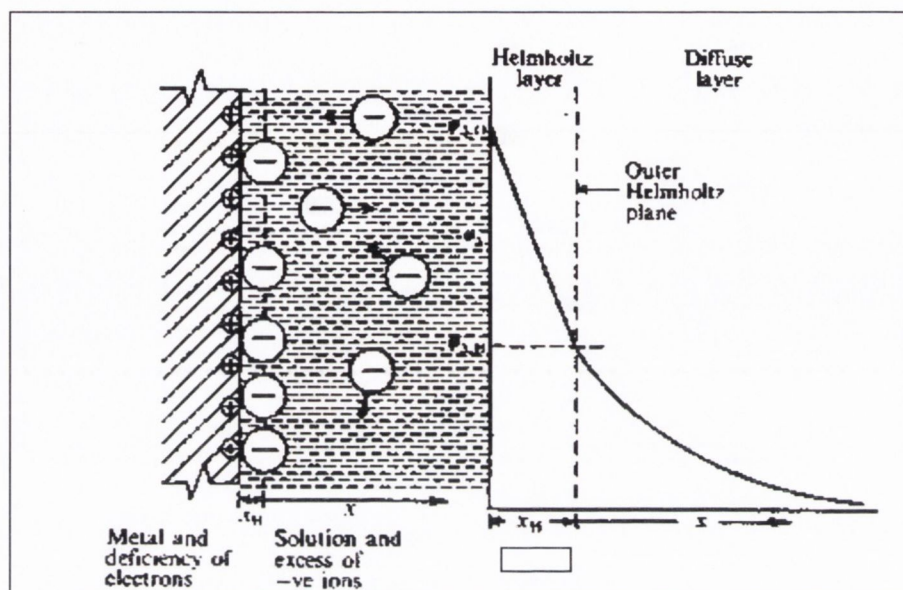
Figure 1.35: Representation of the *Stern Model*

The differential capacitance of the Stern model is given by:

$$\frac{1}{C_d} = \frac{x_2}{\varepsilon\varepsilon_0} + \frac{1}{\left(2\varepsilon\varepsilon_0 z^2 e^2 n^0 / kT\right)^{\frac{1}{2}} \cosh(ze\phi_2 / 2kT)} \qquad (1.3)$$

This expression says that the capacitance is made up of two components that can be separated in the reciprocal, exactly as one would describe two capacitors in series.
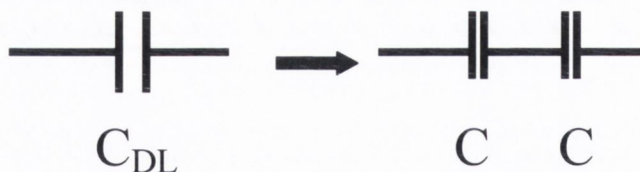
Figure 1.36: *Series arrangement of capacitors*

The terms in the above equation can be identified as the reciprocals of component capacitances, C_H and C_D which can be shown as:

$$\frac{1}{C_d} = \frac{1}{C_H} + \frac{1}{C_D} \qquad (1.4)$$

47

C_H corresponds to the capacitance of the charges held at the O.H.P, whereas C_D is the capacitance of the diffuse charge. The value of C_H is independent of potential, but C_D varies with potential. The smaller of the two capacitances will determine the overall capacitance (C_{DL}). If C_H and C_D are of very different size then the term containing the larger one may be neglected.

1.8.1.4 Capacitance studies

Porter et al.[128] employed electrochemical capacitance measurements to examine the structure of self-assembled monolayers. They saw that the capacitance current is essentially independent of applied potential, scan rate and electrolyte. This behaviour is similar to that predicted by the Helmholtz theory for the electrical double layer which treats the interface as an ideal capacitor. Porter represented the reciprocal of the differential capacitance (C^{-1}) versus n (n is the number of CH_2 groups in the alkane chain). Figure 1.37 illustrates the results of the generalized extension of this characteristic to all n-alkyl thiols studied.
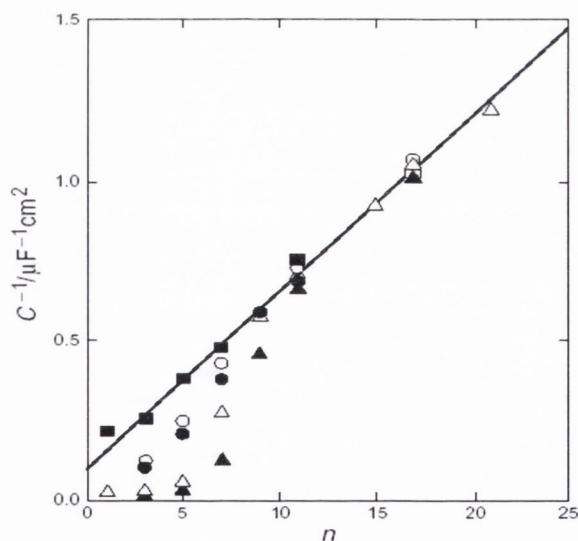
Figure 1.37: *Reciprocal capacitance of alkanethiol SAMs versus chain length n. The symbols represent capacitances obtained from CVs. Filled symbols indicate 10 mVs^{-1} and empty symbols indicate 100 mVs^{-1} scan rate. Δ, ▲ 1 M KCl; ○,● 1 M HClO$_4$; □, ■ 1 M NaF.*[128]

It can be seen that the plots of C^{-1} versus n are linear for longer chain lengths (n≥9). This shows that for n≥9 the differential capacitance is inversely proportional to the alkyl chain length and independent of the electrolyte and scan rate. This indicates the

impervious nature i.e. low structural defects, of alkanethiol self-assembled monolayers. For shorter chain lengths (n<9), it is suggested that the negative ions of the electrolyte partake in the charge redistribution process in some manner. This illustrates the partial permeability of these self-assembled monolayers or the contribution of structural defects of a combination of both. From equation 1.1, the dielectric constant for the monolayers can be calculated. The observed values fall in the range of 2.3-2.6. These dielectric constants are consistent with a close-packed layer of an alkane chain with essentially no penetration by solvent or ions.

Development of mathematical models has aided in predicting the capacitances of SAM-coated electrode when the SAM surface charge changes due to either an acid-base reaction or a redox reaction. Smith and White[129] reported on an analytical expression for the interfacial potential distribution at metal electrodes coated with monolayer films. The interfacial potential distribution is used to calculate the driving force for reversible electron transfer between the metal and the electroactive adsorbate. This is then used in order to predict the current-voltage wave shape in CV experiments.
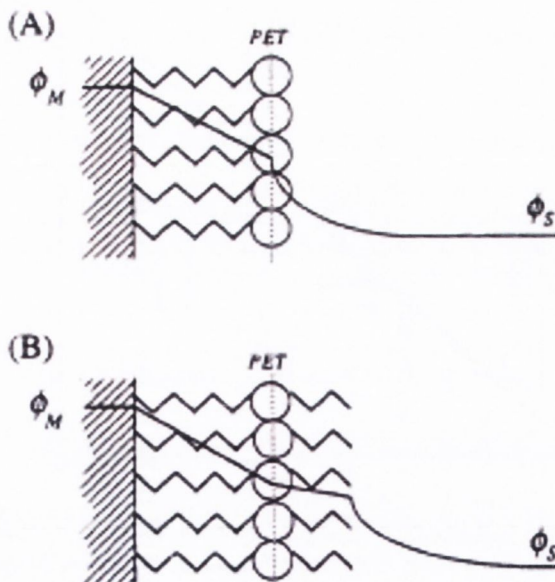
Figure 1.38: *Schematic drawing of irreversibly adsorbed electroactive films in contact with an electrolyte solution. The electroactive O/R centers are indicated by open circles and are separated from the surface by a dielectric film (zigzag lines) of finite thickness. In A and B, the interfacial potential profile (solid line) is linear across the dielectric region between the metal and the PET. In B, a second dielectric layer extends a finite distance beyond the PET introducing a second linear potential decay. For both A and B the potential profile in the solution phase is nonlinear[129].*

The figure above depicts the structures of two electroactive films. The redox centre of the molecule is assumed to be located at a finite distance from the electrode surface, corresponding to the plane of electron transfer (PET). If ions are not permitted to penetrate through the molecular film, the expected interfacial potential profile in this system will be characterized by a linear potential distribution between the electrode surface and the PET and a non-linear distribution in the solution phase (figure 1.38(a)). However, if a portion of the adsorbed molecule extends beyond the redox centers (figure 1.38(b)) then a further linear drop is introduced between the redox center and the solution.

Smith and White saw that by considering the factors controlling the driving force for electron transfer, a dependence of the reversible voltammetric response on the interfacial potential distribution is anticipated. These factors include: thickness of the adsorbate film, dielectric constant of the adsorbate film, the surface concentration of the electroactive adsorbate, the concentration and type of supporting adsorbate and the solvent dielectric constant. It is obvious from figure 1.38, that between the electrode surface and the PET only a fraction of the total interfacial drop occurs (φ_M-φ_S). From this it follows that an equilibrium electrode potential which is a function of the electrostatic potential at the PET (φ_{PET}) governs the surface concentrations of the redox couple. The potential will also be a function of the molecular structure of the film and any parameter of the electrochemical cell that effects the potential distribution (e.g. solvent dielectric constant). As in most experimental systems the electrostatic charges of the redox couple will be different and φ_{PET} will be a function of oxidation state. As a result of all these factors, the driving force for electron transfer will vary continuously during the voltammetric experiment in a way not so straightforward.

From their results Smith and White concluded when analyzing the voltammetric behaviour of electroactive films, the effect of interfacial potential distribution is significant and should be included unless it can be proved that the entire interfacial potential decay takes place within the adsorbed film between the electrode and the PET. They also showed that while the diffuse layer capacitance

(C_{dif}) is much larger than the film capacitance, it is not constant, even in concentrated solutions (>0.1 M) as frequently assumed in SAM analyses. A variation of the diffuse layer capacitance near the peak potential is amplified by the large variation of the charge at the PET which results in a distortion of the voltammetric wave from its normal symmetric shape. This variation of charge may also result in a significant minimum in the charging current near the peak potential. This makes separating the Faradaic and charging components of the voltammetric current impossible. They concluded that the voltammetric response of a reversible redox couple is affected by irreversible adsorption.

Further research by Smith and White[130] looked at the voltammetry of molecular films containing acid/base groups. The electrode/film/electrolyte system considered is shown in figure 1.39.
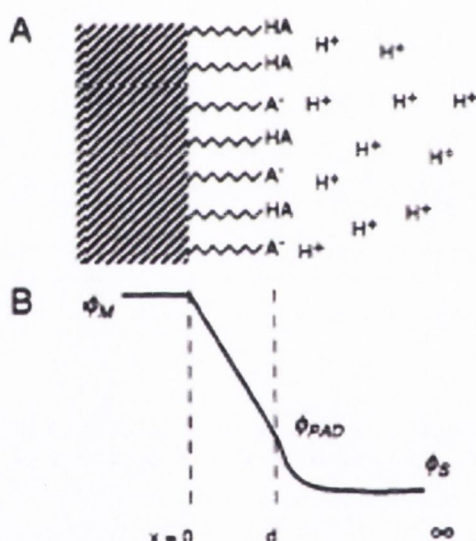
Figure 1.39: *(A) Schematic representation of an adsorbed monolayer of an acid/base pair in contact with an electrolyte solution. (B) Variation of potential from the electrode surface to the bulk of the solution. The acid/base groups of all the molecules are assumed to lie in a common plane, the "plane of acid dissociation" (PAD), located a distance d from the electrode surface.[130]*

Figure 1.39(b) shows the potential distribution that is expected for this acid/base configuration. A linear potential drop occurs between the metal surface and the PAD (φ_M-φ_{PAD}) since there is no charge between the electrode and the PAD. There is a nonlinear potential drop on the electrolyte side of the interface (φ_{PAD}-φ_S) which is assumed to be described by the Guoy-Chapman theory.

They saw that when an acidic head group is contained in a self-assembled monolayer, its degree of ionization depends on electrode potential reflecting the fact that the local potential at the head group also changes. Smith and White discussed the double layer properties of the acid/base system and pointed out that, since a proton can dissociate from the head group, this process gives a contribution to the differential capacity of the polarisable interface. Smith and White in their model assumed that the electrostatic potential at the ionisable head group is equal to that at the outer Helmholtz plane located at the distance of closest approach of the counter-ions to the SAM. From this it can be concluded that a large fraction of potential drop between the electrode and bulk of the solution is attributed to the diffuse part of the double layer.

Simulations of observed differential capacity data requires that the electrode charge density be altered over a large range[131]. Fawcett et al.[132] also looked at the double layer on the ionization of acidic head groups in a self-assembled monolayer on a gold electrode. Fawcett's model was similar to Smith and White's model except that Fawcett's model included a Stern layer. He also included discreteness-of-charge effects. These effects are especially important at a self assembled monolayer containing charged head groups because of the fact that the charge is located in a region where the dielectric permittivity is not uniform[132]. In other words, estimation of the local electrostatic potential at an ionisable head group in self-assembled monolayer requires that one consider the variation in potential both parallel to the interface as well as perpendicular to it. From this section it can be seen that capacitance measurements are useful in observing the process of self-assembly *in situ*. For simple alkanethiol self-assembled monolayers digression of capacitances are helpful in examining such occurrences as poor packing in self-assembled monolayers, variations in the tilt of SAM chains and increased solvents and/or ion penetration.

1.8.2 Blocking Behaviour

Faradaic processes such as oxidation of electrodes and electron exchange between the electrode and solution phase redox couples are inhibited by alkanethiol self-assembled monolayers. This blocking property is recognized to be as a result of the densely packed structure of the hydrocarbon chains which hinder the approach of solution ions and molecules to the electrode surface. Hence, the ET can only proceed via quantum tunneling in this case. Blocking self-assembled monolayers have many feasible applications and can be found in areas of corrosion and nanoscale lithography. However, on closer inspection of SAM-coated electrodes exposes the presence of pinholes (bare metal sites) and other defects, which allow a close approach of the solution species.

Pinholes are formed as a result of the imperfect adsorption of the alkanethiol to the gold electrode during the self-assembly process and/or subsequent loss of the thiol during storage, rinsing or use during experimentation. The redox couple and the electrolyte both have access to the gold substrate surface at the pinholes. The schematic diagram for pinholes is shown in figure 1.40. Here the ET reaction takes place at the patches of bare electrode exposed to the solution via the pinholes.
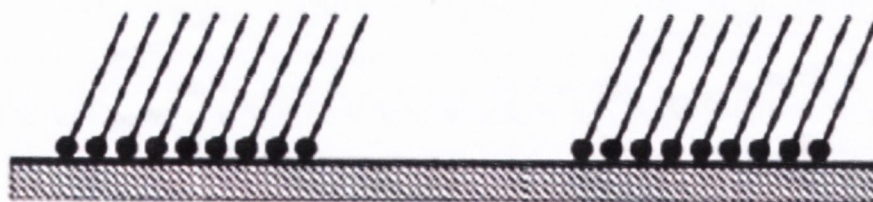
Figure 1.40: *Schematic representation of pinholes in a self-assembled monolayer.*

Of all the methods available in probing SAM structure, electrochemical measurements, namely cyclic voltammetry is the most sensitive tool for detecting pinholes and defects in self-assembled monolayers. Cyclic voltammetry's sensitivity arises from the ability to detect currents corresponding to oxidation and reduction of a fraction of a monolayer and from the high rates of mass transfer of redox couples to small "hot spots" on an otherwise blocked monolayer.

Cyclic voltammogram's of solution redox couples at electrodes with imperfect SAMs show current peaks at low overpotentials. These current peaks greatly exceed the minimal tunneling currents found on electrodes with perfect SAMs. Peak potentials, however, are similar for both imperfect and perfect SAMs. Figure 1.41 shows the blocking of a solution redox couple by an alkanethiol SAM. Qualitative assessment of pinholes and defects in the SAM is often found by looking at the degree of reduction of the current by the SAM at low overpotentials relative to the current at a bare electrode.
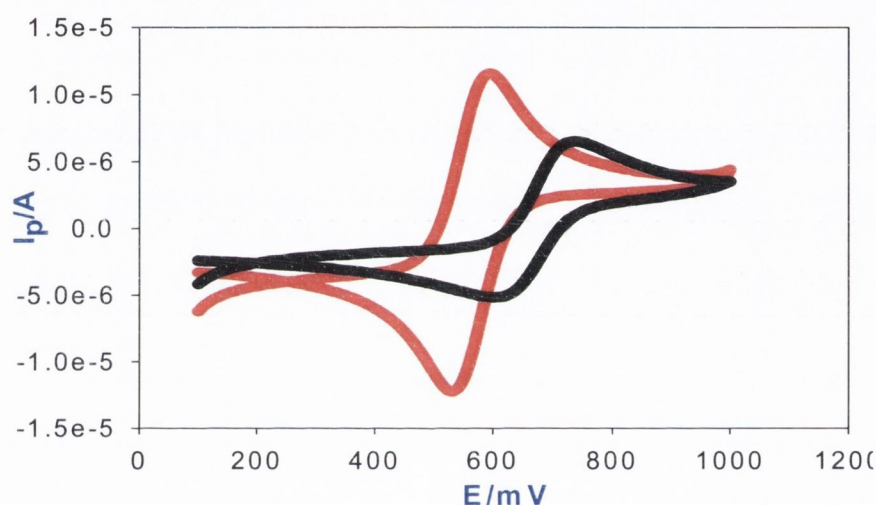
Figure 1.41: *Electrochemical blocking of a solution redox couple by an dodecanethiol SAM. 2mM ferrocyanide/ferricyanide solution in 1M HClO$_4$, polycrystalline gold, 0.1 Vs^{-1} scan rate. Curve (-) is the reversible CV obtained on bare gold. Curve (-) is the monolayer grown on the same electrode.*

Finklea et al.[59,133] were one of the first groups to use cyclic voltammetry to analyse the blocking behaviour of alkanethiol self-assembled monolayers. Finklea looked at alkyl mercaptans with long hydrocarbon chain monolayers and how they strongly blocked electrochemical oxidation of gold and also electron transfer with redox couples in solution. Finklea discovered that electron tunneling across the full width of the oriented monolayer is contraindicated.

It appeared that Faradaic currents at large overpotentials at monolayer coated gold electrodes involved a mechanism of electron transfer at defects in the monolayer. However it was also discovered that another mechanism was involved.

Hence, Finklea[133] proposed a model based on the assumption that: The self-assembled monolayer contained sites at which a redox molecule can approach closely the surface of the electrode but may not come in direct contact with the surface. This type of site can occur when the monolayer collapses or becomes disorganized, such as along the edge of a defect. Finklea assumed that electron tunneling occurs at these collapsed sites (figure 1.42).
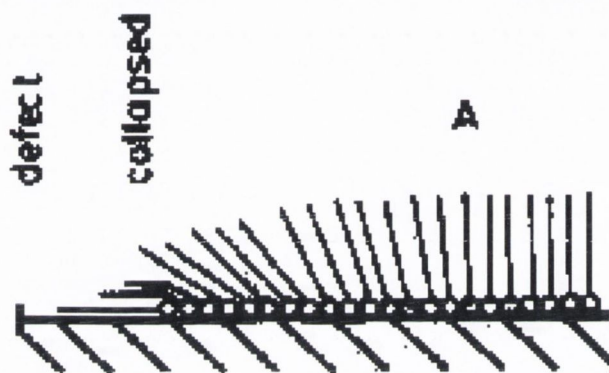
Figure 1.42: *Electron tunneling at defects and collapsed sites in the monolayer. This picture shows a defect and the collapsed monolayer around it. The center of the defect is at the origin.*

As already stated, it is possible to characterize pinholes by electrochemical methods. The total area fraction of pinholes can be calculated from (1) oxide stripping of the gold substrate after anodisation in dilute H_2SO_4 and (2) Faradaic impedance of a redox couple at zero overpotential. Alkanethiol monolayers have pinholes with area fraction ranging from 10^{-2} to 10^{-5} depending on the gold substrate [59,128,134-136].

Sabatani and Rubinstein[134] described in detail the characterisation of monolayer-based microelectrode assemblies. Using the moderately fast redox couple, $Fe(CN)_6^{4-/3-}$, Sabatani and Rubinstein compared k^0 values obtained with monolayer-coated electrodes to those obtained with macroelectrodes. From this they demonstrated excellent agreement for a wide range of coverages[135]. These results provided a strong support for the microelectrode model and were indicative that in the coverage range investigated, the oxide removal peak is a true measure of

the total pinhole area available for an undisturbed penetration of relatively large ions.

The total fraction of pinhole area in a Au/monolayer electrode was determined quantitatively using CV in 0.1 M H_2SO_4[136]. Figure 1.43 shows the typical CV's for different electrodes.
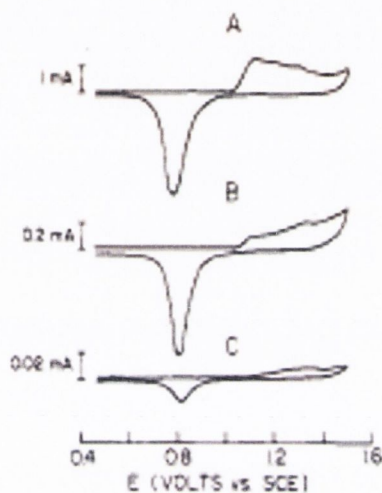
Figure 1.43: *Steady-state voltammograms in 0.1 M H_2SO_4 for (A) bare Au, (B) Au/Octadecyltrichlorsilane of 1-Θ = 0.17 and (C) Au/(Octadecyltrichlorsilane + octadecylmercaptan) of 1- Θ = 0.0024, scan rate 0.1 V/s*[136]

The integrated area under the oxide removal peak indicates the degree at which water penetrates through the monolayer to the gold surface. This is also taken as a measure of the total fractional area of pinholes has been defined as 1-Θ, where Θ is the fractional coverage relative to a complete monolayer. In figure 1.43, 1-Θ is 0.17 and 0.0024 for B and C respectively, compared to the integrated area for the bare gold electrode (A). This is typical behaviour and highly indicative of the improved barrier efficiency obtained with alkyl mercaptans. It is believed that the improved blocking is as a result of the different modes of binding of monolayer forming molecules to the gold surface[135]. Gold oxidation is suppressed by the alkanethiol SAM, except at pinholes. Consequently a measurement of 1-Θ can be obtained from the charge needed to reduce the oxide.

Finklea[137] conducted further work on pinholes, by selectively and permanently passivating pinholes using electrochemical polymerisation of phenol in dilute sulfuric acid. It was known that phenol oxidation in aqueous[138-140] or non-

aqueous[141-147] electrolytes produced a blocking layer of poly (phenylene oxide) [PPO]. The effects of deposits of PPO on the CV's of $Ru(NH_3)_0^{3+}$ is remarkable. The CV characteristic of pinholes (figure 1.44 (a)) is replaced with currents that increase continuously with overpotential (figure 1.44 (b)).
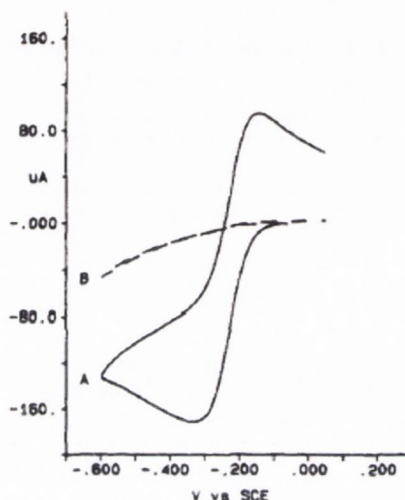
Figure 1.44: *Cyclic voltammograms of a PPO-coated and a $C_{18}SH$ + PPO coated electrode: 1.8 mM $Ru(NH_3)_6^{3+}$ in 1 M KCl, gold mirror with geometric area of 1.0 cm^2, scan rate = 0.1 V/s. Solid curve (A), $C_{18}SH$-coated electrode; dashes (B), $C_{18}SH$ + PPO coated electrode*[137].

From this result it was seen that a PPO film deposited on a $C_{18}SH$ monolayer suppresses the current peaks at low overpotentials which are attributed to pinholes[137]. In contrast, Faradaic currents at all potentials will be uniformly suppressed by a pure PPO film (figure 1.45).

As overpotentials increase, residual currents appear which increase in magnitude. Finklea asserted that the currents due to pinholes are reduced to neglible levels[137]. If retention of the pinhole model occurs, pinhole diameters of the order of angstroms or smaller are among the simulation parameters required to fit the residual currents. What this effectively means is that the pinhole model reduces the penetration of the redox couple through the monolayer. Finklea also found that after deposition of the PPO film on the monolayer, the appearance of further pinholes does not occur[137]. From this it was concluded that PPO deposition permanently blocks pinholes, which are static entities. So once the pinholes are

blocked, CV's are dominated by the Faradaic currents at more intact areas of the monolayer. The redox molecules are prevented from reaching the electrode surface, and electron transfer must proceed by a tunneling mechanism.
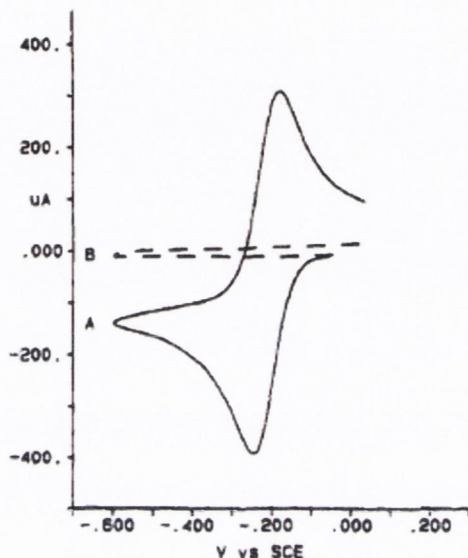
Figure 1.45: *Cyclic voltammograms of a PPO-coated and a $C_{18}SH$ + PPO coated electrode: 1.8 mM $Ru(NH_3)_6^{3+}$ in 1 M KCl gold mirror with geometric area of 1.0 cm², scan rate = 0.1 V/s. Solid curve (A), $C_{18}SH$-coated electrode; dashes (B) $C_{18}SH$ + PPO coated electrode.*

Compton et al.[148] predicted the cyclic voltammetric response of an electrode which was heterogeneous in its electrochemical behaviour. In this electrode some spatial zones were more active than others and this resulted in an array of microelectrodes made of one material which were dispersed over a second, different electrode material. Compton used a simple one electron redox couple whose kinetics were described by two electron transfer rate constants (k^o_1 and k^o_2) and two transfer coefficients (α_1 and α_2) as seen in the figure below (figure 1.46).
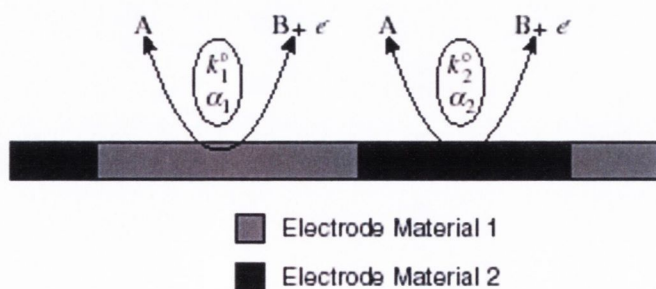
Figure 1.46: *Two adjacent electrochemical reactions on the same electrode surface*[148]

In the figure, k^o_i and α_i are the kinetic redox parameters for electrode material i. The standard potential E^o will be the same for both surfaces as only the kinetic parameters can be altered by a change in electrode material. Compton investigated the diffusional effects and the resulting voltammetry which arose as the distance between the individual microelectrodes varied using a two-dimensional simulation. A finite difference method in a two-dimensional simulation of the system in figure 1.46 was used to determine whether it could be extended to a situation where the blocking material would be more electroactive.

They considered an ensemble of diffusion domains to be any partially covered electrode surface. The diffusion domains were independently interacting cylindrical units with radius (R_0) centred around a circular block of radius (R_b). No significant flux can pass across the vertical boundaries. As a result the voltammetric response of the whole electrode is simply the sum of that for every domain on the electrode surface. A single diffusion domain and the cylindrical polar coordinate employed in Compton's modeling is shown in figure 1.47. Compton's model has electrode 1 partially covered with electrode material 2 and the fraction al coverage is given by (eqn. 1.5) such that the respective surface coverage's of electrode material 1 and 2 are $(1-\theta)\pi R^2_0$ and $\theta)\pi R^2_0$

$$\Theta = R^2_a / R^2_0 \tag{1.5}$$

The basis of the model was used to simulate a wide range heterogeneous mechanisms occurring at partially blocked electrodes by adapting the boundary conditions assigned to the two different surfaces. A previous paper by Compton[149] imposed a no flux boundary condition on electrode surface 2 and Butler-Volmer kinetics on electrode material 1, resulted in a model applicable to electrodes partially covered with random arrays of oil microdroplets immersed in aqueous solution. This was a reversal of the conditions employed by Amatore in an earlier paper[150]. He obtained a domain relevant to an ensemble of microdisks by having electrode material 2 with no flux boundary condition and electrode material 2 having Butler-Volmer kinetics.
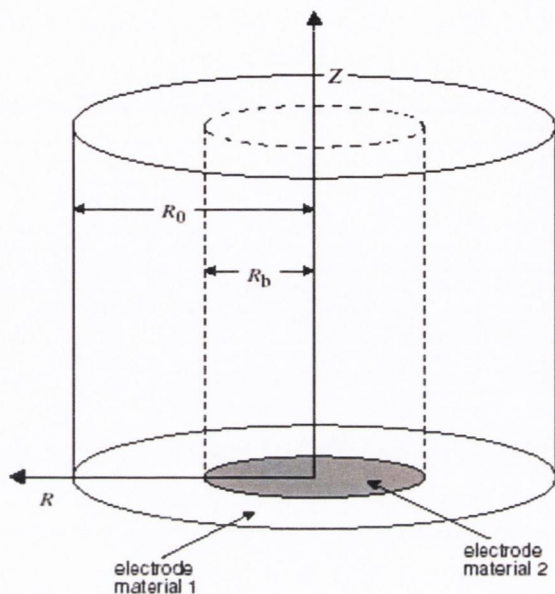
Figure 1.47: *Illustration of a single diffusion domain and the cylindrical polar coordinate system employed in the modeling.*[149]

A similar model to figure 1.46 treats pinholes as an array of microelectrodes in an insulating plane. Finklea and Rubinstein et al.[151] focused on the characterisation of pinholes in the octadecanethiol monolayer as a microarray electrode.

Due to assumptions of uniform size and uniform spacing for microarray electrodes being unrealistic, calculated voltammograms can be included in CV's (□ symbols in figure 1.48) to obtain the relevant parameters in terms of a blocking alkanethiol monolayer with pinholes.

Finklea defined 1-Θ as the area fraction of the microlelectrode, with Θ being the coverage of the blocking layer. When 1-Θ is small (<0.1) then

$$1 - \Theta = R_b^2 / R_0^2 \tag{1.6}$$

where in this case R_b is the radius of the pinhole and R_0 is the radius of the inactive domain surrounding the pinhole; $2R_0$ is the distance between the centers of adjacent pinholes.

Finklea and Rubinstein assumed that oxide formation and stripping occurred only at pinhole sites and, therefore, the ratio of the peak area with the monolayer to the peak area without the monolayer corresponds to the area fraction of the pinholes[151]. Finklea and Rubinstein believed that the oxide stripping scan removed the thiols from pinhole sites of loosely packed monolayer, while densely

packed thiols remained intact. Finklea and Rubinstein investigated some monolayer-coated electrodes which he subjected to multiple oxide stripping scans in order to define the pinhole structure and estimate 1-Θ [151]. Figure 1.48 contains CV's which illustrate the range of behaviour seen for $C_{18}SH$-coated electrodes.
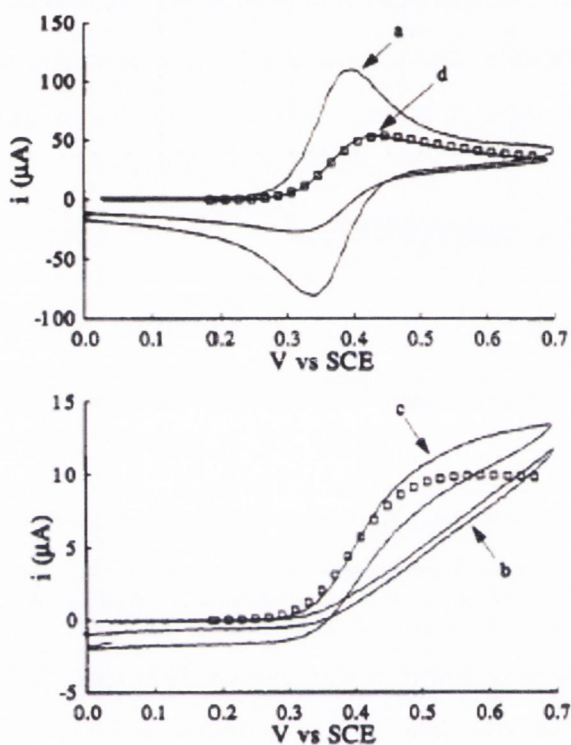
Figure 1.48: *Electrochemical blocking of a solution redox couple by an octadecanethiol SAM. Ferrocenylmethyl-trimethylammonium in 0.5 M H_2SO_4, polycrystalline gold, 0.1 Vs^{-1} scan rate. Curve (a) is the reversible CV obtained on bare gold. Curves (b), (c) and (d) are the different monolayers grown on the same electrode. The symbols are theoretical fits to a microarray electrode model.* [151]

These CV's resulted from an experiment in which a single monolayer-coated electrode was subjected to repeat cyclic voltammograms alternated with ACIS (alternating current impedance spectroscopy) measurements. In ACIS, the electrode is biased at the Nernst potential (at or close to $E^{0'}$) in an electrolyte containing both the oxidized and the reduced forms of a redox couple and the impedance is measured as a function of frequency. From these CV's Finklea obtained values of 10^{-2} to 10^{-4} for 1-Θ and micrometer to submicrometer (0.1-10 µm) dimensions for R_a. Typical pinhole separations are 1-100 µm. Deviations

between the impedance behaviour predicted by the model and the observed impedance behaviour suggest that the pinholes are not uniformly distributed in size and spacing across the monolayer surface[151]. Several groups attempted to use STM to investigate pinholes in self-assembled monolayers and to observe if results were more conclusive than electrochemical methods.

1.8.2.1 STM Characterisation of Pinholes

Kim and Bard[152] reported STM studies of gold coated with $C_{18}SH$. They found that the surface appeared uniform but with some defects (pits) and small bumps. The pits were never seen in freshly prepared Au (111) surfaces. Bard as a result thought that the pits were defects in the adsorbed self-assembled layers. The number and diameter of the pits varied, but the apparent depth of the pits was uniform (8 ± 1 Å). However, the observed depths were much smaller than those expected for the chain lengths of the thiols. Bard assumed that differences in the electronic work function, or tunneling probability, of the exposed gold at the bottom of the pits and the alkanethiol film could explain the apparent small depth of the pits. Bard assumed that the pits were pinholes but the apparent diameters of the "holes" were considerably smaller than the R_a values obtained by the electrochemical methods (0.1-100 μm). Bard could not conclude whether the "holes" were pinholes or an artifact of the STM experiment.

Sun and Crooks[153] also tried to assess the pinhole distribution in a $C_{18}SH$ monolayer by underpotential deposition of copper metal on the Au (111) surface. STM images of the decorated Au surface revealed islands with apparent heights of ca. 6 Å whose density decreased rapidly with increasing time of the gold electrode in the $C_{18}SH$ deposition solution. A 1 day deposition time yielded an island density of $3 \times 10^{10}/$ cm^{-2}. An average R_o of 0.03 μm can be estimated assuming that number density. This figure is roughly 2 orders of magnitude smaller than the smallest R_0 value obtained by ACIS[151]. So it can be concluded that STM is inconclusive in the assessment of pinhole distribution. It also led groups to investigate other defects occuring in self-assembled monolayers.

1.8.3 Au Vacancy Islands

A second typical defect that self-assembled monolayers of alkanethiolates can present on Au (111) is vacancy Au islands produced during the self-assembly process. These vacancy Au islands are of monatomic (0.24 nm) or diatomic (0.48 nm) depth whose bottoms are covered by alkanethiolate molecules. Figure 1.49 shows the STM image of an hexanethiolate-Au(111) SAM. The vacancy Au islands (black regions) in the self-assembled monolayers c(4 x 2) lattices are shown. The schematic of this type of defects is also shown.
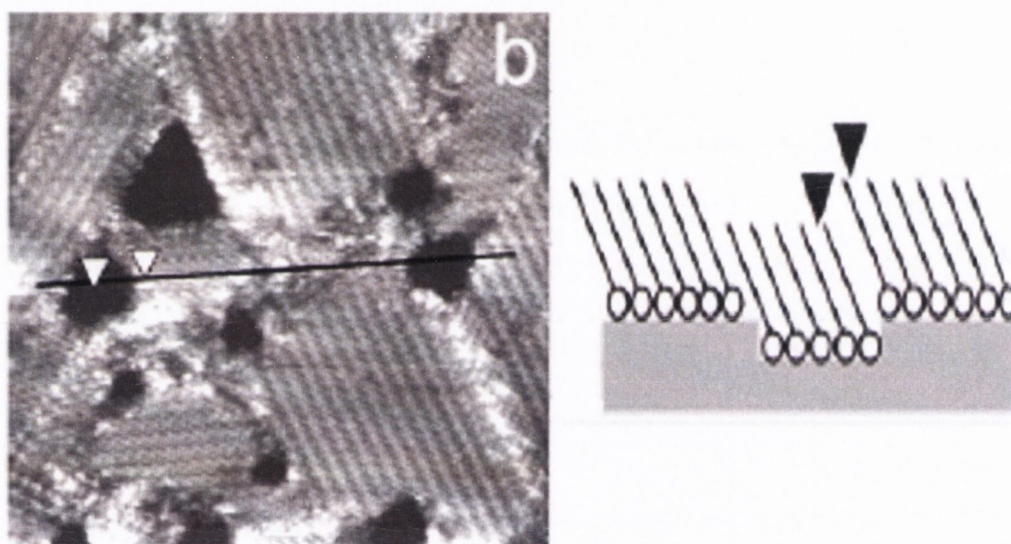
Figure 1.49: *This shows the In situ 35 x 35 nm² STM image of a hexanethiolate-Au(111) SAM. The vacancy Au islands (black regions) in the self-assembked monolayers c(4 x 2) lattices are shown. The schematic of this type of defects is also shown[155].*

These pit-like defects were first observed by Haussling[154]. Edinger et al.[155] showed that the depressions (pits) had a diameter of 20-60 Å and a depth corresponding to the height of a single Au atom substrate step (2.5Å). Edinger provided evidence that the depressions originated from holes within the top layer of the Au atoms and cannot be attributed to the self-assembled monolayer as reported by Haussling[154] and Kim and Bard[152]. Specifically, the defects were assigned to two-dimensional islands of Au vacancies[155]. Edinger also suggested that the presence of holes within the top layer of the Au substrate indicated mass transport

phenomena upon adsorption of the alkanethiols. The Au vacancy island model was later confirmed by other STM studies including one such report by Schönenberger and Sondag-Huethorst et al.[156]. They investigated the nature of "holes" in the self-assembled alkanethiol monolayer (dodecanethiol SAM) using STM with high tunneling resistances. Edinger and Haussling used STM with tunneling resistance of $\leq$ 1 GΩ whereas Schönenberger and Sondag-Huethorst used STM with tunneling resistance of 33 GΩ and 670 GΩ. Figure 1.50 shows two typical STM micrographs of the same surface area obtained for the two different tunneling resistances.
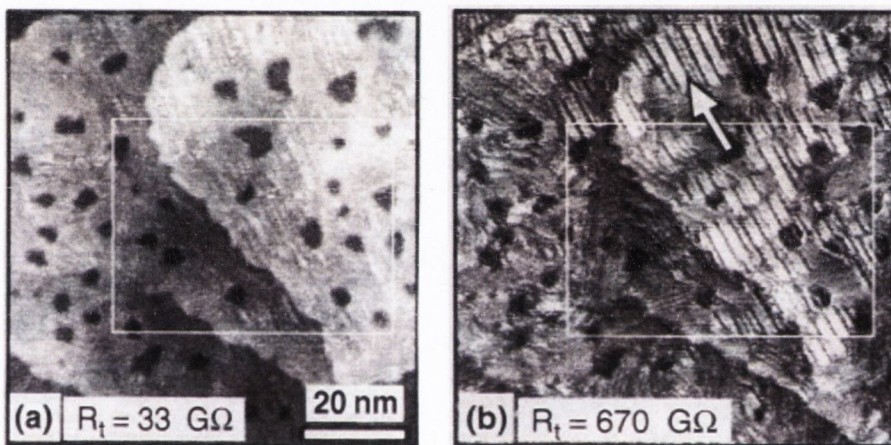
Figure 1.50: *STM images measured on the same 80 x 80 nm^2 area for two different tunneling resistances,(R_t). R_t= 33 GΩ for (a) and R_t = 670 GΩ for (b). While "holes" appearing dark (i.e. topographically lowered) and monoatomic Au step edges are the major feature in (a) (low R_t), a multidomain structure due to the molecular monolayer is in addition visible in (b) (high R_t). The arrow in (b) points to a missing row structure and the area outlined by the white rectangle is represented in Figure M as high resolution STM micrograph.[156]*

Figure 1.50 (a) is similar to a bare gold surface: flat terraces are seen which are separated by monoatomic gold steps of height (2.4 Å). Unlike the bare gold surface, the image exposes many depressions or "holes" which appear topographically lowered (dark spots). Figure 1.50 (b) shows additional structure which is not visible at lower tunneling resistance. The dark lines shown by the arrow are identified as missing rows of thiols[156]. Figure 1.51 presents a magnified area of figure 1.50 (b).
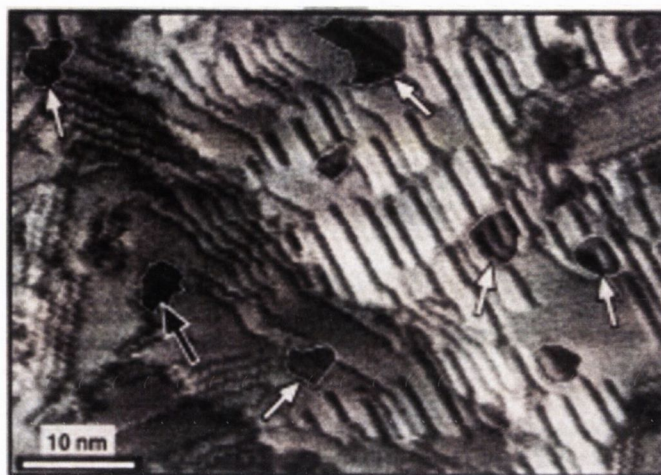
Figure 1.51: *High-resolution atomic-scale STM image obtained at Rt = 670 GQ of the 55 X 40 nm² area indicated in Figure 1.51 (b) by a white box. The regions outlined by white dashed borderlines can clearly be identified in Figure 1.51 (b) as "holes" and are here seen (white arrows) to be covered by ordered molecular structures (exception: the region the black arrow points to is only partially covered*[156.]

The areas with dashed white lines show regions of depressions not clearly apparent as the depressions identified as holes in figure 1.50 (a). The majority of these regions are seen to be covered by molecules (white arrows) and are not empty regions. Hence, the experiment clearly indicates that the depressions are not pinholes.

Schönenberger and Sondag-Huethorst established that the molecules are no longer visible for smaller tunneling resistances $R_t \leq 300$ GΩ[156]. In these cases the electron tunneling is directly to the Au surface, hence the Au surface is imaged. Schönenberger and Sondag-Huethorst noted that by lowering the tunneling resistance there was no change in the average depth of the holes[156]. They deduced that the holes have to be depressions in the Au surface. At small R_t depressions are uniform and flat and their measured depths correspond to the distance between single Au planes in the (111) direction.

Once the correct structural interpretation of the pitlike defects (Au vacancy islands) had been established, the question then turned to the mechanism by which the Au vacancy islands form. Schönenberger and Sondag-Huethorst confirmed also that the vacancy islands were formed from the etching process of the Au

surface intrinsic to the adsorption process of the SH group of the alkanethiol to the Au (111) surface[156], an idea first proposed by Edinger[155]. The confirmation came from the detection of dissolved Au in the alkanethiol solution after immersion, which Edinger also saw. Further work by Schönenberger and Sondag-Huethorst found that by exposing the Au surface to undiluted alkanethiols caused very strong etching and that the original gold terraces could be barely identified[157].

Poirier and Tarlov[101] also concluded from ultrahigh vacuum STM studies of n-alkanethiol self assembled monolayers [$CH_3(CH_2)_{n-1}SH$] (C_n) on Au (111) single crystal structures that the depressions were etch pits. These etch pits were one atom deep (2.4 Å) and were formed from a corrosion process during thiol adsorption. They also found that the self assembled monolayers uniformly covered the terraces and etch pits alike. Poirier and Tarlov observed these depressions or Au vacancy islands of identical depth in STM images of the C_4, C_6 and C_8 self-assembled monolayers.

However, Crooks and Chailapakul[158] questioned this Au-etching mechanism by presenting evidence that Au-vacancy islands were formed during the gas-phase assembly of $(CH_2)_nCH_3SH$ alkanethiols. Crooks and Chailapakul formed both liquid-phase deposited self-assembled alkanethiol monolayers and vapour-phase self-assembled alkanethiol monolayers on gold substrates and then carried out STM experiments on both types of SAM formation. Following this they employed cyanide (CN^-) etching on both sets of self-assembled monolayers. They compared STM images of liquid-phase deposited self-assembled alkanethiol monolayers and vapour-phase self-assembled alkanethiol monolayers (Figure 1.52).

From the STM images Crooks and Chailapakul found that monodispersed pits ranging from 2-5 nm in diameter were contained in liquid-phase deposited self-assembled alkanethiol monolayers. These pits had never been detected on the substrate prior to SAM modification. However, the vapour-phase self-assembled alkanethiol monolayers was found to contain two different pit types: the first type is identical in appearance to the pits found in the liquid-phase deposited self-assembled alkanethiol monolayers while the second pit type is much longer[158].

Regardless of whether self-assembled monolayers are deposited from the liquid or vapour phase, the number density of pits is about the same for both phases, prior to etching. From this, Crooks and Chailapakul suggested that pit formation is governed more by the Au-substrate or perhaps the Au/ HS-R interactions than by the n-alkanethiol ordering or chain-length. From figure 1.53 (d) it can be seen that pits appear in the self-assembled monolayers formed from the vapour phase. This clearly shows that the Au-dissolution model is incorrect[158].

(a) Liquid, before etching **(c) Vapor, before etching**

(b) Liquid, after etching **(d) Vapor, after etching**
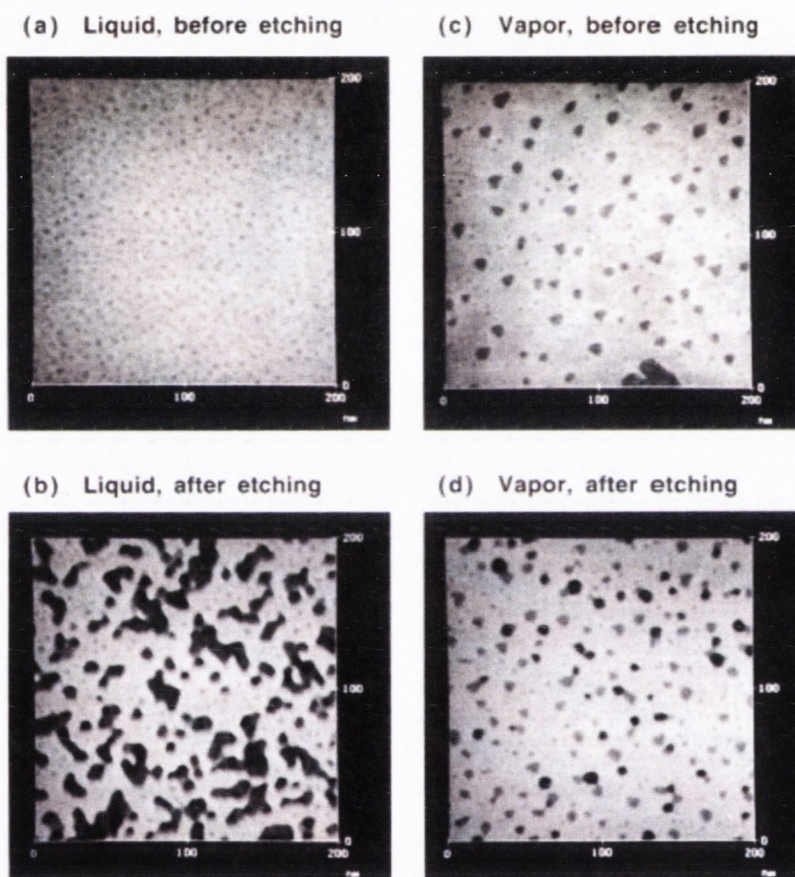
Figure 1.52: *STM images of a Au/HS(CH$_2$)CH$_{11}$CH$_3$ SAM: (a) liquid-phase-deposited SAM before CN$^-$ etching; (b) liquid-phase-deposited SAM after CN$^-$ etching; (c) vapor-phase-deposited SAM before CN$^-$ etching; (d) vapor-phase-deposited SAM after CN$^-$ etching. All images represent a 200 nm x 200 nm field & the full gray scale for all images is 4 nm[140].*

McDermott et al.[159] provided additional support for Crooks and Chailapakul's pathway by presenting a mechanism for vacancy island initiation based on reconstruction processes. McDermott's mechanism invoked compression at the

gold surface due to adsorbate nucleation and aggregation as a pathway for depression formation i.e. that the vacancy islands were formed by adsorbate-induced shrinkage of the surface lattice constant. However, Poirier and Tarlov indicated that the surface lattice constant increased during monolayer assembly[101], as did Fenter[103] and Camillone[102].

Poirier[160] discovered evidence for the formation of Au vacancy islands during self-assembly of alkanethiol monolayers on Au (111) by a novel mechanism. Poirier used gas-phase transport of alkanethiol vapour onto clean Au (111) single crystals in an ultrahigh vacuum STM. He suggested that Au atoms are ejected from the surface layer in an amount that is related to the herringbone compression[142]. The driving force for Au atom ejection appears to be relaxation of the Au (111) herringbone reconstruction[160]. The Au vacancy islands are covered uniformly by alkanethiols, at saturation monolayer coverage (Figure 1.53).
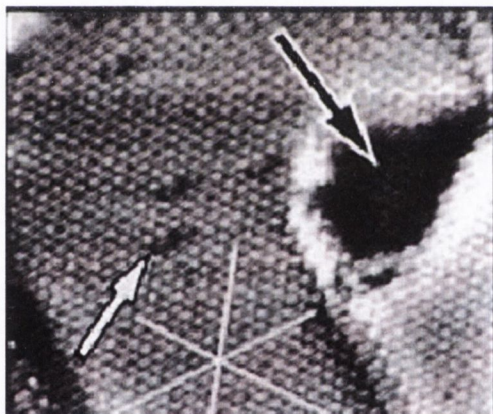
Figure 1.53: *Molecular-resolution topograph of domain boundary. Molecular lattice is apparent in Vacancy Island (black arrow).*

The highly dispersed vacancy islands have a large perimeter-length to area ratio. It has been reported by several studies, a coarsening of the vacancy island size distribution that is consistent with an Ostwald ripening process. Poirier and Tarlov[161], using STM on butanethiol self-assembled monolayers looked at this Ostwald ripening process. A distribution of particles under going Ostwald ripening is characterized by the growth of large particles at the expense of small particles (figure 1.54)[161].
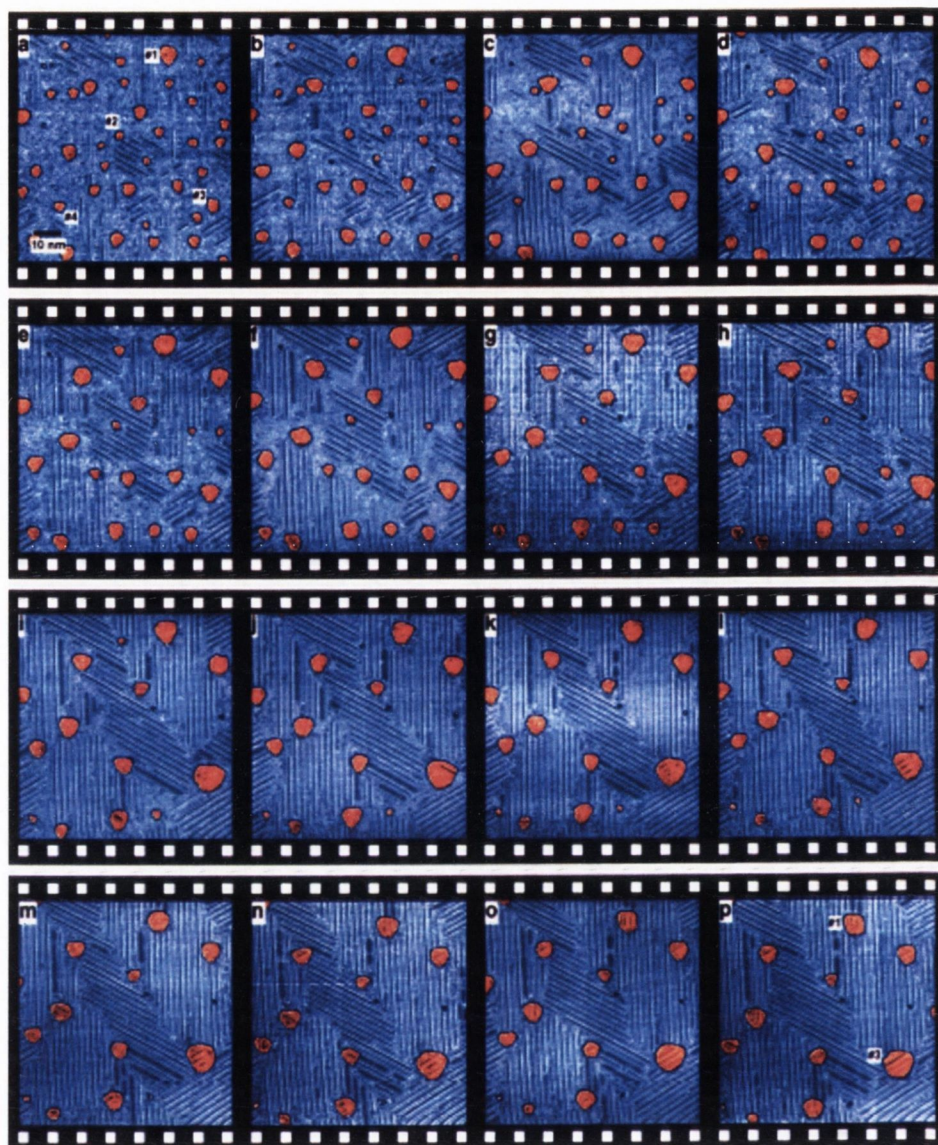
Figure 1.54: *Temporal evolution of a butanethiol SAM on Au(lll). Topographs a-p were acquired 5, 9, 12, 13, 20, 21, 30, 31, 47, 56, 61, 72, 83, 100, 126, and 127 h after solution-phase deposition of the monolayer. The image area is 100 nm x 100 nm. The orange features are depressions in the top layer Au that are created by the deposition process. The SAM has reached 95% solidification by frame j. In the later stages of sintering, anisotropic domain-wall energy polygonalizes the domains as seen in the central domain in frame p.*[161]

From figure 1.54 it is seen that the pit-like distribution alters from a large number of small pits to a small number of large pits. It also seen that the surface evolves from a disordered state to an ordered state. This pit coarsening is as a result of the Ostwald ripening, a mechanism involving diffusion of single Au atoms or Au

vacancies. In figure 1.54, frame (a) pits #1 and #3 grow larger with time and this growth is seen through each frame up to frame (p). The smaller pits #2 and #4 shrink and eventually disappear[161]. Poirier and Tarlov's results suggested that migration of Au adatoms or Au adatom vacancies causes pit coarsening and that the rate of ripening significantly increases when the monolayer is in a state of liquidlike disorder.

McCarley et al. used STM to observe the motion of pits on the $CH_3(CH_2)_nSH/Au$ surface for n = 5,15 and 17. They found that invasive tunneling conditions activated the coarsening of vacancy islands and can be accelerated at elevated temperatures. McCarley heated the $CH_3(CH_2)_{15}SH/Au$ surface for 2 hours at 100°C and found that this caused removal of the pits from the surface without causing damage to the monolayers. This can be seen from figure 1.55, which shows the STM image before heating (figure 1.55 (a)) and the same area after heating (figure 1.55 (b)) for the $CH_3(CH_2)_{15}SH$ monolayer.
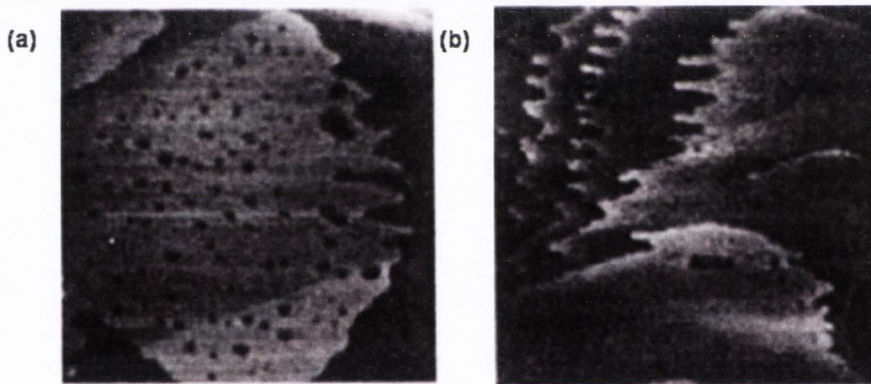
Figure 1.55: *(a) 175 x 175 nm constant current STM image of $CH_3(CH_2)_{15}SH/Au(111)$ immediately after imaging the 70 X 70 nm area of B-D. (b) 175 x 175 nm constant current STM image of $CH_3(CH_2)_{15}SH/Au(111)$ after heating for2 hours at 100° C. All images obtained with V =0.5 V and i_t= 0.7 nA. Z-range is 5 nm full scale[162]*

From figure 1.55 it is quiet clearly seen that the pits disappear on heating. Similar decreases were seen for the n =17 monolayer. McCarley proposed that Au-S bonds are labile and that only Au atoms diffuse. The pits are shown to be defects in the Au (111) surface formed during thiol adsorption.

1.9 Growth of Self-assembled Monolayers

Since self-assembly is the defining feature of self-assembled monolayers, the understanding of this self-assembly process i.e. the growth, is of fundamental importance.

Self-assembled monolayers are formed by the spontaneous adsorption onto an appropriate, usually gold (figure 1) support surface.

← Alkanethiol molecules

←Au(111) substrate
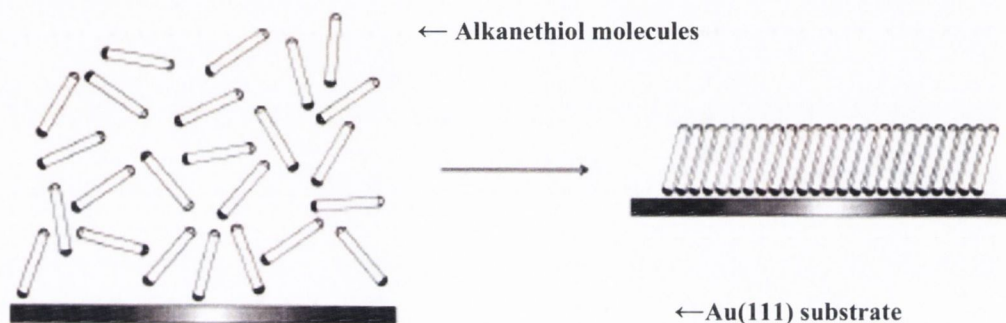
Figure 1.56: *Schematic of the self-assembly process.*

The initial driving force for alkanethiol self-assembly is the strong chemical interaction between the adsorbate (alkanethiol) and the surface (gold). This interaction is considered a result of chemisorption that forced a thiolate molecule (sulfur head group) to adsorb commensurate with a gold lattice. Figure 1.56 depicts the overall self-assembly process, where the tail-to-tail interactions of the molecules created by lateral interchain nonbonded interactions, such as by van der Waals, steric, repulsive and electrostatic forces, is strong enough to align the molecules parallel on the gold surface and create a crystalline film. The magnitude of this lateral interaction can be controlled by changing the length of the hydrocarbon.

From previous investigations the mechanism of formation of gold-alkanethiol monolayers is well known. XPS analyses of sulfur 2p peak in monolayers indicate that adsorption of alkanethiols and disulfides on gold produces thiolate species (RS$^-$)[163,164], Raman spectra of monolayers adsorbed on gold[165] and silver[166] also showed the absence of otherwise strong peaks of S-S[167]

and S-H vibrations. From this it is suggested that alkanethiols are oxidized on metal surfaces producing surface bound thiolates (equation 1.7).

$$Au + RSH \rightarrow \text{Au-SR} + \frac{1}{2}H_2 \qquad (1.7)$$
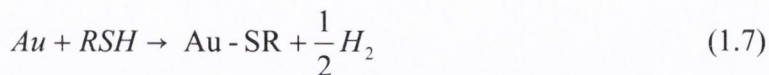
The fate of the hydrogen atom is not well understood, but evolution of oxygen is suggested by the fact that monolayers can be formed from the gas phase in the complete absence of oxygen[158,168].

Adsorption of disulfides also produces a thiolate species and it is believed to proceed via S-S bond cleavage (equation 1.8).

$$2Au + RS - SR \rightarrow 2\text{Au-SR} \qquad (1.8)$$

Apart from XPS[42] and Raman data[167], the evidence for the S-S bond breakage comes from a replacement experiment. Biebuyck et al.[169] showed that exposure of the monolayer prepared from the mixed disulphide $CF_3(CH_2)_{10}S\text{-}S(CH_2)_{10}OH$, to the solution of another thiol showed that the $CF_3(CH_2)_{10}S$ group in the mixed monolayer is replaced approximately 10^3 times faster than the $HO(CH_2)_{10}S$ group.

Ishida et al.[170] proved that the S-S bond is cleaved during deposition by showing that the two different "halves" of the mixed disulphide molecules behave independently in the monolayer. Porter et al.[171] concluded that adsorption of dialkyl sulfides proceeds via breakage of one of the C-S bonds, and the adsorbed species are thiolate moieties (RS⁻). They reached this conclusion due to the similarity of between the XPS spectra and voltammetric curves of monolayers and thiols RSH and the corresponding dialkyl sulphide, RSR. Beulen et al.[172] however, showed the presence of strong peaks of the intact disulphide [M + Au] and [M-H] where M = RSR', the asymmetrical sulphide, when they carried out a detailed secondary ion mass spectrometry (SIMS) study of monolayer of the asymmetrical sulfides. From this Beulen suggested that the adsorption of sulfides occurs without the breakage of any chemical bond. Schlenoff et al.[173] conducted coverage measurements which showed that C-S bond cleavage during deposition of sulfides is minimal.

Nuzzo et al.[43] estimated the energy of the adsorption process using the bong energies for RS-H (87 kcal mol^{-1}), H$_2$ (104 kcal mol^{-1}), RS-SR (74 kcal mol^{-1}) and RS-Au (40 kcal mol^{-1}). Values of -5 and -6 kcal mol^{-1} per gold thiolate unit are obtained for adsorption of thiols and disulfides, respectively. Schlenoff et al. estimated values of -5 and -12 kcal mol^{-1} for adsorption of thiols and disulfides from data on the voltammetric curves corresponding to the equilibrium electrodeposition of alkanethiolates on gold[173].

Schessler et al.[174] obtained accurate thermodynamic parameters from kinetic data on thiol adsorption, which agreed with work carried out by Karpovich[175] using the electrochemical quartz crystal microbalance. Schessler and Karpovich found that for adsorption of 1-octadecanethiol from hexane onto gold, ΔG_{ads} is temperature dependent and, at temperatures between 288 K and 303 K is approximately -5.5 kcal mol^{-1}. Schessler's and Karpovich's data also allowed the calculation of the equilibrium constant for adsorption (K_{eq}) over this range. From the temperature dependence of K_{eq}, ΔH_{ads} was found to be -20 ± 1 kcal mol^{-1}. These values are related to the entropy of adsorption (ΔS_{ads}) by the equation:

$$\Delta G_{ads} = \Delta H_{ads} - T\Delta S_{ads} \qquad (1.9)$$

The temperature dependence of ΔG_{ads} was used to determine a value of ΔS_{ads} equal to -48 ± 1 cal mol^{-1} K^{-1} [15,16]. Karpovich proposed that the modest value of ΔG_{ads} indicated a balance between enthalpic and entropic contributions to adsorption[174]. The total free energy of adsorption is, therefore, rather small. The relatively large magnitude and negative value of ΔS_{ads} apparently reflects the great degree of ordering that occurs as the alkanethiols change from randomly distributed orientations in solution to highly oriented 2D crystalline lattices on the surface. The relatively high energy of the Au-S bond compensates for the unfavourable entropic effect of immobilizing the molecules on the surface, as indicated by the large negative entropy of adsorption. It appears that disulfides monolayer formation is more favourable then alkanethiol formation, thermodynamically. However, the opposite is seen experimentally, where adsorption of thiols on gold appears to be a more positive process than sulfide or disulfide adsorption, at least kinetically.

Bain and Whitesides[176] investigated the competitive adsorption of sulfides, disulfides and thiols using XPS and found that adsorption of thiols to form monolayers was preferred. If the presence of a charged or a bulky functionality group or another destabilizing group in the adsorbate makes monolayer formation less favourable, then thiols give superior quality monolayers then disulfides and sulfides form the poorest quality monolayers. Alkanethiols form monolayers with a higher coverage than monolayers formed by corresponding disulfides for sterically hindered alkanethiols[177] and a heavily charged violegen derivative[178].

Whitesides et al.[60] investigated the exposure of evaporated Au films supported on silicon wafers to solutions of dialkyl sulfides [R-$(CH_2)_mS(CH_2)_n$-R], where R= CH_2 or CO_2H and the same exposure to alkanethiols [R$(CH_2)_n$SH], where R is CH_2 or CO_2H in ethanol using XPS and IRS. They found that the dialkyl sulfides (R-S-R) and alkanethiols (R-SH) gave well packed monolayers. However, the presence of a polar functional group (R=CO_2H) in the molecule of the sulfide makes the monolayers formed from the sulfide disordered and incomplete. This work was confirmed by Zhang and Anderson[179]. Bain and Whitesides[180] also showed that alkanethiols adsorb preferentially over amines, phosphines and other compounds.

It has also been suggested that adsorption of thiols takes place electrochemically i.e. there are possible electron transfers involved in the adsorption step. Reductive cathodic desorption of thiolates and sulfur-containing amino acids at extremely negative potentials were reported by many groups[181-185]. Porter et al.[183] were the original group to investigate electrochemical formation of thiolate monolayers on gold. Their findings came from earlier reductive desorption studies Porter had conducted on thiolate monolayers using the reaction in equation 1.10[186,187].

$$X(CH_2)SAu + e^- \rightarrow Au + X(CH_2)_n S^- \qquad (1.10)$$

Porter showed that the reverse of equation 1.10 could be used for the electrodeposition of thiolate monolayers[183]. Their method involved reversible desorption of self assembled monolayers achieved by driving the potential of gold to a negative value in strongly alkaline thiolate solution. Porter found that the

electrodeposited monolayers have structures and interfacial properties similar to those of their self-assembled analogs. The most important finding discovery made was that the extent of the deposition could be controlled by the reaction thermodynamics[183]. The observed current transients with the potentiostatic adsorption and the reported electrochemical desorption indicate clearly that the adsorption of a neutral thiol is not a single chemical process, such as equation 1.10. Paik[188] proposed an electrochemical oxidation mechanism for the adsorption of thiols:

$$RSH + Au \rightarrow RS - Au + H^+ + e^-(Au) \tag{1.11}$$
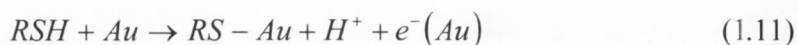
where $e^-(Au)$ represents an electron on the gold metal. The thiol molecules adsorb on Au through an anodic reaction, whereas dialkyl sulfides adsorb by a reaction that gives a net cathodic current.

$$RSSR + e^-(Au) \rightarrow RS - Au + RS^- \tag{1.12}$$

Paik[189] demonstrated that the adsorption rates of thiols and disulfides are strongly influenced by the electrochemical potential of the metals with respect to the solution containing the adsorbate species as would be expected from the electrochemical reactions (equations 1.11 and 1.12). Paik found that adsorption of thiols was facilitated by maintaining the potential of gold near or above the usual open-circuit potential, or by the presence of dissolved oxygen in the solution when there was no potential control[190]. Formation of the thiolate layer from adsorption of a dialkyl sulfide was found to be favoured at lower potentials.

Formation of self-assembled monolayers on a gold substrate held at positive potentials was discovered to be beneficial as it was found to be fast and to yield self-assembled monolayers of improved structure. Rubenstein and Ron were the first to demonstrate self assembly of alkylthiol and dialkyl sulfide monolayers in ethanol solutions onto gold surfaces held at positive applied potentials[191]. They found that alkylthiol monolayers are formed faster (by 2 orders of magnitude) by this technique than by the regular adsorption process. These monolayers also show exceptional coverage of the Au surface. Rubenstein and Ron also discovered that both alkylthiol and dialkyl sulfides form densely packed monolayers. This is a property which is common to both the normal adsorption process and the applied

potential process. Lennox et al.[192] also carried out potential-assisted deposition of alkanethiols on Au and found similar results as Rubenstein and Ron[191]. He found that a modest anodic potential applied to the electrode surface facilitates the chemisorption of an alkanethiol to a clean gold surface. Lennox also found that an excellent blocking monolayer could be formed in a short space of time (minutes) compared to hours/days used in passive self-assembly methods.

Until recently, self-assembled monolayer formation was believed to proceed via simple Langmuir kinetics. Bain et al.[193] employed *ex situ* thickness determinations using ellipsometry. Bain demonstrated that only the first adsorption step, which lead to an adsorption of ~80% of a monolayer in the case of docosanethiol ($CH_3(CH_2)_{21}SH$), could be described by simple diffusion-controlled Langmuir kinetics. The adsorption of the last 20% was found to take place with a significantly longer time constant. This second step was attributed to a consolidation of the film. However, it wasn't truly investigated. Several groups agreed with this theory using various techniques including second harmonic generation[194], electronic quartz crystal microbalance[175], surface acoustic wave (SAW) devices[195], near-edge X-ray absorption fine-structure[196], atomic force spectroscopy[197], X-ray and helium diffraction[198,199] and scanning tunneling microscopy[160,200-202].

Buck et al.[194] employed *in situ* second harmonic generation techniques on n-alkyl thiols in ethanolic solutions and found only a single prominent, relatively fast time scale (< 1 min for 0.045 mM solution). Karpovich and Blanchard[175] carried out *in situ* QCM measurements which were followed up by Schessler[174], these reported that only a single time scale for self-assembled monolayers grown over a wide range of concentrations occurred, using hexane as the solvents.

Langmuir growth kinetics was found by these studies[176,192,194,203] and it was also discovered that monolayer assembly takes place via nucleation and growth of a phase characterized by alignment of the molecular axes in the surface plane and, subsequently a phase characterized by alignment of the molecular axes close to the surface normal[200,202].

Surface plasmon resonance (SPR) and quartz crystal microbalance (QCM) are the simple methods allowing monitoring of the adsorption *in situ*. Shimazu et al.[204] used *in situ* QCM experiments of ferrocene substituted alkanethiols in hexane solution. A fast adsorption step of a few seconds in 0.5 mM solution was observed, this was followed by a process whose timescale was ~2 orders of magnitude slower. After a time of 15 minutes their results were consistent with a single molecular layer. Kim et al.[205] employed QCM and STM studies on quenched monolayers of C_{18} alkanethiol grown in an ethanol solution. Kim detected a slow build up of multilayers over a period of days during SAM growth. DeBono et al. used *in situ* SPR experiments and found two adsorption time scales differing by a factor of ~100 (Figure 1.57)[206].
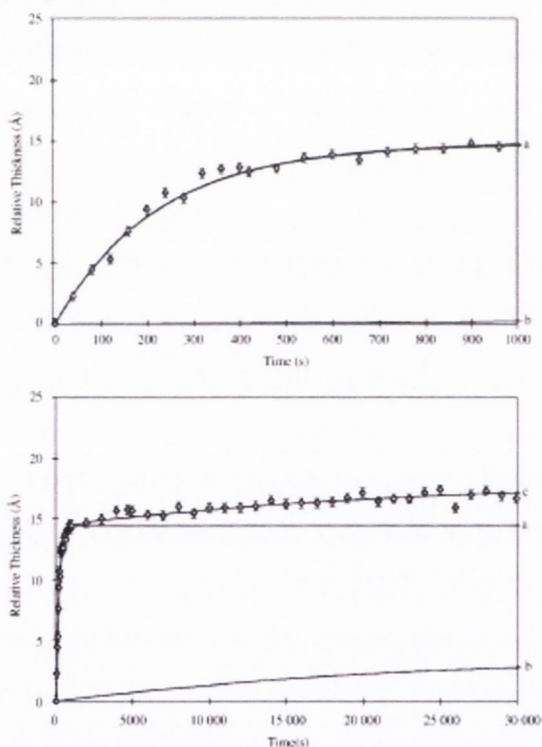
Figure 1.57: *Two-step adsorption of dodecanethiol on the gold surface. (a) First step of adsorption, (b) second step of adsorption, (c) combined two-step model*[206]

DeBono et al. showed that the first step is first order with respect to concentration of adsorbate and is well described by a Langmuir isotherm. The reaction is fast and is comprised of adsorption and desorption processes in equilibrium. According to DeBono, C_{12} or C_{16} thiols from ethanolic solution, the initial fast step resulted in

80% of monolayer adsorbs during this step. From work carried out by Grunze using near-edge X-Ray absorption fine structure[196], it is accepted that the first step produces physisorbed or chemisorbed structure with alkane chains.

Frübose and Doblhofer's[207] experiments using *in situ* QCM revealed two distinct time scales in the adsorption from a 0.1 mM thiol solution. The first scale was the initial adsorption (~2 min), followed by a process which was much slower (>1 hour). Frübose and Doblhofer measured the decreasing electrochemical impedance during the secondary process and it was suggested that the slow timescale corresponded to "healing" of the self-assembled monolayer. Hatchett et al.[182] examined the electrochemical deposition of ethanethiolate on the Ag (111) surface and found that the surface showed two energetically-distinct reaction steps. The second step is slower and is accompanied by the ordering of the monolayer.

Peterlinz and Georgiadis[208] carried out *in situ* SPR experiments on n-alkyl thiol self-assembled monolayers grown from ethanol and heptane solutions (figure 1.58). Peterlinz and Georgiadis observed multiple time scales for ethanol solutions. From figure 1.58(a) it can be seen that the rate decreased with increasing chain length for the initial fast adsorption step (25 min for a 1 mM solution), whereas the opposite trend is seen in the second step lasting several hours and the rate increased with increasing chain length (figure 1.58(b)). For monolayers of the shorter chain molecules (C_8 and C_{12}) a final thickness in the region of ≥ 80 % was achieved in the first adsorption step while the longer chain length monolayers (C_{16} and C_{18}) reached only 40%-50% of final thickness in the same time. Peterlinz and Georgiadis observed a third step with an even longer time scale for the longer chain length thiols (C_{16} and C_{18}). For heptane solutions C_{16} growth had a rate somewhat faster than that for ethanol solution and a final thickness of > 80% was achieved in the first step. A gradual evolution to the final film thickness followed over a ~2 day period.
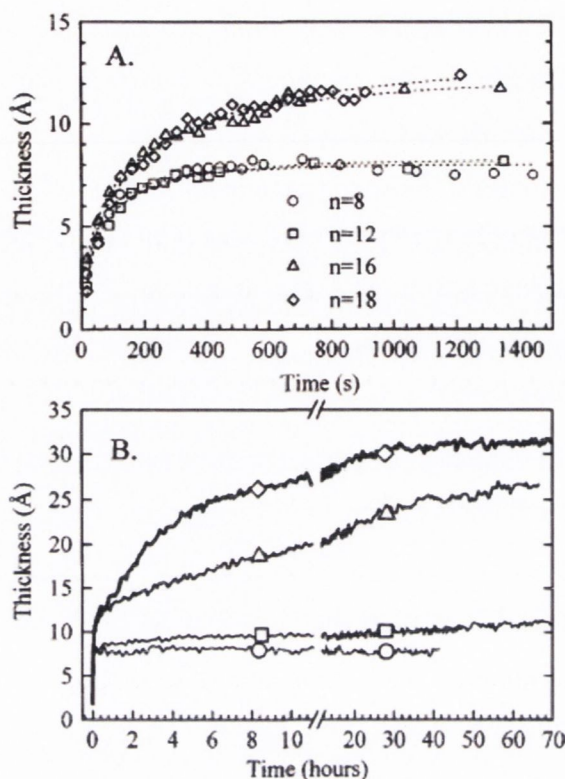
Figure 1.58: *Chain length dependence of formation kinetics for C_8 (circles), C_{12} (squares), C_{16} (triangles), and C_{18} (diamonds) thiols from 1.0 mM ethanolic solutions. The film thicknesses were calculated from in situ surface plasmon resonance measurements. Up to three distinct kinetic regimes were observed, depending on chain length. (a) Details of kinetics at short times. (b) Overview of kinetics for 48–72 hr[208]*

Truong and Rowntree[209] followed the spectra in the C-H region of quenched C_4 alkanethiol self assembled monolayers as a function of immersion time in 5 μM methanolic solutions. These experiments probed the structure evolution in the initial period of self assembled monolayer formation and it was seen that significant changes in the spectra occurred over the first 10-15 min. From the band intensities Truong and Rowntree showed that the alkyl chains were lying close to the surface normal after 15 min of immersion. The band frequency invariance was suggestive that the local molecular environments were insensitive to coverage. These data were consistent with a picture in which islands of vertically oriented molecules form and grow to cover the surface.

Terrill et al.[210] studies quenched C_{16} alkanethiol self-assembled monolayers grown in ethanolic solutions ($10^{-6} - 10^{-12}$ M) for periods of ≤ 11 days and obtained

IR spectra for these self-assembled monolayers[53]. Using the position of the antisymmetric methylene stretch as a signature of chain disorder, Terrill et al. discovered that long times (from several hours to several days depending on concentration) were required to attain the most conformationally ordered state. Terrill et al. also saw that the ordering was much quicker on smoother surfaces. Bensebaa et al.[211] studied quenched films of a C_{22} alkanethiol in a 5 μM ethanol solution and reported that this same peak position reached its ultimate value, representative of well-ordered alkyl chains, after only a 45-s immersion in the solution.

Himmelhaus et al.[212] used sum frequency generation spectroscopy to study quenched C_{22} alkanethiol self-assembled monolayers grown in 3 μM ethanolic solutions. They then monitored the various C-H stretch bands over 2 days of immersion time. Himmelhaus et al. discovered three distinct regions of growth. In the first stage, the initial 5 min of immersion involved the formation of Au-S bonds. After this stage total coverage of the monolayer had reached 80%-90%. In the second stage of growth, from 5-15 min, there was a transition of the hydrocarbon chains from a highly kinked to an all-*trans* conformation. The third and final stage of growth (20 min to 2 days) involved the orientation of the terminal methyl groups from a disordered state relative to one another to a state in which they were aligned. Himmelhaus et al. suggested that this stepped sequence implied that the ordering process could be viewed as consecutive steps originating at the gold surface and moving towards the film surface. Humbert et al.[213] used a similar study to look at the growth of alkanethiols. He also used sum frequency generation spectroscopy and studied quenched para-nitroanilino C_{12} alkanethiol self-assembled monolayers grown from 2 μM ethanolic solutions. Humbert et al observed a change in the molecular orientation over the initial 30 min of growth, followed by a slower change during the next 90 minutes.

The effect of terminal functionality and the effect of chain length on the first equilibrium step rate of adsorption were also studied. From these studies it appeared that intermolecular interactions between functional alkanethiols play only a minor role in the kinetics of monolayer adsorption. It has also been shown that

alkanethiol and ω- hydroxyalkanethiol form monolayers at almost the same rate[214,215]. Several other studies found that short-chain alkanethiols adsorb quicker than longer chain alkanethiols[206,216,217]. The reason for this was that the first step of adsorption includes most of the loss of entropy of the process; it is this major factor which slows down long-chain molecule assembly.

The rate of monolayer formation was also found to be significantly affected by solvent. Schneider and Buttry[181] observed that alkanethiol monolayers formed much faster in dimethylformamide then acetonitrile solutions. However, in dimethylformamide a complete monolayer was never found whereas in acetonitrile solution the physisorbed film was slowly converted from a disordered monolayer to a reorganized, densely packed monolayer. Schneider and Buttry suggested that the final monolayer quality had an inverse relationship with the solubility of the alkanethiol in the solvent.

As we have seen the second step of the adsorption is much slower and is zeroeth order with respect to the alkanethiol concentration[208]. The period of saturation is usually between 16-24 hrs of exposure. From the studies above it is quite obvious that during the second step, the monolayer reorganizes from a disordered form to produce a well-packed structure. This action then frees some more gold surface which is then occupied by additional alkanethiol molecules. This results in the straightening of alkane chains. The order and orientation of the alkanethiol self-assembled monolayer also improves. It is this reorganization which produces highly organized quasi-crystalline structures[196,218]. This reorganization also makes the self-assembled alkanethiol monolayers impermeable to ions, as shown by electrochemical measurements[219]. The possibility of self-assembled monolayer rearrangement and the improvement in packing advocates that the thiolate moieties retain some lateral mobility on the gold surface. Poirier and Tarlov[220] employed STM studies and found the presence of the facile transport of gold atoms on the surface and also found mobile defect sites on the gold surface[161]. Real time motion of the domain boundaries in $CH_3O_2C(CH_2)_{15}SH$ self-assembled monolayers and it was directly observed by time-lapse imaging using STM was seen by Stranick et al[221]. Therefore, the movement of the thiolate

moieties RS-Au plays an important function in the adsorption process. It is the head group of the self-assembled monolayer that determines the migration of defects and does not depend on the chain length of the alkane chain[162].

The two-step process as discussed in the above section is a simplified version and formation of gold-alkanethiol monolayers actually involves a number of physical and chemical processes. Contrary to Wasserman et al.'s[222] suggestion that self-assembled monolayers grown uniformly on the gold surface there appears to be an increasing amount of evidence, formed mainly from STM studies that formation of self-assembled monolayers starts with nucleation and growth of islands[209,223,224]. Yamada and Uosaki[224] performed *in situ* STM experiments monitoring alkylthiol growth on Au (111) from micromolar heptane solutions, where they observed three basic steps. Initially, Yamada and Uosaki observed patches of adsorbed molecules; however, there was no detection of periodic structure on molecular length scales. Yamada and Uosaki suggested that these patches corresponded to a disordered phase. During this phase of growth, vacancy islands were formed in the gold. In the second step of growth there was the appearance of patches with what Yamada and Uosaki described as "striped" patterns observed in the patches. Yamada and Uosaki suggested that at low coverage, a highly mobile lattice-gas phase is formed on the gold surface which then forms a striped-phase surface. It is believed that the stripe-phase domains are composed of alkanethiol molecules, which are in a lying down state on the surface in various arrangements. In the third and final phase stage of growth, islands of apparently greater film thickness formed and grew to cover the surface. A hexagonal pattern was seen on these islands which was consistent with the ($\sqrt{3}$ x $\sqrt{3}$)R30° structure of thiol molecules. Above the critical coverage, nucleation of dense and well-packed islands occurs and these islands then grow until saturation is reached on the surface[200]. This mechanism is seen in figure 1.59.
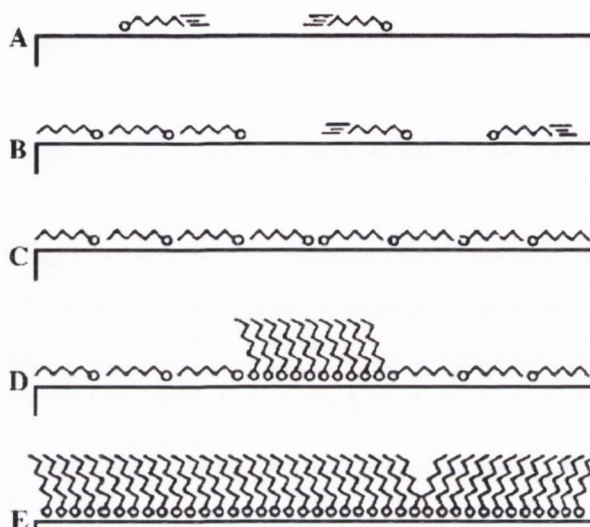
Figure 1.59: *Schematic of self-assembly mechanism for alkanethiols on Au (111). (A) Thiols adopt the highly mobile lattice-gas phase at very low coverage. (B) Above a critical value of surface coverage, striped-phase islands nucleate and grow in equilibrium with lattice-gas phase. (C) Surface reaches saturation coverage of striped phase. (D) High-density islands nucleate at striped-phase domain boundaries. (E) High-density islands grow at the expense of the striped phase until the surface reaches saturation[200].*

Xu et al.[197] employed *in situ* atomic force microscopy to perform detailed and quantitative experiments to follow the growth of C_{18} and C_{22} alkanethiol molecules from 2-butanol solution (see figure 1.60). Xu's observations were consistent with those of Yamada and Uosaki, however, Xu's data also provided height information. Xu et al. first saw the patches forming that were 0.5 nm in height. This is consistent with molecules lying on the surface of the gold substrate. After longer times of exposure to the solution, Xu observed islands that were 1.8 nm higher than the lying down phase and these were seen to nucleate and grow, which is consistent with a structure in which the molecules were approximately vertically orientated. The C_{22} alkanethiol self-assembled monolayer transition from lying down to vertically standing up was faster then the C_{18} alkanethiol self-assembled monolayer transition. The time elapsed between the initial appearance of the lying-down patches and almost complete coverage of the standing up phase for a 0.3 mM C_{18} self assembled alkanethiol monolayer was 10-15 min.

It has been shown by voltammetric studies that the effective surface area of the gold electrodes is irreversibly increased upon alkanethiol adsorption[184]. The

reasons for these morphological changes are that some gold is probably etched away during deposition as seen by Delamarche et al.[104]. After 10 min of exposure to dodecanethiol the average amount of gold in the deposition solution corresponds to dissolution of approximately 25% of a monolayer of Au (111). However, this gold erosion depends on the alkanethiol concentration in the deposition solution and the erosion will increase with more concentrated solutions[157].
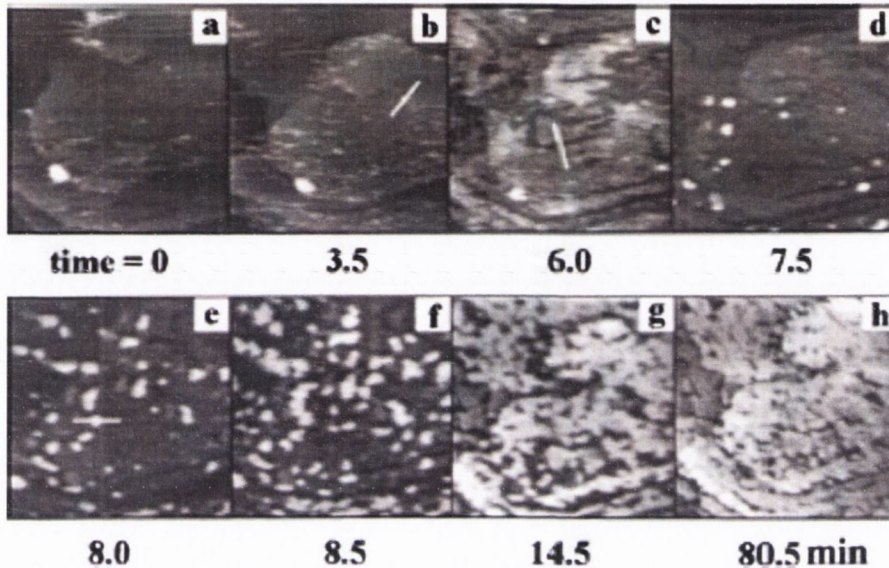
Figure 1.60: *In situ topographic atomic-force microscopy images of Au (111) obtained at various times after injection of a solution of C18 thiol (0.2 mM in 2-butanol). The area of each frame is 150 nm x 150 nm^2, and the bright spot in the lower left corner and the Au (111) steps at the bottom of each frame provide landmarks for comparison of the images[197].*

1.10 The Langmuir Adsorption Isotherm

The Langmuir adsorption isotherm is used to model the adsorption process of self assembled monolayers. The Langmuir isotherm is based on several assumptions. The first is that adsorption is limited to a single monolayer. This is clearly valid based on the chemical identity of the adsorbate species.

The second assumption is that all the surface sites are equivalent. What this is saying is that the surface is defect free. However, this assumption is not physically realistic. It is known that there are a host of defects at the surface of the gold; associated grain boundaries, step edges, adatoms and vacancies. However,

the Langmuir approximation holds as the resulting modulation of surface site energies is relatively small.

The third and final assumption is that adsorption to one site is independent of the occupancy condition of the adjacent sites. The physical and chemical basis for this third assumption can be questioned. There is interaction between adsorbate alkyl chains. However, the interaction is probably only significant for nearly complete surface coverage because of the short range nature of dispersive forces. Also, the interchain interaction will proceed at a longer timescale than that of the gold thiolate bond. Initially, the Langmuir adsorption isotherm was derived for physisorption and not chemisorption, however the bond strength of the alkanethiolate-gold bond is so small that this condition is not violated seriously. Self assembled monolayer coverage is expressed in terms of the fractional coverage (Θ) with $0 \leq \Theta \leq 1$. The latter quantity represents the fraction of available site on the surface which have reacted:

$$\Theta = \frac{\Gamma}{\Gamma_m} = \frac{N_U}{N_\Sigma} \tag{1.13}$$

Where Γ is the surface coverage ($nmol/cm^{-2}$) and Γ_Σ is the monolayer surface coverage. From eqn. 1.13 we get:

$$N_\Sigma = N_U + N_V \tag{1.14}$$

Where N_Σ is equal to the total number of sites, N_U is the number of occupied sites and N_V is the number of vacant sites.

The Langmuir isotherm dictates that the net rate of surface reaction is given by

$$\frac{d\Theta}{dt} = k_A(1-\Theta)c - k_D\Theta \tag{1.15}$$

Where Θ is the fraction of surface covered, $(1-\Theta)$ is the fraction of surface exposed. C is the concentration of the alkanethiol, and k_A and k_D are the adsorption ($M^{-1}s^{-1}$) and desorption (s^{-1}) rate constants. Integration of this equation using the initial condition: $\Theta=0$, t=0 gives the time course of the monolayer formation

$$\Theta(t) = \frac{c}{c + \dfrac{k_D}{k_A}} \{1 - \exp[-(k_A c + k_D)]t\} \tag{1.16}$$

This result is simplified by the following substitutions

$$k_{obs} = k_A c = k_D \tag{1.17}$$

and

$$\kappa = \frac{c}{c + \dfrac{k_D}{k_A}} \tag{1.18}$$

giving

$$\Theta(t) = \kappa(1 - \exp[-k_{obs} t]) \tag{1.19}$$

Analysis of the data for figure 1.61 below, it is seen that upon injection of the alkanethiol the maximum initial rate of monolayer formation is not immediately achieved.
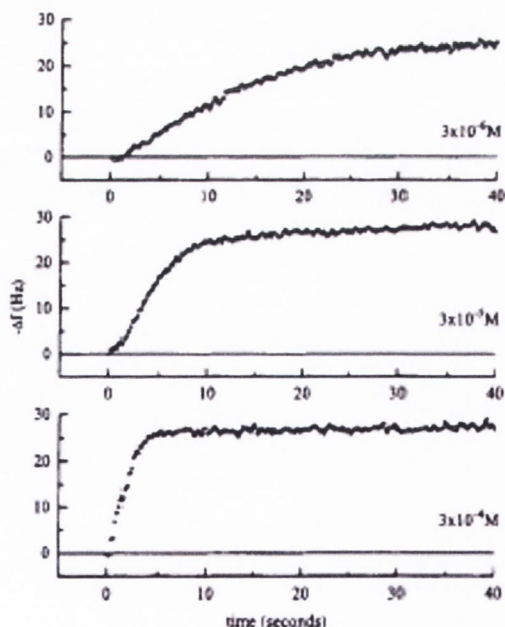
Figure 1.61: *Alkanethiol concentration dependence of QCM frequency change for 1-octadecanethiol in n-hexane. The top panel is data for a 3 x10⁻⁶ M final thiol concentration, the center panel is for a 3 x 10⁻⁵ M final thiol concentration, and the bottom panel is for a 3 x 10⁻⁴ M thiol concentration[175].*

It may take several seconds to reach maximum adsorption rate due limitations inherent to mixing of the solvent and the alkanethiol. This is dependent on the volume and concentration of the alkanethiol being added. Karpovich and Blanchard[175] determined that the mixing time for the alkanethiol volume added is substantially shorter than the monolayer formation time by measurement of the mixing time using a coloured dye. The time required for thorough mixing is related to both the volume of the alkanethiol added and the concentration of the alkanethiol. A decrease in either of these quantities will cause an increase in the mixing time. The onset of the maximum initial rate is caused by the concentration gradient introduced by mixing. Karpovich and Blanchard accounted for this mixing effect by modifying the variable "t" in eqn.1.19 to "t-t_0" where t_0 is the time needed to achieve a homogeneous solution:

$$\Theta(t - t_0) = \kappa[1 - \exp(-k_{obs}(t - t_0))] \tag{1.20}$$

Karpovich and Blanchard fitted the raw data they achieved to eqn. 1.20 and the agreement between the fit and data for a representative scan is shown in figure 1.62.
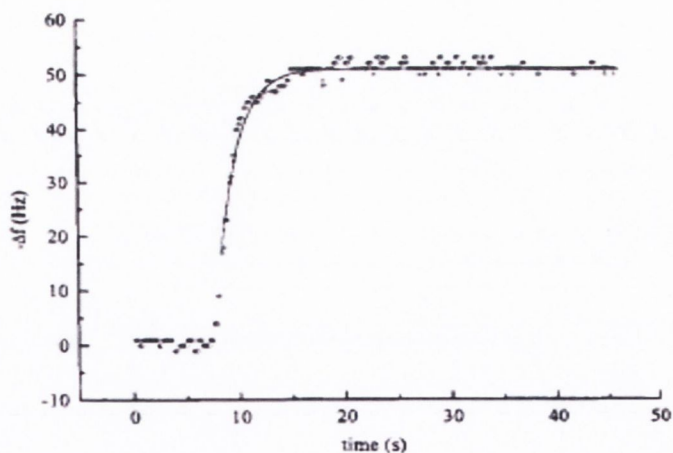
Figure 1.62: *Fit of Langmuir adsorption isotherm (eqn. 1..20) to raw experimental data.*

It can be seen that the fit and the raw data are very similar. Fitting of experimental data to eqn. 1.20 will also give k_{obs}. Since eqn.1.18, a diagnostic plot of k_{obs} versus

C for a series of alkanethiol concentrations yields a line with a slope of k_A and an intercept of k_D, as shown in figure 1.63.
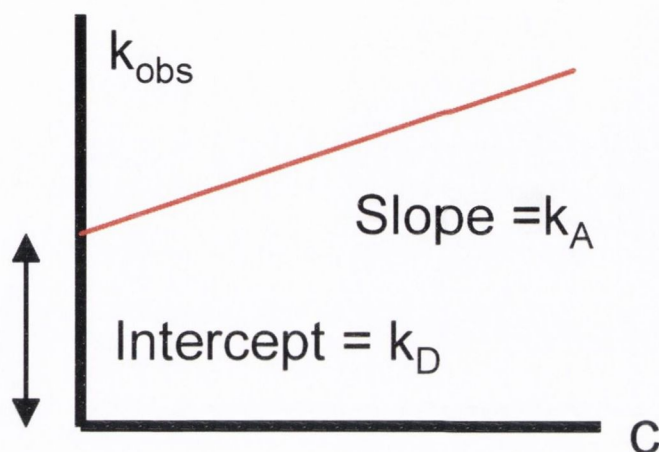
Figure 1.63: *Theoretical diagnostic plot of concentration dependence of k_{obs} for an n-alkanethiol in hexane. The line of best fit has a slope of k_A and an intercept of k_D.*

Karpovich and Blanchard results showed that desorption plays a vital role in the formation of alkanethiol self assemble monolayers, i.e. $k_D > 0$. This is an important discovery as the existence of a nonzero k_D for the alkanethiolate-gold self-assembled monolayers are equilibrium systems and, therefore, at any given instant in time, some fraction of the adsorbate sites on the surface is unoccupied[175].

The equilibrium constant (K, M^{-1}) for the monolayer system can also be determined

$$K = \frac{k_A}{k_D} \qquad (1.21)$$

From K two important physical quantities can be obtained. The steady-state fractional coverage of the gold surface, $\Theta(\infty)$ occurs when $t \to \infty$ and is given by

$$\Theta(\infty) = \frac{Kc}{1+Kc} \qquad (1.22)$$

It is noted that $\Theta(\infty)$ values tend toward unity at relatively high alkanethiol concentrations. The Gibbs free energy of adsorption is also calculated directly from the equilibrium constant data.

$$\Delta G_{ads} = -RT \ln K \qquad (1.23)$$

1.11 Utilization of SAMs

The utilization of SAMs in electrochemistry stems from their ability to survive the electrochemical experiment. The reason for this is that the sulfur atoms resist the processes which occur in an electrochemical experiment i.e oxidation, reduction and desorption. The SAMs deposited on electrodes are stable over a wide range of potentials and electrolyte compositions. A means of controlling the electrode/electrolyte interfacial properties and accessibility of the electrode surface to solution molecules is afforded to the SAMs.

Specific applications include the development of more selective and sensitive electrochemical sensors, especially biosensors. A further application is the control of Faradaic reaction mechanisms and a better understanding of the factors controlling electron transfer over long distances and under large driving forces.

1.11.1 Sensors

In analytical chemistry one of the most frequent applications of self-assembled monolayers is the area of sensor development. In this area the self-assembled monolayers are employed to in part selectivity onto an electrode for a particular analyte. Sensors using self-assembled monolayers have been employed in monitoring pH values. They have also been used in monitoring organic and inorganic species using both chemical and biological recognition elements.

1.11.1.1 pH Sensors

Since the early 1990's there have been several attempts using integrated molecular systems at sensing pH voltammetry. One of the first attempts was by Wrighton et al.[225] who employed a two terminal pH sensor where quinone was used as the pH indicator as it had pH sensitive electrochemistry. They employed pH insensitive ferrocene as a reference electrode. The method used involved a co-immobilisation of redox species onto a self-assembled monolayer. Wrighton found that there was a linear shift in the oxidation and reduction peaks of the quinone, which allowed accurate measurement of pH between pH 1-11. Azobenzenes and nitrobenzoic acid

are other molecules which have been recently employed due to their pH sensitive electrochemistry[226]. Beulen et al.[227] demonstrated an experiment where the different components of a self-assembled monolayer acted cooperatively to allow sensing of pH. Beulen synthesized a mixed carboxylic acid-ferrocene sulfide to form a bifunctional monolayer adsorbate. They found that as a result of through space interactions with the carboxylic acid adjacent, the ferrocene self-assembled sulfide monolayer showed a pH dependent electrochemistry as opposed to the normal pH independent electrochemistry of the ferrocene unit. Deprotonation of the adjacent carboxylic acid stabilised the oxidised state of the ferrocene resulting in a pH sensitive cathodic shift.

Willner and co-workers[228] demonstrated complex integration of molecular involving pH sensing. They assembled pyrroloquinoline quinone (PQQ) as a monolayer onto an Au electrode. The self-assembled monolayer based voltammetric pH sensor acts as a transducer for enzyme biosensors where the enzyme reaction results in a change in the pH of its local environment. The electrode assembly is shown in figure 1.64.
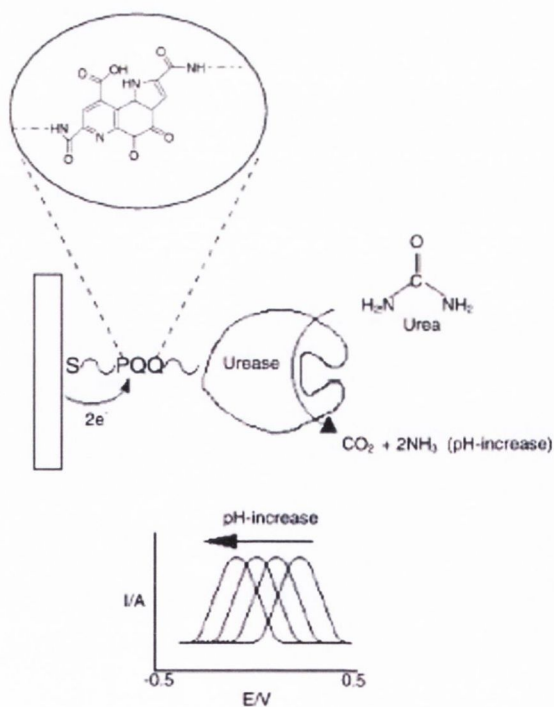
Figure 1.64: *Schematic of the urea biosensor developed by Willner and co-workers[4] where the pH sensitivity of the redox chemistry of pyrroloquinoline quinone (PQQ) is used to transducer the pH change as a result of the enzyme activity of urease when reacting with urea[228].*

The enzyme (either α-chymotrypsin or urease) were covalently linked to the pH sensitive pyrroloquinoline quinone-monolayer electrode. The ferrocene internal standard is then attached to the enzyme to give the final sensor.

1.11.1.2 Inorganic Sensors

The application of self-assembled monolayer based modifications on electrodes to detect both redox active and redox inactive inorganic species has bee demonstrated several times. Electrode surface modification has been designed to: preconcentrate the metal, prevent electrode fouling or enhance selectivity of the interface for that metal. Turyan et al.[229,230] conducted one of the earliest experiments, where he employed carboxylic acid terminated SAMs to detect Cd^{2+} or 4–(alkylthiol) pyridine SAMs to determine Cr(VI) in the presence of Cr(III). The simple approach in both of these experiments gave rise to detection limits below 10^{-10} M with good selectivity. The selectivity appears to be a result of the potential window of the ions as much as the selectivity of the ligand for the metal. Carboxylic terminated SAMs have also been studied bt Nagaoka et al.[231]. They used 3,3-thiodipropionic acid to detect the metal ions Cu^{2+} and Ag^+. In this experiment, although both Cu^{2+} and Ag^+ were bound to the ligand, problems of interference did not occur due to their differing reduction potentials. The short chain 3,3-thiodipropionic acid, allowed the metal to approach the electrode close and served as the recognition element. The decanethiols had two main functions, to block direct access of the metal to the electrode and to prevent the test proteins (bovine serum albumin) fouling the electrode.

However, there were problems with multiple metal ions binding to the same ligand as some had a higher affinity to a ligand then other metals. In order to overcome this problem, ligands with selectivity that was reliant on more than electrostatic attraction. Ligands were required that would provide the appropriate number of coordinating sites and the correct size of the given metal ion. Rubinstein et al. achieved selectivity for Cu^{2+} over Fe^{3+} using 2,2-thiobisethyl acetoacetate (TBEA) as the tetradentate ligand satisfied the four coordinate complexation preference of Cu(II)[8]. The metal ion sensors were prepared with a mixed SAM

octaeyclmercaptan (OM) and TBEA. Rubinstein et al. found that the OM passivated the electrode with the TBEA providing defect sites where the Cu^{2+} bound.

However, the one key drawback in employing selective ligands is that a new ligand is required to be designed and synthesized for each metal ion. However, Gooding et al. addressed this issue by developing a simple generic synthetic strategy that would allow arrays of metal ion sensors to be developed. Gooding et al.[233-236] borrowed from nature by employing amino acids[233], polypeptides[234] and oligopeptides[236] as the selective ligands for metal ions. Gooding et al. achieved a high degree of selectivity for Cu^{2+} with ultraflow detection limits. Gooding found that one of the most attractive features of this method was that most peptide sequences required could be formed from similar synthetic protocols.

While the above describes work carried out on the detection of redox active metals there have also been some ingenious approaches used in non-redox active metal ion detection. Flink et al[237,238] and Yang et al.[239] described procedures for the preparation of aliphatic alkanethiols terminated in crown ethers. Binding of potassium (when 15-crown-5 was used) or sodium (12-crown-4) to the crown either was transduced by employing $Ru(NH_3)_6^{2+/3+}$ as a reporter ion. $Ru(NH_3)_6^{2+/3+}$ was able to penetrate the SAM and showed redox activity in the absence of the metal ion. On binding of the metal ion a net positive charge appeared on the interface thereby causing the reporter ion to be repelled and resulting in an increase in the charge transfer resistance. Manipulation of the selectivity of the interface for a metal by altering the density of the crown ether in the recognition interface was shown by Flink et al.[237]. They found that when the receptor molecule densities were high they formed a sandwich complex with the metal which increased the selectivity. Flink et al. also found that increasing the concentration of a diluent thiol caused a dilution of the receptor surface concentration which prevented the sandwich complex forming and also caused a concomitant reduction in the selectivity for Na^+/K^{+13}. The diluent thiol molecule served two functions, the first

being the separating of the receptor molecules but it also blocked direct access to the electrode.

Liu et al.[240] detected metal ions by coupling of a redox species with a ligand receptor in the same molecule. They synthesised a tetrathiafulvalene (TTF) based SAMs with a crown ether attached. Liu et al. found that a change in the redox properties of the TTF was caused by the binding of metal ions to the SAM. Normally TTF exhibited two one electron redox couples; however Liu et al. found that shifts were found with both peaks for Na^+ and to a lesser extent for K^+ with no interference from Li^+. Liu et al. also discovered that each TTF has two thioactic acid moieties attached which provided four attachments to the gold. Liu et al. reported that these SAMs showed excellent long-term stability which could be attributed to the four attachment points. This finding was compounded by Fujihara et al.[241] when they synthesised TTF with four thiol groups and found that a more stable SAM was formed than a SAM with only one thiol.

Several other SAM modified electrodes employed for the detection of metal ions have been developed including ion-channel mimetic sensors[242,243] and assembling a bilayer onto the SAM which contained an ion selective component[244].

One method where self-assembled monolayers employed as an inorganic sensor has been developed by Pacific Northwest National Laboratory. They formed self-assembled monolayers on Mesoporous supports (SAMMS) and found that the sensor has a broad range of applications in the remediation, water treatment and waste disposal markets. SAMMS were created by attaching a monolayer of molecules to mesoporous ceramic supports. The mesoporous materials offer larger pore size which enables attachment of the SAM along with access to the binding sites within the pores. These SAMMS were then employed to develop a cleanup system that combines a porous structure offering high surface areas and monolayers that interacted with toxic metals. These self-assembled monolayers provide a platform for removing arsenic, mercury and other health hazards from water (figure 1.65). It was reported that the mercury adsorbing SAM on mesoporous supports captured up to 99 % of mercury in a solution. Presently,

this technique is being used to develop a cartridge that can then be removed and disposed in a landfill.
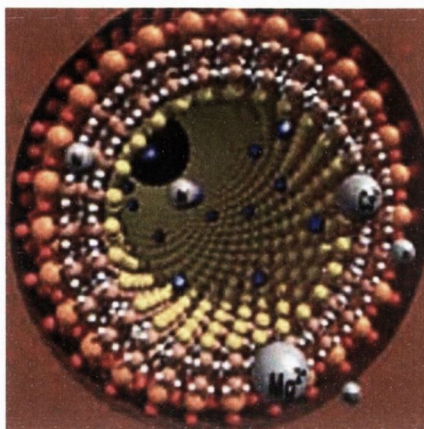
Figure 1.65: *A SAM on mesoporous supports that provides a platform for removing arsenic, mercury and other health hazards from water.*

1.11.1.3 Biosensors and Organic Sensors

Organic and biochemical species detection has been the most frequent application of SAM modified electrodes. Self-assembled monolayers have been employed to manufacture enzyme electrodes. The electrodes have then been investigated with a view to greater control of enzyme immobilization.

One of the main areas of study has been the improving and control of the transduction of the biorecognition reaction. A redox mediator is employed in the sample solution or attached to the enzyme in SAM based enzyme electrodes[245]. The access of the mediator to the enzyme interface was modulated by Willner et al. using nitrospiropyran (figure 1.66)[246,247]. Willner et al. found that by irradiating nitrospiropyran with UV light reversible photoisomerism will occur to form the cationic nitromerocyanine, which will switch back to the nitrospiropyran using light of wavelengths greater then 475 nm. Covalent attachment of the nitrospiropyran to the enzyme the access of the charged mediator, ferrocene monocarboxylic acid, was modulated by charge exclusion by switching between the two photoisomers[246].

However, attachment of the nitrospiropyran direct to the redox center of glucose oxidase (GOD), flavin adenine dinucleotide caused improved exclusion of the mediator and, therefore, improved switching[247].
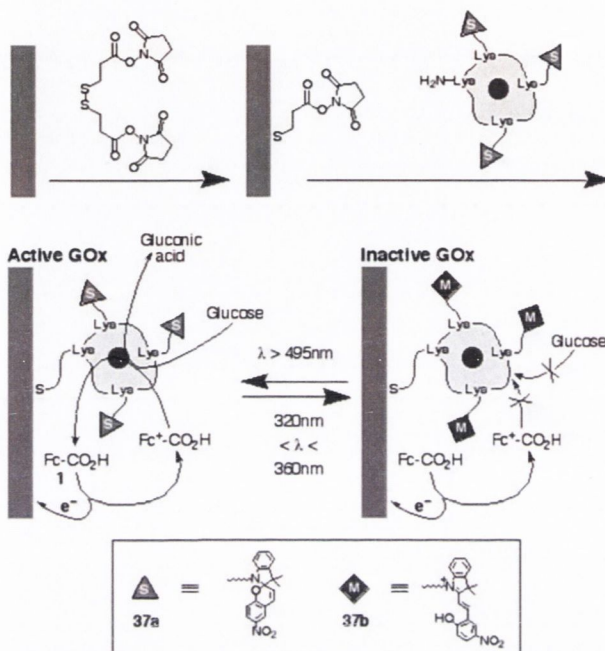
Figure 1.66: *A nitrspiropyran-funtionalised glucose oxidase layer for the photo-controlled oxidation of glucose, with ferrocene carboxylic acid as a diffusional electron mediator[246].*

Lotzbeyer[248] achieved direct electron transfer with SAM based enzyme electrodes where peroxidase enzymes were employed. This group investigated the distance dependence of long range electron transfer by using hydrogen peroxide reducing enzymes of different size b covalent attachment to short chain alkanethiol SAM-modified electrodes[248,249]. The reason for studying peroxidase was that they have redox sires which are located close to the enzyme surface.

Patolsky et al.[250] investigated the coupling of horse radish peroxidase (HRP) with oxidase enzymes employing a mediator for HRP which produced an insoluble product. They found that an insoluble product benzo-4-chlorohexadienone was produced from the H_2O_2 biocatalysed oxidation of 4-chloro-1-naphtol. The insoluble product was found to passivate the HRP-modified electrode. The monitoring of the transduction of the hydrogen peroxide with HRP

occurred by an increase in the Faradaic impedance of the electrode. Patolsky et al. also found that immobilisation of glucose oxidase over the HRP gave rise to a bienzyme sensor.

Katz et al.[251] have developed a most important biomolecular component using self-assembled monolayers by developing a self-powered enzyme-based biosensor for glucose and lactate. The glucose sensor is shown in figure 1.67.
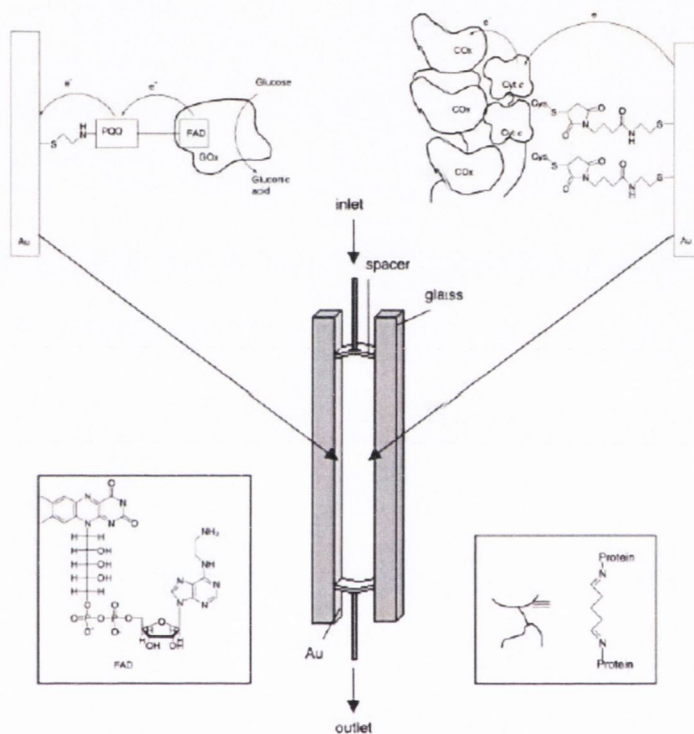
Figure 1.67: *Schematic of the self-powered biofuel cell-based biosensor composed of a PQQ-FAD/GOx-functionalized anode which uses the analyte glucose as the fuel and cytochrome c/cytochrome c oxidase functionalized cathode which utilizes O_2 as an oxidizer. The anode PQQ refers to pyrroloquinoline quinone, FAD is flavin adenine dinucleotide (see inset), the redox active center of glucose oxidase, which is attached to the PQQ modified electrode followed by reconstitution with apo-GOx to produce an active glucose enzyme electrode[251].*

In the biosensor above it can be seen that the electrochemical cell is made up of two electrodes. One is the "wired" GOD enzyme electrode. The second SAM modified electrode has cytochrome c attached directly to the SAM and cytochrome c oxidase cross-linked to the cytochrome c. The fuel in this system came from the biocatalysed oxidation of glucose. The systems' open circuit potential was sensitive to the fuel concentration. There are two main advantages of this device.

The first is that the device can operate at the open potential thereby removing electrochemical interference problems. The second advantage is that the device does not require a power source thereby making it attractive for implantable devices.

Self-assembled monolayers have also been applied to biosensors which have then been employed in the detection of specific DNA sequences. In this class of electrodes a single strand of DNA is attached to the electrode surface. Exposure of the DNA strand to the sensing interface causes a hybridization which results in a duplex being formed. There are two main reasons why self-assembled monolayers are attractive for DNA detection. The first reason is that the DNA immobilisation end-point allows hybridisation to occur. This can easily be achieved by synthesising DNA with an alkanethiol linker at either the 3' or the 5' end of the DNA sequence. The second reason is that formation of a mixed monolayer of thiolated DNA and an alcohol terminated SAM has been shown to orientate the immobilised single strand DNA away from the electrode surface thereby increasing hybridisation efficiency[252].

An ion-channel biosensor has been developed by AMBRI[29]. This involved a recognition interface that was made up of a lipid bilayer which was then anchored to the underlying gold electrode using alkanethiol chemistry. Gramicidin ion channels were one of ten or more components contained in the lipid bilayer. The ion channels in the lower layer of the bilayer were fixed to the electrode while the ion channels in the upper layer were free floating. The upper layer ion channels were derivatised in order to allow transduction of a biorecognition event. In the main variation of the biosensor the upper ion channel was modified with antibody fragments (F_{ab}). Using a thiol terminated membrane-spinning lipid the second half of the antibody-binding site was locked into its position. In the absence of analyte, the floating gramicidin channel moves through the top layer and allowed the formation of a complete ion-channel. A flow of ions through the bilayer occurs when the ion-channel opens and causes a large increase in conductivity. The opposite also occurs however; when the analyte is present the two halves of the

F_{ab}-binding site bind to the analyte. As a result of this binding event the ion-channel is locked in a closed position and the conductivity decreases.

This system has been patented by AMBRI as the "AMBRI Ion Channel Switch[TM]" (ICS[TM]). The ICS[TM] acts as a biological switch and is capable of detecting a range of biological and chemical substances including drugs, hormones, DNA and ions, in any body fluid, including blood, urine and saliva. The biological switch is triggered when a molecule binds to an antibody fragment in the same way as explained above. This then changes the number of conducting ion channel pairs within the membrane, which consequently, alters the way the membrane conducts. The resulting ion change is measured by AMBRI's analytical software as a variation in current which determines the identity of the material under investigation.

1.12 Objectives of this work

The objective of this work is to develop a high yield yet simple synthesis of well defined redox active nanostructured monolayer assemblies. It was then our objective to develop successful methods for electrochemical characterisation of redox active monolayers: via standard techniques such as cyclic voltammetry, complex impedance spectroscopy and potential step chronoamperometry.

The properties of redox active n-ferrocenyl alkanethiol SAM films formed under a new process of self-assembly involving the controlled electrochemical potential chemisorption of the alkanethiol are examined in detail largely using cyclic voltammetry and compared with similar films formed via the commonly employed method of passive incubation.

Work will also be carried out to determine whether redox behaviour of SAM model systems is affected by the presence of an external magnetic field. This type of experimentation has never before been attempted on ferrocene alkanethiol SAMs. Finally, quantitative kinetic data for through bond electron transfer between a ferrocene group and the underlying gold substrate using well defined electrochemical methods will be analysed.

References

1. Swalen, J.D.; Allara, D.L.; Andrade, J.D.; Chandross, E.A.; Garoff, S.; Israelachvili, J.; McCarthy, T.J.; Murray, R.; Pease, R.F.; Rabolt, J.F.; Wynne, K.J.; Yu, H. *Langmuir* **1987**, *3*, 932.

2. Ulman, A. *Introduction to Ultrathin Organic Films*; Academic: Boston, MA, **1991**.

3. Ulman, A. *Chemical Reviews* **1996**, *96*, 1533.

4. Kumar, A.; Abbott, N.L.; Kim, E.; Biebuyck, H.A.; Whitesides, G.M. *Accounts of Chemical Research* **1995**, *28*, 219.

5. Schomburg, K. C.; McCarley, R. L. *Langmuir* **2001**, *17*, 1983.

6. Hickman, J.J.; Ofer, D.; Laibinis, P.E.; Whitesides, G.M.; Wrighton, M.S. *Science* **1991**, *252*, 688.

7. Schierbaum, K.D.; Weiss, T.; Thoden van Welzen, J.F.J.; Reinhoudt, D.N.; Goepel, W., *Science* **1994**, *265*, 1413.

8. Duan, C.M.; Meyerhoff, M.E., *Analytical Chemistry* **1994**, *66*, 1369.

9. Novotny, V.J., *J. Chem. Phys.* **1990**, 3189.

10. Li, D.Q.; Ratner, M.A.; Marks, T.J.; Zhang, C.H.; Yang, J.; Wong, G.K.J., *J. Am. Chem. Soc.* **1990**, *112*, 7389.

11. Ogawa, K.; Mino, N.; Tamura, H.; Hatada, M., *Langmuir* **1990**, *6*, 1807.

12. Roscoe, S.B.; Yitzchaik, S.; Kakkar, A.K.; Marks, T.J.; Lin, W.L.; Wong, G.K. *Langmuir* **1994**, *10*, 1337.

13. Siewierski, L.M.; Brittain, W.J.; Petrash, S.; Foster, M.D. *Langmuir* **1996**, *12*, 5838.

14. Kim, H.; Jang, J., *Polymer* **2000**, *41*, 6553.

15. Inagaki, N.; Tasaka, S.; Onodera, A. J., *J. Applied Polymer Sci.* **1999**, *73*, 1645.

16. Gonon, L.; Chadert, B.; Bernard, A.; Van Hoyweghen, D.; Gerard, J.F. *Journal of Adhesion* **1997**, *61*, 271.

17. Itoh, M.; Nishihara, H.; Aramaki, K. *J. Electrochem. Soc.* **1994**, *141*, 2018.

18. Zamborini, F. P.; Crooks, R. M. *Langmuir* **1998**, *14*, 3279.

19. Tremont, R.; Cabrera, C.R., *J. Electrochem. Soc.* **2002**, *32*, 783.

20. Yamamoto, Y.; Nishihara, H.; Aramaki, K., *J. Electrochem. Soc.* **1993**, *140*, 436.

21. Haneda, R.; Aramaki, K., *J. Electrochem. Soc.* **1998**, *145*, 1856.

22. Laibinis, P.E.; Whitesides, G.M., *J. Am. Chem. Soc.* **1992**, *114*, 9022.

23. Li, Q.; Marthur, G.; Homsi, M.; Surthi, S.; Misra, V.; Malinovskii, V.; Schweikart, K.-H.; Yu, L.; Lindsey, J.S.; Liu, Z.; Dabke, R.B.; Yasseri, A.; Bocian, D.F.; Kuhr, W.G., *Applied Physics Letters* **2002**, *81*, 1494.

24. Eckhardt, A.E., *Electrochemical detection of single nucleotide polymorphisms using capture probe immobilized on self-assembled monolayer;* Xanthon, Inc: US, **2002**.

25. Buriak, J.M.; Stewart, M. P.; Robins, E. *Functionalized silicon surfaces for electronic device fabrication;* Purdue Research Foundation:, 2002.

26. Fukushima, H.; Miyashita, S.; Ishida, M.; Holmes, A., *Fabrication of Self-Assembled monolayers* USA, **2002**.

27. Bamdad, C.C.; Sigal, G.B.; Strominger, J.L.; Whitesides, G.M., *Molecular recognition at surfaces derivatized with self-assembled monolayers*; President and fellows of Harvard College: USA, **2002**.

28. Iwayama, M.; Tanaka, M. *Method for forming pattern by electroplating using self-assembled monolayers*; Star Mfg Co.: Japan, **2002**.

29. Ramanath, G.; Krishnamoorthy, A.; Chanda, K.; Murarka, S.P. *Diffusion barriers comprising a self-assembled monolayer for integrated circuits* USA, **2002**.

30. Lee, R. T.; Colorado, R. *Dithiocarboxylic acid self-assembled monolayers and methods for their use in microcontact printing* USA, **2002**.

31. Tsuji, N.; Nozawa, K.; Aramaki, K. *Corrosion Science* **2000**, *42*, 1523.

32. Lee, S.; Puck, A.; Graupe, M.; Colorado, R.; Shon, Y.S.; Lee, T.R.; Perry, S.S. *Langmuir* **2001**, *17*, 7364.

33. Miura, Y. F.; Takenaga, M.; Koini, T.; Graupe, M.; Garg, N.; Graham, R. L.; Lee, R. T. *Langmuir* **1998**, *14*, 5821.

34. Clegg, R.S.; Reed, S.M.; Huthchinson, J.E., *J. Am. Chem. Soc.* **1998**, *120*, 2486.

35. Clegg, R.S.; Reed, S.M.; Smith, R.K.; Barron, B.L.; Rear, J.A.; Huthchinson, J.E. *Langmuir* **1999**, 15, 8876.

36. Clegg, R. S.; Huthchinson, J.E., *J. Am. Chem. Soc.* **1999**, *121*, 5319.

37. Bain, C.D.; Whitesides, G.M., *Science* **1988**, *240*, 62.

38. Azzam, W.; Wehner, B.I.; Fischer, R.A.; Terfort, A.; Woll, C., *Langmuir* **2002**, 18, 7766.

39. Bain, C.D.; Whitesides, G.M. *Ange. Chemie. International Edition in English* **1989**, *28*, 506.

40. Nuzzo, R. G.; Korenic, E. M.; Dubois, L. H. *J. Phys. Chem.* **1990**, *93*, 767.

41. Laibinis, P. E.; Whitesides, G. M.; Allara, D. L.; Tao, Y. T.; Parikh, A. N.; Nuzzo, R. G. *J. Am. Chem. Soc.* **1991**, *113*, 7152.

42. Nuzzo, R. G.; Fusco, F. A.; Allara, D. L. *J. Am. Chem. Soc.* **1987**, *109*, 2358.

43. Nuzzo, R. G.; Dubois, L. H.; Allara, D. L. *J. Am. Chem. Soc.* **1990**, *112*, 558.

44. Whitesides, G. M.; Laibinis, P. E. *Langmuir* **1990**, *6*, 87.

45. Schreiber, F., *Progress in Surface Science*, **2000**, 65, 151-256,

46. Finklea, H.O., *Electrochemistry of Organised Monolayers of Thiols and Related Molecules on Electrodes*, in *Electroanalytical Chemistry*, Marcel Dekker, NY, Vol.19, 1996

47. Franklin, B. *Philos. Trans. R. Soc. London*, 64 **1774**, 445

48. Pockels, A.; *Nature*, 43 **1891**, 437

49. Langmuir, I. *J Chem. Phys.* **1933**, 1, 756-776

50. Blodgett, K.B.; Langmuir, I. *Phys. Rev.* **1937**, 51, 964

51. Bigelow, W.C.; Pickett, D.L.; Zisman, W.A. *J. Colloid Sci.* **1946**, 1, 513

52. Zisman, W.A. *In Friction and Wear*; Davies, R., Ed.; Elsevier: New York, **1959**

53. Zisman, W.A. *in contact angles, Wettability, and Adhesion* (ED. Fowkes, F.M.), Advances in Chemistry Series 43, Am. Chem. Soc. Washington, DC, **1964**, 1

54. Polymeropoulos, E.E.; Sagiv, J. *J. Chem. Phys.,* **1978**, 69, 1836

55. Sagiv, J. *J. Am. Chem. Soc.,* **1978**, 102, 2

56. Sagiv, J *Isr. J. Chem.,* **1979**, 18, 339

57. Sagiv, J *Isr. J. Chem.*, **1979**, 18, 346

58. Allara, D.L; Nuzzo, R.G, US Patent Application 389/775 (June 18) **1982**.

59. Finklea, H.O.; Avery, S.; Lynch, M.; Furtsch., T. , *Langmuir*, **1987**, 3, 409

60. Troughton, E.B.; Bain, C.D.; Whitesides, G.M.; Nuzzo, R.G.; Allara, D.L.; Porter, M.D., *Langmuir*, **1988**, 4, 365

61. Steiner, U.B.; Caseri, W.R.; Suter, U.W., *Langmuir*, **1992**, 8, 2771.

62. Hickman, J.J.; Zou, C.; Ofer, D.; Harvey, P.D.; Wrighton, M.S.; Laibinis, P.E.; Bain, C.D.; Whitesides, G.M., *J. Am. Chem. Soc.*, **1987**, 111, 7271.

63. Nuzzo, R.G.; Dubois, L.H.; Allara, D.L. *Langmuir*, **1997**, 13, 2973.

64. Bain, C.D.; Whitesides, G.M., *J. Am. Chem. Soc.*, **1988**, 110, 5897–5898.

65. Pale-Grosdemange, C.; Simon, E.S.; Prime, K.L.; Whitesides, G.M., *J. Am. Chem. Soc.*, **1991**, 113, 12.

66. Chang, S.-C.; Chao, I.; Tao, Y.-T., *J. Am. Chem. Soc.*, **1994**, 116, 6792.

67. Chidsey, C.E.D.; Bertozzi, C.R.; Putvinski, T.M.' Mujsce, A.M.; *J. Am. Chem. Soc.* **1990**, 112, 4301.

68. Collard, D.M.; Fox, M.A., *Langmuir* **1991**, 7, 1192.

69. Rowe, G.K.; Creager, S.E.; *Langmuir* 7, **1991**, 2307

70. Rowe, G.K.; Creager, S.E.; *J. Phys. Chem.* 98, **1994**, 500

71. Weber, K.; Creager, S.E.; *Anal. Chem.* **1994**, 66, 3164

72. Carter, M.T.; Rowe, G.K.; Richardson, J.N.; Tender, L.M.; Terrill, R.H.; Murray, R.W., *J. Am. Chem. Soc.* **1995**, 117, 2896.

73. Smalley, J.F.; Feldberg, S.W.; Chidsey, C.E.D.; Linford, M.R.; Newton, M.P.; Yi-Ping Liu,; *J. Phys. Chem.* **1995**, 99, 13141.

74. Kondo, T.; Takechi, M.; Sato, Y.; Uosaki, K., *J. Electroanal. Chem.* **1995**, 381, 203.

75. C.K. Mann and K.K. Barnes, Electrochemical Reactions in Nonaqueous Systems, Dekker, New York, **1970**, p. 418.

76. Peck, S.R.; Curtin, L.S.; Tender, L.M.; Carter, M.T.; Terrill, R.H.; Murray, R.W.; Collman, J.P.; Little, W.A.; Duan, H.M.; Dong, C.; Hermann, A.M., *J. Am. Chem. Soc.* **1995**, 117, 1121.

77. Green, J.B.D.; McDermott, M.T.; Porter, M.D., *J. Phys. Chem.* **1996**, 100, 13342.

78. Weber, K.; Hockett, L.; Creager, S., *J. Phys. Chem.* **1997**, 101, 8286.

79. Closs, G. L.; Calcaterra, L. T.; Green, N. J.; Penfield, K. W.; Miller, J. R., *J. Phys.Chem.* **1986**, 90, 3673.

80. Ellis et al.

81. Chung, C.; Lee, M., *Bull. Korean Chem. Soc.* **1999**, 20, 1.

82. Sumner, J.J.; Weber, K.S.; Hockett, L.A.; Creager, S.E., *J. Phys. Chem.* **2000**, 104, 7449.

83. Creager, S.E.; Wooster, T.T., *Anal. Chem.* **1998**, 70, 4257.

84. Viana, A.S.; Jones, A.H.; Abrantes, L.M.; Kalaji, M.; *J. Electroanal. Chem.* 500, **2001**, 290-298

85. Napper, A.M.; Liu, H.; Waldeck, D.H., *J. Phys. Chem. B* **2001**, 105, 7699.

86. Sumner, J.J.; Creager, S.E., *J. Phys. Chem. B,* **2001**, 105, 8739.

87. Kawaguchi, T.; Tada, K.; Shimazu, K. *J. Electroanal. Chem.* 543, **2003**, 41.

88. Smalley, J.F.; Finklea, H.O.; Chidsey, C.E. D.; Linford, M.R.; Creager, S.E.; Ferraris, J.P.; Chalfant, K.; Zawodzinsk, T.; Feldberg, S.W.; Newton, M.D., *J. Am. Chem. Soc.* **2003**, 125, 2004.

89. Dong, T.Y.; Chang, L.S.; Tseng, I.M.; Huang, S.J., *Langmuir* **2004**, 20, 4471.

90. Chambers, R.C.; Inman, C.E.; Hutchison, J.E., *Langmuir* **2005**, 21, 4615.

91. Chidsey, C. E. D.; Loiacono, D. N.; Sleator, T.; Nakahara, S. *Surf.Sci.* **1988**, 200, 45.

92. Sandy, A. R.; Mochrie, S. G. J.; Zehner, D. M.; Huang, K. G.; Gibbs, D. *Phys. Rev. B* **1991**, 43, 4667.

93. Woll, C.; Chiang, S.; Wilson, R. J.; Lippel, P. H. *Phys. Rev. B* **1989**, 39, 7988.

94. Chambliss, D. D.; Wilson, R. J.; Chiang, S. *J. Vac. Sci. Technol. B* **1991**, 9, 933.

95. Strong, L; Whitesides, G.M. *Langmuir* **1988**, 4, 546

96. A.J. Bard. L.R. Faulkner, Electrochemical Methods-Fundamentals and Applications, J. Wiley & Sons, **1980**.

97. Chidsey, C.E.D.; Loiacono, D.N. *Langmuir* **1990**, 6, 682

98. Alves, C.A.; Smith, E.L.; Porter, M..D. *J. Am. Chem. Soc.* **1992**,114, 1222

99. Widrig, C.A.; Alves, C.A.; Porter, M..D. *J. Am. Chem. Soc.* **1991**,113, 2805

100. Dubois, L.H.; Zegarski, B.R.; Nuzzo, R.G. *J Chem. Phys.* **1993**, 98, 678

101. Poirier, G.E.; Tarlov, M.J. *Langmuir*, **1994**, 10, 2853

102. Camillone, N.; Chidsey, C. E. D.; Liu, G.-y.; Scoles, G., *J. Chem. Phys.* **1993**, 98, 3503.

103. Fenter, P.; Eisenberger, P.; Liang, K. S. *Phys. Rev. Lett.* **1993**, 70, 2447.

104. Delamarche, E; Michel, B; Gerber, C; Anselmatti, D; Guntherodt, H.J; Wolf, H; Ringsdorf, H. *Langmuir*, **1994**, 10, 2869

105. Fenter, P.; Eisenberger, P.; Liang, K. S. *Phys. Rev. Lett.* **1993**, 70, 2447.

106. Fenter, P.; Eberhardt, A.; Eisenberger, P. *Science* **1994**, 266, 1216.

107. Villarrubia, J. S. *Surf. Sci.* **1994**, 321, 287.

108. Nuzzo, R. G.; Korenic, E. M.; Dubois, L. H. *J. Chem. Phys.* **1990**, 93, 767.

109. Camillone, N.; Chidsey, C. E. D.; Liu, G.-y.; Scoles, G. *J. Chem. Phys.* **1993**, 98, 3503.

110. Mar, W.; Klein, M. L. *Langmuir* **1994**, 10, 188.

111. Fenter, P.; Eberhardt, A.; Eisenberger, P. *J. Chem. Phys.* **1997**, 106, 1600

112. Dishner, M.H.; Hemminger, J.C.; Feher, F.j. Langmuir, **1997**, 13, 2318

113. Voets, J.; Gerritsen, J.W.; Grimberge, R.F.P.; van Kempen, H. *Surf. Sci.* **1998**, 399, 316.

114. Yourdshahyan, Y.; Zhang, H.K; Rappe, A.M.; *Phys. Rev. B*, **2001**, 63, 081405R.

115. Grönbeck, H.; Curioni, A.; Andreoni, W. *J. Am. Chem. Soc.* **2000**,122, 2805

116. Hayashi, T.; Morikawa, Y.; Nozoye, H. *J. Phys. Chem.* **2001**, 114, 7615

117. Vargas, M.C.; Giannozzi, P., Selloni, A.; Scoles, G. *J. Phys. Chem B* **2001**, 105, 9509.

118. Fischer, D.; Curioni, A.; Andreoni, W. *Langmuir*, **2003**, 19, 3567.

119. Franzen, S. *Chem. Phys. Lett.* **2003**, 381, 315.

120. Molina, L.M., Hammer, B. *Chem. Phys. Lett.* **2002**, 360, 264.

121. Kondoh, H.; Iwasaki, M.; Shimada, T.; Ameniya, K.; Yokohama, T.; Ohta, T.; Shimomura, M.; Kono, S. *Phys. Rev. Lett.,* **2003**, 90, 066102.

122. Noh, J.; Hara, M. *Langmuir*, **2002**, 18, 1953

123. Liu, G.; Qian, Y.; Yang, G.; Yu, J.; Jung, T.A. *Langmuir*, **2003**, 19, 6056

124. O' Dwyer, C.; Gay, G.; Viaris de Lesegno, B.; Weiner, J. *Langmuir*, **2004**, 20, 8172

125. Godin, M.; Williams, P.J.; Tabard-Cossa, V.; Laroche, O.; Beaulieu L.Y.; Lennox, R.B.; Grütter, P. *Langmuir*, **2004**, 20, 7090

126. Lüssem, B.; Müller-Meskamp. L.; Karthäuser, S.; Waser, R. *Langmuir*, **2005**, 21, 5256

127. Torrelles, X.; Barrena, E.; Munuera, C.; Rius. J.; Ferrer, S.; Ocal. C. *Langmuir*, **2004**, 20, 9396

128. Porter, M.D.; Bright, T.B.; Allara, D.L. *J. Am. Chem. Soc.,* **1987**, 109, 3559.

129. Smith, C.P.; White, H.S. *Anal. Chem.* **1992**, 64, 2398.

130. Smith, C.P.; White, H.S. *Langmuir* **1993**, 9, 1.

131. Bryant, M.A.; Crooks, R.M.; *Langmuir* **1993**, 9, 385.

132. Fawcett, W.R.; Fedurco, M.; Kovacova, Z., *Langmuir* **1994**, 10, 2403

133. Finklea, H.O.; Robinson, L.R.; Blackburn, A.; Richter, B.; Allara, D.L.; Bright, T.B., *Langmuir* **1986**, 2, 239.

134. Sabatani, E.; Rubinstein, I. *J. Phys. Chem.* **1987**, 91, 6663.

135. Sabatani, E.; Rubinstein, I.; Maoz, R.; Sagiv, V. *J. Electroanal Chem.* **1987**, 219, 365.

136. Rubinstein, I; Steinberg, S.; Tor, Y.; Shanzer, A.; Sagiv, J. *Nature* **1988**, 332, 426.

137. Finklea, H.O.; Snider, D.A.; Fedyk, J. *Langmuir* **1990**, 6, 371.

138. Koile, R. C.; Johnson, D. C. *Anal. Chem.* **1979**, 51, 741.

139. Bejerano, T.; Gileadi, E. *J. Electroanal. Chem.* **1970**, 27, 69.

140. Zeigerson, E.; Gileadi, E. *J. Electroanal. Chem.* **1970**, 28, 421.

141. Finklea, H. O.; Vithanage, R. S. *J. Electroanal. Chem.* **1984**, 161, 283.

142. Bruno, F.; Pham, M.-C.; Dubois, J.E. *Electrochim. Acta* **1970**, 22, 451.

143. Pham, M.C.; Lacaze, P.C.; Dubois, J.E. *J. Electroanal. Chem.* **1978**, 86, 147.

144. Pham, M.C.; Dubois, J. E.; Lacaze, P.C. *J. Electroanal. Chem.* **1979**, 99, 331.

145. Pham, M.C.; Tourillon, G.; Lacaze, P.C.; Dubois, J.E. *J. Electroanal. Chem.* **1980**, 111, 385.

146. Dubois, J.E.; Lacaze, P.C.; Pham, M.C. *J. Electroanal. Chem.* **1981**, 117, 233.

147. Pham, M.C.; Dubois, J.E.; Lacaze, P.C. *J. Electrochem. Soc.* **1983,** 130, 346.

148. Davies, T.J.; Moore, R.R.; Banks, C.E.; Compton, R.G., *J. Electroanal. Chem.* **2004**, 574, 123.

149. Davies, T.J.; Brookes, B.A.; Fisher, A.C.; Yunus, K.; Wilkins, S.J.; Greene, P.R.; Wadhawan, J.D.; Compton, R.G., *J. Phys. Chem. B* **2003**, 107, 6431.

150. Amatore, C.; Saveant, J.-M.; Tessier, D., *J. Electroanal. Chem.* **1983**, 147, 39.

151. Finklea, H. O.; Snider, D.A.; Fedyk, J.; Sabatani, E.; Gafni, Y.; Rubinstein, I. *Langmuir* **1993**, 9, 3660.

152. Kim, Y.K.; Bard, A.J., *Langmuir* **1992**, 8, 1096.

153. Sun, L.; Crooks, R.M., *J. Electrochem. Soc.* **1991**, 138, L23

154. Haussling, L.; Michel, B.; Ringsdorf, H.; Rohrer, H. *Angew. Chem., Znt. Ed. Engl.* **1991**, *30,* 569.

155. Edinger, K.; Golzhauser, A.; Demota, K.; Woll, C.; Grunze, M. *Langmuir* **1993**, 9, 4.

156. Schönenberger, C.; Sondag-Huethorst, J. A. M.; Jorritsma, J.; Fokkink, L.G.J. *Langmuir* **1994**, 10, 611.

157. Schönenberger, C.; Sondag-Huethorst, J. A. M.; Fokkink, L.G.J. *J. Phys. Chem.* **1994**, 98, 6826

158. Chailapakul, O.; Sun, L.; Xu, C.; Crooks, R.M., *J. Am. Chem. Soc.* **1993**, 115, 12459

159. McDermott, C. A.; McDermott, M. T.; Green, J. B.; Porter, M..D. *J. Phys. Chem.* **1995**, *99,* 13257.

160. Poirier, G.E. *Langmuir* **1997**, 13, 2019.

161. Poirier, G. E.; Tarlov, M. J. *J. Phys. Chem.* **1995**, *99,* 10966.

162. McCarley, R. L.; Dunaway, D. J.; Willicut, R. J. *Langmuir* **1993**, *9,* 2775.

163. Laibinis, P. E. ; Whitesides, G. M. ; Allara, D. L.; Tao, Y. T.; Parikh A. N.; Nuzzo, R. G., *J. Am. Chem. Soc.*, **1991**, 113, 7152.

164. Nuzzo, R. G.; Zegarski, B. R.; Dubois, L. H. , *J. Am. Chem. Soc.*, **1987**, 109, 733.

165. Ford, J. F.; Vickers, T. J.; Mann, C. K.; Schlenoff, J. B., *Langmuir* **1996**, 12, 1944.

166. Futamata, M., *J. Phys. Chem.* **1995**, 99, 11901.

167. Garrell, R. L.; Chadwick, J. E., *Coll. Surf. A.* **1994**, 93, 59.

168. Dubois, L. H.; Zegarski, B. R.; Nuzzo, R. G., *J. Chem. Phys.* **1993**, 98, 678.

169. Biebuyck, H. A.; Whitesides, G. M., *Langmuir* **1993**, 9, 1766.

170. Ishida, T.; Yamamoto, S.; Mizutani, W.; Motomatsu, M.; Tokumoto, H.; Hokari, H.; Azehara, H.; Fujihira, M., *Langmuir* **1997**, 13, 3261.

171. Zhong, C.J.; Porter, M. D.; *J. Am. Chem. Soc.* **1994**, 116, 11616.

172. Beulen, M. W. J.; Huisman, B.H.; van der Heijden, P. A.; van Veggel, F. C. J. M.; Simons, M. G.; Biemond, E. M. E. F.; de Lange, P. J.; Reinhoudt, D. N., *Langmuir* **1996**, 12, 6170.

173. Schlenoff, J. B.; Li, M.; Ly, H., *J. Am. Chem. Soc.*, **1995**, 117, 12528.

174. Schessler, H. M.; Karpovich, D. S.; Blanchard, G. J., *J. Am. Chem. Soc.* **1996**, 118, 9645.

175. Karpovich, D. S.; Blanchard, G. J. *Langmuir* **1994**, *10*, 3315.

176. Bain, C. D.; Biebuyck, H. A.; Whitesides, G. M., *Langmuir* **1989**, 5, 723.

177. Chechik, V.; Schonherr, H.; Vancso, J. G.; Stirling, C. J. M., *Langmuir* **1998**, 14, 3003.

178. Tang, X. Y.; Schneider, T. W.; Walker, J. W.; Buttry, D. A., *Langmuir*, **1996**, 12, 5921.

179. Zhang, M. H.; Anderson, M. R., *Langmuir* **1994**, 12, 2807.

180. Bain, C. D.; Evall, J.; Whitesides, G. M., *J. Am. Chem. Soc.* **1989**, 111, 7155.

181. Schneider, T. W.; Buttry, D. A., *J. Am. Chem. Soc.* **1993**, 115, 12391.

182. Hatchett, D. W.; Stevenson, K. J.; Lacy, W. B.; Harris, J. M.; White, H. S., *J. Am. Chem. Soc.* **1997**, 119, 6596.

183. Weisshar, D. E.; Lamp, B. D.; Porter, M. D., *J. Am. Chem. Soc.* **1992**, 114, 5860.

184. Calvente, J. J.; Kovacova, Z.; Sanches, D.; Andreu, R.; Fawcett, W. R.; *Langmuir* **1996**, 12, 5696.

185. Hagenstrom, H.; Schneeweiss, M.A.; Kolb, D. M., *Langmuir* **1999,** 15, 2435.

186. Widrig, C. A,; Chung, C.; Porter, M. D., *J. Electroanal. Chem.* **1991,** 310, 335.

187. Walczak, M. M.; Popenoe, D. D.; Deinhammer, R. S.; Lamp, B. D.; Chung, C.;

    Porter, M. D., *Langmuir* **1991,** 7, 2687.

188. Eu, S.; Paik, W., *Chem. Lett.* **1998**, 405.

189. Chon, S.; Paik, W., *Phys. Chem. Chem. Phys.* **2001**, 3, 3405

190. Paik, W.; Eu, S.; Lee, K.; Chon, S.; Kim, M., *Langmuir* **2000**, 16, 10198.

191. Ron, H.; Rubinstein, I., *J. Am. Chem. Soc.* **1998**, 120, 13444.

192. Ma, F.; Lennox, R.B., *Langmuir* **2000**, 16, 6188.

193. Bain, C. D.; Whitesides, G. M. *J. Am. Chem. Soc.* **1989**, *111*, 7164.

194. Buck, M. et al. *J. Vac. Sci. Technol., A* **1992**, *10*, 926.

195. Thomas, R. C.; Sun, L.; Crooks, R. M.; Ricco, A. J. *Langmuir* **1991**, *7*, 620.

196. Hahner, G.; Woll, C.; Buck, M.; Grunze, M. *Langmuir* **1993**, *9*, 1955.

197. Xu S.; Cruchon-Dupeyrat, S.J.N.; Garno, J.C.; Liu, G.Y.; Jennings, G.K., *J. Chem. Phys.* **1998**, *108*, 5002.

198. Schreiber, F. et al. *Phys. Rev. B* **1997**, *57*, 12476.

199. Eberhardt, A.; Fenter, P.; Eisenberger, P. *Surf. Sci.* **1998**, *397*, L285.

200. Poirier, G. E.; Pylant, E. D. *Science* **1996**, *272*, 1145.

201. Yamada, R.; Uosaki, K. *Langmuir* **1998**, *14*, 855.

202. Kondoh, H.; Kodama, C.; Nozoye, H. *J. Phys. Chem.* **1998**, *102*, 2310.

203. Eberhardt, A. S. Ph.D. Thesis, Princeton University, Princeton, NJ, 1997.

204. Shimazu, K.; Yagi, I.; Sato, Y.; Uosaki, K., *Langmuir* **1992**, 8, 1385.

205. Kim, Y-T.; McCarley, R.L.; Bard, A.J., *Langmuir* **1992**, 8, 1941.

206. Debono, R. F.; Loucks, G. D.; Dellamanna, D. Krull, U. J., *Can. J. Chem.* **1996**, 74, 677.

207. Frübose, C.; Doblhofer, K., *J. Chem. Soc. Faraday Trans.* **1995**, 91, 1949.

208. Peterlinz, K.A.; Georgiadis, R., *Langmuir* **1996**,12,4731.

209. Truong, K.D.; Rowntree, P.A., *J. Phys. Chem.* **1996**, 100, 19917.

210. Terrill, R.H.; Tanzer, T.A.; Bohn, P.W., *Langmuir* **1998**, 14, 845.

211. Bensebaa, F.; Voicu R.; Huron, L.; Ellis, T.H.; Kruus, E., *Langmuir* **1997**, 13, 5335.

212. Himmelhaus, M.; Eisert, F.; Buck, M.; Grunze, M., *J. Phys. Chem. B* **2000**, 104, 576.

213. Humbert, C.; Buck, M.; Calderone, A.; Vigneron, J.P.; Meunier, V., *Phys. Status Solidi A.* **1999**,129, 175.

214. Pan, W.; Durning, W.C.; Turro, N.J., *Langmuir*, **1996**, 12, 1023.

215. Bain, C. D.; Troughton, E. B.; Tao, Y. T.; Evall, J.; Whitesides, G. M.; Nuzzo, R. G., *J. Am. Chem. Soc.*, **1989**, 111, 321.

216. Ishida, T.; Nishida, N.; Tsuneda, S.; Hara, M.; Sasabe, H.; Knoll, W., *Jpn. J. Appl. Phys. 2*, **1996**, 35, L1710 .

217. Tamada, K.; Hara, M.; Sasabe, H.; Knoll, W., *Langmuir*, **1997**, 13, 1558.

218. Truong, K.D.; Rowntree, P.A., *Prog. Surf. Sci.,* **1995**, 50, 207.

219. Deweldige, K.; Rohwerder, M.; Vago, E.; Viefhaus, H.; Stratmann, M., *Fresenius J. Anal. Chem.* **1995**, 353, 329.

220. Poirier, G. E.; Tarlov, M. J.; Rushmeier, H. E., *Langmuir* 1994, 10, 3383.

221. Stranick, S. J.; Parikh, A. N.; Allara, D. L.; Weiss, P. S., *J. Phys. Chem.* **1994**, 98, 11136.

222. Wasserman, S. R.; Whitesides, G. M.; Tidswell, I. M.; Ocko, B. M.; Pershan, P.S.; Axe, J. D.; *J. Am. Chem. Soc.*, **1989**, 111, 5852.

223. Woodward, J. T.; Schwartz, D. K., *J. Am. Chem. Soc.*, **1996**, 118, 7861.

224. Yamada, R.; Uosaki, K., *Langmuir* **1997**, 13, 5218.

225. Hickman, J.J.; Ofer, D.; Laibinis, P.E.; Wrighton, W.S., *Science* **1991**, 252, 688.

226. Casero, E.; Darder, M.; Takada, K.; Abruna, H.D.; Pariente, F.; Lorenzo, E. *Langmuir* **1999**, 15, 127.

227. Beulen, M.W.J.; van Heggel, F.C.J.M.; Reinhoudt, D.N., *Chem. Commun.* **1999**, 503.

228. Bardea, A.; Katz, E.; Willner, I., *Electroanalysis* **2000**, 12, 731.

229. Turyan, I.; Mandler, D., *Anal. Chem.* **1994**, 66, 58.

230. Turyan, I.; Mandler, D., *Anal. Chem.* **1997**, 69, 894.

231. Nagaoka, T.; Chen, Z.D.; Okuno, H.; Nakayama, M.; Ogura, K., *Anal. Sci.* **1999**, 15, 857.

232. Rubinstein, I.; Steinberg, S.; Tor, Y.; Shanzer, A.; Sagiv, J., *Nature* **1988**, 36, 73.

233. Yang, W.; Gooding, J.J.; Hibbert, D.B., *J. Electroanal. Chem.* **2001**, 516, 10.

234. Yang, W.; Gooding, J.J.; Hibbert, D.B., *Analyst* **2001**, 126, 1573.

235. Gooding, J.J.; Hibbert, D.B; Yang, W., *Sensors* **2001**, 1, 75.

236. Yang, W.; Jaramillo, D.; Gooding, J.J.; Hibbert, D.B.; Zhang, R.; Willett, G.D.; Fisher, K.J., *Chem. Commun.* **2001**, 1982.

237. Flink, S.; Boukamp, B.A.; van der Berg, A.; van Heggel, F.C.J.M.; Reinhoudt, D.N., *J. Am. Chem. Soc.* **1998**, 120, 4652.

238. Flink, S.; Schonherr, H.; Vansco, G.J.; Geurts, F.A.J.; van Leerdam, K.G.C.; van Heggel, F.C.J.M.; Reinhoudt, D.N., *J. Chem. Soc.-Perkin Trans.* **2000**, 2, 2141.

239. Yang, X.; Kumar, N.; Gooding, J.J.; Hibbert, D.B., *Org. Prep. Proc. Intern.* **1999**, 31, 425

240. Liu, H.Y.; Liu, S.G.; Echgoyen, L., *Chem. Commun.* **1999**, 1493.

241. Fujihara, H.; Nakai, H.; Yoshihara, M.; Maeshima, T., *Chem. Commun.* **1999**, 737.

242. Ito, T., *J. Electroanal. Chem.* **2001**, 495, 87.

243. Takaya, M.; Buhlmann, P.; Umezawa, Y., *Mikrochim. Acta.* **1999**, 132, 55.

244. Li, J.H..; Ding, L.; Wang, E.K.; Dong, S.J., *J. Electroanal. Chem.* **1996**, 414, 17.

245. Gooding, J.J.; Hibbert, D.B., *TrAC- Trends Anal. Chem.* **1999**, 18, 525.

246. Willner, I.; Lion-Dagan.; Marx-Tibbon, S.; Katz, E., *J. Am. Chem. Soc.* **1995**, 117, 6581.

247. Blonder, R.; Katz, E.; Willner, I.; Wray, V.; Buckmann, A.F., *J. Am. Chem. Soc.* **1997**, 119, 11747.

248. Lotzbeyer, T.; Schuhmann, W.; Schmidt, H.-L., Bioelectrochem. Bioenerg. **1997**, 42, 1.

249. Lotzbeyer, T.; Schuhmann, W.; Schmidt, H.-L., *Sensors Actuators* **1996**, B33,

250. Patolsky, F.; Zayats, M.; Katz, E.; Willner, I., *Anal. Chem.* **1999**, 1, 65.

251. Katz, E.; Buckmann, A.F.; Willner, I., *J. Am. Chem. Soc.* **2001**, 123, 10752.

252. Levicky, R.; Herne, T.M.; Tarlov, M.J.; Satija, S.K., *J. Am. Chem. Soc.* **1998**, 120, 9787.

CHAPTER 2

Experimental Theory
and
Methodology

2.1 Introduction

The instrumentation and experimental techniques employed for the characterization of the ferrocene-terminated alkanethiols shall be described in this chapter. The source and purity of all materials used is noted in this chapter along with the method of elemental analysis used. An initial discussion of the instrumentation shall be followed by a description of the electrochemical cell and its components. The pre-treatment techniques employed on the electrodes and a description of the electrode modification techniques used will be outlined. Finally, the experimental applications and the relevant theoretical foundations of the principle techniques employed in this study (cyclic voltammetry, electrochemical impedance spectroscopy) will be outlined.

2.2 Instrumentation

2.2.1 BAS 100W Workstation

All experimental work was conducted using the BAS 100W electrochemical workstation. The three main components of the workstation are the PC, potentiostat and electrochemical cell. All the experimental/control parameters are entered through the BAS 100W/Windows interface. This information is transferred to the BAS 100W microprocessor where optimum hardware settings are calculated for the specified technique. These values are then loaded automatically and after the experiment is run the data are collected and transmitted to the PC where they are displayed in virtual real-time. The data may subsequently be processed using options such as peak height determination or transformations e.g. Cotrell or Anson transforms. Figure 2.1 shows a block diagram of the BAS 100B/W Electrochemical workstation

EXTERNAL | INTERNAL | EXTERNAL
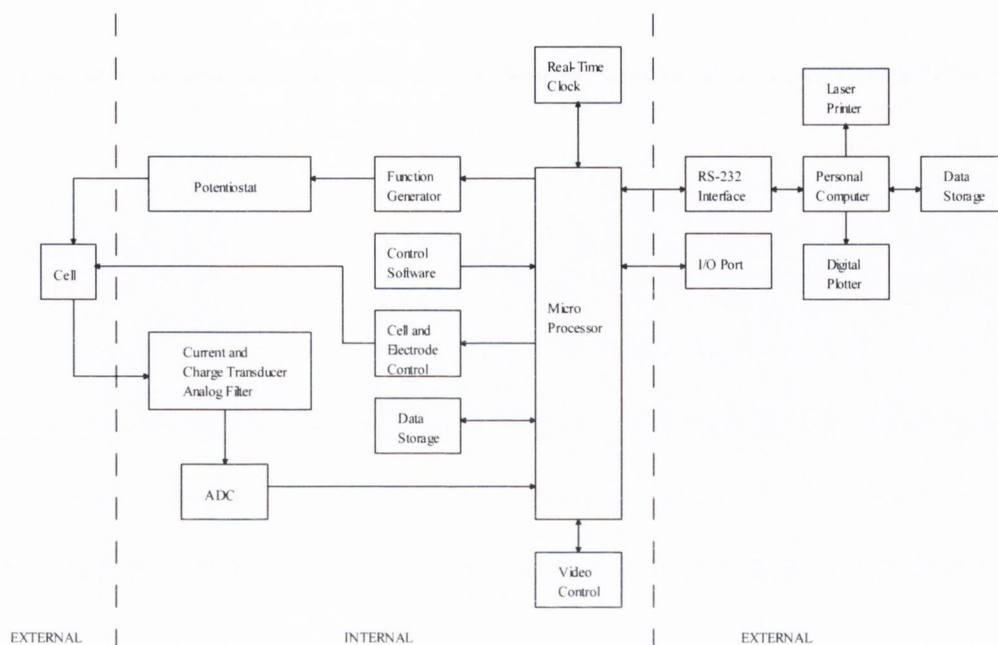
Figure 2.1: *Block diagram of the BAS 100B/W Electrochemical Workstation*

2.2.2 Potentiostat

In order to carry out voltammetric experiments it is necessary to have potentiostatic measurement and control. A potentiostat is an instrument to keep voltammetric sample under potential (voltage) control and monitors the current. In the construction of a potentiostat device, the basic building block is called an operational amplifier. This component comes in the form of an integrated circuit, often with different characteristics, depending on its destined application or requirement. A more comprehensive discussion of the device can be found in many electrochemical texts[1-3]; however, this section contains a short description of the potentiostat's operation and incorporation into a potentiostat's circuitry.

The operational amplifier, as stated already is the basic building block of a potentiostat. This is shown in figure 2.2. The operational amplifiers' fundamental concept is that e_o, the output, is the inverted, amplified voltage difference. Also, e_s, is the voltage of the inverting input with respect to the non-inverting input. i.e.

$$E_0 = -Ae_s \qquad (2.1)$$

Where A is the open loop gain.
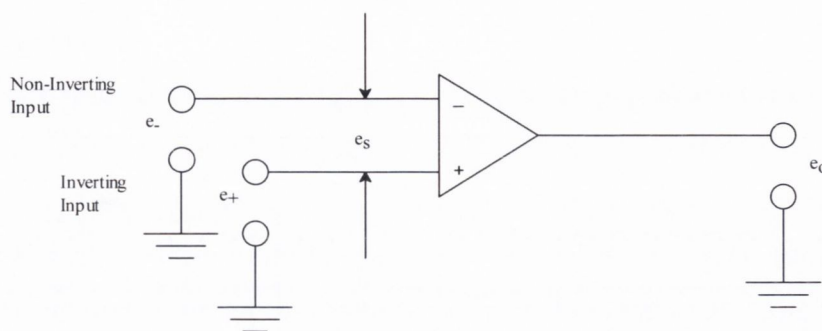
Figure 2.2: *Schematic diagram of an operational amplifier*

There are several important properties possessed by the operational amplifier. The first important property is that the open loop gain (A) is effectively infinite so that the smallest input, e_s, will cause the output to achieve the limit transferable by the power supply. Also, infinite input impedance should occur in the operational amplifier. This would result in the operational amplifier accepting input voltages without taking any current from the voltage surfaces. In addition, the device should contain zero output impedance, resulting in the supply of any desired current to its load. Finally, an infinite bandwidth should be present, allowing the amplifier to respond to signals of any frequency.

A previously stated, the operational amplifier is the back-bone unit of a potentiostat, however, a several alterations and additions are needed in the potentiostat's basic circuitry to enable the potentiostat to be at full operational capacity. Figure 2.3 shows a schematic diagram of how an operational amplifier may be used in controlling a voltage at a fixed point.
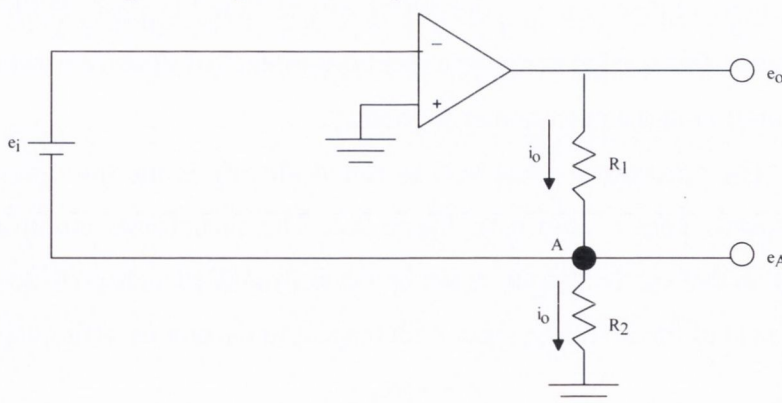
Figure 2.3: *Schematic diagram of a circuit for controlling the potential at a fixed point, A. The potential may be controlled independently of the changes in the two resistors R_1 and R_2.*

The input voltage is applied so that the top terminal is at e_i, with respect to the bottom one. However the inverting input is a virtual ground, resulting in the lower terminal and the point A on the diagram being at *versus* ground. The output will be adjusted by the amplifier to control the currents through the resistors so that this condition is maintained therefore facilitating the means to control the potential at a fixed point in the network of resistance's. This in essence is the task of a potentiostat during voltammetric studies. Figure 2.4 shows how this type of circuit is used in operating a basic potentiostat. The current that flows through the cell is controlled by the amplifier so that the reference electrode is *–versus* ground, as was previously stated, since the working electrode is grounded irrespective of the fluctuations in the interfacial impedance's at the counter and working electrodes.
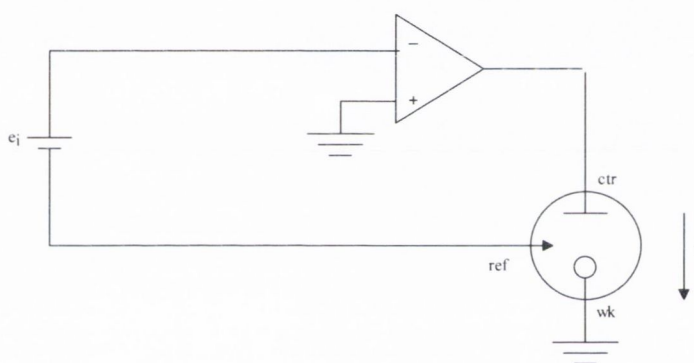
Figure 2.4: *Schematic diagram of a simple potentiostat based on a control circuit*

Eventhough the potentiostat described already will accomplish the basic tasks, there a number of alterations which need to be taken into consideration. Firstly, the function generator supplying the waveform for potential control has to possess a differential floating output so it should be noted that neither input terminal is a true ground. Second, there is no facility for inputting complicated waveforms at e_i. This is a necessity required when AC polargraphic experimentation. However, with the application of more than one input by a device called an adder potentiostat, renders both drawbacks obsolete i.e. all the inputs are true grounds and the requirement of producing complex waveforms is achieved by the addition of the input signals. However, this device alone will not be sufficient and other alterations to the basic adder potentiostats circuit are required in advance of its use as an operational

amplifier. It is also necessary to insert a voltage follower into the feedback loop of the reference electrode. This ensures that the electrode supplies a significant current to the summing point. Another further alteration in the circuitry includes adding a current follower, which the working electrode supplies, hence making the measurement of current in the cell possible. Finally a booster (non-inverting amplifier) is placed in series with the operational amplifier, resulting in the increase in the power available at the cell. All these modifications together produce the final product, a full potentiostatic system based on an operational amplifier, which is illustrated in figure 2.5.

The potentiostat used as the control element in this body of work was incorporated into the BAS 100B electrochemical workstation analyser. The potentiostat was connected to the electrochemical cell as shown in figure 2.5.
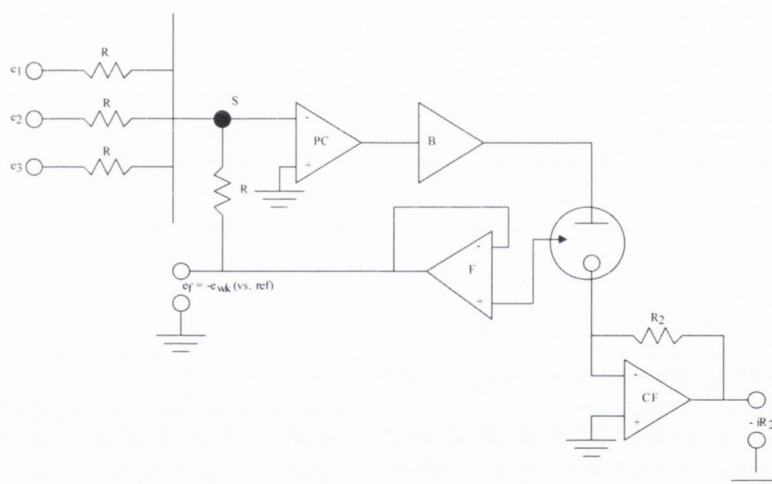
Figure 2.5: *Schematic diagram of a full potentiostat based on an adder control amplifier.*

2.2.3 C2 Cell Stand

The C2 cell stand, figure 2.6, is used for completely isolating the electrochemical cell during experimentation. The cell is enclosed in a Faraday cage to shield the cell from external electrical interference, this being an important factor when working with microelectrodes where the measured currents are at submicroampere level. Another advantage of the cell stand is that the cell is completely isolated from light during experimentation therefore facilitating work with light sensitive chemicals. The cell also features manual and computer controlled gas purging and stirring of solutions.
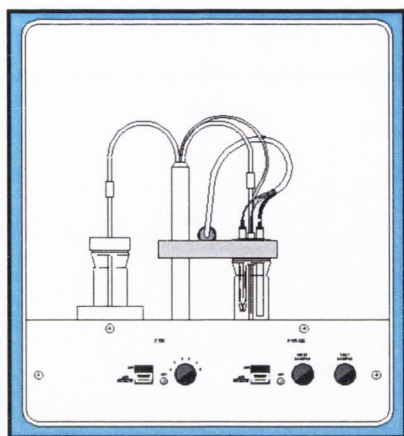
Figure 2.6: *Illustration of the C2 cell stand*

2.3 The Electrochemical Cell

The electrochemical cell consists of three main parts, namely a working vessel, electrodes and an electrolyte solution. A Teflon cell top sealed the vessel at all times with inlets for the electrodes and for the gas purger. Nitrogen gas was used to purge the solution for 15 minutes before experimentation to ensure complete saturation. During experimentation a blanket of the inert gas was maintained above the solution. All work was conducted at $25°C \pm 1°C$. A standard three electrochemical cell was employed at all times during the study, consisting of a working electrode, which defines the interface under study, a reference electrode, which maintains the reference potential and an counter (auxiliary) electrode which allows the passage of current. The working vessel employed had a volume of 30 cm^3 for the C2 cell stand work. The work was conducted at room temperature $(25°C \pm 1°C)$. The experimental cell set up is depicted in figure 2.7.
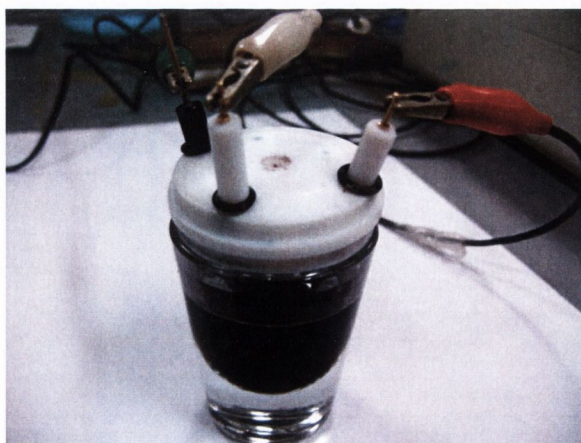
Figure 2.7: *The three electrode Electrochemical Cell. Left: The working electrode (green clamp), Centre: The reference electrode (white clamp), Right: The counter electrode (red clamp).*

117

The working electrode material is normally chosen to complement the requirements of a particular experiment. An important feature is that the electrode should not react chemically with the solvent or solution components. Another main consideration is that the potential range desired can be obtained by the working electrode. The working electrode range in terms of accessible potentials is limited by a number of processes such as electrolyte and solvent decomposition, hydrogen and oxygen evolution and oxide formation on the electrode surface. To minimise the effects of these phenomena and to maximise electrode reliability, various different solid materials may be used in these electrodes. Materials such as platinum, carbon, mercury and gold have all been used. In order to ensure uniform current and potential distribution the area of the working electrode should be smaller than the counter/ auxiliary electrode.

In this study gold macroelectrodes were employed at all times. The gold macroelectrodes were 2 mm in diameter and had an area of 0.0314 cm^2. The gold macroelectrodes were produced by embedding the disc of gold into a PTFE plastic rod. These gold electrodes were supplied by IJ Cambria. Before experimentation the electrodes were polished (section 2.4.1) to a mirror finish to ensure that a reproducible state of oxidation, surface morphology and freedom from adsorbed impurities was achieved.

2.3.1 Reference Electrode

The purpose of a reference electrode is to provide a fixed potential which is invariant with respect to time during the experiment. The potential of the reference electrode is in turn related to other scales, for example, to the normal hydrogen electrode (NHE). Hence, any change in applied potential in the cell appears at the working electrode/solution interface. Ideally, if a small current passes through the reference electrode, the potential change should be negligible and should return to its initial value when the current ceases. The reference electrode most widely employed for aqueous systems are the saturated calomel (mercury/mercurous chloride) electrode and the silver/silver chloride electrode. In the case of the Ag/AgCl electrode, the electrolyte is usually saturated KCl or NaCl. The reference potential is dependent on

the concentrations of the chloride concentration in the electrolyte as well as the standard redox potential of the electrochemical reaction. It should also be noted that any changes in the salt concentration within the reference electrode will affect its potential. Hence, a porous Vycor barrier is normally placed between the internal solution of the electrode and the electrolyte. This allows contact between the two solutions but minimises effective mixing thereby keeping the salt concentration within the reference electrode virtually constant. The Ag/AgCl, KCl electrode (sat.) was used in this body of work.

2.3.2 Counter (Auxiliary) Electrode

The purpose of the counter electrode is to supply the current required by the working electrode thus preventing the polarisation of the reference electrode due to the passage of current. It should be insoluble and inert in the supporting electrolyte solution and should not impose its characteristics upon the measured cell response. The size, shape and position of the auxiliary electrode are important considerations since these factors determine whether the working electrode is an equipotential surface. In this work a platinum wire of area 1.3 cm^2 was used as a counter electrode. This was positioned close to the working electrode to minimise overall cell resistance. The surface area of the counter electrode is deliberately kept high to minimise polarisation on the electrode, thus, avoiding unwanted contributions to the cell response.

2.3.3 Electrolyte Solutions

All electrode reactions are conducted in solutions containing a high concentration of inert electrolyte called a supporting electrolyte. The reason for using this solution is to minimise the phenomenon of migration of the electroactive ions caused by the electric field and to confine the interfacial potential difference to the distance of closest approach of solvated ions to the electrode. The supporting electrolyte is the principal source of electrically conducting ionic species and has a concentration of at least 100 times that of the electroactive species, normally varying between 0.01M and 1.0 M. The supporting electrolyte must truly be inert in the potential range of the

experiment, not reacting with the electrode or with the products of the electrode reaction. It is for this same reason that the reagent used for preparing the electrolyte must be of a high purification grade.

A number of different electrolytes were used in this work for both aqueous and nonaqueous solvents. Ultra-pure water from a Millipore water purification system was used in the preparation of aqueous electrolytes. The electrolytes potassium chloride (KCl, 99%), perchloric acid ($HClO_4$, 70%) and sodium perchlorate ($NaClO_4$, 97%) were purchased from Aldrich Ireland.

It should be mentioned that dissolved oxygen in the electrolyte solution is an undesirable impurity in electrochemical experimentation. Some problems which might arise due to the presence of oxygen include: oxygen reduction at cathodic potentials, oxide formation on the electrode surface and reaction with intermediates formed during electrode reactions. As a result degassing of the working solution with a fine stream of nitrogen gas was conducted for approximately fifteen minutes before experimentation and during experimentation a blanket of the inert gas was maintained over the solution.

2.4 Electrode Modification Techniques

2.4.1 Electrode pre-treatment

All electrodes were pre-treated to ensure a reproducible surface morphology and freedom from adsorbed impurities. However, due to the different nature of the electrode materials employed slightly differing regimes were engaged.

The gold electrodes used were initially polished on a cloth pad with diamond lapping compounds of 15, 3 and 1 micrometre dimensions. Following this treatment the electrode was polished with an alumina oxide paste in distilled water on a fine grit pad so as to remove any solid polishing residues. A clean, reproducible, uniform electrode surface was obtained following this treatment. Lastly, the electrode was rinsed thoroughly with Millipore water to remove traces of the solid alumina residues.

2.4.2 Monolayer Deposition

Following the pre treatment steps as described in section 2.4.1 the electrodes were ready for the deposition phase. An alkanethiol monolayer can be deposited on an electrode surface in several ways. As well as solution adsorption alkanethiols may be deposited from the vapour phase[4] and ambient pressures[5] providing the alkanethiol is sufficiently volatile. The resulting SAMs appear identical to those formed from the solution phase.

In this body of work solution adsorption was employed to ensure minimum product loss. After the cleaning process described above, the ferrocene alkanethiol thiol monolayer was formed by immersing clean bare gold electrodes in 1mM ferrocene alkanethiol in ethanol (EtOH) solution for 24-48 h. Following this, the electrodes were then washed several times with EtOH and water[6]. The typical experimental setup for solution adsorption is shown in figure 2.8.
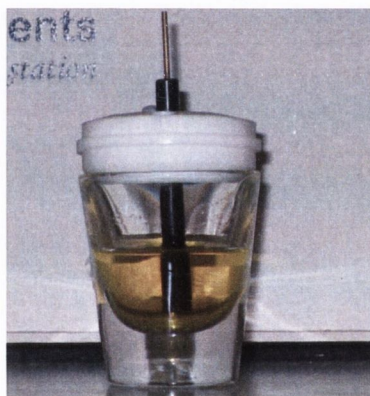
Figure 2.8: *Typical experimental setup for solution adsorption*

2.4.3 Monolayer Polarisation

It was reported by Lennox[7] alkanethiols that alkanethiols could be quickly and reliably assembled onto gold surfaces by holding the potential of the working electrode in the alkanethiol solution for a period of time (15 min-2 h).

A clean bare gold electrode is placed into an electrochemical cell containing the ferrocene alkanethiol solution along with a reference electrode and a counter electrode. A current of 0.4 V is passed through the gold working electrode for the duration of the experiment. The electrodes are usually polarized for between 1-2 hours.

2.5 Experimental Techniques

2.5.1 Potential Sweep Techniques

Polarography was the best known measuring method in electroanalytical chemistry, however, the emergence of cyclic voltammetry, has seriously challenged polarography for this title. Cyclic voltammetry (CV) is a technique which mainly involves applying a time dependant potential to the working electrode of an electrochemical cell. This cell will contain the solution of interest, and possibly an electroactive substrate, electrolyte excess, a counter electrode and a reference electrode. The potential is cyclically swept between two predetermined voltage limits, an initial voltage (E_1) and a final voltage (E_2). The sweep direction is reversed at E_2, also known as the switching potential and continues in the opposite direction at a known scan rate, υ, where $\upsilon = dE/dt$. The triangular waveform which results is illustrated in figure 2.9.
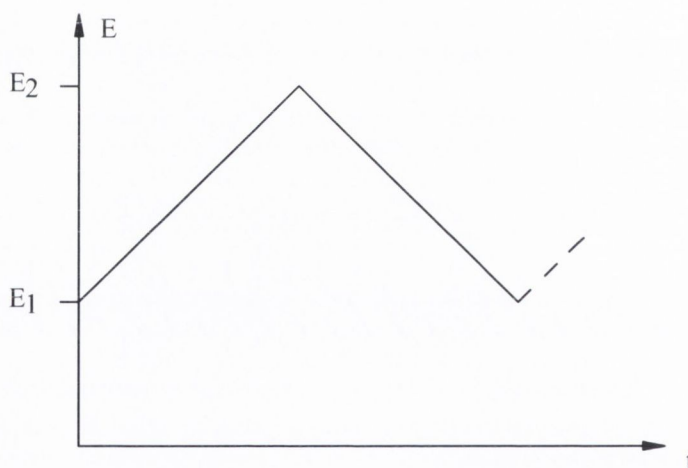
Figure 2.9: *Illustration of the linear potential sweep with a triangular waveform, which is applied to the working electrode. This excitation signal scans the electrode between two potentials E_1 and E_2.*

Usually, the initial working electrode potential (E_1) is chosen where a substrate is electroactive. Subsequently, the potential is altered at a constant scan rate through a potential window where the interested redox reaction occurs until the switching potential is reached. The voltammogram which results, records the measured cell current as a function of the applied potential. The current peaks display the initiated redox activity of the substrate due to the applied potential. The standard redox

potential (E_o) can be determined i.e. the potentials where these reactions occur.

The reason that cyclic voltammetry has become so important is that information on the presence of electroactive moieties in the solution or at the electrode interface can be obtained from the technique[8-12]. The roles of adsorption, diffusion and coupled homogeneous chemical reactions can be identified from the sweep rate dependence of the observed peaks.

Normally, there are the three categories into which electrochemical systems are classified. They are reversible, irreversible and quasi-reversible systems. The allocation of classification for a particular system is determined by the magnitude of the electrode transfer rate constant. Also, redox reactions may involve either solution phase or immobilised couples. The current response is mainly dependant on two steps; the transport of electroactive species from the bulk solution to the electrode surface and secondly, the electron transfer reaction between the species and the electrode surface. A reversible system occurs when the oxidised and reduced species are in equilibrium at the electrode surface. In this situation the Nernst equation (Eqn 2.2) can be applied. The electrode reaction is known as reversible since its follows exactly the condition for thermodynamic reversibility. The application of the Nernst equation and, hence, the criteria for reversibility, is related to the time taken for the electrode solution to achieve equilibrium. The concentration of the electroactive species at the interface is dependant on the mass transport of these moieties from bulk solution and depends on the mass transfer coefficient, α. The standard rate constant, k_0, occurs where $E = E_o$. In the case of a reversible reaction the kinetics of the electrode reaction is much faster than the transport. For this electrochemical process it is useful to consider a simple n electron reversible electron reaction

$$R \leftrightarrow O + ne^-$$

where R and O represent the reduced and oxidized forms respectively.

For a reversible redox process, the ratio of the concentration of the oxidized form to reduced form, C_O/C_R, within the region next to the electrode surface follows the applied potential in a Nernstian manner,

$$E = E^0 + 2.303\left(\frac{RT}{nF}\right)\ln\left(\frac{C_0}{C_R}\right) \tag{2.2}$$

where E^0 is the formal potential of the redox couple. The current (I), is proportional to the concentration gradient near the electrode surface according to Fick's first law

$$I = nFAD\left(\frac{dC_0}{dx}\right) \tag{2.3}$$

The shape of the cyclic voltammogram may be explained in terms of the concentration profiles shown in figure 2.10. Initially at cathodic potentials there is no cell current produced however as the potential is swept anodically towards E_0 the electrode becomes a sufficiently strong oxidant converting R to 0 (figure 2.10 (a)), resulting in a small anodic current flowing. At E^0, the ratio of concentrations, C_o/C_R,is always unity. As the potential is swept further the current continues to rise, past E^0, until the concentration gradient reaches a maximum resulting in a peak current, i_{pa}.
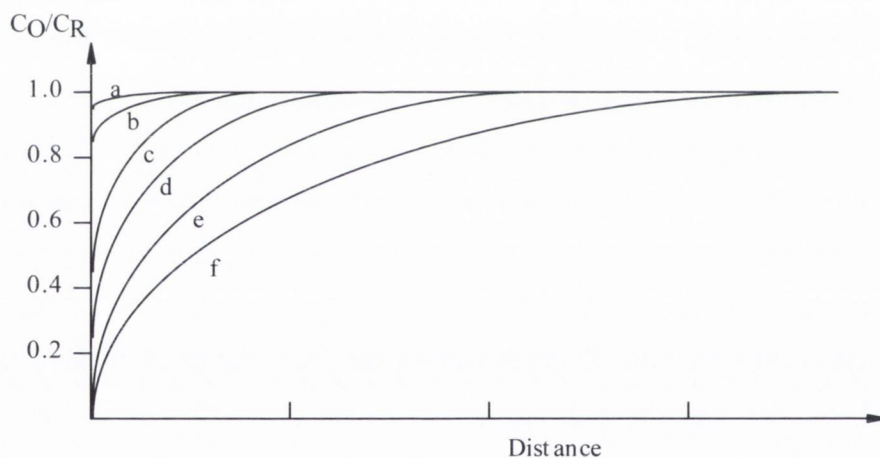
Figure 2.10: *The concentration-distance profiles for an electroactive species, R, during linear sweep voltammetry. The overall reaction sequence is $R \leftrightarrow O + ne^-$.. The curves correspond to the following approximate potentials; (a) E^0 –90mV; (a) E^0 –90mV; (b) E^0 –50mV; (c) E^0 ;(d) E^0 +30mV; (e) E^0 +130mV; (f) E^0 +280mV.*

Further potential increase leads to the consumption of the reduced form of the electroactive species at the electrode surface resulting in the depletion of the R species concentration to almost zero. On reverse scanning the described series of events is repeated for the generation of 0, the oxidised form of the electroactive species which now predominates at the electrode surface. This opposite process results in the generation of a reduction peak on the reverse scan, the net process

producing a current/potential trace similar to that illustrated in figure 2.11.

The redox species diffuses to the electrode surface due to the generation of an interfacial concentration gradient. Migration effects are eliminated ensuring there is a presence of a relatively large amount of electro-inactive ions, while convection is avoided by working with unstirred solutions.

Under the conditions of semi-infinite linear diffusion, the peak current i_p, is given by[13-15].

$$i_p = 0.4663nFA\left(\frac{nF}{RT}\right)^{\frac{1}{2}} C_0^{\infty} D^{\frac{1}{2}} \upsilon^{\frac{1}{2}} \tag{2.4}$$

where D is the diffusion coefficient, υ is the scan rate and C_o is the concentration of the bulk solution of electroactive species.
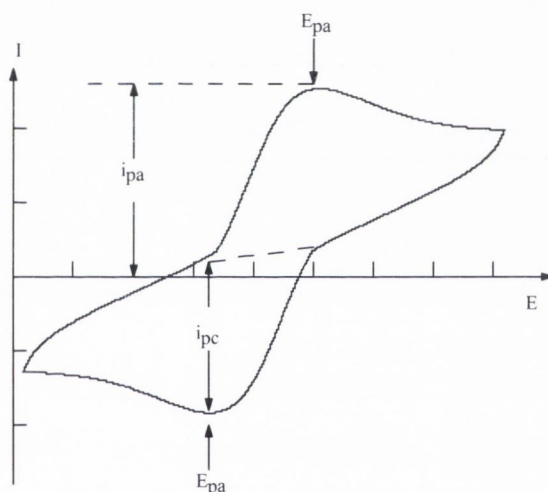
Figure 2.11: *Cyclic Voltammogram for a model reversible process, $R \leftrightarrow O + ne^-$.*

This is known as the Randles-Sevcik equation and shows that the peak current is proportional to the square root of the scan rate. However, it must be noted, that the diffusion characteristics of the system may only apply for a short time, as thermal and concentration gradients may induce random convection processes, resulting in fluctuations of the resulting current. For this reason, only data obtained from analysis of the first sweep is normally used to deduce kinetic parameters. A direct test of whether or not a system is reversible is to plot peak current versus sweep rate. If this plot is linear it is a good indication that the system is reversible. However, several other diagnostic tests can be utilized to verify this. These include: (1) The

potential difference between the anodic and cathodic peaks is 59 mV. (2) The ratio of the anodic and cathodic is uniform. (3) The voltage at which peaks appear is independent of the sweep rate. (4) At potentials beyond the peak potential is proportional to time.

For irreversible systems, the electron transfer rates at all potentials are significantly less than the transfer rate of mass transfer. As a result, Nernstian equilibrium is not maintained at the electrode surface.

At low potential sweep rates the rate of electron transfer is great enough that a reversible voltammetric response may be recorded. As the sweep rate increases and the rate of mass transport is increased, the electron transfer processes are insufficient to maintain this surface equilibrium, then an alteration of the shape of the cyclic voltammogram is seen. The most notable effect this has on the CV response is to increase the separation between the peaks.

It is also seen that as well as an increase in peak separation a peak height decrease is also normally observed. The reason the peak height is diminished is related to the fact that in an irreversible process the peak is more drawn out. This is because the surface concentration of the reduced form changes more slowly with potential in irreversible systems.

Probably the most marked feature of a cyclic voltammogram recorded for a totally irreversible system, is total absence of a reverse peak. However, this alone is not conclusive evidence of a reversible system and other diagnostic tests are necessary for verification[16]. A description of the various diagnostic tests for reversible and irreversible systems can be found in research carried out by Nicholson and Shain[17].

Frequently, processes under cyclic voltammetric examination appear reversible at low values of scan rate, but appear to become irreversible at higher values of sweep rate. This scan dependence is illustrated in figure 2.12. If the extent of irreversibility increases with increasing scan rate, the system is said to be quasi-reversible.

This type of system is mathematically complex as it necessitates simultaneous consideration of both the oxidation and the reduction reactions and the rate of

material transport to the electrode surface. These kinetics are described by the Butler-Volmer equation. Here the observed current is proportional to the difference between the rate of the oxidation and reduction reactions at the electrode surface and is given by:

$$I = nFA(k_a[C_R] - k_c[C_O])$$
(2.5)

Where k_a and k_c are the anodic and cathodic rate constants respectively.
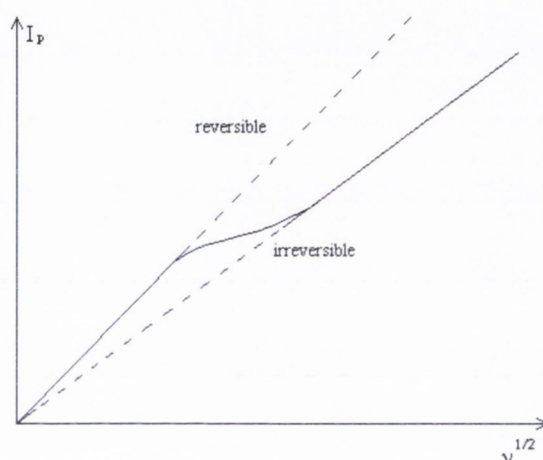
Figure 2.12: *Transition from reversible to irreversible behaviour of the redox couple due to change of scan rate.*

2.5.1.1 Cyclic Voltammetry of Electroactive SAMs

As the main investigation of this work is self-assembled monolayers with an electroactive ferrocene headgroup it is necessary to introduce the response obtained for the electroactive SAM to the cyclic voltammetry method. Figure 2.13 shows a typical CV for an electroactive monolayer.

A CV for an electroactive SAM usually exhibits anodic and cathodic peaks which are exactly similar. E^0 represents the standard potential of the SAM and was calculated from:

$$E^0 = \frac{E_{p,ox} + E_{p,red}}{2}$$
(2.6)

where $E_{p,ox}$ is the anodic peak potential and $E_{p,red}$ is the cathodic peak potential calculated from figure. The anodic and cathodic peak potentials also provide the

potential peak splitting (ΔE_p) which is calculated from the change in potential. The change in potential was calculated from:

$$\Delta E_p = \left| E_{p,ox} - E_{p,red} \right| \tag{2.7}$$
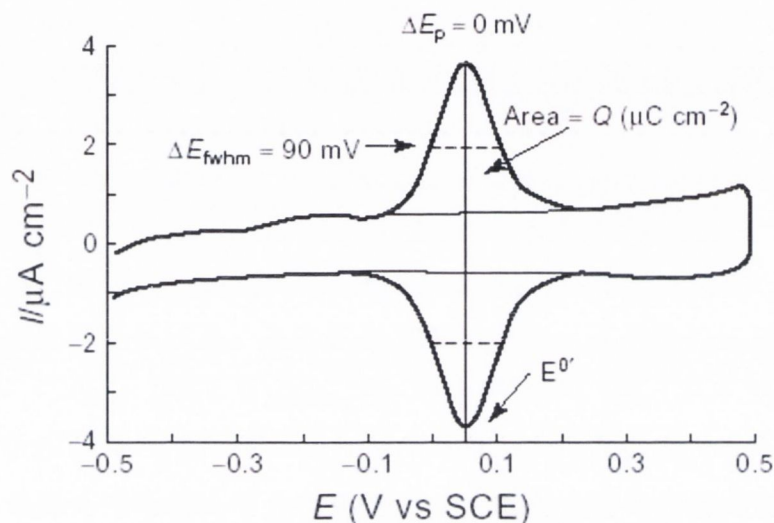
Figure 2.13: *Reversible Cyclic Voltammogram of an electroactive SAM. The redox thiol is $HS(CH_2)_{11}CONHCH_2pyRu(NH_3)_5^{2+/3+}$ and the diluent thiol is $HS(CH_2)_{11}COOH$. The electrolyte is 1 M H_2SO_4 at pH4. From reference 18.*

The surface coverages of the redox center (Γ) on the electrode surface are then obtained by current integration after extrapolating and subtracting the charging current baseline underneath either of the peaks. The surface coverage of ferrocene redox active sites on the electrode is calculated from the following:

$$\Gamma_{FC} = \frac{Q}{nFA} \tag{2.8}$$

Where Q is the peak area in coulombs, n is the number of electrons transferred in the redox center half reaction, F is Faraday's constant and A is the area of the gold electrode ($0.0314 cm^2$). Chidsey et al.[19] estimated that the maximum surface coverage of ferrocene alkanethiol SAM (Γ_{max}) should be 4.5×10^{-10} mol cm^{-2} based on a close-packed layer of 6.6 Å diameter spheres.

The shape of the CV can be quantitatively described using a theory described by Laviron[20]. We can show that the current response for a reversible surface redox process is given by:

$$\Psi = \frac{i}{n^2 F^2 A \Gamma_\Sigma \upsilon / RT} = \frac{e^{-\xi}}{\left(1 + e^{-\xi}\right)^2} = \frac{1}{4} \sec h^2 \frac{\xi}{2} \qquad (2.9)$$

Where Ψ is the normalised current and ξ is the normalised potential given by:

$$\xi = \frac{nF}{RT}\left(E - E^0\right) \qquad (2.10)$$

The normalized current reaches a maximum value of $\Psi = \Psi_M = \frac{1}{4}$ when $\xi = 0$ or

when $E = E^0$. Under such circumstances:-

$$i_p = \frac{n^2 F^2 A \Gamma \upsilon}{4RT} \qquad (2.11)$$

Where n, F, A and Γ are the values explained in equation 2.8, R is the gas constant
and T is the temperature. The CV of an electroactive SAM is reversible if its shape
and the peak positions do not change with scan rate. According to equation 2.11, the
peak current, i_p, is proportional to the scan rate, υ.

For an ideally shaped CV the current obeys equation (2.12):

$$i = \frac{4i_p e^\theta}{\left(1 + e^\theta\right)^2} \qquad (2.12)$$

where θ is given by equation (2.13).

$$\theta = \frac{nF\left(E - E^0\right)}{RT} \qquad (2.13)$$

where E^0 is the peak potential of the redox species.

The peak half-width, ΔE_{FWHM} can also be calculated. This value corresponds
to peak width of either the anodic or cathodic peak at the point where half the current
maximum occurs. The expected behaviour for non-interacting electroactive groups
attached to the surface ($\Delta E_{FWHM} = 90.6$ mV) and in rapid equilibrium with the
electrode, which is calculated from the following:

$$\Delta E_{FWHM} = \frac{2RT}{F} \ln(3 + 2\sqrt{2}) \qquad (2.14)$$

The above represents ideal CV diagnostics for an electroactive monolayer. However, deviations in ideal behaviour in ferrocene alkanethiol SAMs are common. Such deviations reveal much about the redox centre and/or the SAM in terms of molecular detail. Differences in the peak potentials of the oxidative and reductive waves (non-zero ΔE_p) indicates possible intermolecular interactions between the redox centres or a change in the SAM structure with respect to the oxidation sate of the redox centres (e.g. structure may change due to ion pairing).

The peak width at half maximum (ΔE_{FWHM}) can also deviate from its ideal value. However, ΔE_{FWHM} may be smaller or larger than the theoretical 90.6 mV. Theoretical values which are larger than normal indicate a wide spread of formal potentials, possibly indicating a disorganized SAM with a range of local environments, intermolecular interactions between redox centres or double layer effects. Double layer effects occur when the charge density on the SAM surface causes a change in the local electrostatic potential[21,22]. Such distortions are reduced when the fraction of redox sites on the surface is reduced. Smaller than theoretical values are manifested by a sharp CV are obtained of the redox centres tend to form a solid like phase. This occurs in the most densely packed electroactive SAMs.

A typical CV for a ferrocene alkanethiol SAM is presented in figure 2.14. The main sharp peaks observed may be attributed to a very densely packed monolayer[23]. It was proposed by Labinis et al[24] that a change in the structure of the monolayer upon oxidation/reduction of the ferrocene groups causes these sharp peaks.
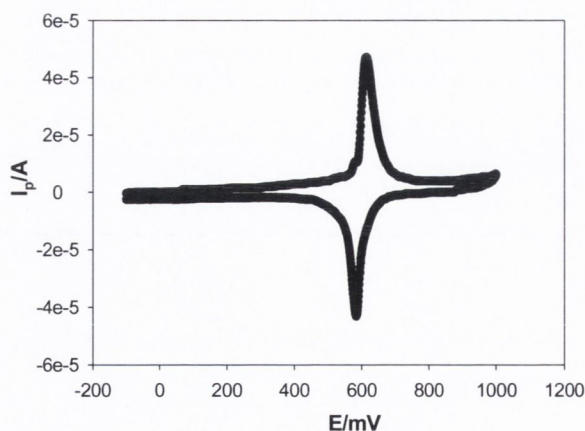
Figure 2.14: *Cyclic voltammogram in 1M HClO₄ of 1mM FcCO₂(CH₂)₁₂SH monolayer formed from EtOH solutions. Scan rate 100 mVs⁻¹. ΔEₚ= 30 mVs⁻¹*

However, later studies by Sato et al.[25] disagrees with the postulations of Labinis. Sato noted that the terminal group of the ferrocene labeled SAM is neutral in the reduced form and has a positive charge in the oxidized form. As the terminal ferrocene group is oxidized to the ferricinium cation an ion pair is formed between the positively charged ferrocene group and an electrolyte ion. Since the distance between the ferrocene group and the positively charged gold electrode is smaller than the distance between the electrolyte ion and the gold electrode there will be an electrostatic repulsion between the gold and the ferricinium ion.

This repulsion results in the SAM rotating to a more perpendicular position relative to the electrode in order to increase the distance between the two positively charged surfaces. Upon reduction the pendant ferrocene molecules become neutral and the ion pairing is lost as is the repulsion between the ferrocene molecules and the electrode. This causes the SAM to relax in a less perpendicular position relative to the electrode. This structure change is more likely to manifest itself in a non zero peak splitting rather than sharp peaks, as different orientations of the SAM are likely to have different redox potentials.

2.5.2 Chronoamperometry

Another commonly employed electroanalytical technique is chronamperometry. Chronamperometry is a useful tool in the determination of coefficients and the investigation of the kinetics of a system. These experiments involve an instantaneous change in the applied potential to the working electrode and the resulting current-time response recorded as the system relaxes towards its new steady state. The best method to describe chronoamperometry is using the simple n electron reversible electrode reaction;

$$R \leftrightarrow O + ne^-$$

A potential-time profile such as the one shown in figure 2.15(a) is applied to the working electrode. The initial potential (E_1) is chosen so that no current is flowing (i.e. the electrode is held at a potential that neither oxidises nor reduces the predominant form(R) of the analyte). At t =0, the potential is instantaneously changed from E_1 to E_2, where oxidation of the R species occurs at a diffusion controlled rate.

Figure 2.15(b) depicts the resulting current-time transient. The current will be the sum of the electrochemical double layer charging current and the Faradaic current. The potential change results in the reorganization of the species in the double layer and causes the double layer charging current. This double layer charging current manifests itself as a sharp spike in the current at short times with a typical lifetime of a few hundred microseconds. Electron transfer to the R species in solution causes the Faradaic current.

Concentration profiles develop near the electrode surface with time. At t=0, the surface concentration of species R (C_R) changes from its initial value (C_R^∞) to a value 0. This will occur very near the electrode surface and consequently the concentration profile will be steep. With increasing time, diffusion causes the concentration profiles to relax towards their steady state by extending into solution and becoming less steep.

According to Fick's Law, which describes the change in C_R with time, equations are solved to obtain more detailed knowledge of the current-time transient,

$$\frac{\partial C_R}{\partial t} = D_0 \left(\frac{\partial C_R}{\partial x^2} \right) \tag{2.15}$$

subject to the boundary conditions appropriate for semi-infinite diffusion:

At t=0 and for all x=0, $C_R = C_R^\infty$,

For t>0, at x=0, $C_R = 0$,

At x=∞, $C_R = C_R^\infty$.

For purely planar diffusion to the electrode, solution of the differential eqn 2.15 gives the Cottrell equation:

$$i = \frac{nFAD_0^{1/2}C_R^\infty}{\pi^{1/2}t^{1/2}} \tag{2.16}$$

where n is the number of electrons transferred, D is the diffusion coefficient, F is the Faraday constant and A is the area of the electrode. Hence, if the reaction is diffusion controlled a plot of I versus $t^{1/2}$ should be linear and pass through the origin.
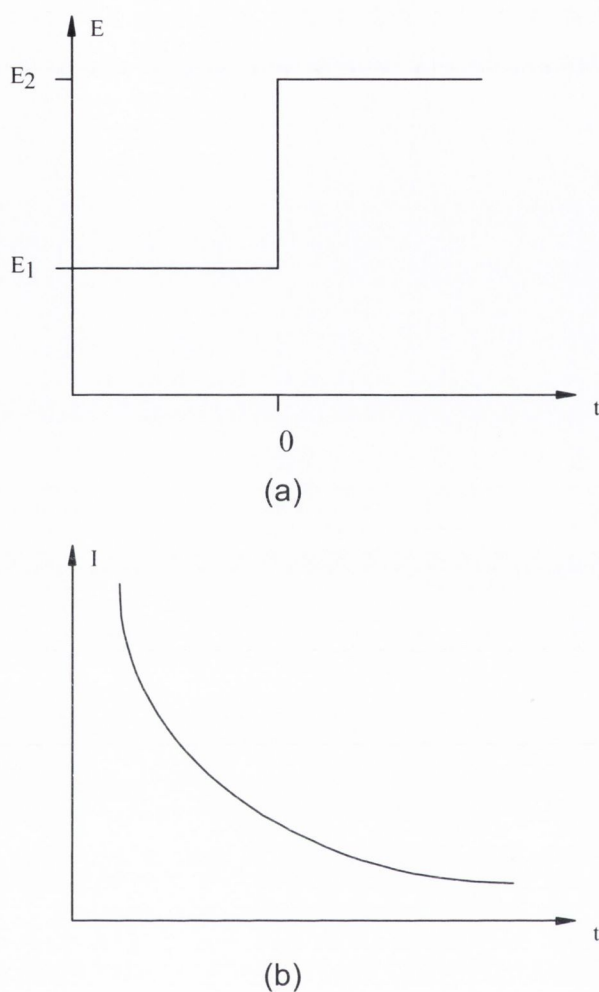
Figure 2.15: *(a) The potential-time profile for a single potential step chronoamperometric experiment, (b) The resulting current-time transient for the reaction $O + ne^- \Leftrightarrow R$*

2.5.2.1 Chronoamperometry of Electroactive SAMs

The electroactive monolayer chronoamperometric response has previously been investigated by Lyons[26]. If one considers the potential step such as the one represented in figure 2.15 applied to a redox couple A/B immobilized on a surface and Γ_A and Γ_B represent the surface coverage of either surface components. The total surface coverage can then be described by:

$$\Gamma_{\varepsilon} = \Gamma_A + \Gamma_B \tag{2.17}$$

Simply the reaction can be treated as irreversible and can thus be written by:

$$\frac{-d\Gamma_A}{dt} = \frac{d\Gamma_B}{dt} = k_E' \Gamma_A \tag{2.18}$$

Where $k_E^{'}$ is the heterogeneous electrochemical rate constant of the form given by:

$$k_E^{'} = k^0 \exp[\beta\xi] \qquad (2.19)$$

Where the standard rate constant is denoted by k^0, β is the symmetry factor and ξ is a normalized potential given by $\xi = \dfrac{F}{RT}\left(E - E_{A/B}^0\right)$. The current response to the applied potential step can then be written as:

$$i(t) = nFAf_c(t) = nFAk_E^{'}\Gamma_A(t) \qquad (2.20)$$

In the above equation f_c is the net flux, A represents the electrode area, F is Faraday's constant and n is the number of electrons transferred during the surface redox process. On integration of equation 2.20 the variation of surface coverage with time is obtained. It is assumed that t=0 and all redox active sites are of the form A. From this:

$$\Gamma_A = \Gamma_\varepsilon \exp(-k_E t) \qquad (2.21)$$

from this equation the surface redox process can be written as:

$$i(t) = k_E^{'}Q\exp(-kt) \qquad (2.22)$$

where the charge Q is related to the surface coverage of the electroactive groups by equation 2.8. Taking the natural logarithm of equation 2.22 we obtain:

$$\ln i = \ln(k_E^{'}Q) - k_E t \qquad (2.23)$$

Thus a plot of ln(i) versus t is expected to be linear with a slope that corresponds to the heterogeneous rate constant. Many research groups have applied this approach to investigate the theories of long range electron transfer[27-34]. These plots can be used to test the quality of self assembled monolayers.

2.5.3 AC Impedance

AC impedance measurements allow a greater amount of information to be obtained and this allows the separate determination of the components of the metal-solution interface. AC impedance employs the approach of perturbing the cell with an alternating signal of small magnitude and observing the way in which the system follows the perturbation at steady state. In AC impedance an alternating current signal is applied in the presence of a DC ramp allowing the phase of the AC current along

with the electrochemical cell resistance and the capacitance to be measured. The electrical circuit equivalent to the electrochemical cell is shown in figure 2.16.
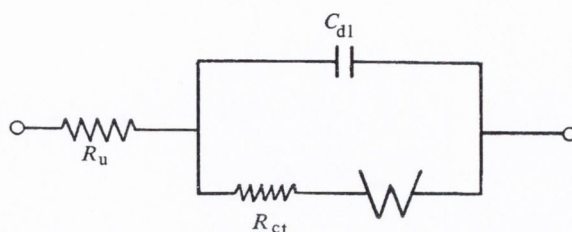
Figure 2.16: *Electrical circuit equivalent to an electrochemical cell with mixed kinetic and charge transfer control.*

There are three components to the electrical circuit: the double layer capacitance (C_{dl}), a solution resistance (R_u) and a complex impedance due to any Faradaic processes at the electrode. This impedance can also be expressed as the charge transfer resistance (R_{ct}) in series with a second impedance called the Warburg impedance (ω).

As shown in figure 2.17, at high frequencies the system is kinetically controlled by the Faradaic process. This results in the appearance of a semi circle in the impedance spectrum. This semicircle is centred at $(R_u + R_{ct})/2$ with a diameter of R_{ct}.
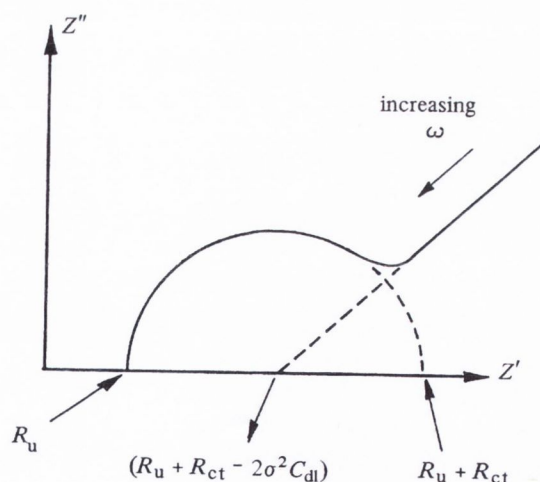
Figure 2.17: *AC Impedance Spectrum of the electrochemical cell.*

At low frequencies diffusion becomes more important and the plot is dominated by the double layer capacitance, C_{dl}. This leads to a linear plot with unit slope that intercepts the real axis at $R_u + R_{ct} - 2\sigma^2 C_{dl}$. In this equation the variables σ and R_{ct} are given by:

$$\sigma = \frac{\left(\dfrac{\alpha_0}{D_O^{1/2}} - \dfrac{\alpha_n}{D_R^{1/2}} \right)}{nFAz^{1/2}} \qquad (2.24)$$

$$R_{CT} = \frac{RT}{nFi_0} \qquad (2.25)$$

Thus the transfer coefficient of the reaction σ and the diffusion coefficients of the oxidised and reduced species D_O and D_R, may be determined from the impedance plot.

2.5.4 Electrochemical Impedance Spectroscopy

In a controlled electrochemical impedance spectroscopy experiment, the system is held at equilibrium at a fixed DC potential, and a small amplitude (5-10 mV) AC wave form is superimposed on the DC potential. Then the response of the system to this perturbation from equilibrium is measured in terms of the impedance (Z) of the system. The frequency of the AC wave form is varied and, hence, the impedance of the system is obtained as a function of frequency. Since an AC potential is applied to the electrochemical cell, there will probably be a phase shift between the applied AC potential and the AC current response. Therefore, the impedance can be represented using a vector diagram displaying the in-phase (Z') and out-of-phase (Z'') impedances, the total impedance and the phase angle. Since complex number terminology is also used when analysing impedance spectra, the in-phase and out-of-phase impedances are often referred to as real and imaginary impedances.

The Nyquist plot displays the imaginary impedance versus the real impedance (Z' vs. Z'') at each frequency (the positive y-axis generally correspond to –Z''). In the Nyquist plot each point is the impedance at one frequency. On the Nyquist plot the impedance can be represented as a vector of length |Z|. The angle between this

vector and the x-axis is φ. However, there is one shortcoming in the Nyquist plot in that the data is often poorly resolved particularly at high frequencies, and the explicit frequency dependence is not displayed.
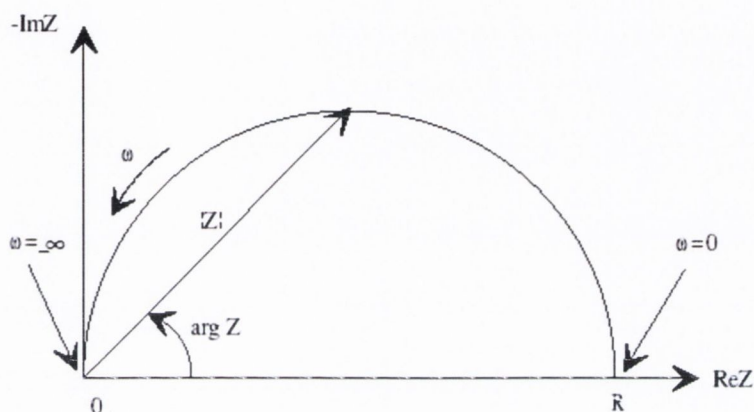
Figure 2.18: *The Nyquist plot here results from the electrical circuit of Figure 2.16. The semicircle is characteristic of a single "time constant". Electrochemical Impedance plots often contain several semicircles. Often only a portion of a semicircle is seen.*

The Nyquist plot in figure 2.18 results from the electrical circuit of figure 2.19. The semicircle is characteristic of a single "time constant". Electrochemical impedance plots often contain several time constants.
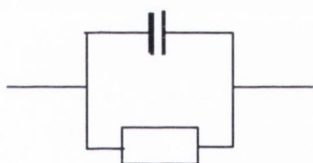
Figure 2.19: *Simple equivalent circuit with one time constant.*

The Bode plot displays both the logarithm if the total impedance and the phase angle as a function of the logarithm of the frequency. The Bode plot displays directly the frequency dependence; in addition, the data is well resolved at all frequencies, since a logarithmic frequency scale is employed (figure 2.20).

The total impedance of a system is determined from the impedances of the various components of the electrochemical cell including electron transfer kinetics, passivating layers and diffusion. The relative contribution of the various components

typically varies with frequency: e.g. electron transfer kinetics may dominate at high frequencies, whereas diffusion may dominate at lower frequencies. Measuring over a wide frequency range allows processes with different time scales to be detected within the same experiment.
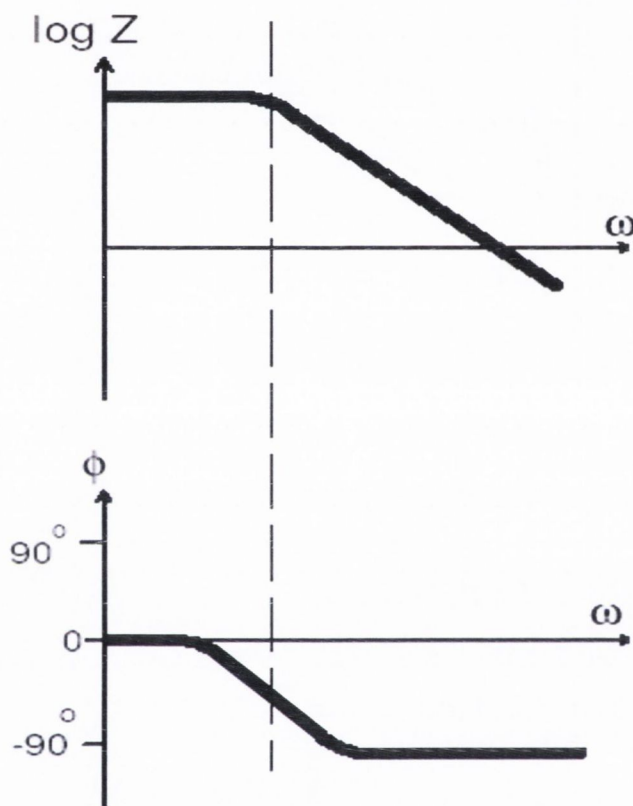
Figure 2.20: *Bode plot with one time constant*

2.6 Magnetic Field

Magnetoelectrochemistry is a term used to describe the effect of applied magnetic field on material transport and electron transfer processes at the interface between an electrode and an electrolyte solution. Although studies in this area have been reported for more than 30 years, much of the published data is characterised by apparent contradictions and lack of reproducibility[35].The present research programme has an objective of addressing and clarifying fundamental yet still outstanding issues related to the influence of external magnetic fields on electrochemical reactions and systems by focusing on the behaviour of well defined nanostructured assemblies such as self-

assembled redox active monolayers, electroactive polymer thin films and metal oxyhydroxide surface species[36-37]. In particular, the effect of external magnetic fields (if any) on the dynamics of electron transfer reactions, metal nucleation and growth kinetics, the surface redox chemistry of metals, and the conductivity, charge storage and electrocatalytic behaviour of electroactive thin films will be determined.

The performance of electrochemical measurements in a well defined external magnetic field environment is not trivial. Firstly one must ensure that the electrochemical cell can be placed within the magnetic field and second, the magnetic field must be uniform and exhibit a minimal field gradient. Static magnetic fields may be produced by either a steady electric current or a permanent magnet.

The conventional method by which a magnetic field is produced is to pass a current through a solenoid. From basic physics we can readily show that the magnetic field strength $\mathbf{H}$ (units: A m^{-1}) depends on the product of the current (I) and the number of turns per unit length of the coil n: $\mathbf{H} = nI$. The magnetic field strength is therefore easily varied. The field can be amplified and directed by winding the solenoid on a ferromagnetic iron yoke with an air-gap. This is the basis of the solenoidal electromagnet, which can be used to generate fields up to about 1600 kA m^{-1}. However in a solenoid with electrical resistance R, energy will be dissipated as heat at a rate proportional to I^{2}R. Of course if the heat is not removed, the resistance of the coils will increase, thereby reducing the current and hence the magnetic field. Heat removal requires a cooling system which can prove expensive and for increasingly large fields the DC current, solenoid size and cooling system must be scaled correspondingly. Furthermore, maintenance of the field requires a continuous expenditure of energy and if the field strength is critical an expensive current control device will also be required. If it is essential that the field created be homogeneous (as is the case in electrochemical work) then a further constraint is placed on the design leading to a greater complexity and cost. An alternative approach (especially for the generation of fields greater than 1600 kA m^{-1}) is to use non-resistive superconducting solenoids. Using modern superconducting materials it is possible to generate fields of 10^7 A m^{-1}.

In an environment where there is no source of electric power or cooling water or if there are constraints on the device dimensions, permanent magnets offer a clear advantage over electromagnets. Permanent magnet devices generally consist of a number of other components besides the magnetic material. These may include soft ferromagnetic materials used to guide and concentrate the magnetic flux into the working area. The entire assembly of magnets, soft iron and air gap is termed a magnetic circuit. The two major rare earth permanent magnets (REPM) are samarium-cobalt ($SmCo_5$ and Sm_2Co_{17}) and the more recently developed neodynium-iron-boron ($Nd_2Fe_{14}B$). These materials afford the possibility of the generation of homogeneous magnetic fields of high intensity in a permanent magnet structure. Also the high energy density exhibited by these materials (values in excess of 400 kJ m^{-3} have been observed for $Nd_2Fe_{14}B$) means that permanent magnets made from such materials have smaller volumes than those made with conventional magnetic materials.
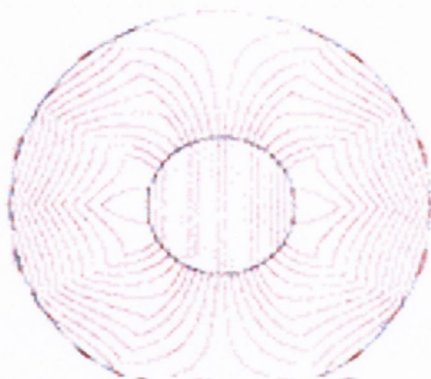
Figure 2.21: *Magnetic flux profile in the central plane of the 5.4 cm bore Halbach Cylinder with a magnetic field strength 0.5T.*

In our electrochemical work we have found that long permanent magnet cylinders known as Halbach cylinders or dipole rings create a magnetic field in their bore which, to a good approximation, is uniform . The computed flux distribution within a Halbach cylinder is illustrated in figure 2.21. Also, two such cylinders can be coaxially nested and rotated about their common axis to create a variable magnetic field.

Two different sources of magnetic field were employed in this work. The first was a Magnetic Solutions HC-500-54 Halbach cylinder which was constructed from

sintered $Nd_2Fe_{14}B$ and consists of twelve segments and generated a fixed static field of 0.5 T transverse to the bore which was 54 mm diameter. The electrochemical cell sat in the bore during polymerizations performed in the magnetic field. Figure 2.21 shows the magnetic flux profile in the central plane of the magnet.

Figure 2.22 shows a photograph of the cell system used, including the magnet. A standard three electrode electrochemical cell is used. A three electrode electrochemical cell was placed in the bore of a permanent magnet with a fixed static field of 0.5T transverse to the bore. The magnetic field was applied parallel to the working electrode surface.
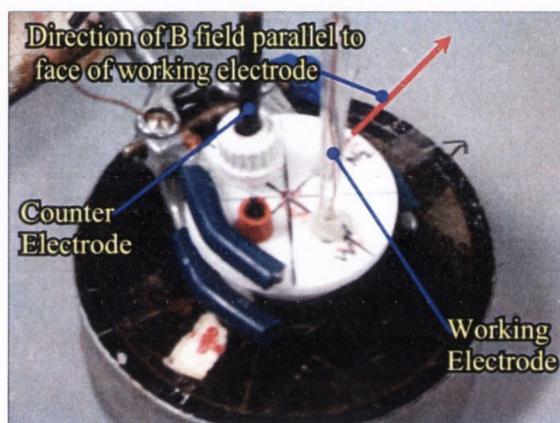
Figure 2.22: *Cell placement used throughout the characterization*

The second magnetic field source employed was a Magnetic Solutions MM-1000-48 Multimag. The latter system consisted of two nested Halbach cylinders which could be rotated relative to one another by stepper motors to produce a variable static magnetic field in the range 0 – 1 T. In this case the bore diameter was 48 mm. Photographs of the experimental setup employed using the Multimag system are presented in figure 2.23.

The magnetic field is applied to the working electrode by placing the entire electrochemical glass cell in the bore of the Halbach magnet. Since the working electrodes usually consist of discs inlaid in glass the latter arrangement ensures that the lines of magnetic flux density are oriented parallel to the surface of the working electrode.
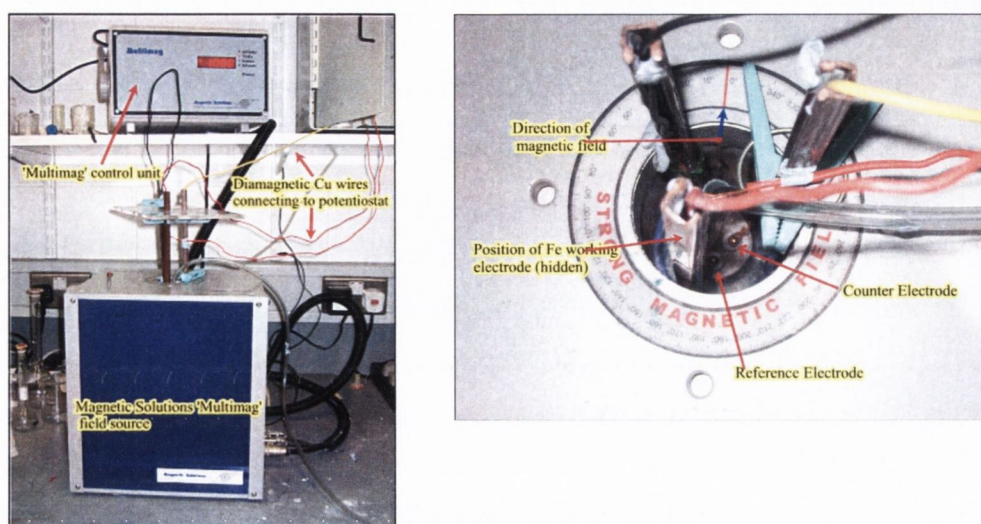
Figure 2.23: *Variable magnetic field Hallbach based Multimag System (Magnetic Solutions Ltd) setup for electrochemistry experiments. The custom built electrochemical cell is located within the bore of the cylindrical magnet.*

2.7 Summary

Initially an explanation of the basic three-electrode electrochemical cell is presented. The various types of working, auxiliary and reference electrodes as well as the numerous electrolyte solutions utilised during this work are outlined. Subsequent to this an in-depth description of the instrumentation used to drive the cell was given. This analysis included a step by step discussion of how a working potentiostat is developed and built from its primary component, the operational amplifier. Finally the various experimental techniques applied during experimentation were outlined. The experimental set-up and availability of techniques allowed for the conduction of experiments such as cyclic voltammetry, chronoamperometry, AC impedance and electrochemical impedance spectroscopy.

References

1. Bard., A.J.; Faulkner, L.R., *Electrochemical Methods-Fundamentals and Applications*, J. Wiley & Sons, **1980**.

2. Brett, C.M.A.; Brett, A.M.O., *Electrochemistry-Principles, Methods and Applications*, Oxford Science Publications, **1993**.

3. Von Fraunhofer, J.A.; Banks, C.H., Potentiostat *and its Applications*, Butterworth & Co. Ltd., Ist Edition, **1972**.

4. Poirier, G.E.; Pylant, E.D., *Science* **1996**, 272, 1145.

5. Chailapakul, O.; Sun, L.; Xu, C.; Crooks, R.M., *J. Am. Chem. Soc,* **1993**, 115, 12459.

6. Shimazu, K.; Kawaguchi, T.; Isomura, T., *J. Am. Chem. Soc.* **2002**, 124, 654.

7. Lennox, R.B., Ma, F., *Langmuir* **2000**, 16,6188.

8. Aoki, K., *J. Electroanal Chem.* **1983**, 146, 417.

9. Mabbott, G.A., *J. Chem. Educ.,* **1983**, 60, 697.

10. Nicholson, R.S., *Anal. Chem.,* **1965**, 37, 1351.

11. Kissinger, P.T.; Heineman, W.R., *J. Chem. Educ.,* **1983**, 60, 702.

12. Heinze, J., *Angew. Chem. Int. Ed. Engl.,* **1984**, 23, 831.

13. Randels, J.E.B., *Trans. Faraday Soc.,* **1948**, 44, 327.

14. Sevick, A., *Coll. Czech. Chem. Commun.,* **1958**, 13, 349.

15. Nicholson, R.S.; Shain, I., *Anal. Chem.,* **1966**, 36, 702.

16. Southampton Electrochemistry Group, *Instrumental Methods in Electrochemistry*, ed. T.J. Kemp, Ellis Hardwood, Chicester, **1985**.

17. Nicholson, R.S.; Shain, I., Chem. Commun., **1964**, 36, 702.

18. Finklea, H.O.; *Electrochemistry of Organised Monolayers of Thiols and Related Molecules on Electrodes*, in *Electroanalytical Chemistry*, Marcel Dekker, NY, Vol.19, **1996**

19. Chidsey, C.E.D.; Bertozzi, C.R.; Putvinski, T.M.' Mujsce, A.M.; *J. Am. Chem. Soc.* **1990**, 112, 4301.

20. Laviron, E., *J. Electroanal. Chem.,* **1979**, 100, 263.

21. Smith, C.P.; White, H.S. *Anal. Chem.* **1992**, 64, 2398.

22. Calvente, J. J.; Kovacova, Z.; Sanches, D.; Andreu, R.; Fawcett, W. R.; *Langmuir* **1996**, 12, 5696.

23. Sato, K.; Uosaki, K., *The Electrochemical Society, Pennington, NJ.* **1993**, 299.

24. Laibinis, P. E.; Whitesides, G. M.; Allara, D. L.; Tao, Y. T.; Parikh, A. N.; Nuzzo, R. G. *J. Am. Chem. Soc.* **1991**, *113*, 7152.

25. Sato, Y.; Ye, S.; Uosaki, K., *Langmuir*, **1997**, 13, 3157.

26. Lyons, M.E.G.L., Sensors, **2002**, 2,314.

27. Finklea, H.O., *J. Electroanal. Chem.* **2001**, 495, 79.

28. Chidsey, C.E.D., *Science*, **1991**, 251, 919.

29. Sabatani, E.; Rubinstein, I. *J. Phys. Chem.* **1987**, 91, 6663.

30. Strong, L; Whitesides, G.M. *Langmuir* **1988**, 4, 546

31. Troughton, E.B.; Bain, C.D.; Whitesides, G.M.; Nuzzo, R.G.; Allara, D.L.; Porter, M.D., *Langmuir*, **1988**, 4, 365

32. Bain, C.D.; Whitesides, G.M., *J. Am. Chem. Soc.* **1988**, 110, 3665.

33. Sumner, J.J.; Creager, S.E., *J. Phys. Chem. B* **2001**, 105, 8739.

34. Sabatani, E.; Rubinstein, I.; Maoz, R.; Sagiv, V. *J. Electroanal Chem.* **1987**, 219, 365.

35. Fahidy, T.Z., *J. Appl. Electrochem.* **1983**, 13, 553.

36. Uhlemann, M.; Krause, A.; Chopart, J.P.; Geberta, A., *J. Electrochem. Soc.* **2005**, 152, C817.

37. Devos, O.; Aaboubi, O.; Chopart, J.P.; Olivier, A.; Gbrielli, C.; Tribollet, B., *J. Phys. Chem. A* **2000**, 104, 1544.

CHAPTER 3

Synthesis of n-Ferrocenyl Alkanethiols

3.1 Materials and Methods

3.1.1 Reagents

Dodecanethiol (98+%, Aldrich), perchloric acid (70%, Merck) and ethanol were used as received. Thiourea (99%), potassium hydroxide, (2-chlorobenzoyl) chloride, N, N'- dicyclohexylcabodiimide (DCC), 4-(dimethylamino)pyridine (DMAP), sodium hydride (95%) and 12-bromo-1-dodecanol were purchased from Sigma-Aldrich. Dichloromethane and dimethylether (DME) were distilled over calcium hydroxide. Water for preparing electrolyte solutions and rinsing of electrodes was purified using a Millipore system.

3.1.2 Nuclear Magnetic Resonance

NMR spectra were recorded, by Dr. John O'Brien, on a Bruker DPX 400 machine operating at 400 MHz for ^{1}H and 100 MHz for ^{13}C. Samples were dissolved in deuterated chloroform (CDCl$_3$). Standard abbreviations; s— singlet, d —doublet, t —triplet, m—multiplet, br— broad, vbr— very broad, aps— apparent singlet.

3.2 Synthesis of Redox-Active Ligands

3.2.1 Ferrocene Carboxylic Acid

Ferrocene carboxylic acid was prepared by a literature method developed by Reeves[1]. This synthesis consists of two simple steps and uses readily available and inexpensive starting materials, producing pure material in high overall yield. The most important and standard method for the preparation of an aryl ketone is a procedure known as a Friedel Crafts Acylation. In the first step (Scheme 3.1), the acylation of ferrocene was achieved through the treatment of ferrocene with aluminium chloride and 2-chlorobenzoyl chloride in dry dichloromethane (DCM). The product (2-chlorobenzoyl)ferrocene is obtained in 96% yield, as a viscous, red liquid, which gradually solidifies. Although this product can be recrystallized from heptane affording scarlet needles, the crude product (~5% unreacted ferrocene) can be used without further purification for the second step.
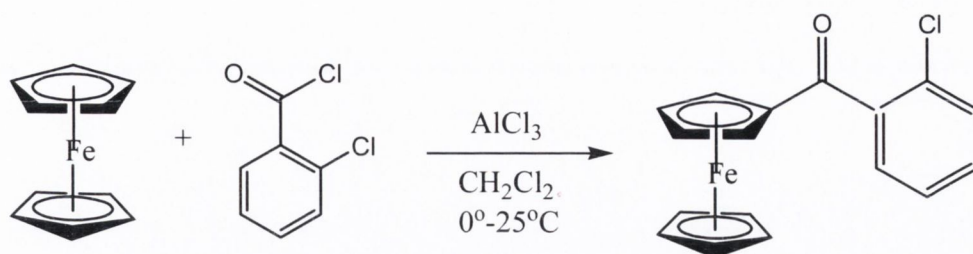
Scheme 3.1: *Synthesis of (2-chlorobenzoyl)ferrocene).*

The second step (Scheme 3.2) consists of the cleavage of this non-enolizable ketone to a carboxylic acid by the use of a potassium tertiary butoxide-water suspension. ferrocene carboxylic acid is, thus, produced as an air stable yellow powder in an 82% yield, which is comparable with literature results.
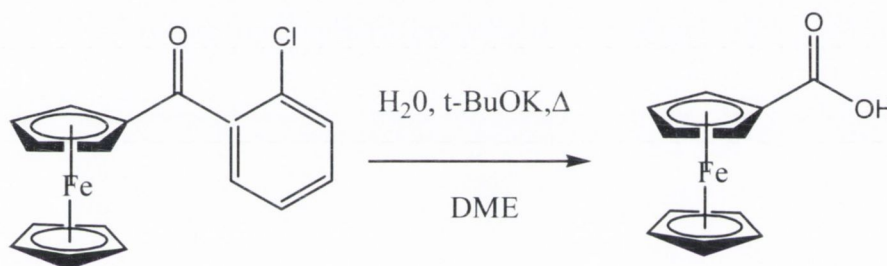
Scheme 3.2: *Synthesis of Ferrocene Carboxylic Acid.*

3.2.2 Preparation of N-(Ferrocenylcarbonyloxy)alkyl Bromides

n-(ferrocenylcarbonyloxy)alkyl bromides are synthesized via esterification of ferrocene carboxylic acid and a n-bromoalcohol in a Mitsunobu coupling reaction[1]. DCC is used as a coupling reagent and the reaction is catalysed by DMAP, producing the desired product in ~50% yield and DCU as a by-product. By varying the chainlength of the bromo-alcohol reactant in this reaction, the corresponding chainlength is obtained in the alkyl halide product.
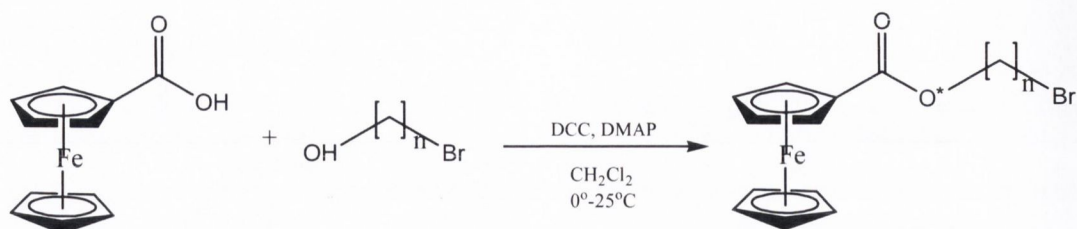
Scheme 3.3: *Synthesis of N-(Ferrocenylcarbonyloxy)alkyl Bromide*

n-(ferrocenylcarbonyloxy)alkyl bromide		Yield %
12-(ferrocenylcarbonyloxy)dodecyl bromide	n=12	49.3
10-(ferrocenylcarbonyloxy)decyl bromide	n=10	48.4
8-(ferrocenylcarbonyloxy)octyl bromide	n=8	47.5
6-(ferrocenylcarbonyloxy)hexyl bromide	n=6	45

Table 3.1: *Yields of bromide species.*

3.2.3 Preparation of N-(Ferrocenylcarbonyloxy)alkyl Thiols

The bromide product is then refluxed with thiourea in absolute ethanol, causing the nucleophilic displacement of the alkyl halide and the formation of an isothiuronium salt. The thiol is then generated by base hydrolysis of the isothiuronium salt. The thiols were obtained as light brown solids in ~50% yield.
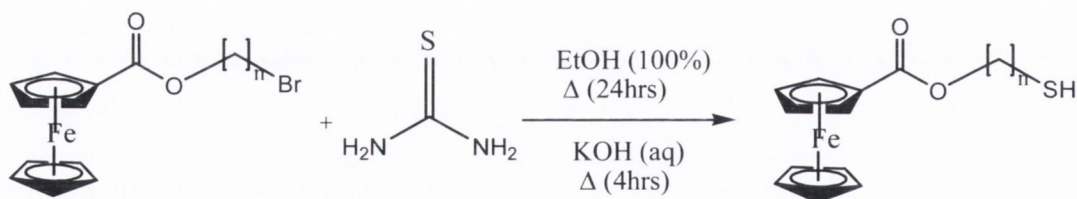
Scheme 3.4: *Synthesis of N-(Ferrocenylcarbonyloxy)alkyl Thiol.*

n-(ferrocenylcarbonyloxy)alkyl thiol		Yield %
12-(ferrocenylcarbonyloxy)dodecyl thiol	n=12	52
10-(ferrocenylcarbonyloxy)decyl thiol	n=10	53
8-(ferrocenylcarbonyloxy)octyl thiol	n=8	50
6-(ferrocenylcarbonyloxy)hexyl thiol	n=6	48

Table 3.2: *Yields of n-Ferrocenyl alkanethiol species.*

3.3 Synthesis of Redox-Active Ligands

3.3.1 Preparation of Ferrocene Carboxylic Acid

3.3.1.1 Preparation of (2-Chlorobenzoyl) Ferrocene
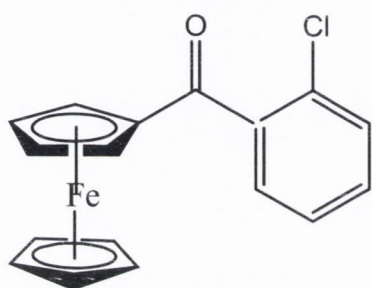
A thoroughly dried, three-necked, round-bottomed flask (500 ml) was charged under nitrogen with ferrocene (9.3 g, 0.05 mol), (2-chlorobenzoyl) chloride (6.33 ml, 0.05 mol) and dry DCM (100 ml), forming an orange solution. Anhydrous aluminum chloride (6.67 g, 0.05 mol) was slowly added over a period of fifteen minutes, while the reaction mixture was kept below 5°C. The mixture was stirred with cooling for a further 30 minutes and then for another 2 hours at room temperature by which time the reaction mixture had turned a deep blue. The reaction mixture was once again cooled and water (100ml) was cautiously added. The resulting two-phase mixture was vigorously stirred for a further 30 minutes. The layers were then extracted using DCM (2 x 30 ml). The combined extracts were then washed with water (50 ml) and 10% NaOH (2 x 50 ml), before being dried over magnesium sulphate. After filtration and evaporation to dryness at reduced pressure, the product was found to be a red crystalline substance (15.3 g, 94.3% yield).

^{1}H NMR (400Hz, CDCl$_3$): δ 4.28ppm (s, Cp, 5H), 4.6ppm (aps, 2(CHCHCCO), 2H), 4.76ppm (aps, CHCCO, 2H), 7.36-7.54ppm (m, Ar, 4H).

3.3.1.2 Preparation of Ferrocene Carboxylic Acid
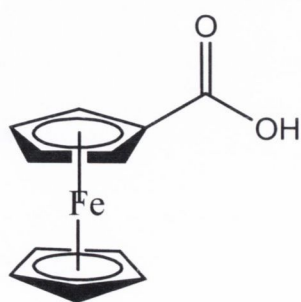
Potassium tertiary butoxide (13.46 g, 0.12 mol) was dissolved in dry DME (150 ml) and left to stir under nitrogen for 10 minutes. Water (0.657 ml, 0.0365 mol) was added to the reaction mixture, producing a white slurry. (2-chlorobenzoyl)ferrocene (11.85 g, 0.0365 mol) was added and the reaction mixture was refluxed for 1 hour. The

reaction was accompanied by a colour change from red to tan. The reaction mixture was then cooled and poured into water (500 ml). The resulting solution was then washed with diethyl ether (3 x 75 ml) and back-extracted with 10% NaOH (2 x 50 ml). The aqueous phases were combined, acidified with concentrated HCl, and the resulting precipitate was collected by filtration. The required product was air dried to yield a yellow powder (6.85 g, 81.6%).

^{1}H NMR (400Hz, CDCl$_3$): δ 4.28 (s, Cp, 5H), 4.49 (aps, 2(CHCHCCO), 2H), 4.88ppm (aps, CHCCO, 2H).

^{13}C NMR (400Hz, CDCl$_3$): δ 70.1 (Cp), 70.6 (2 x CHCHCCO), 72.0 (2 x CHCCO), 177.1ppm (C=O).

3.3.2 Preparation of N-(Ferrocenylcarbonyloxy)alkyl Bromides

3.3.2.1 Preparation of 12-(ferrocenylcarbonyloxy)dodecyl bromide n=12

A thoroughly dry Schlenk tube was equipped with a mechanical stirrer and a stopper. The reaction vessel was evacuated and a N$_2$ atmosphere was established. Ferrocene carboxylic acid (0.9541 g, 4.15 mmol), 12-bromo-1-dodecanol (1 g, 3.7 mmol) and DMAP (50.7 mg, 0.415 mmol) were placed in the tube. The tube was stoppered and dry DCM (25 ml) was injected under N$_2$ into the system. The dark yellow reaction mixture was then cooled to 0°C and DCC (0.9335 g, 4.52 mmol) was added. The reaction was left to stir for 1 hour at 0°C and stirred overnight at RT. After removal of the precipitated dicyclohexylurea (DCU) by filtration, the product was recovered by extraction with DCM. The DCM extracts were then washed with dilute HCl (2 x 25 ml), water (2 x 25 ml), dried over magnesium sulphate, filtered and evaporated under reduced pressure. The product was dissolved in DCM and chromatographed on silica with DCM. The first yellow band contained the required product which was isolated by column chromatography and evaporated to dryness (a light brown solid, 0.867 g, 49.3%).

^{1}H NMR (400Hz, CDCl$_3$): δ 1.31-1.44ppm (broad, 16H), 1.72ppm (t, J= 6.83 Hz, 2H), 1.85ppm (t, J= 6.83 Hz, 2H), 3.41ppm (t, J= 6.83 Hz, 2H), 4.22ppm (s, 7H), 4.41ppm (s, 2H), 4.83ppm (s, 2H).

3.3.3 Preparation of N-(ferrocenylcarbonyloxy)alkyl thiols

3.3.3.1 Preparation of 12-(ferrocenylcarbonyloxy)dodecyl thiol n=12

A thoroughly dry Schlenk tube was equipped with a mechanical stirrer and a stopper. The reaction vessel was evacuated of air and a N$_2$ atmosphere was established. 12-(ferrocenylcarbonyloxy)dodecyl bromide (0.551 g, 1.15 mmol) and thiourea (0.263 g, 3.45 mmol) were added to absolute ethanol (25 ml), and the resulting solution was stirred and refluxed under N$_2$ overnight. The solvent was then removed under vacuum and an aqueous solution of potassium hydroxide (25 ml, 0.193 g, 3.45 mmol) was added, and then the mixture was refluxed for 4 hours under N$_2$ and then cooled to room temperature. The resulting solution was extracted with DCM (3 x 50 ml) and the combined extract was washed with dilute HCl (2 x 50 ml) and water (2 x 50 ml). The extract was dried over magnesium sulphate, filtered, concentrated under reduced pressure and chromatographed on silica with DCM. The first yellow band contained the required product (a brown solid, 0.26 g, 52% yield).

^{1}H NMR (400Hz, CDCL$_3$): δ 1.3 - 1.44ppm (broad, SH, (CH$_2$)$_8$ 17H), 1.58ppm (m, CH$_2$, 2H), 1.71ppm (m, CH$_2$ 2H), 2.51ppm (q, OCH$_2$ J= 7.51Hz, 2H), 4.25ppm (s, CH$_2$S, Cp 7H), 4.43ppm (s, Cp 2H), 4.85ppm (s, Cp, 2H).

The ^{1}H NMR of the 12-(ferrocenylcarbonyloxy)alkyl thiol is presented in the appendix.

References

1. Reeves, P.C., *Organic Syntheses*, **2002,** *6*, 625.

CHAPTER 4

Characterisation of Non-Redox Active Alkanethiol SAMs

4.1 Introduction

In order to check the integrity of self-assembled monolayers investigations of unsubstituted alkanethiol monolayers were undertaken. In initial work, conducted to optimize monolayer deposition protocol and quality, the corresponding non-redox active C_{12} alkanethiol monolayer was fabricated via immersing a clean bare gold substrate electrode in 1mM dodecanethiol in EtOH solution for 48 h.

The effect of an external magnetic field (0.5 T) on the growth of the unsubstituted alkanethiol was also investigated. The monolayer was fabricated via immersing a 1mM dodecanethiol in EtOH solution the magnetic field for the duration of the 48 h growth. The magnet employed was a Halbach bore magnet.

4.2 Characterisation of non-redox active C_{12} alkanethiol SAM

The integrity of the monolayer formed via self assembly was then checked by immersion of the electrode in 2mM ferrocyanide/ferricyanide solution in 1M $HClO_4$ for 24 h and recording the resultant cyclic voltammogram, (Figure 4.1 (a) and (b)). The ferrocyanide/ferricyanide redox reaction is well defined and understood at a bare gold electrode, exhibiting quasi-reversible electron transfer behaviour.
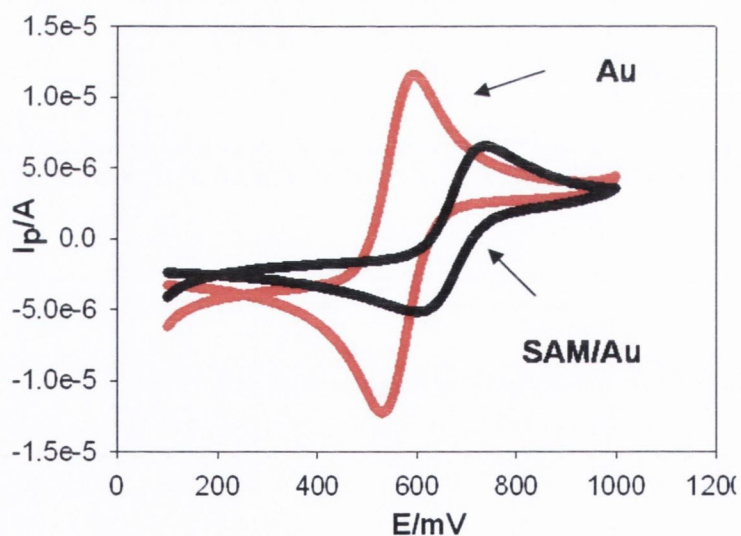
Figure 4.1(a): *Defect monolayer- CV contains a bare gold electrode (-) and a unsubstituted alkanethiol SAM (-) in 2mM Ferrocyanide/Ferricyanide in 1M KCl solution. v = 100mVs⁻¹.*

Figure 4.1(a) and figure 4.1(b) above, represent two contrasting behaviours, that of a "defect containing" and that of a "defect free" monolayer. In the case of both figures, the red line shows a typical CV result for a bare gold electrode in ferrocyanide/ferricyanide and the black line represents that of the ferroccyanide/ferricyanide response in contact with the immersed monolayer.
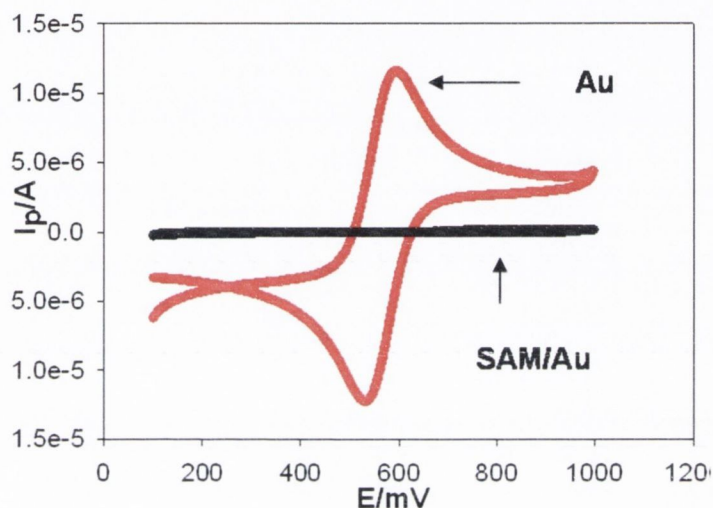
Figure 4.1(b): *Defect free monolayer- CV contains a bare gold electrode (-) and a unsubstituted alkanethiol SAM (-) in 2mM Ferrocyanide/Ferricyanide in 1M KCl solution.. v = 100mVs⁻¹.*

Figure 4.1(a) corresponds to a defective monolayer situation. The latter terminology is suggested because it is seen that some characteristics of the ferrocyanide/ferricyanide kinetics at the underlying gold support surface still show. In the absence of measurable defects in the monolayer film (figure 4.1(b)) no trace of any direct ferrocyanide/ferricyanide redox activity at the underlying gold surface is observed.

However, figures 4.1(a) and (b) also indicate the difficulty there is in obtaining information on electron transfer at low over potential because the measured current is small and difficult to separate from the charging current[1]. The charging current is the non–Faradaic current associated with the charging of the electrical double layer at an electrode-solution interface.

A schematic representation of the interfacial process that is occurring in figures 4.1 (a) and figure 4.1 (b) is shown in figure 4.2 (a) and figure 4.2 (b). Figure

4.2 (a) is a schematic of the process that occurs for the bare gold electrode and the ferrocyanide/ferricyanide redox couple, while figure 4.2 (b) represents the process that occurs between the alkanethiol monolayer coated electrode and the ferrocyanide/ferricyanide redox couple.
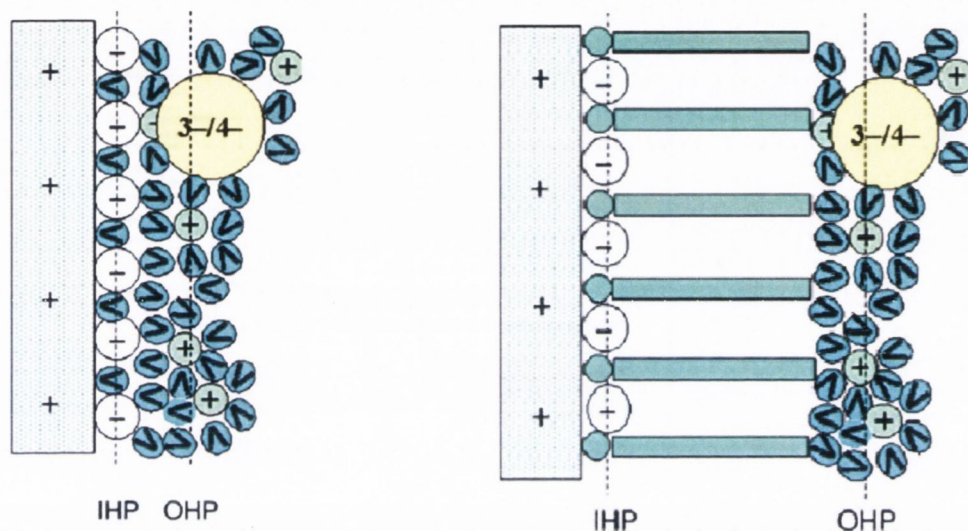
Figure 4.2: *Schematic of the electrode surface and ferrocyanide/ferricyanide in 1M KCl. (a) includes the Au/Fe(CN)$_6^{4-/3-}$(KCl (aq)) without the SAM, while (b) includes Au/SAM/Fe(CN)$_6^{4-/3-}$ (KCl (aq)).*

From figure 4.2 (b) it is seen that when a non-redox active C_{12} alkanethiol is formed on the surface of a bare gold electrode, a blocking effect is caused and the CV response of the SAM shows no trace of any direct ferrocyanide/ferricyanide redox activity at the underlying gold surface. Instead, long range electron transfer between the solution phase redox couple and the underlying gold surface occurs via a tunneling mechanism through the hydrocarbon layer. This "blocking" property is attributed to the packed structure of the hydrocarbon chains which can impede the approach of solution ions and molecules to the electrode surface. The shape of the voltammogram indicates that the electron transfer across the interface is determined by mass transfer effects for the bare electrode, whereas for the dodecanethiol monolayer coated gold, a significant current reduction is seen and the rate of the process is determined by electron transfer between weakly coupled states. The latter process is best understood in terms of quantum mechanical electron tunneling across the low dielectric constant hydrocarbon barrier. The latter is assumed to proceed via a

through bond super-exchange model rather then via a through space mechanism[2]. A partially blocking monolayer suggests that the useful property that heterogeneous electron transfer reactions of particular facile redox molecules can be slowed so that they are easily measured at a certain potential. We note, therefore, that cyclic voltammograms allow one to judge the quality of the SAM, particularly regarding pinhole defects, due to the ability detect currents corresponding to the oxidation and reduction of a test redox couple at a partially covered electrode.

A quantitative description of the electrochemical response of a defect monolayer is complicated and can be described using a microelectrode array model[3,4]. In order to study the kinetics of electron tunneling through a SAM, a compact nearly perfect insulating film on the electrode must be ensured.

4.3 Unsubstituted Growth in the presence and absence of 0.5 T Magnetic Field

Work was also carried out on the non-redox active C_{12} alkanethiol monolayer in the presence of a 0.5 T magnetic field strength. The monolayer was fabricated via immersing a clean bare gold substrate electrode in 1mM dodecanethiol in EtOH solution for 48 h. The solution was placed in the magnetic field for the duration of the growth. This work was carried out in order to investigate whether the magnetic field has an effect on the growth of an unsubstituted dodecanethiol SAM.
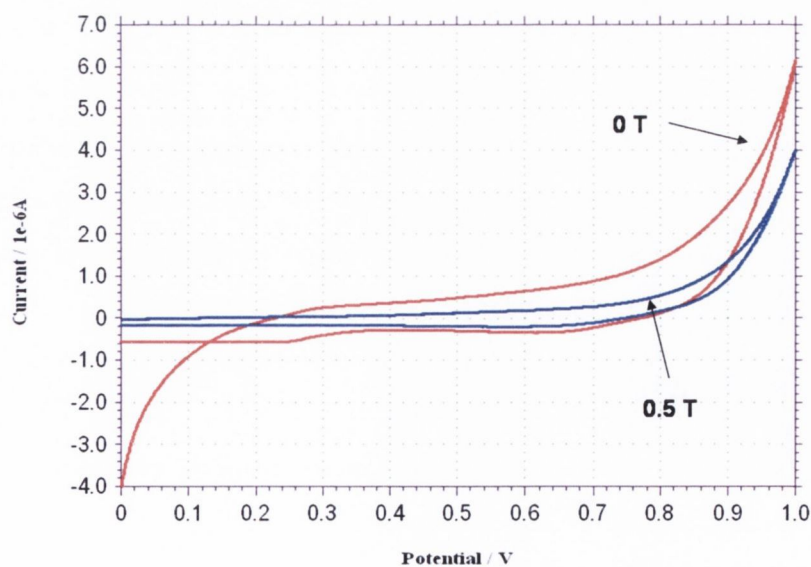
Figure 4.3: *Cyclic voltammogram in 2 mM ferrocyanide/ferricyanide in 1 M KCl of a 12-dodecanethiol SAM immersed in a 1 mM solution in Ethanol for 48 hs in the presence and absence of a magnetic field. Scan rate 100 mVs^{-1}.*

It is observed that the capacitance is:

$$\frac{1}{C_T} = \frac{1}{C_{DL}} + \frac{1}{C_{Film}}$$

(4.1)

If C=1 M: then C_{DL} is negligible as the potential drop across the diffuse layer is small. From

$$C_{SAM} = \frac{\varepsilon\varepsilon_o}{d}$$

(4.2)

a value of 2-7µF is obtained for a C12 SAM in 1M $HClO_4$. From figure 4.3 values of C_{Film}= 6.9µF at 0 T and C_{Film}= 0.3µF at 0.5 T are obtained. Therefore, it can be concluded that the application of a magnetic field causes a sharp decrease in the capacitance of a C12 SAM. The magnetic may effect the distance between the layer of charge (d) or the dielectric constant of the SAM may change.

4.4 Complex Impedance Spectroscopy

Electrochemical impedance spectroscopy is a more powerful method to study thin films on electrodes than cyclic voltammetry because the effects of solution resistance, double layer charging and currents due to diffusion or to other processes occurring in the SAM are observed explicitly[6], provided that the frequency range examined is wide enough. AC measurements can be made by superimposing a fixed DC potential on the AC potential of a known amplitude and frequency. In many situations the DC potential is set at the formal potential of the surface immobilized redox groups, but it need not be.

The complex impedance measurements reported here are not intended to represent a comprehensive study. We merely report the impedance response for both non-redox active C_{12} alkane thiols and the corresponding redox active C_{12} ferrocenyl alkane thiol recorded at open circuit and in the presence and absence of 0.5 T magnetic field. These experiments were performed merely to note the presence of qualitative differences in the impedance response – not as a means to quantitatively analyze the systems. The latter will be performed in the future. As a result of this qualitative analysis an equivalent circuit for the SAM will be presented.
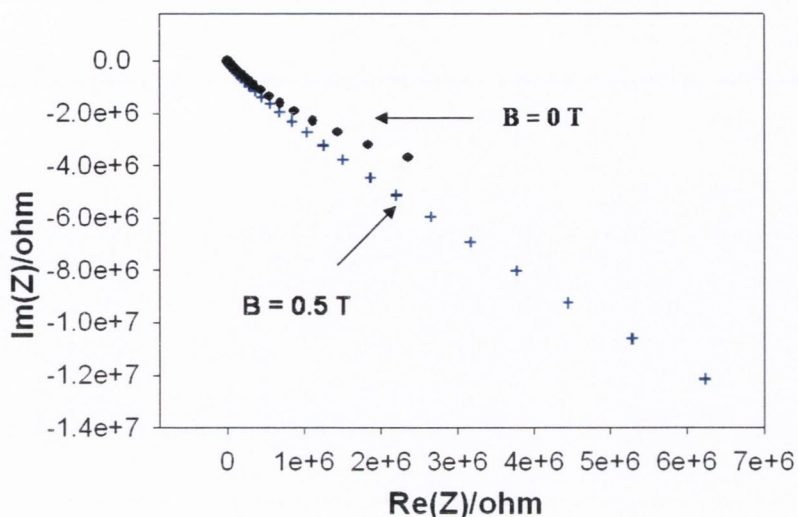
Figure 4.4: *Nyquist plot of dodecanethiol coated gold in 1 mM $K_3[Fe(CN)_6]$/$K_4[Fe(CN)_6]$ with 1 M KCl as supporting electrolyte at an open circuit in the presence and absence of a magnetic field.*

Figures 4.4 and 4.5 shows the impedance spectrum in a Nyquist and Bode presentation obtained for a dodecanethiol modified gold electrode at an open circuit in the presence of 1mM ferrocyanide/ferricyanide with 1M KCl as the supporting electrolyte, respectively. Experiments were performed in the presence and absence of external magnetic field.

From the graphs it can be seen that while there is a deviation in the Nyquist plot when the magnetic field is presence, the greatest difference can be seen in the Bode plot.
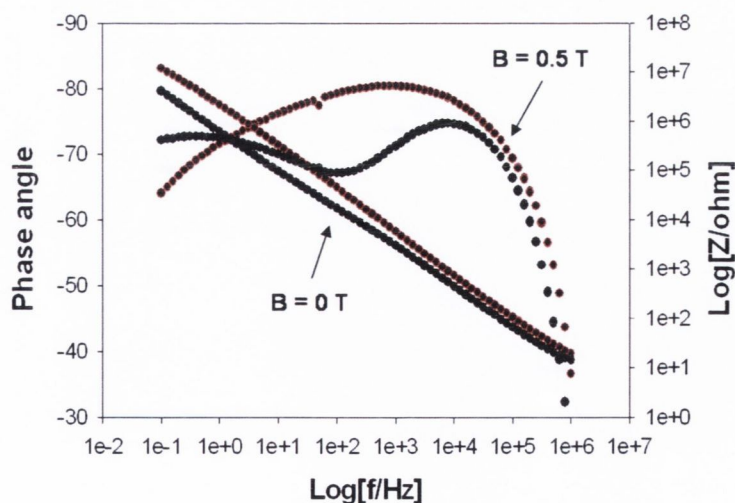
Figure 4.5: *Bode plot of dodecanethiol coated gold in 1 mM $K_3[Fe(CN)_6]$/$K_4[Fe(CN)_6]$ with 1 M KCl as supporting electrolyte at an open circuit in the presence and absence of a magnetic field.*

Figures 4.6 and 4.7 shows the impedance spectrum in a Nyquist and Bode presentation obtained for a ferrocenyl alkanethiol modified gold electrode at an open circuit in the presence of 1mM ferrocyanide/ferricyanide with 1M KCl as the supporting electrolyte, respectively.

Figure 4.6: *Nyquist plot of ferrocenyl alkanethiol coated gold in 1 mM $K_3[Fe(CN)_6]/K_4[Fe(CN)_6]$ with 1 M KCl as supporting electrolyte at an open circuit in the presence and absence of a magnetic field.*

Figure 4.7: *Bode plot of ferrocenyl alkanethiol coated gold in 1 mM $K_3[Fe(CN)_6]/K_4[Fe(CN)_6]$ with 1 M KCl as supporting electrolyte at an open circuit in the presence and absence of a magnetic field.*
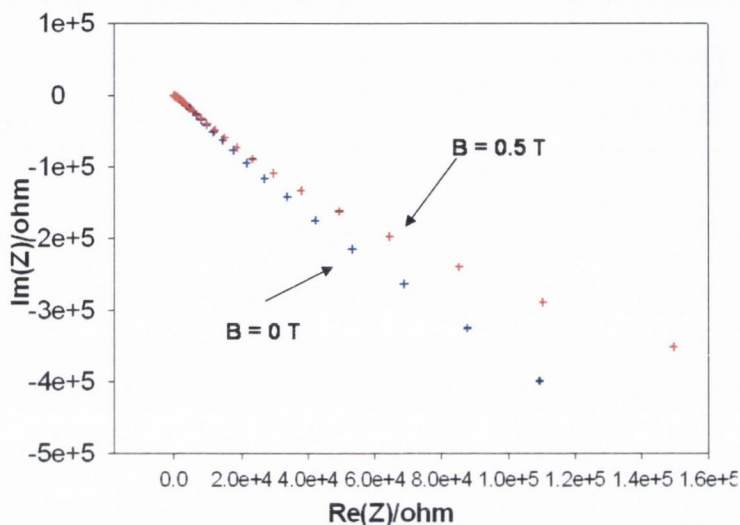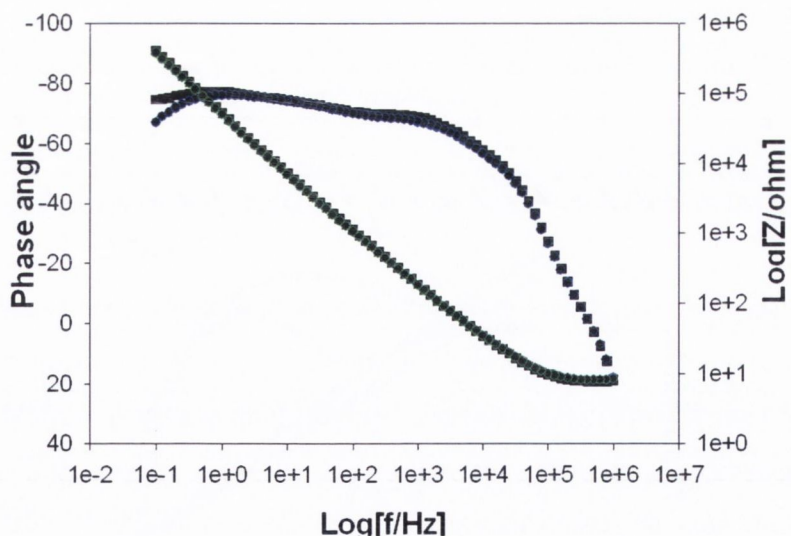
However, in contrast to the results obtained for the non-redox dodecanethiol, the results for the redox active ferrocenyl alkanethiol are the opposite for the redox active ferrocenyl active alkanethiol. From figures 4.6 and 4.7 it can be seen that while there is a large effect of external B field observed for Nyquist plot, there is little or no effect in the Bode plot when the magnetic field is present.

Figure 4.8 shows two possible paths for an electron transfer reaction between a modified gold electrode and a diffusing redox species in solution: (a) the electron tunnels through the electroinactive film, and (b) the electron transfers at film detects where gold is exposed to the solution. Either path alone exhibits a substantial decrease in the observed reaction rate compared to the rate at an unmodified gold electrode.
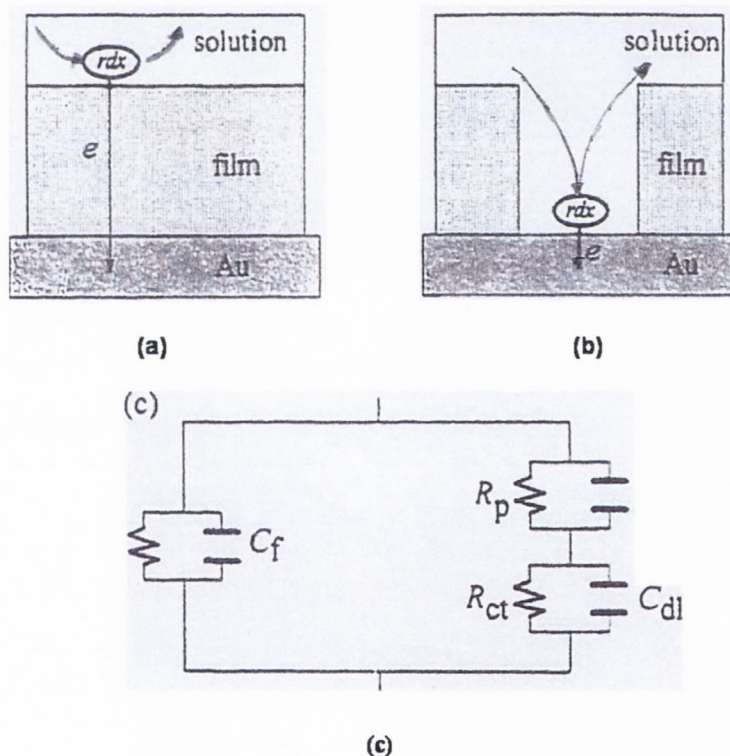
Figure 4.8: *Paths of electron transfer between a solution redox species and a gold electrode modified by a thin electroinactive film: (a) the defect free film blocks the approach to the gold surface and electrons may tunnel through the film; and (b) defect sites allow an electron transfer at the interface of bare gold and solution. (c) An equivalent circuit when both (a) and (b) paths are considered. Reproduced from reference 6.*

In path (a) this observation is attributed to the diminished magnitude of the rate constant as a result of the long electron-transfer distance through the film between the electrode and the redox species[7] and in path (b) the apparent decrease in reaction rate is due to diffusion of the redox species to a much smaller area of exposed gold[8,9]. When film defects are present and the film is thin enough to allow significant tunneling, both electron-transfer paths should be considered. Therefore, figure 4.8 (c) suggests an equivalent circuit that includes three resistor-capacitor parallel couples: R_f and C_f are the charged-transfer resistance and the geometric capacitance, respectively, that represent the electron tunneling through the film, *ie* case (a); R_p and C_p correspond to the diffusion of the redox species to a partially blocked electrode, *i.e.* case (b) and R_{ct} and C_{dl} represent the usual electrochemistry at the bare gold electrode-solution interface[10].

When an electrode is modified by an electroactive film, like the ferrocenyl alkanethiol used here, the impedance is expected to be similar to that for a defect-free system, since the electron transfer is allowed only through the carbon chain. The only difference appears at high frequencies when the response of the electroactive film becomes capacitive[11].

4.5 Polarisation of a non-redox active C_{12} alkanethiol SAM

The most common method of self-assembled monolayer formation has been by passive deposition (PD). This involves the immersion of a bare gold electrode in an alkanethiol containing solution. However, this method can be difficult to reproduce. Lennox et al.[11] were the first to discover that the chemisorption of the alkanethiol could be controlled electrochemically. Lennox et al. applied a potential to the bare gold electrode during alkanethiol adsorption and found that in a short time scale self-assembled monolayers of high quality with very high performance characteristics were formed.

In order to investigate whether the polarisation of a gold electrode causes a high quality n-ferrocenyl alkanethiol SAM to be formed the method was tested using a non-redox active C_{12} alkanethiol. A clean bare gold electrode was then placed in a cell containing the dodecanethiol alkanethiol solution. A reference electrode and a

counter electrode were also included in the electrochemical cell design. A current was then passed through the gold working electrode for the duration of the experiment (2 h). The experiment was repeated employing varying currents (0.2 V, 0.4 V and 0.6 V)
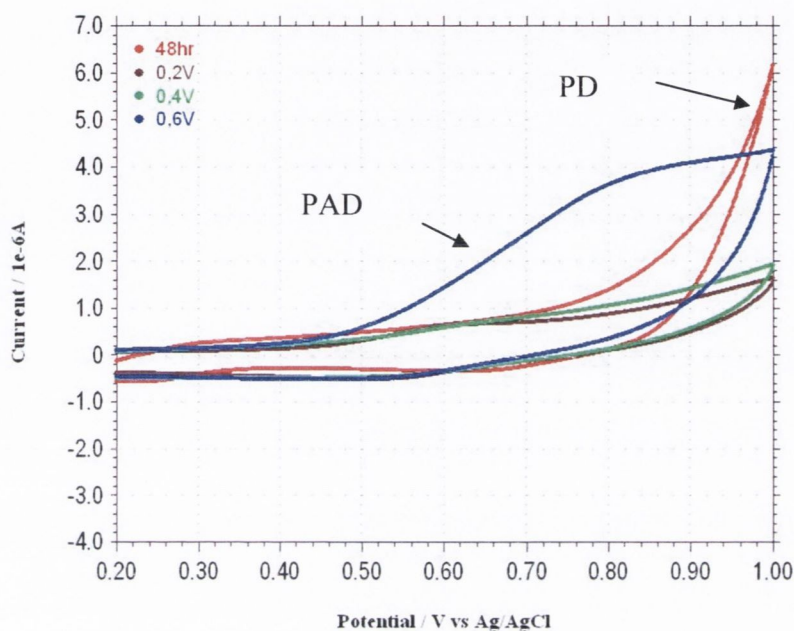
Figure 4.9: *Cyclic voltammograms of the 48 h PD and the PAD non-redox C_{12} monolayer. The currents at which potential growth is measured are 0.2 V, 0.4 V and 0.6 V. Scan rate 100 mVs^{-1}.*

During potential assisted deposition (PAD), the sulfur atom in the alkanethiol SAM can be reduced or oxidised at relative low or high potentials, respectively, resulting in the desorption of the thiol molecules. It is evident that different substrate potential (E_s) will lead to different film quality. In other words, the defect concentration of SAMs prepared by potential-assisted assembly is dependent on the potentials applied. Therefore, it is important to know how to select potentials during the potential controlled assembly.

From the cyclic voltammograms it is seen that the 0.4 V potential assisted SAM voltammogram is the one resembling the 48 h PD. The effects of E_s on the formation and integrity of SAMs can be ascribed to the following two aspects: (1) increasing E_s will facilitate the adsorption of thiol molecules onto gold[12,13]. (2) however, as E_s exceeds some extent, the already assembled thiol molecules begin to desorb due to the oxidation of sulfur[14]. When $E_s \leq 0.4$ V, the potential is not large

enough to oxidise the sulfur atom and the first aspect dominate the formation of SAMs. When $E_s \geq 0.6$ V, the second aspect begins to take effect, resulting in the poorest film quality. Using the electron energy diagram of $Au-SCH_3$ we can semi-quantitatively explain the reason why Au-S bonds begin to break oxidatively at ≈ 0.6 V. This energy diagram is an analog of $Au-S(CH_2)_{11}CH_3$ and is presented in figure 4.10.
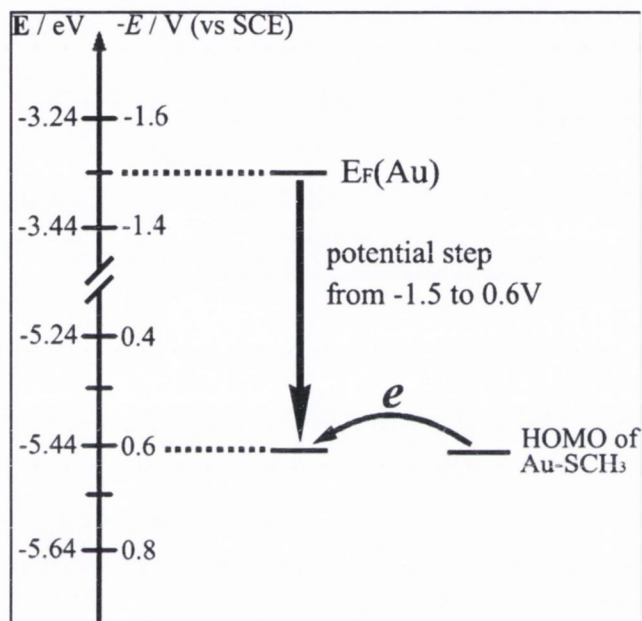
Figure 4.10: *The diagram of the energy level and the corresponding electrode potential, showing the energy position of $Au-SCH_3$ and the changing of Fermi-level of Au with the potential step from -1.5 V to 0.6 V. Reproduced from reference 14.*

The energy position of the highest occupied molecular orbital (HOMO) of $Au-SCH_3$ lies in ≈ 5.48 eV[15], which corresponds to 0.6 V with respect to SCE[9]. When $E_s \geq 0.6$ V, the Fermi-level of Au ($E_F(Au)$) is close to or lower than the HOMO of $Au-SCH_3$. As a result, electrons can transfer from the HOMO of $Au-CH_3$ to the bulk Au, leading to the oxidative break of the $Au-SCH_3$ bond. And the higher the E_s, the lower the Fermi level of Au, and then the faster the oxidative desorption rate, This explains the fact that when E_s is greater than 0.4 V the integrity of SAMs deteriorates.

4.6 Conclusion

From the characterisation of a non-redox active C_{12} alkanethiol SAM (Section 4.1) it is obvious that the formation of a non-redox active C_{12} alkanethiol self-assembled monolayer on a bare gold electrode causes a change in the interfacial process which normally occurs for a bare gold electrode. It has been shown how this change or blocking effect is caused and that the CV response of the SAM shows no trace of any direct ferrocyanide/ferricyanide redox activity at the underlying gold surface. Instead long range electron transfer between the solution phase redox couple and the underlying gold surface occurs via a tunneling mechanism through the hydrocarbon layer. This result is further reinforced by the results obtained for the electrochemical impedance spectroscopy.

On applying a magnetic field strength of 0.5 T to a non-redox active C_{12} alkanethiol SAM a collapse in the formation of a SAM is seen. From this it is observed that an external magnetic field causes some deviance in the CV.

From the polarisation experiments it is obvious that the addition of a potential to a bare gold electrode immersed in a dodecanethiol solution has a positive growth effect on the adsorption of the dodecanethiol on the gold electrode. It is obvious that the 0.4 V potential is the recommended potential for use in the potential assisted adsorption of the SAM. This result is concluded as the 0.4 V potential has a similar CV response to the CV response obtained for a SAM grown without the potential and confirmed by analysing the electron energy diagram of Au-SCH$_3$. From the result it is obvious that the method of potential assisted growth does cause enhanced adsorption on a non-redox active alkanethiol and can therefore be employed to form SAMs of the redox active n-ferrocenyl alkanethiol.

References

1. Terrettaz, S.; Becka, A.M.; Traub, M.J.; Fettinger, J.C.; Miller, C.J., *J. Phys. Chem.* **1995**, 99, 11216.

2. Petrov, E.G.; Zelinskyy, Y.R.; May, V., *J. Phys. Chem. B*, **2002**, 106, 3092.

3. Amatore, C.; Saveant, J.M.; Tessier, D., *J. Electroanal. Chem.*, **1983**, 147, 39.

4. Brookes, B.A.; Davies, T.J.; Fisher, A.C.; Evans R.G.; Wilkins, S.J.; Yunus, K.; Wadhawan, J.D.; Compton, R.G., *J. Phys. Chem. B*, **2003**, 107, 1616.

5. Finklea, H.O., *Electrochemistry of Organised Monolayers of Thiols and Related Molecules on Electrodes*, in *Electroanalytical Chemistry*, Marcel Dekker, NY, Vol.19, 1996

6. Janek, R.P.; Fawcett, W.R., *Langmuir* **1998**, 14, 3011.

7. Miller, C.; Cuendet, P.; Gtatzel, M., *J Phys. Chem.* **1991**, 95, 877.

8. Gueshi, T.; Tokuda, K.; Matsuda, H., *J. electroanal. Chem.* **1978**, 89, 247.

9. Amatore, C.; Saveant, J. M.; Tessier, D., *J. electroanal. Chem.* **1983**, 147, 39.

10. Bard, A.J.; Faulkner, L.R., *Electrochemical Methods: Fundamentals and Applications*, Wiley, New York, **1980**.

11. Chidsey, C.E.; *Science* **1991**, 251, 919.

12. Ma, F.; Lennox, R.B., *Langmuir* **2000**, 16, 6188.

13. Ron, H.; Rubinstein, I.; *J. Am. Chem. Soc.,* **1998**, 120, 13444.

14. Brett, C.M.A.; Kresak, S.; Hianik, T.; Brett, A.M.O., *Electroanalysis*, **2003**, 15, 557.

15. Diao, P.; Hou, Q.; Guo, M.; Xiang, M.; Zhang, Q., *J. Electroanal. Chem.*, **2006**, doi: 10.1016/j.jelechem.2006.09.008.

16. Larsson, J.A.; Nolan, M.; Creer, J.C., *J. Phys. Chem. B.*, **2002**, 106, 5931.

CHAPTER 5

Potential Assisted Deposition of Redox Active Alkanethiol SAMs

5.1 Electrochemically formed SAM Films

For many years the properties and applications of SAMs of alkanethiols deposited on Au supports have been examined. However, the mechanism of their formation is still surprisingly poorly understood. Previous investigations have found that it is difficult to obtain SAM films with similar structure e.g. diffraction determination[1], or function e.g. electron-transfer blocking ability[2] even though identical preparative conditions were employed. As has been stated many times previously, self-assembled monolayers offer the ability to engineer a surface with "tuned" properties. However, the preparation of both multi-component and single-component self-assembled monolayers in a predictable manner has proved difficult. Lennox and Ma[3] were interested in obtaining self-assembled monolayers of high quality with extensive blocking properties which were also reproducible and predictable. The workers were the first to discover that the chemisorption of the alkanethiol could be controlled electrochemically. Lennox et al. applied a potential to a bare gold electrode during alkanethiol adsorption and found that self-assembled monolayers of high quality with very high performance characteristics were formed over a short time scale.

The most common method of SAM formation has been by passive incubation. This involves the immersion of a bare gold electrode in a thiol containing solution. A second method is deposition from the gas phase[4]. The concurrent theme in these two methods is that the potential of the gold electrode is not fixed. The process of self-assembly, while simple, is irreproducible and very time consuming. In passive incubation the amount of alkanethiol adsorbed on the surface (surface coverage) will increase with increased incubation time. Fully saturated, highly ordered SAM need days or even weeks to prepare.

The only previous attempts employing potential effects were on self-assembled monolayers already formed. Stolberg et al.[5] and Sondag-Huethorst et al.[6-9] discovered that application of a potential to alkanethiol SAM films influenced the structure of the latter. Porter et al.[10] reported that the structure of the SAM changes with applied potential in non-aqueous media, but not in aqueous media. Whitesides investigated the potential control of a SAM and discovered that the wettability of an alkanethiol monolayer adsorbed on gold is influenced once it was formed[11].

5.2 PAD n-Ferrocenyl Alkanethiol SAM formation

In this chapter the properties of redox active n-ferrocenyl alkanethiol SAM films formed under potential control (PAD) are examined in detail largely using cyclic voltammetry and compared with similar films formed via passive incubation (PD). In particular, characteristic voltammetric parameters such as anodic/cathodic peak separation, standard potential, peak widths at half maximum are examined for ferrocenyl alkanethiol films as a function of electrolyte nature, concentration and experimental time scale.

Figure 5.1 shows the voltammetric response recorded for 8, 10 and 12-ferrocenyl alkanethiol SAMs formed under potential control in varying concentrations of $HClO_4$ (1M $\rightarrow$0.01M) at a scan rate of 100 mVs^{-1}. It is clearly seen that as concentration of electrolyte decreases so too does the current. The peak potential at each scan rate is shifted in a positive direction also. The error in the E^0 values is very small as they are calculated via the computer program used (CHI). The E^0 values were also calculated by hand. The error is in the region of $\pm$ 0.1-0.2 mV.

PAD SAM films : HClO$_4$ solutions.

100 mV/s, E$_{PAD}$ = 0.40V, 2hr immersion.
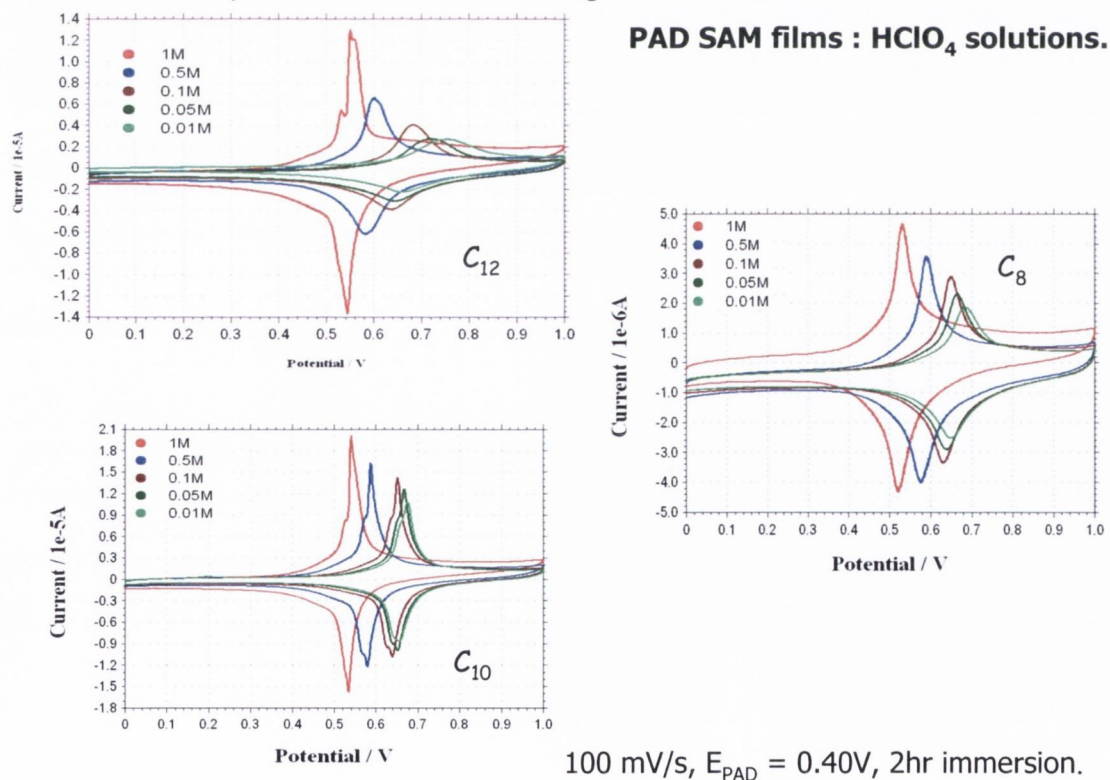
Figure 5.1: *Graph of the current (I_p/A) versus potential (E/mV) for the 8, 10 and 12-ferrocenyl alkanethiol PAD SAMs in varying concentrations of HClO$_4$ (1M $\rightarrow$0.01M) at a scan rate of 100 mVs^{-1}.*

For the 12-ferrocenyl alkanethiol SAM, at the 1 M concentration a "kink" appears in the cyclic voltammogram that doesn't appear in any of the other cyclic voltammograms measured at lower concentrations.

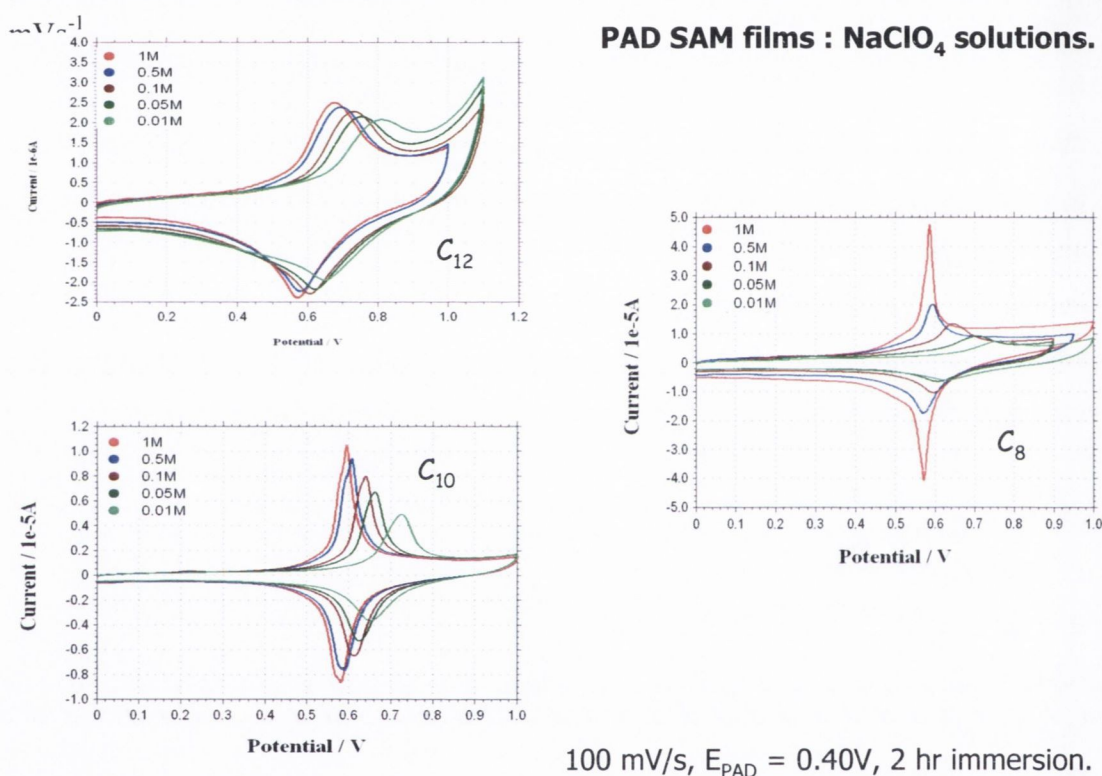Cyclic voltammetry was also carried out on varying concentrations of $NaClO_4$ at various scan rates. Figure 5.2 below shows the cyclic voltammetric response observed for 8, 10 and 12-ferrocenyl alkanethiol SAMs formed under potential control in varying concentrations of $NaClO_4$ (1M →0.01M) at a scan rate of 100 mVs^{-1}

Figure 5.2: *Graph of the current (I_p/A) versus potential (E/mV) for an 8, 10 and 12-ferrocenyl alkanethiol PAD SAM in varying concentrations of $NaClO_4$ (1M →0.01M) at a scan rate of 100 mVs^{-1}.*

It is clearly seen that as concentration decreases so too does the current. The potential of each scan rate is shifted in a positive direction also. However, as the concentration decreases the cyclic voltammograms becoming quasi reversible. In comparison to the shape obtained for the CV's recorded in $HClO_4$, the voltammograms observed in $NaClO_4$ are broader and not as well defined especially for the 12-ferrocenyl alkanethiol SAM. The redox switching involving the ferrocene/ferricinium redox

couple coupled with the ClO_4^- ion pairing is not as reversible when the redox groups are in contact with $NaClO_4$ as compared with $HClO_4$. This may suggest that the cation (Na^+ versus H^+) plays a role in the redox switching reaction.

A comparison of the $HClO_4$ and $NaClO_4$ electrolytes at the benchmark 100 mVs^{-1} was undertaken. The change in potential (ΔE_p), standard potential (E^0) and surface coverage (Γ_{Fc}) were all examined at this sweep rate in both electrolytes over a range of concentrations (0.01 M -1.0 M).

5.2.1 ΔE_p versus Concentration

The change in potential (ΔE_p) versus solution concentration in $HClO_4$ and $NaClO_4$ was examined. The change in potential was calculated from equation 2.7.

Figure 5.3 shows the comparison of the change in potential versus concentration for the 8, 10 and 12-ferrocenyl alkanethiol PAD SAMs in varying concentrations of $HClO_4$ and $NaClO_4$.
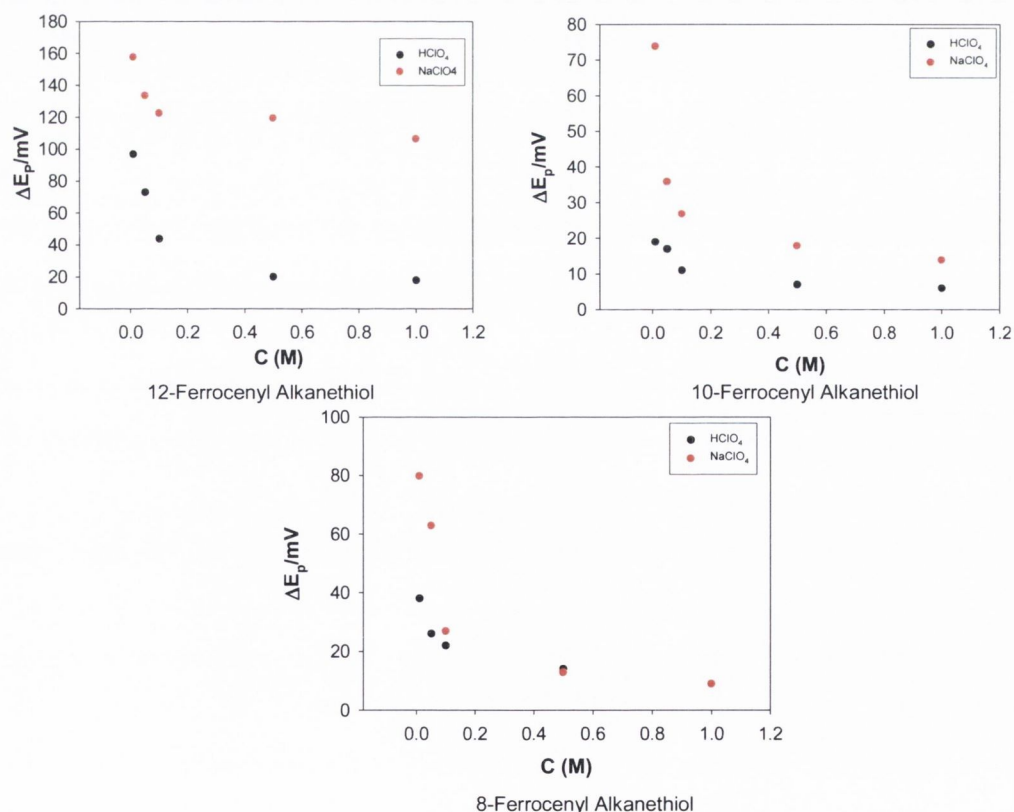
Figure 5.3: *Graph of the comparison of change in potential (ΔE_p/mV) versus conc (M) for a 12-ferrocenyl alkanethiol PAD SAM in varying concentrations of $HClO_4$ (1M →0.01M) and $NaClO_4$ (1M →0.01M) at a scan rate of 100 mVs^{-1}.*

For both species, in all three SAM chain lengths, as the concentration increases there are a decrease in the values of the anodic/cathodic peak separation. The nature of the electrolyte (as well as the concentration) clearly affects the redox switching behaviour of the surface immobilised redox groups. The values obtained for $NaClO_4$ are far higher than those obtained for the $HClO_4$.

In the ideal case there is no peak splitting and this informs us that there are no interactions between the molecules in the SAM. However, in this case we have peak splitting. Non zero peak splitting can arise from a number of causes. For example the degree of solvation of the redox centers may change with the degree of oxidation of the SAM. This may be due to a change in the local structure of the SAM film. The process is described in terms of a square scheme:

$$R \leftrightarrow O + ne^-$$
$$\downarrow$$
$$R' \leftrightarrow O' + ne^-$$
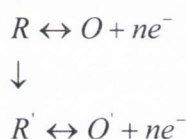
It is also widely accepted that peak splitting occurs due to interactions between adjacent redox centers in the monolayer.

5.2.2 E^0 versus Logarithm of Solution Concentration

A comparison of the standard potential (E^0) versus logarithm of solution concentration was also examined. The standard potential was calculated from equation 2.6. Figure 5.4 shows the graph of the comparison of potential (E_p/mV) versus log of concentration (M) for an 8, 10 and 12-ferrocenyl alkanethiol PAD SAMs in varying concentrations of $HClO_4$ (1M →0.01M) and $NaClO_4$ (1M →0.01M) at a scan rate of 100 mVs^{-1}.

There is a definite trend in the case of both species. As log C decreases i.e. concentration increases both the $HClO_4$ and $NaClO_4$ peak potential values shift more positively in an approximately linear manner. It can be clearly seen that the potential values for the $NaClO_4$ are far more positive then the $HClO_4$ values. The trend in $NaClO_4$ peak shifts is more linear than the $HClO_4$ peak shifts which tend to be more curved.

From the literature it is observed that the $E^0(Fc/Fc^+)$ in aqueous phosphate buffer is ≈0.4 V-0.5 V. When we compare this value to the values obtained for E^0 for the SAM in $HClO_4$ and $HClO_4$ we see that the E^0_{SAM} is more positive than E^0_{soln}. This indicates that the salvation environment of ferrocene has lower dielectric constant which in turn indicates that ferrocene sites are buried in the SAM.

The presence of an electron withdrawing COO group next to the cyclopentadienyl ring also causes the E^0 of Fc/Fc^+ redox couple to be more positive.

12-Ferrocenyl Alkanethiol

10-Ferrocenyl Alkanethiol

8-Ferrocenyl Alkanethiol
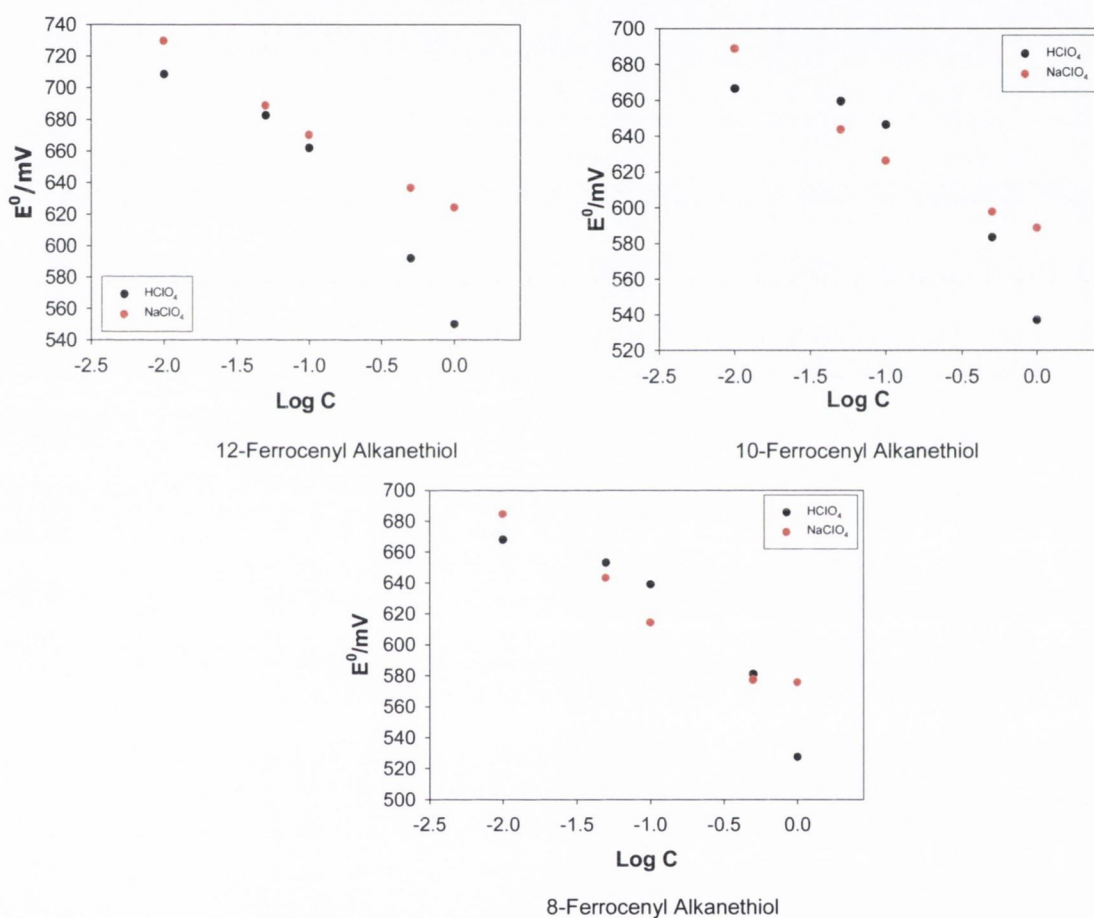
Figure 5.4: *Graph of the comparison of potential ($\Delta E_p/mV$) versus Log of conc (M) for an 8, 10 and 12-ferrocenyl alkanethiol PAD SAM in varying concentrations of $HClO_4$ (1M →0.01M) and $NaClO_4$ (1M →0.01M) at a scan rate of 100 mVs^{-1}.*

A similar graph is observed for both the fast 500 mVs^{-1} and slow 20 mVs^{-1} scan rates. The $NaClO_4$ values are linear whereas the $HClO_4$ values are curvilinear. Looking at the Nernst equation:

$$E = E^0 + \frac{RT}{F} \ln\left(\frac{\left[Fc^+ X^-\right]}{\left[Fc\right]}\right) - \frac{RT}{F} \ln K - \frac{RT}{F} \ln\left[X^-\right] \qquad (5.1)$$

It is expected that a plot of E against $\log_{10}[X^-]$ will produce a slope of $2.303RT/F$ where $2.303RT/F = 60$ mV/decade. However, the ideal version of the Nernst equation is unlikely to hold true in the case where the interactions occur between the ferrocene alkanethiol molecules.

C_n	Slope(mV/decade)		α	
	$HClO_4$	$NaClO_4$	$HClO_4$	$NaClO_4$
8	68.8	63.6	0.82	0.92
10	65.3	49.6	0.86	1.09
12	80.3	52.8	0.74	1.12

Table 5.1: *Table of the slope of graphs for the PAD SAM in $HClO_4$ and $NaClO_4$ at the 100 mVs^{-1} scan rate. Interaction parameters are also shown.*

For each of the SAMs, both sets of slopes differ from the ideal and indicate that interactions occur between the ferrocene alkanethiol molecules in both electrolytes.

From section 5.2.1 it was seen that peak splitting occurs due to interactions between adjacent redox centers in the monolayer. Returning to the Nernst equation it is possible to represent these interactions by the dimensionless interaction factor α. Equation 5.1 may then be written to include this factor as:

$$E = E^0 + \frac{RT}{\alpha F} \ln\left(\frac{\left[Fc^+ X^-\right]}{\left[Fc\right]}\right) - \frac{RT}{\alpha F} \ln K - \frac{RT}{\alpha F} \ln\left[X^-\right] \qquad (5.2)$$

By applying this equation to figure 5.22 a slope of $2.303\ RT/\alpha F$ is produced. From this interaction parameters were calculated. These values are shown in table 5.1. In an ideal situation $\alpha = 1$, however, for both the electrolytes our values deviate from the ideal value. From this it is further confirmed that interactions do occur between ferrocene molecules in the monolayer.

5.3 Comparison of Redox Characteristics of a PAD SAM versus a PD SAM

A comparison of potentially assisted growth versus passive incubation was undertaken for all n-ferrocenyl alkanethiols. Again the PAD SAM was formed from a 2 hour immersion in a 1 mM solution of n-ferrocenyl alkanethiol in ethanol with a potential of 0.4 V being passed through the working electrode. The PD SAM was immersed in the 1 mM ferrocenyl solution for a period of 48 hours without application of a potential.

5.3.1 Comparison of n-Ferrocenyl Alkanethiol SAMs

A comparison of potentially assisted growth versus passive incubation was undertaken for the 8, 10 and 12-ferrocenyl alkanethiol. The PAD SAM and the PD SAM were formed as in section 5.3
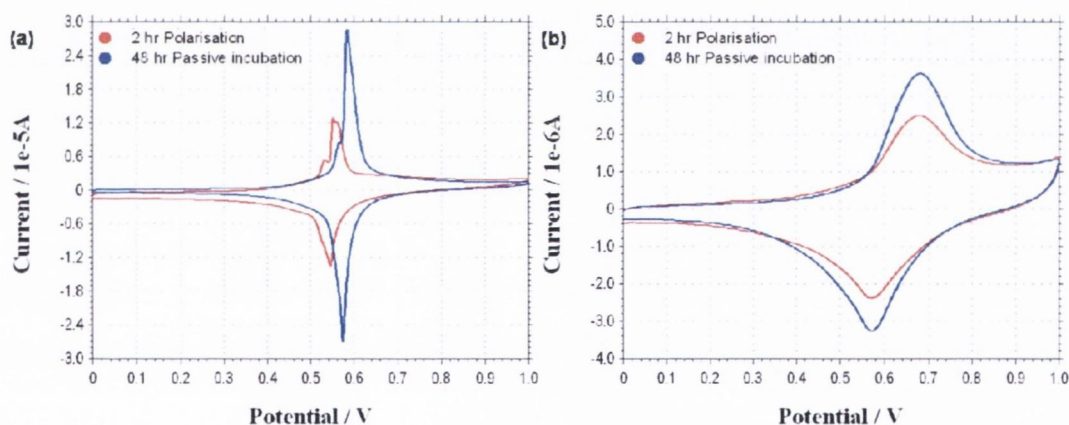
Figure 5.5: *CV of PD SAM (blue) versus PAD SAM (red) at a concentration of 1M HClO$_4$ (a) and 1 M NaClO$_4$ (b) at a scan rate of 100 mVs^{-1}.*

The comparative cyclic voltammogram of the deposited SAMs in 1 M and HClO$_4$ and NaClO$_4$ for the 12-ferrocenyl alkanethiol SAM are shown in figure 5.5. From figure 5.5 (a) we see almost ideal behaviour but there is the presence of a "spike" which is indicates the presence of poorly solvated phases in the SAMs. In figure 5.5 (b) we see a broadening of the peak potentials. This peak broadness is attributed to distribution of E^0 values of ferrocene/ferricinium in the SAM. It can also be attributed to the interaction effects between ferrocene sites.

In contrast the potentially-assisted SAM is less ordered. It also contains a sharp and well formed "kink" in its formation. This "kink" is also seen in the PD SAM, however, it is less pronounced. The prepeak may be formed due to some ferrocene sites being more oxidisable than others. In the 1 M NaClO$_4$ solution the shape of the peaks are wider than in the HClO$_4$ solution.
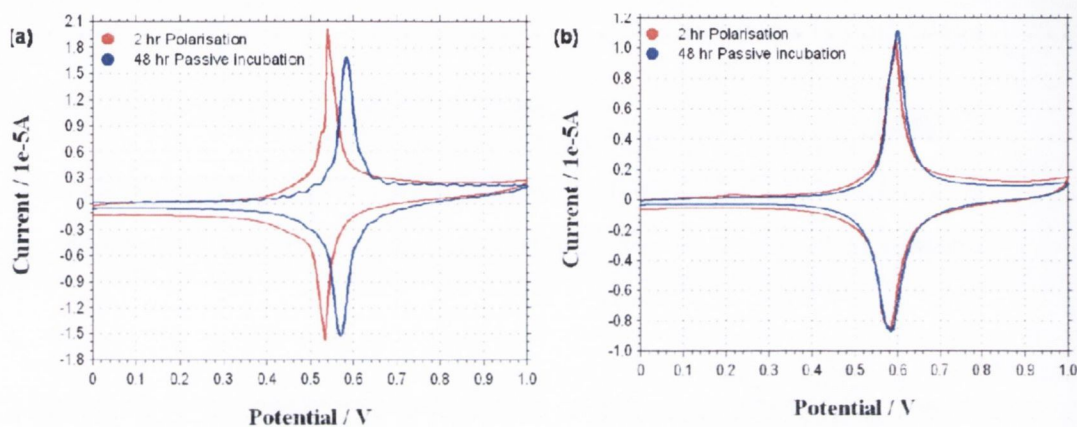
Figure 5.6: *(a) CV of PD 10-Ferrocenyl alkanethiol SAMs (blue) versus PAD SAMs (red) at a concentration of 1M HClO$_4$ at a scan rate of 100 mVs^{-1}.(b) CV of PD SAMs (blue) versus PAD SAMs (red) at a concentration of 1M NaClO$_4$ at a scan rate of 100 mVs^{-1}.*

We then analysed the 10-ferrocenyl alkanethiol SAM. From figure 5.6 it can be seen that for the 1M HClO$_4$ solution, the 10 ferrocenyl alkanethiol PADSAM is higher in current then the 10-ferrocenyl alkanethiol PD SAM. However, the peak on the PD SAM is broader then the PAD SAM. This is reflected in the surface coverage of both SAM species.

For the NaClO$_4$ 1 M solution it is seen that the shape of the voltammograms are very similar for both the PAD SAM and the PD SAM. It does appear that the current of the PD SAM is minimally higher than the PAD SAM and the width of the peak is similar. From both of these results, for the HClO$_4$ and the NaClO$_4$ it is obvious that the PD SAM is more ordered than the PAD SAM.
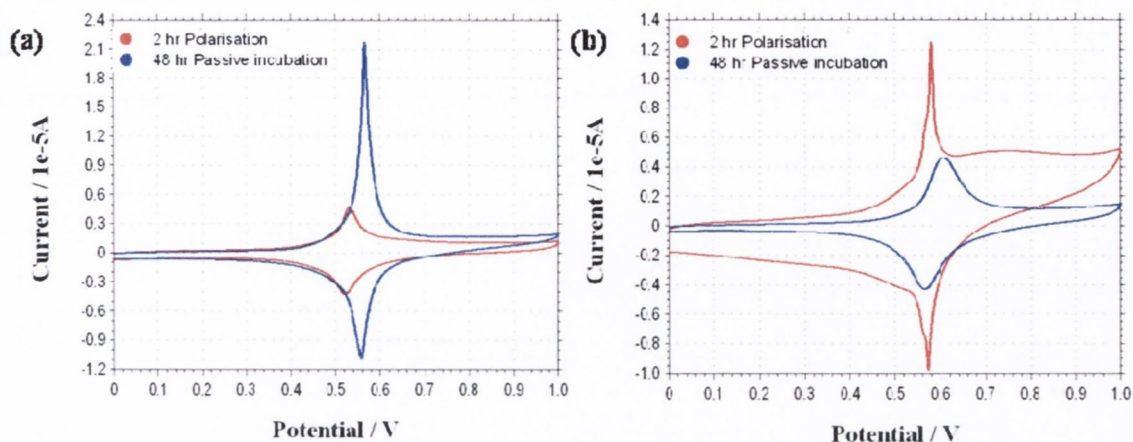
Figure 5.7: *(a) CV of PD 8-Ferrocenyl alkanethiol SAMs (blue) versus PAD SAM (red) at a concentration of 1M HClO₄ at a scan rate of 100 mVs⁻¹. (b) CV of PD SAM (blue) versus PAD SAMs (red) at a concentration of 1M NaClO₄ at a scan rate of 100 mVs⁻¹.*

Finally, we analysed the 8-ferrocenyl alkanethiol. From figure 5.7, the 8-ferrocenyl alkanethiol PD SAM is higher in current than the PAD SAM for the 1 M HClO₄ concentration. The potential peaks of both the PD SAM and the PAD SAM are well defined and sharp. The area under the peaks is vastly different with the PD SAM value larger than the PAD SAM. This difference is seen in the surface coverage of the SAMs.

From the ratio of passive incubation to PAD growth it is observed that the surface coverage of the PD SAM is 36 % of the PAD SAM. The E^0 value of PD SAM is more positive than that of the PAD SAM.

For the NaClO₄, the PAD SAM voltammogram is larger than that of the PD SAM. However, the PD SAM better defined in the 1 M concentration than the corresponding PAD SAM. The current of the PAD SAM is higher than the PD SAM current. From figure 5.7 (b) the surface coverage of the PAD SAM looks to be far larger than the surface coverage of the PD SAM but the results show otherwise. From the ratio of passive incubation to PAD growth it is observed that the surface coverage of the PD SAM is 66 % of the PAD SAM.

5.3.2 Voltammetric Measurables as a Function of Electrolyte Nature and Concentration

From section 5.2 it was seen that the effect of PD for the differing chain lengths causes major differences in the voltammograms compared to a PAD SAM. We now examine the voltammetric measurables: peak potential difference (ΔE_p), standard potential (E^0), peak width at half maximum (ΔE_{FWHM}) and surface coverage (Γ) and analyse the changes observed with each of the different self-assembly methods.

5.3.2.1 Voltammetric Peak Splitting as Function of Electrolyte Nature and Concentration

The difference in peak potential fro each of the chain length PD and PAD SAMs was analysed. From figure 5.8 and table 5.2 it is seen that for voltammetry conducted in $HClO_4$ and $NaClO_4$ solution, ΔE_p decreases with increasing electrolyte concentration for all chain lengths.
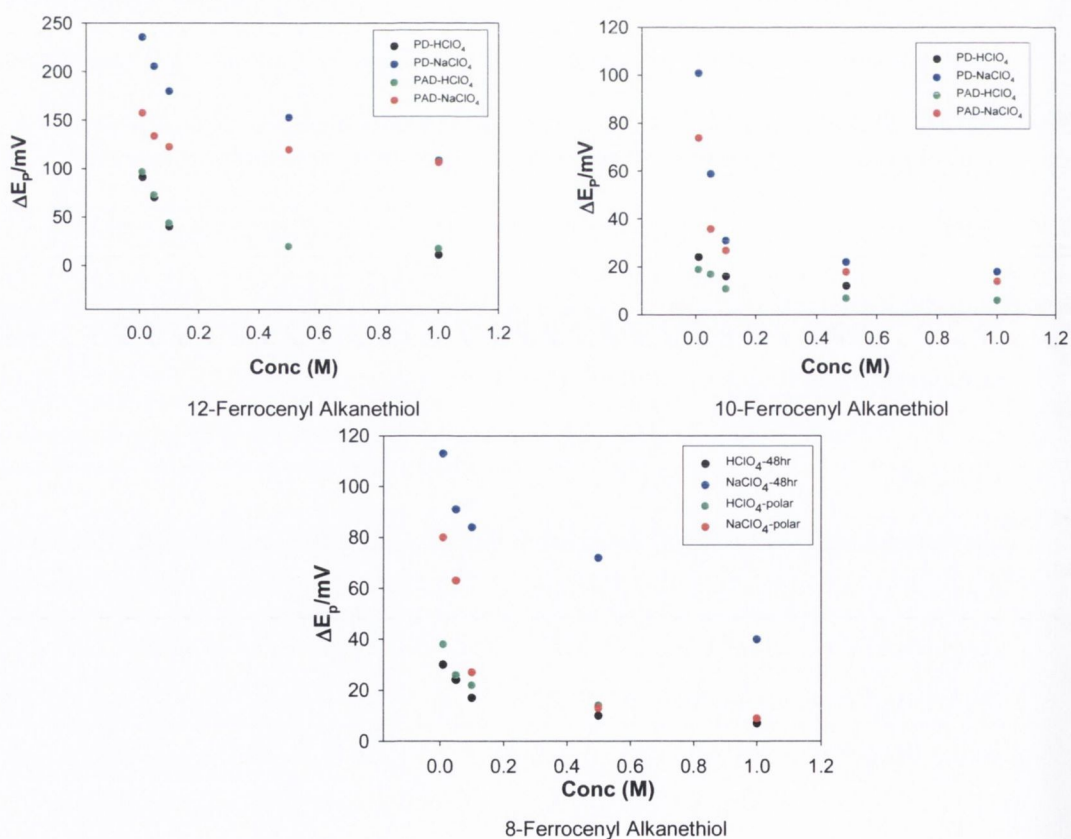
Figure 5.8: *Comparison of change in potential ($\Delta E_p/mV$) versus conc (M) for an 8,10 and 12-ferrocenyl PAD SAM and a 8,10 and 12-ferrocenyl PD SAM in varying concentrations of $HClO_4$ and $NaClO_4$ (1M →0.01M) at a scan rate of 100 mVs⁻¹.*

Taking NaClO$_4$, it is seen that the PD SAM has the largest values of change in potential. This trend is also observed for the PAD SAM films in contact with NaClO$_4$, where a decrease is seen in ΔE_p as each concentration decreases. It is also noted that for the HClO$_4$ the values for the ΔE_p of the potentially-assisted SAM are slightly higher than the values obtained for the PD self-assembled monolayer in the 8 and 12 alkanethiols. From this it can be concluded that the 2 hr potentially-assisted self-assembled monolayers are less ordered than the PD SAMs. This is self-explanatory as the PD SAMs are in solution for almost 12 times longer than the PAD SAMs. However, for NaClO$_4$ the opposite occurs. The values of the PAD SAMs are smaller and closer to the ideal than the PD SAMs for all three chain lengths.

	12-ferrocenyl alkanethiol		10-ferrocenyl alkanethiol		8-ferrocenyl alkanethiol	
	HClO$_4$ PAD	HClO$_4$ PD	HClO$_4$ PAD	HClO$_4$ PD	HClO$_4$ PAD	HClO$_4$ PD
0.01 M	97	91	19	24	38	30
0.05 M	73	70	17	17	26	24
0.1 M	44	40	11	16	22	17
0.5 M	20	20	7	12	14	10
1.0 M	18	11	6	14	9	7

	12-ferrocenyl alkanethiol		10-ferrocenyl alkanethiol		8-ferrocenyl alkanethiol	
	NaClO$_4$ PAD	NaClO$_4$ PD	NaClO$_4$ PAD	NaClO$_4$ PD	NaClO$_4$ PAD	NaClO$_4$ PD
0.01 M	158	236	74	101	80	113
0.05 M	134	206	36	59	63	91
0.1 M	123	180	27	31	27	84
0.5 M	120	153	18	22	13	72
1.0 M	107	109	14	18	9	40

Table 5.2: *Table of change in potential values (ΔE_p/mV) for the PD SAMs and PAD SAMs in HClO$_4$ and NaClO$_4$ at 100mVs^{-1}.*

5.3.2.2 Variation of Standard Potential versus Logarithm of Solution Concentration as a Function of Electrolyte Nature and Concentration

The variation in E^0 values for the Fc/Fc^+ redox transformation at passive and electrochemical SAM films with changes in the solution concentration are presented in figure 5.9 for the $HClO_4$ and $NaClO_4$ electrolytes. This data was recorded at a sweep rate of 100 mVs^{-1}.

12-Ferrocenyl Alkanethiol

10-Ferrocenyl Alkanethiol

8-Ferrocenyl Alkanethiol
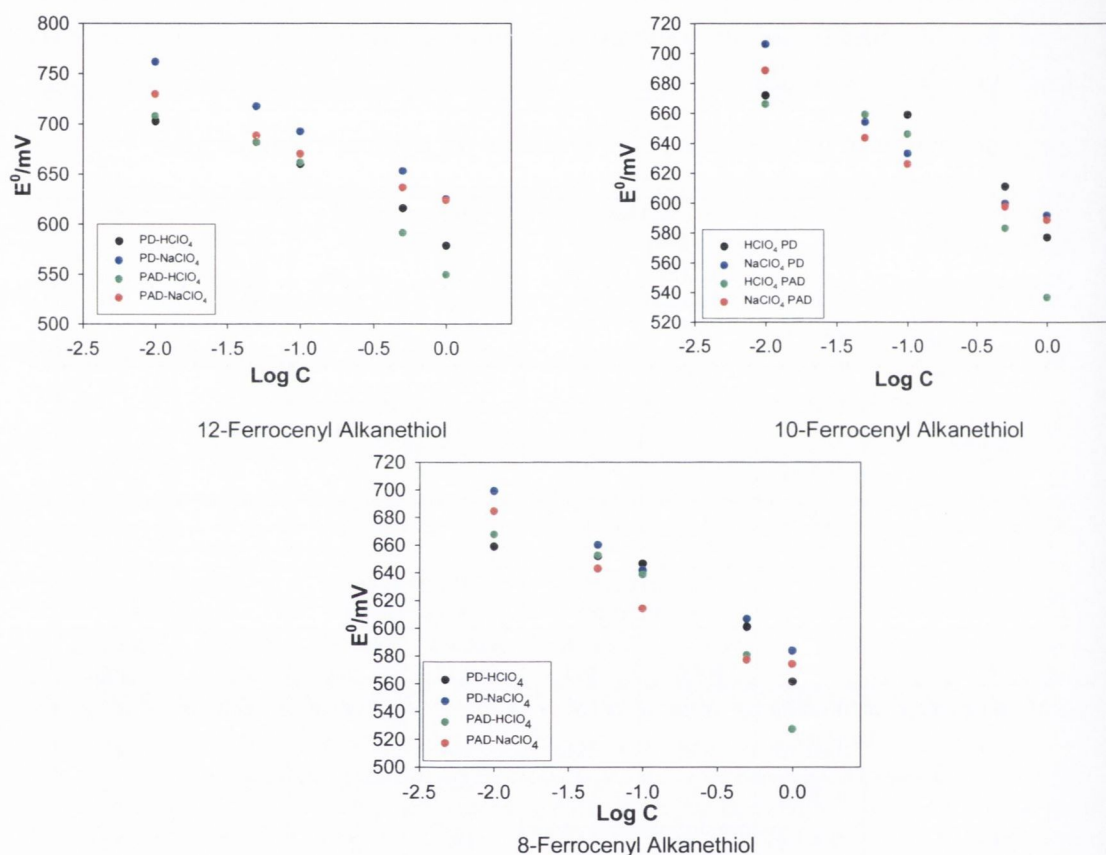
Figure 5.9: *Graph of the comparison of potential ($\Delta E_p/mV$) versus Log of conc (M) for the 8, 10 and 12-ferrocenyl alkanethiol PAD and PD SAMs in varying concentrations of $HClO_4$ (1M →0.01M) and $NaClO_4$ (1M →0.01M) at a scan rate of 100 mVs^{-1}.*

It is observed that for all chain lengths the E^0 values shift positively as the concentration decreases for both electrolytes. Looking closely at the $NaClO_4$ electrolyte, the peak potential values of the PD SAM are larger than the PAD SAMs at all concentrations. As the concentration of the $NaClO_4$ decreases both sets of potential values increase, however, the PD SAM increases to a higher value.

For HClO$_4$, it is seen that the PD SAM and the PAD SAM potential values are closer in value. Compared to the NaClO$_4$ however the results are different. For the 8, 10 and 12-ferrocenyl alkanethiol SAMs the PD values are more positive than the corresponding PAD values at high concentrations (1.0 M and 0.5 M). As the concentrations decrease the PAD values of the 8 and 12-ferrocenyl alkanethiol SAMs are similar to the PD values. At the lowest concentration (0.01 M) the PAD values are more positive.

	12-ferrocenyl alkanethiol		10-ferrocenyl alkanethiol		8-ferrocenyl alkanethiol	
	HClO$_4$ PAD	HClO$_4$ PD	HClO$_4$ PAD	HClO$_4$ PAD	HClO$_4$ PAD	HClO$_4$ PD
0.01 M	708.5	702.5	666.5	672	668	659
0.05 M	682.5	682	659.5	659.5	653	652
0.1 M	662	660	646.5	659	639	646.5
0.5 M	592	616	583.5	611	581	601
1.0 M	550	578.5	537	577	527.5	561.5

	12-ferrocenyl alkanethiol		10-ferrocenyl alkanethiol		8-ferrocenyl alkanethiol	
	NaClO$_4$ PAD	NaClO$_4$ PD	NaClO$_4$ PAD	NaClO$_4$ PD	NaClO$_4$ PAD	NaClO$_4$ PD
0.01 M	730	762	689	706.5	685	699.5
0.05 M	689	718	644	654.5	643.5	660.5
0.1 M	670.5	693	626.5	633.5	614.5	642
0.5 M	637	653.5	598	600	577.5	607
1.0 M	624.5	625.5	589	592	574.5	584

Table 5.3: *Table of potential values (E^0/mV) for the PD SAMs and PAD SAMs in HClO$_4$ and NaClO$_4$ at 100mVs^{-1}.*

Again looking at the graph, the trend in the plots is noted. For both the potential-assisted SAM and the PD SAMs in NaClO$_4$ the E^0 versus logarithm of concentration is linear for the 8, 10 and 12-ferrocenyl alkanethiol SAMs. However, for the HClO$_4$ the dependence of E^0 versus logarithm of concentration is curvilinear for each SAM type.

Slope mV/decade	HClO$_4$-PAD	HClO$_4$-PD	NaClO$_4$-PAD	NaClO$_4$-PD
8-ferrocernyl alkanethiol	67.8	47.9	57.7	56.6
10-ferrocernyl alkanethiol	65.3	46.6	49.5	57.2
12-ferrocernyl alkanethiol	80.3	61.4	52.7	67

α	HClO$_4$-PAD	HClO$_4$-PD	NaClO$_4$-PAD	NaClO$_4$-PD
8-ferrocernyl alkanethiol	0.87	1.23	1.02	1.04
10-ferrocernyl alkanethiol	0.9	1.27	1.19	1.03
12-ferrocernyl alkanethiol	0.74	0.96	1.12	0.88

Table 5.4: *Table of the slopes of E^0 versus Log C for the both the 12-ferrocenyl alkanethiol PAD and PD SAM in HClO$_4$ and NaClO$_4$ electrolytes at the 100 mVs^{-1} scan rate. Interaction parameters are also shown.*

From table 5.4 it is observed that the slopes of both the PAD and PD SAMs in the HClO$_4$ and NaClO$_4$ electrolytes all deviate from the ideal Nernstian value of 60 mV/decade. The double layer theory proposed by Smith and White can be used to predict the dependence of the peak potential on electrolyte concentration. When the coverage of redox centers is relatively high or the concentration of the electrolyte is low, the peak potential shifts negative at a Nernstian rate (-60 mV per decade increase in concentration for the electrolyte). The E$_p$ shift arises from the dependence of φ_S on the electrolyte concentration:

$$\varphi_s = \frac{2.3RT}{nF}(\log\zeta - \log C) \qquad (5.3)$$

ζ represents a collection of constants. E$_p$ approaches the true E$^{0'}$ asymptotically as the coverage of redox centers decreases and the concentration of the electrolyte increases. The Nernstian shift of E$_p$ with log C can be equivalently explained by viewing the electroactive SAM as a permiselective membrane for counter-ions of the opposite charge[ref]. When the surface coverage of the charged redox centers is high, the concentration of counter-ions can be significantly greater at the surface than in the bulk concentration. Donnan potential develops between the plane of redox centers

and the bulk of the electrolyte because the counterions tend to diffuse away from the surface of the monolayer. The Donnan potential changes with the oxidation state because a counterion must move toward or away from the redox center to provide charge compensation. The half-reaction can be written with the counterions shown:

$$O^{z+} + zX_{surf} \leftrightarrow R^{z-n} + (z-n)X_{surf} + nX_{so\,\ln} \tag{5.4}$$
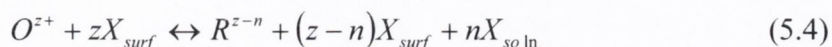
where X is either Na^+ or H^+. Migration of counterions is assumed to be the only method of charge transport between the surface of the monolayer and the bulk solution. The Nernst equation for this half-reaction is

$$E = E^0 - \frac{2.3RT}{nF} \log \frac{a_R(a_{X,sol})^n}{a_o(a_{X,surf})^n} \tag{5.5}$$

where a represents the activity of the subscripted species. If the standard states of O and R are defined as pure monolayers of attached O and R respectively, an if the apparent formal potential is defined for the point where f = 0.5 i.e. the fraction of attached redox centers in the oxidised state, then

$$E_{app}^{0'} = E^{0'} - \frac{2.3RT}{F} \log \frac{a_{X,sol}}{a_{X,surf}} \tag{5.6}$$

When the surface activity of the counterion is constant, the apparent formal potential $E_{app}^{0'}$ shifts at a Nernstian rate with respect to logarithm of the activity of the counterion in the bulk of the solution. This effect is purely electrostatic, and is not necessary to invoke ion pairing to explain shifts in the formal potential with counterion concentration.

5.3.2.3 Surface Coverage Variation

The quantity of electroactive ferrocene in the monolayers can be determined. For the positive peak, the charging current is removed by the subtraction of a linear background. The area under the peak is then integrated to obtain the amount of charge ($Q/\mu C$) passed in order for the ferrocene sites to be oxidized. The ferrocene surface coverages of the redox center (Γ_{FC}) on the electrode surface are then obtained from equation 2.8.

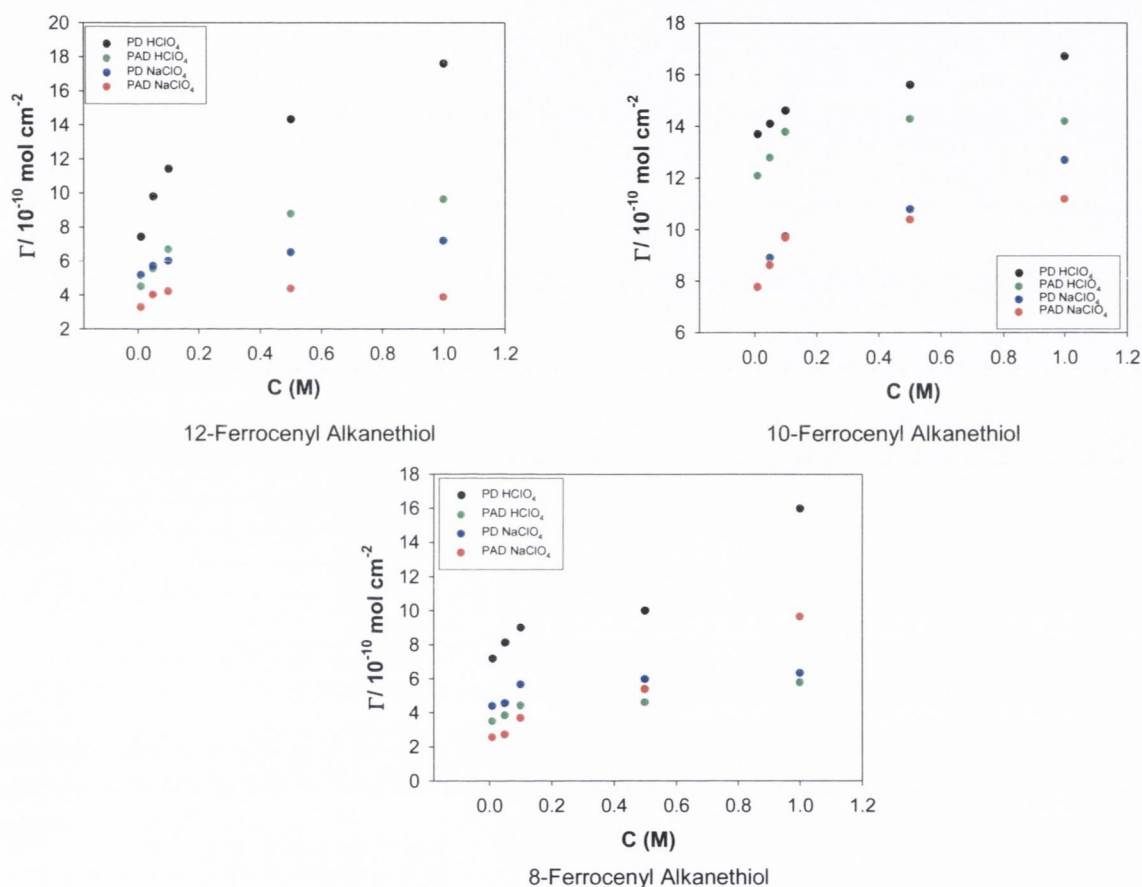|	12-ferrocenyl alkanethiol		10-ferrocenyl alkanethiol		8-ferrocenyl alkanethiol	
C (M)	$HClO_4$ PAD	$HClO_4$ PD	$HClO_4$ PAD	$HClO_4$ PD	$HClO_4$ PAD	$HClO_4$ PD
0.01	4.54	7.43	12.1	13.7	3.53	7.18
0.05	5.59	9.79	12.8	14.1	3.87	8.13
0.1	6.71	11.42	13.8	14.6	4.45	9.00
0.5	8.81	14.34	14.3	15.6	4.63	10
1.0	9.67	17.60	14.2	16.7	5.79	16

	12-ferrocenyl alkanethiol		10-ferrocenyl alkanethiol		8-ferrocenyl alkanethiol	
C (M)	$NaClO_4$ PAD	$NaClO_4$ PD	$NaClO_4$ PAD	$NaClO_4$ PD	$NaClO_4$ PAD	$NaClO_4$ PD
0.01	3.32	5.21	7.79	7.79	2.59	4.41
0.05	4.04	5.73	8.63	8.92	2.76	4.58
0.1	4.24	6.03	9.71	9.75	3.73	5.69
0.5	4.41	6.55	10.4	10.8	5.42	5.99
1.0	3.91	7.23	11.2	12.7	9.67	6.34

Table 5.5: *Table of surface coverages ($\Gamma_{FC}/10^{-10}$ mol cm^{-2}) for the PD SAMs and PAD SAMs in $HClO_4$ and $NaClO_4$ at 100 mVs^{-1}.*

For the studies conducted in $HClO_4$ it can be concluded that the surface coverages of the PD SAM are greater than the surface coverage of the PAD self-assembled monolayers for each chain length. This would be expected as the PD SAM has more time to form an ordered monolayer. This allows more electroactive ferrocenes to form on the surface of the electrode. It is also observed that as the concentration increases so too does the surface coverage of the SAM for all chain lengths.

As stated earlier, Chidsey et al. estimated that $\Gamma_{max} \approx 4.5 \times 10^{-10}$ mol cm^{-2} for an alkanethiol SAM on Au based on a close-packed layer of 6.6 Å diameter spheres. Larger Γ values probably reflect the presence of some disorder in the SAM which prevents all the ferrocenes from lying in a common plane. Also the real surface area of the Au(111) surface plays a role.

Figure 5.10: *graph of the comparison of surface coverage (Γ/mol cm^{-2}) versus conc (M) for 8,10 and 12-ferrocenyl alkanethiol PAD SAMs and the PD 8,10 and 12-ferrocenyl alkanethiol SAMs in varying concentrations of HClO$_4$ and NaClO$_4$ (1M →0.01M) at a scan rate of 100 mVs^{-1}.*

From the table it is observed that the 10-ferrocenyl alkanethiol SAM ratios are the highest values compared to the remaining chain lengths. This indicates that the 10-ferrocenyl alkanethiol SAM has similar quantities of ferrocenes showing on its surface for both self-assembly methods.

$\Gamma_{PAD} / \Gamma_{PD}$	12-ferrocenyl alkanethiol		10-ferrocenyl alkanethiol		8-ferrocenyl alkanethiol	
	$HClO_4$	$NaClO_4$	$HClO_4$	$NaClO_4$	$HClO_4$	$NaClO_4$
0.01 M	0.61	0.64	0.88	1	0.49	0.59
0.05 M	0.57	0.71	0.91	0.97	0.48	0.6
0.1 M	0.59	0.70	0.95	0.99	0.49	0.66
0.5 M	0.61	0.67	0.92	0.99	0.46	0.90
1.0 M	0.55	0.54	0.85	0.86	0.36	1.53

Table 5.6: *Table of surface coverage ratios for the PD SAMs and PAD SAMs in $HClO_4$ and $NaClO_4$ at $100mVs^{-1}$.*

Because SAMs form by self-assembly, that is, because they adopt adsorbed structures that are directed by the thermodynamics of a reasonably complex chemisorption process, SAMs provide, in theory, convenient access to highly ordered organic interfaces whose molecular and aggregate structures can be varied by principles of rational design. The structures of SAMs are generally regarded as if they contained few defects.
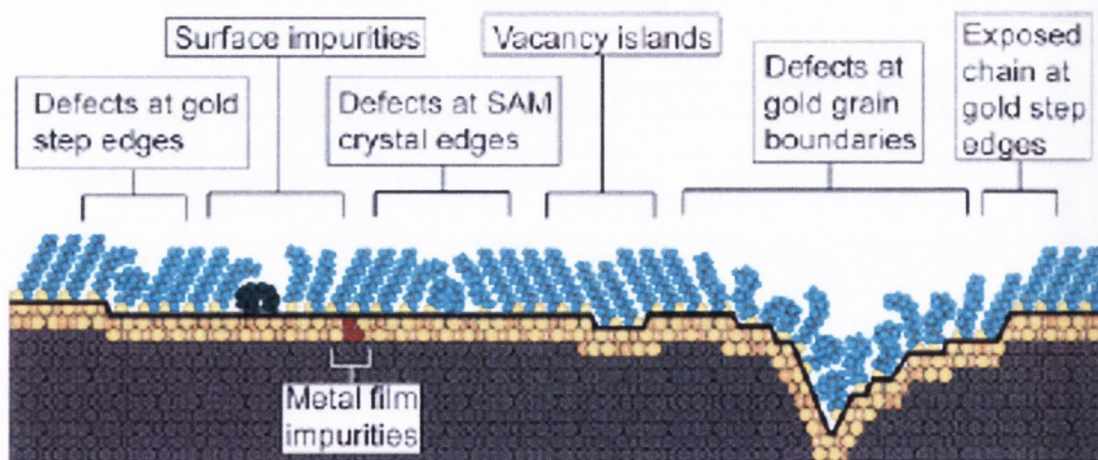

Figure 5.11: *Schematic illustration of some of the intrinsic and extrinsic defects found in SAMs formed on polycrystalline substrates. The dark line at the metal-sulfur interface is a visual guide for the reader and indicates the changing topography of the substrate itself.*

We have seen that the expected surface coverage value for a close packed SAM is 4.5 x 10^{-10} mol cm^{-2}. Our typical values are greater than this- Indicating that the surface of our electrode is rougher and contains defects which allow greater adsorption. These defects are shown in figure 5.11. These defects are not visible to the naked eye and only manifest themselves under microscopic techniques. As chain length increases there is more chance of defects in the SAM-defects may form at gold grain boundaries which allow more alkanethiol chains to adsorb onto the gold surface. Alkanethiol chains can also fold over due to reduced van der Waals forces. At high concentration (1 M) it is evident that as chain length increases so too does surface coverage i.e. there are more ferrocenes "spotted" on the surface of the electrode. Ion pairing may also take place between electrolyte ion and ferrocene buried in the SAM.

The adsorption mechanism may also account for greater surface coverages as chain length increases. The rearrangement of alkanethiol molecules in the lying down physisorbed state to a fully formed SAM may be more difficult as the chain length increases. Thus longer tail groups may form SAMs more quickly but defect concentration will be higher. Therefore greater surface coverages will be recorded.

5.3.2.4 Variation in Peak Half-Width with Electrolyte Concentration

A comparison of variation of peak half-width (ΔE_{fwhm}) with electrolyte concentration in both the $HClO_4$ and $NaClO_4$ solutions was undertaken for the 8, 10 and 12-ferrocenyl alkanethiol SAMs.

12-Ferrocenyl Alkanethiol

10-Ferrocenyl Alkanethiol

8-Ferrocenyl Alkanethiol
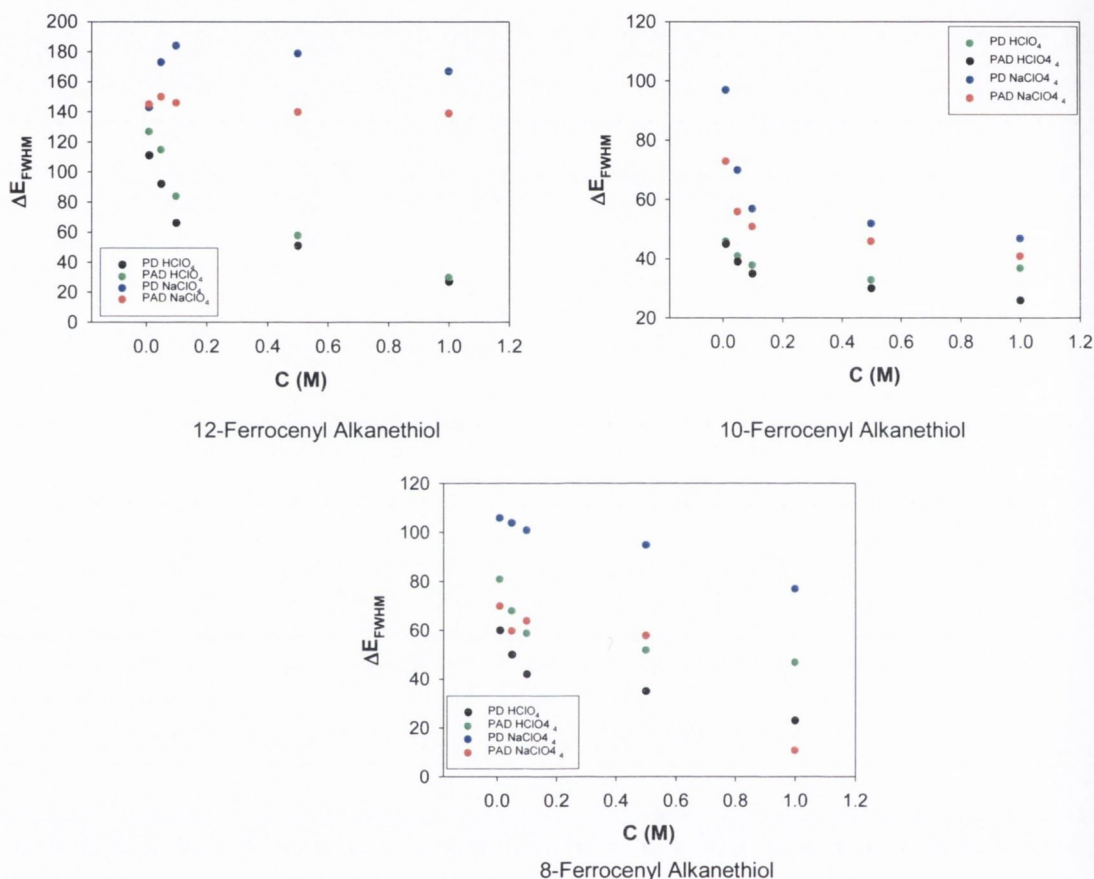
Figure 5.12: *Graphs of peak half-width (ΔE_{fwhm}) versus concentration for both the 2 h PAD and PD self-assembly methods in both the $HClO_4$ and $NaClO_4$ electrolytes (0.01 M-1 M) at a scan rate of 100 mVs^{-1}.*

Figure 5.12 shows the graph obtained using the both the $HClO_4$ and $NaClO_4$ concentration ranges for all three chain length SAM formed by both the PAD and the PD self–assembly method. In an ideal situation the peak is symmetrical with a ΔE_{fwhm} of 3.53RT/nF, or 90.6/n mV at 25°C. However, seldom are preceding diagnostics for ideal behaviour observed.

From the graph it is observed that at low concentrations the ΔE_{fwhm} values are the broadest and are generally greater than the expected 90 mV. As concentration increases the peak widths become narrower. Though not shown, it also observed that the ΔE_{fwhm} values decrease as the scan rate decreases for each concentration.

C(M)	12-Ferrocenyl Alkanethiol		10-Ferrocenyl Alkanethiol		8-Ferrocenyl Alkanethiol	
	$HClO_4$ PAD	$HClO_4$ PD	$HClO_4$ PAD	$HClO_4$ PD	$HClO_4$ PAD	$HClO_4$ PD
0.01	127	111	45	46	81	60
0.05	115	92	39	41	68	50
0.1	84	66	35	38	59	42
0.5	58	51	30	33	52	35
1.0	30	27	26	37	47	23

C(M)	12-Ferrocenyl Alkanethiol		10-Ferrocenyl Alkanethiol		8-Ferrocenyl Alkanethiol	
	$NaClO_4$ PAD	$NaClO_4$ PD	$NaClO_4$ PAD	$NaClO_4$ PD	$NaClO_4$ PAD	$NaClO_4$ PD
0.01	145	143	73	97	70	106
0.05	150	173	56	70	60	104
0.1	146	184	51	57	64	101
0.5	140	179	46	52	58	95
1.0	139	167	41	47	11	77

Table 5.7: *Table of peak half-width values (ΔE_{fwhm}) for the PD SAMs and PAD SAMs in $HClO_4$ and $NaClO_4$ at 100 mVs^{-1}.*

5.4 Voltammetric Comparison of 2 h PAD versus 2 h PD

A qualitative comparison using cyclic voltammetry between the 2 hour PAD n-ferrocenyl alkanethiol SAM versus a 2 hour PD n-ferrocenyl alkanethiol SAM for each chain length (n= 8,10 and 12) was then undertaken in order to discover just how efficient the method of PAD self-assembly was. For this a bare gold electrode was placed in a 1 mM solution of 2-ferrocenyl alkanethiol and ethanol for a period of two hours. Following this immersion, cyclic voltammetry was carried out on this new monolayer in varying concentrations of $HClO_4$ and $NaClO_4$ at a fast scan rate (500 mVs^{-1}), a moderately fast scan rate (100 mVs^{-1}) and a slow scan rate (20 mVs^{-1}). The following section deals with the 100 mVs^{-1} scan rate only.

5.4.1 Voltammetric comparison of n-Ferrocenyl alkanethiols

A qualitative comparison using cyclic voltammetry between the 2 hour PAD 12-ferrocenyl alkanethiol SAM versus a 2 hour PD 12-ferrocenyl alkanethiol SAM is described in this section.
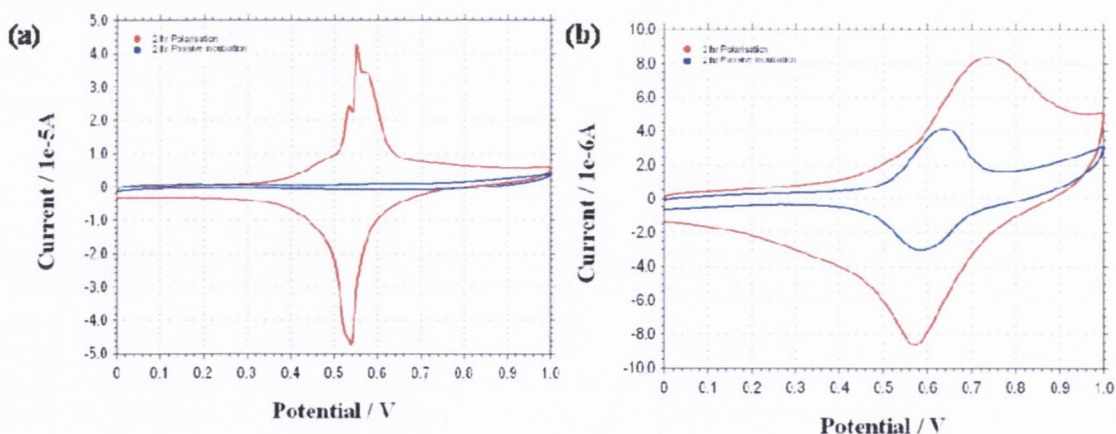
Figure 5.13: *(a) CV of 2 h PD SAM (blue) versus PAD SAM (red) at a concentration of 1M $HClO_4$ at a scan rate of 500 mVs^{-1}. (b) CV of 2 h PD SAM (blue) versus PAD SAM (red) at a concentration of 1M $NaClO_4$ at a scan rate of 500 mVs^{-1}.*

Figure 5.13 presents the comparison of the PAD SAM versus the PD SAM in $HClO_4$ (a) and $NaClO_4$ (b). Whereas, the 2 hour PAD SAM has a number of well defined peaks, the 2 hour PD SAM seems to have no peak definition and the current is relatively minute. However, when the 2 h passive incubation is taken on its own, a slightly different picture is observed.

Figure 5.14 presents the voltammograms recorded for PD (2 h) 12-ferrocenyl alkanethiol SAM in various concentrations of $HClO_4$. The voltammograms were recorded over a range of scan rates. Looking closely at figure 5.12(a) it is seen that at high concentrations (1 M and 0.5 M) there is some redox peaks observed signifying the surface attached ferrocene.

The $HClO_4$ solution shows a small peak formation for the 2 hour PD SAM. For the 2 h polarized SAM a standard potential of 653 mV is obtained at the 1 M concentration for the 500 mVs^{-1} scan rate whereas the corresponding value for the 2 h PD SAM is 612.5 mV. From the voltammograms it is clear that a 2 h passive incubation of a 12-ferrocenyl alkanethiol SAM does not show any potential peak for the 100 mVs^{-1} scan rate in the $HClO_4$ concentration range.
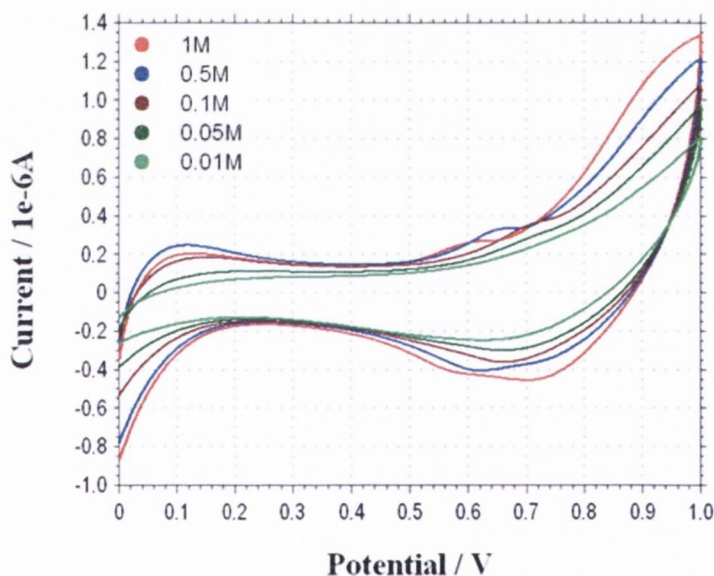
Figure 5.14: *Graphs of voltammograms of a 2 h PD of a 12-ferrocenyl alkanethiol SAM in various concentrations of $HClO_4$ at the 100 mVs^{-1} scan rate.*

When the experiment is repeated in $NaClO_4$ at the 100 mVs^{-1} scan rate, there is a similar result with only one minor difference. At 1 M concentration a potential peak for both oxidation and reduction are seen. The voltammograms for the 2 h PD SAM in $NaClO_4$ are in figure 5.15.

The change in potential (ΔE_p) between the oxidative and reductive potential peaks was also obtained at the 500 mVs^{-1} for the 1 M concentration. For the 2 h PAD

SAM a value of 158 mV is obtained. The corresponding value of the 2 h PD SAM is 55 mV. The 2 h PD SAM has a lower value ΔE_p value then that of the 2 h PAD SAM.

Finally the surface coverage (Γ_{FC}) of the electroactive ferrocenes on the surface of the electrode was calculated. A value of 2.4×10^{-10} mol/cm^{-2} was obtained for the 2 h PAD SAM whereas the corresponding 2 h PD SAM was 1.84×10^{-10} mol/cm^{-2}. From this it is clear that the 2 h PAD SAM has a higher surface coverage than the 2 h passive incubation. The $\dfrac{\Gamma_{PA}}{\Gamma_P}$ is 0.77.

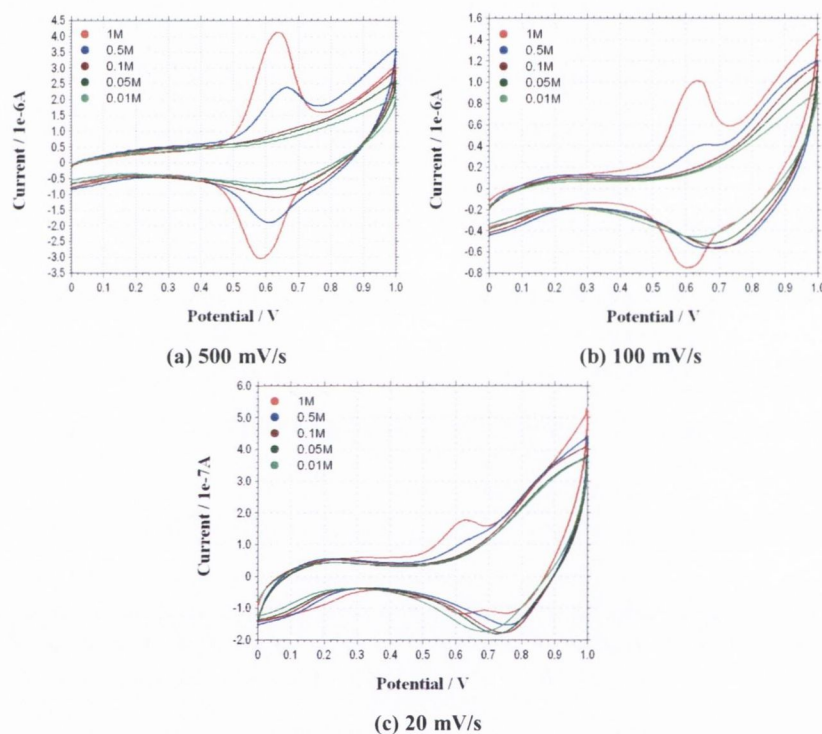**Figure 5.15:** *Graphs of voltammograms of a 2 h PD of a 12-ferrocenyl alkanethiol SAM in various concentrations of NaClO$_4$ at (a) 500 mVs^{-1} (b) 100 mVs^{-1} and (c) 20 mVs^{-1} scan rates.*

From the voltammograms it is clear that a 2 h passive incubation of a 12 ferrocenyl alkanethiol SAM does not allow for any significant adsorption of the 12 ferrocenyl alkanethiol onto the bare gold electrode. However, on looking at the surface coverages it is clearly observed that the application of a potential to a gold electrode does cause a positive effect on the adsorption of ferrocene to the surface of the electrode.

For the 10-ferrocenyl alkanethiol SAM, Figure 5.16 (a) & (b) presents the graphs of current voltammograms of a 2 h passive incubation in 1 M concentrations of $HClO_4$ (a) and $NaClO_4$ (b) at a scan rate of 100 mVs^{-1}. It is observed that the gold electrode undergoes adsorption at the surface of the electrode after a 2 h passive incubation in the 1 mM solution of 10-ferrocenyl alkanethiol. For the $HClO_4$ electrolyte a sharp peak is observed at both the oxidative and reductive peaks. This indicates that fast electron transfer occurs in the system. It is noted that the oxidative peak is not as well formed as the reductive peak.
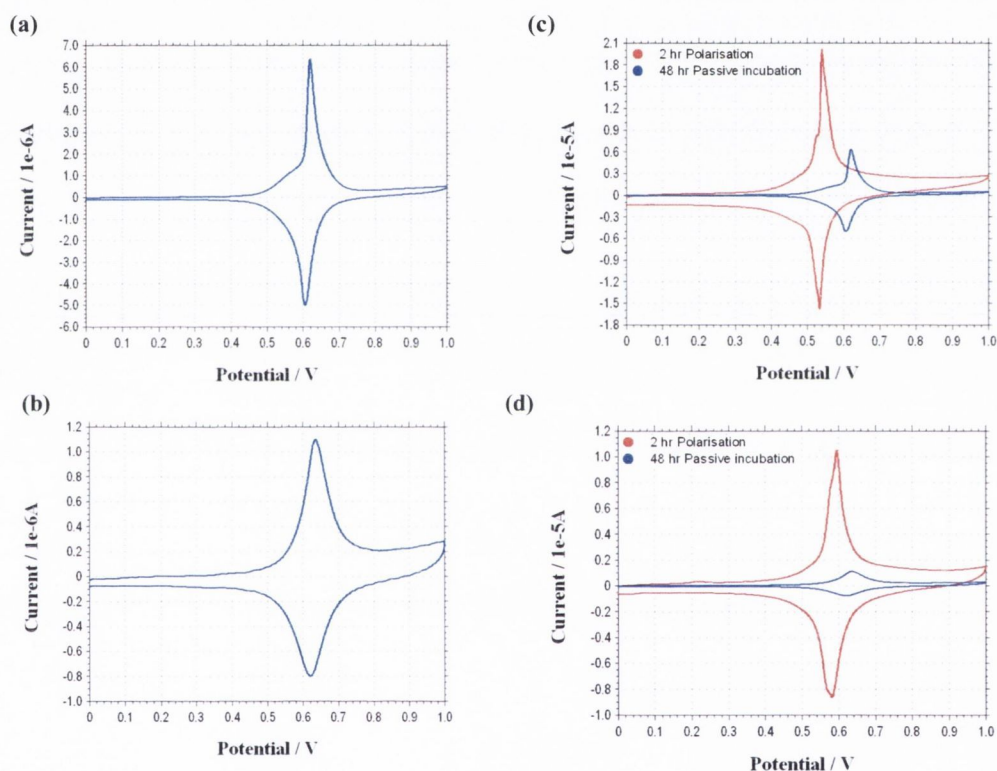
Figure 5.16: *CV of a 10-Ferrocenyl alkanethiol 2 h PD SAM at a concentration of 1 M $HClO_4$ (a) and 1 M $NaClO_4$ (b) at a scan rate of 100 mVs^{-1}. CV of 2 h PD SAM (blue) versus PAD SAM (red) at a concentration of 1 M $HClO_4$ (c) and 1 M $NaClO_4$ (d) at a scan rate of 100 mVs^{-1}.*

For the $NaClO_4$ electrolyte, well formed oxidative and reductive peaks are again seen. However, the peak shapes are broader than the corresponding $HClO_4$ peaks, suggesting slower electron transfer in the $NaClO_4$.

On first glance, the 2 h passive incubation of 10-ferrocenyl alkanethiol looks to adsorb well on the surface of the electrode. However, on comparison of the 2 h PD

SAM with the 2 h PAD SAM in $HClO_4$ (figure 5.16(c)) and $NaClO_4$ (figure 5.16(d)) at 100 mVs^{-1} it is seen that the voltammograms of the 2 h r PAD SAM are much larger than those of the 2 h PD SAM.

For the $HClO_4$ (figure 5.16(c)), the E^0 values of the PD SAM are more positive than the 2 h PAD SAM values. However, the change in potential values (ΔE_p) are both small. While both values are close to the ideal value of 0 mV, the 2 h PD SAM value is slightly higher. The main difference between the voltammograms is the surface coverage of the respective SAMs. The PAD SAM at 100 mVs^{-1} has a surface coverage value of 1.43×10^{-9} mol cm^{-2} whereas the corresponding value of the 2 h PD SAM is 5.9×10^{-10} molcm^{-2}. From the ratio of the 2 h PD SAM to the 2 h PAD SAM it is observed that the surface coverage of the 2 h PD SAM is 41.5 % smaller than the value of the 2 h PAD SAM.

Looking at the 1 M $NaClO_4$ concentration (figure 5.16(d)), it is clear that when the 2 h PD SAM and the 2 h PAD SAM are compared, a different picture than figure 5.16(c) appears. On comparison, again the voltammograms show vast differences in size. The 2 h PAD SAM voltammogram is far larger than the 2 h PD SAM voltammogram. The E^0 values of the 2 h PD SAM appear more positive than the 2 h PAD SAM. The ΔE_p values of both the 2 h PD SAM and the 2 h PAD SAM are the same at 14 mV, which is again small and not to far from the ideal value. Again the surface coverage of the SAMs is the main difference. The 2 h PAD SAM has a value of 1.12×10^{-9} molcm^{-2} and the corresponding 2 h PD SAM surface coverage is 1.57×10^{-10} molcm^{-2}. There is a large difference in the surface coverages of the SAMs and the ratio of the 2 h PD SAM to the 2 h PAD SAM is implies that the surface coverage of the PD SAM is 14.2 % the size of the PAD SAM.

For the 8-ferrocenyl alkanethiol SAM, Figure 5.17 (a) and (b) presents the graphs of current voltammograms of a 2 h passive incubation in 1 M concentrations of $HClO_4$ (a) and $NaClO_4$ (b) at a scan rate of 100 mVs^{-1}. It is observed that the gold electrode undergoes adsorption at the surface of the electrode after a 2 h passive incubation in the 1 mM solution of 8-ferrocenyl alkanethiol.
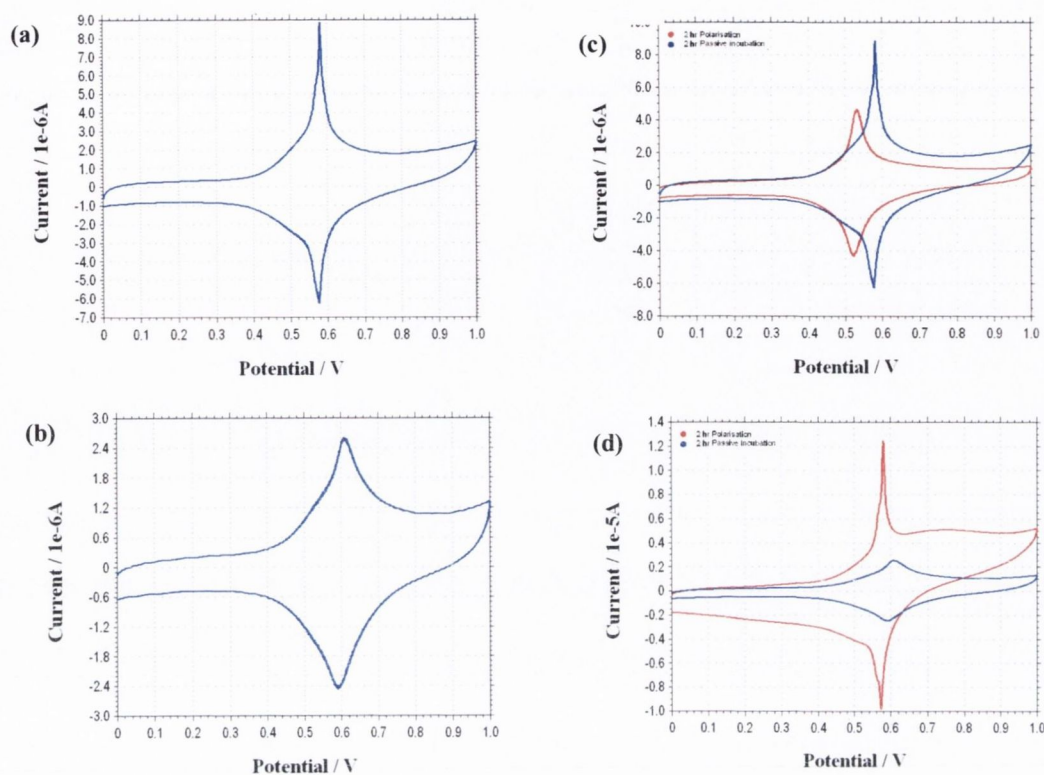
Figure 5.17: *CV of a 2 h PD SAM at a concentration of 1 M HClO₄ (a) and 1 M NaClO₄ (b) at a scan rate of 100 mVs⁻¹. CV of 2 h PD SAM (blue) versus PAD SAM (red) at a concentration of 1 M HClO₄ (c) and 1 M NaClO₄ (d) at a scan rate of 100 mVs⁻¹.*

For the HClO₄ electrolyte a sharp peak is observed at both the oxidative and reductive peaks. This indicates that fast electron transfer occurs in the system. For the NaClO₄ electrolyte, well formed oxidative and reductive peaks are again seen. However, the peak shapes are broader than the corresponding HClO₄ peaks, suggesting slower electron transfer in the NaClO₄.

The 2 h PD of 8-ferrocenyl alkanethiol looks to adsorb well on the surface of the electrode. On comparison of the 2 h PD SAM with the 2 h PAD SAM in HClO₄ (figure 5.17(c)) and NaClO₄ (figure 5.17(d)) at 100 mVs⁻¹ it is seen that the voltammograms of the 2 h PAD SAM are much larger than those of the 2 h PD SAM in NaClO₄, however, in HClO₄ the opposite is seen. The voltammograms of the 2 h PD SAM are larger than those of the 2 h PAD SAM. For the HClO₄ (figure 5.17(c)), the E^0 values of the PD SAM are more positive than the 2 h PAD SAM values. While both values are close to the ideal value of 0 mV, the 2 h PD SAM value is slightly higher.

The main difference between the voltammograms is the surface coverage of the respective SAMs. In 1 M HClO$_4$ the PAD SAM at 100 mVs^{-1} has a surface coverage value of 3.53x10^{-10} molcm^{-2} whereas the corresponding surface coverage of the 2 h PD SAM is 4.63 x10^{-10} molcm^{-2}. From the ratio of the 2 h PD SAM to the 2 h PAD SAM it is seen that the surface coverage of the 2 h PAD SAM is 24 % smaller.

Looking at the 1 M NaClO$_4$ concentration (figure 5.17(d)), it is clear that when the 2 h PD SAM and the 2 h PAD SAM are compared, a different picture than figure 5.17(c) appears. On comparison, again the voltammograms show vast differences in size. The 2 h PAD SAM voltammogram is far larger than the 2 h PD SAM voltammogram. The E^0 values of the 2 h PD SAM appear more positive than the 2 h PAD SAM and the values confirm this. The ΔE_p values of both the 2 h PD SAM and the 2 h PAD SAM are low with the 2 h PD SAM (17 mV) being slightly higher than the 2 h PAD SAM (9 mV). The values are again small and not to far from the ideal value.

Even though the voltammograms are vastly different in size, the surface coverage values of the SAMs are not too different. There is a small difference in the surface coverage values of the SAMs and the ratio of the 2 h PD SAM to the 2 h PAD SAM confirms this with a value of 0.912. This value is extremely high and implies that the surface coverage of the PD SAM is just 9 % larger than the surface coverage of the PAD SAM.

In order to carry out a full comparison of the 2 h PAD SAM and the 2 h PD SAM the standard potentials (E^0), change in potential values (ΔE_p) and surface coverage values (Γ) of both the 8 and 10-ferrocenyl alkanethiol SAMs in various concentrations of HClO$_4$ and NaClO$_4$ at the different scan rates are examined and the results compared.

5.4.1.1 Comparison of Standard Potentials

A comparison of the standard potentials of the 8 and 10 ferrocenyl alkanethiol 2 h PD SAMs and the 2 h PAD SAMs in the various concentrations of $HClO_4$ at the 100 mVs^{-1} scan rate was undertaken. The results are shown in figure 5.18 and table 5.8.
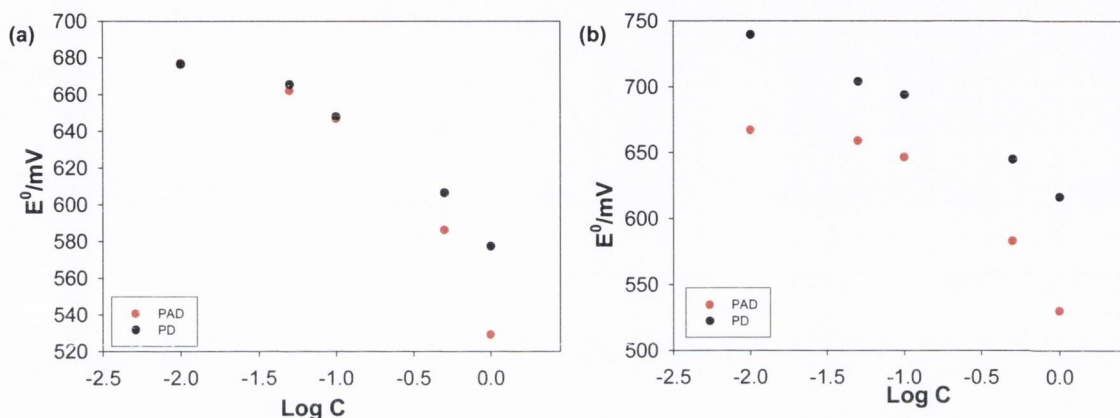
Figure 5.18: *Comparison of standard potential (E^0/mV) versus the logarithm of solution concentration for an 8-ferrocenyl alkanethiol (a) and 10-ferrocenyl alkanethiol (b) 2 h PAD SAMs and a 2 h PD SAMs in varying concentrations of $HClO_4$ (1M →0.01M) at the 100 mVs^{-1} scan rate.*

From the graphs and the table it is observed that the E^0 values of the 2 h PD SAM are more positive compared to the E^0 values of the 2 h PAD SAM for both chain lengths.

For both chain lengths, the E^0 values of both the 2 h PD SAM and the 2 h PAD SAM are shifted positively as the concentration decreases. Though not shown the E^0 values of the 2 h PD SAM also decrease as the scan rate decreases.
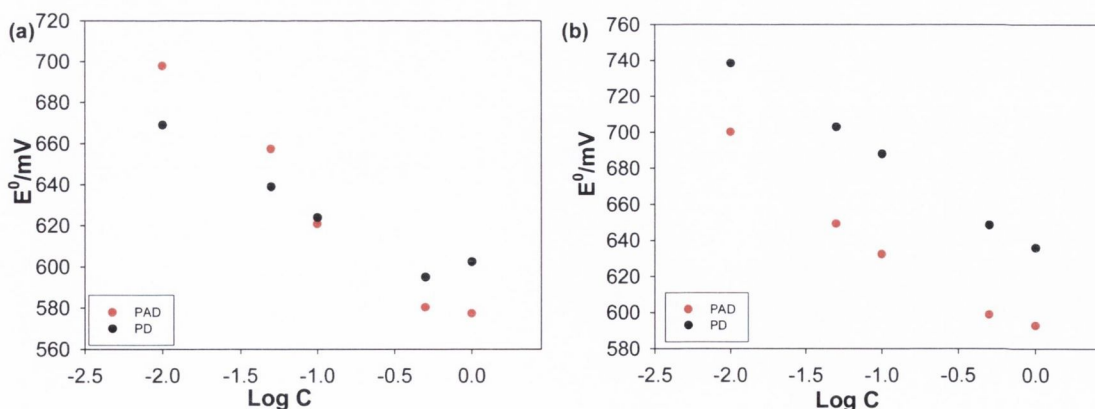
Figure 5.19: *Comparison of standard potential (E^0/mV) versus the logarithm of solution concentration for an 8-ferrocenyl alkanethiol (a) and 10-ferrocenyl alkanethiol (b) 2 h PAD SAMs and a 2 h PD SAMs in varying concentrations of $NaClO_4$ (1M →0.01M) at the 100 mVs^{-1} scan rate.*

For the $NaClO_4$ electrolyte a similar result is obtained for the 10-ferrocenyl alkanethiol. From figure 5.19 (b) and table 5.8 the E^0 values of the 2 h PD SAM are more positive than those of the 2 h PAD SAM. In contrast to the $HClO_4$ both the 2 h PD and the 2 h PAD SAMs are linear with respect to the logarithm of solution concentration. However, for the 8-ferrocenyl alkanethiol a different trend is seen: the E^0 values of the 2 h PD SAM are more positive than those of the 2 h PAD SAM at high concentrations only (0.1 M-1 M). For low concentrations we see a reverse.

For both the 8 and 10-ferrocenyl alkanethiols, the 2 h PD and the 2 h PAD SAM E^0 values are again shifted positively as concentration decreases. The E^0 values of both SAM types also decrease as the scan rate decreases.

	10-Ferrocenyl Alkanethiol				10-Ferrocenyl Alkanethiol			
	2 h PD $HClO_4$	2 h PAD $HClO_4$	2 h PD $NaClO_4$	2 h PAD $NaClO_4$	2 h PD $HClO_4$	2 h PAD $HClO_4$	2 h PD $NaClO_4$	2 h PAD $NaClO_4$
0.01 M	736.5	666.5	739.5	689	674.5	668	676	685
0.05M	696	659.5	699.5	644	665	653	637	643.5
0.1 M	687.5	646.5	681	626.5	649.5	639	635	614.5
0.5 M	639	583.5	642	598	607.5	581	584	577.5
1.0 M	613	537	628	589	578.5	527.5	598.5	574.5

Table 5.8: *Table of standard potential values (E^0/mV) for the 2 h PD and the 2 PAD SAMs of the 8 and 10-ferrocenyl alkanethiol in $HClO_4$ and $NaClO_4$ at 100mVs^{-1}.*

5.4.1.2 Change in Potential (ΔE_p) versus Scan Rate

A comparison of the change in potential versus concentration at the 100 mVs^{-1} was undertaken for the 8 and 10-ferrocenyl alkanethiols. Figure 5.20 presents the comparison of the change in potential values (ΔE_p) of a 10-ferrocenyl alkanethiol 2 h PD SAM and a 2 h PAD SAM in varying concentrations of $HClO_4$ and $NaClO_4$.
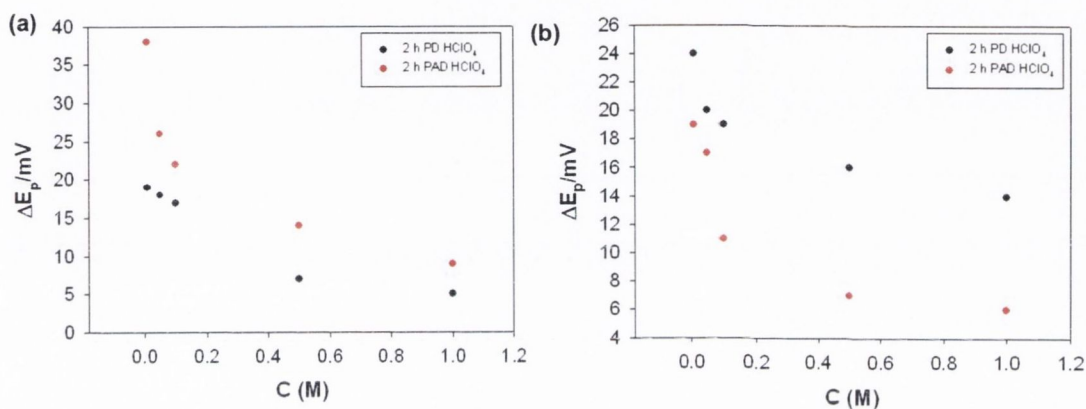
Figure 5.20: *Comparison of change in potential ($ΔE_p$/mV) versus the solution concentration for an 8-ferrocenyl alkanethiol (a) and 10-ferrocenyl alkanethiol (b) 2 h PAD SAMs and a 2 h PD SAMs in varying concentrations of $HClO_4$ (1M →0.01M) at the 100 mVs^{-1} scan rate..*

For 10-ferrocenyl alkanethiol SAM (figure 5.20 (b)) it is observed that the ΔE_p values of the 2 h PAD SAM are lower than those of the 2 h PD SAM and therefore closer to the ideal at the 100 mVs^{-1} scan rate.

For the 8-ferrocenyl alkanethiol SAM there is a major change seen in the graph. From figure 5.21(a) it is observed that the ΔE_p values of the 2 h PD SAM are lower than those of the 2 h PAD SAM in the $HClO_4$ electrolyte. For both the 8 and 10-ferrocenyl alkanethiols the ΔE_p values of the 2 h PD SAM and 2 hr PAD SAM decrease as concentration decreases.

In the $NaClO_4$ electrolyte, the 2 h PD SAM values are higher than those of the 2 h PAD SAM at higher concentrations (1 M-0.01 M) for the 8-ferrocenyl alkanethiol. However, at the low concentrations the 2 h PAD SAM values are now higher than the 2 h PD SAM.
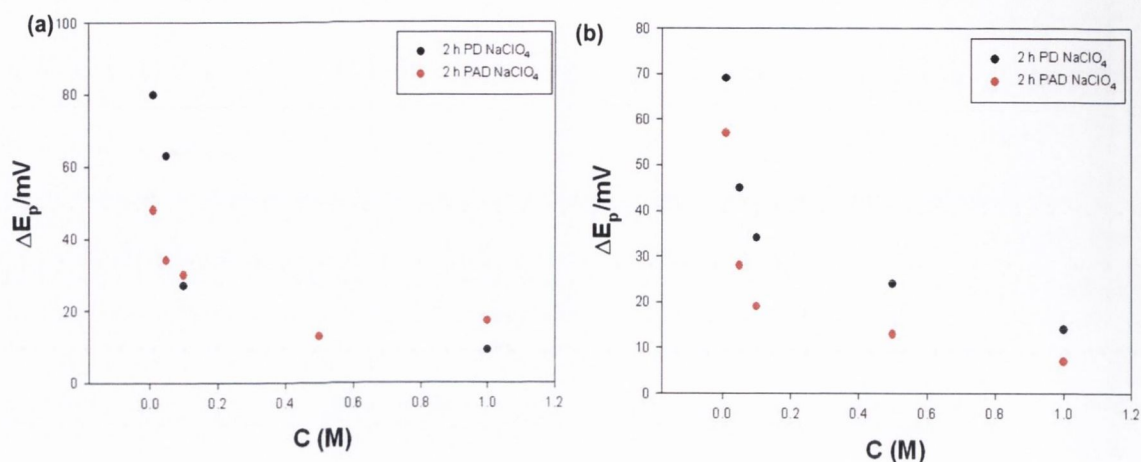
Figure 5.21: *Comparison of change in potential (ΔE$_p$/mV) versus the solution concentration for an 8-ferrocenyl alkanethiol (a) and 10-ferrocenyl alkanethiol (b) 2 h PAD SAMs and a 2 h PD SAMs in varying concentrations of NaClO$_4$ (1M→0.01M) at the 100 mVs^{-1} scan rate..*

The 2 h PD SAM values are larger than those of the 2 h PAD SAM for the 10-ferrocenyl alkanethiol SAM. For both chain lengths, the ΔE$_p$ values of the 2 h PD and 2 h PAD SAMs in NaClO$_4$ decrease towards the ideal as the concentration increases.

	10-Ferrocenyl Alkanethiol				18-Ferrocenyl Alkanethiol			
	2 h PD HClO$_4$	2 h PAD HClO$_4$	2 h PD NaClO$_4$	2 h PAD NaClO$_4$	2 h PD HClO$_4$	2 h PAD HClO$_4$	2 h PD NaClO$_4$	2 h PAD NaClO$_4$
0.01 M	24	19	69	57	19	38	80	48
0.05M	20	17	45	28	18	26	63	34
0.1 M	19	11	34	19	17	22	27	30
0.5 M	16	7	24	13	7	14	13	26
1.0 M	14	6	14	7	5	9	9	17

Table 5.9: *Change in potential values (ΔE$_p$/mV) for the 2 h PD 8 and 10-ferrocenyl alkanethiol SAMs and the 2 h potentially assisted SAMs in HClO$_4$ at 500 mVs^{-1}, 100 mVs^{-1} and 20 mVs^{-1}.*

5.4.1.3 Comparison of Surface Coverage

The amount of electroactive ferrocene adsorbed on the surface of the electrode was calculated. Figure 5.22 shows the comparison of surface coverage versus concentration for both the 2 h passively incubated SAM and the 2 h potential assisted SAMs in $HClO_4$ and $NaClO_4$ at the 100 mVs^{-1} for the 8 and 10-ferrocenyl alkanethiols.
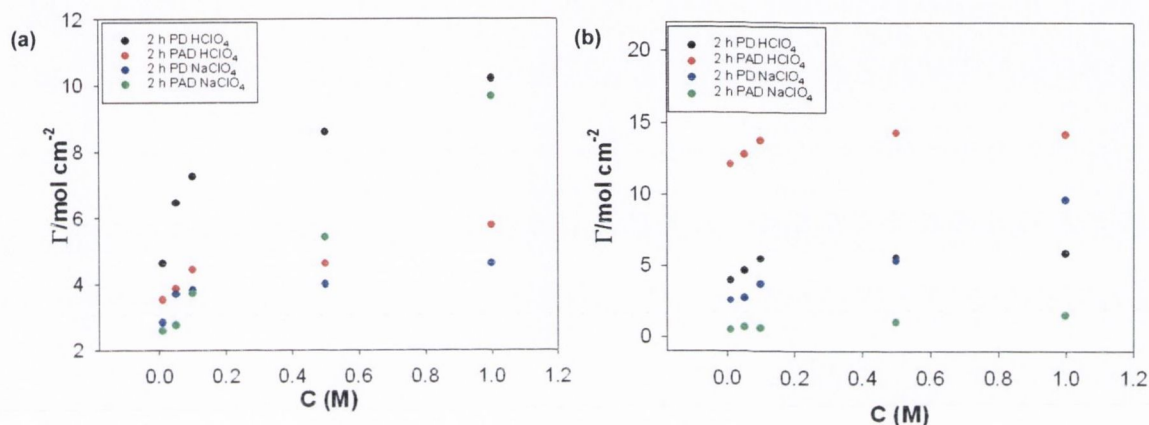
Figure 5.22: *Graph of the comparison of surface coverage (Γ_{FC}) versus the solution concentration for a 8-ferrocenyl alkanethiol (a) and 10-ferrocenyl alkanethiol (b) 2 h PAD SAM and a 2 h PD SAM in varying concentrations of $HClO_4$ and $NaClO_4$ (1 M →0.01 M) at 100 mVs^{-1}.*

For the 8 and 10-ferrocenyl alkanethiols, the surface coverage of both the 2 h PAD and 2 h PD SAM's in $HClO_4$ and $NaClO_4$ increase as the concentrations increases. For the 8-ferrocenyl alkanethiol SAM the 2 h PD surface coverage values are larger than the corresponding values of the 2 h PAD SAM. For the $NaClO_4$ electrolyte, the surface coverage values of the 8-ferrocenyl alkanethiol 2 h PD SAM are larger than the 2 h PAD SAM at low concentrations (0.01 M and 0.05 M). As the concentration increases the 2 hr PAD surface coverage value are larger.

For the 10-ferrocenyl alkanethiol SAM the the 2 h PAD surface coverage values are larger than the correspondong values of the 2 h PD SAM at all concentrations. For the $NaClO_4$ electrolyte, the surface coverage values of the 10-ferrocenyl alkanethiol 2 h PAD SAM are larger than the 2 h PD SAM at all concentrations.

C (M)	10-Ferrocenyl Alkanethiol				8-Ferrocenyl Alkanethiol			
	PD $HClO_4$	PAD $HClO_4$	PD $NaClO_4$	PD $NaClO_4$	PD $HClO_4$	PAD $HClO_4$	PD $NaClO_4$	PAD $NaClO_4$
0.01	4.01	12.1	2.59	0.5	4.63	3.53	2.84	2.59
0.05	4.65	12.8	2.76	0.71	6.45	3.87	3.71	2.76
0.1	5.49	13.8	3.73	0.68	7.25	4.45	3.82	3.73
0.5	5.61	14.3	5.42	1.07	8.60	4.63	4.00	5.42
1.0	5.89	14.2	9.67	1.57	10.2	5.79	4.62	9.67

Table 5.10: *Table of surface coverage values ($\Gamma/10^{-10}$ mol cm^{-2}) versus concentration for the 8 and 10-ferrocenyl alkanethiol 2 h PD SAMs and the 2 h PAD SAMs in $HClO_4$ and $NaClO_4$ at 100 mVs^{-1}.*

For both the 8 and 10-ferrocenyl alkanethiols the $HClO_4$ electrolyte the ratio of the surface coverages of the PAD SAM to the PD SAM (Γ_P/Γ_{PA}) was calculated for the 100 mVs^{-1} scan rate (table 5.31). The ratios of the 10-ferrocenyl alkanethiol increase as the concentration increases, however, the values are low. The ratios for the 8-ferrocenyl alkanethiol are very high (i.e. >1) as the 2 h PD surface coverage values are larger than the correspondong values of the 2 h PAD SAM.

The ratio of the surface coverage values of the PAD SAM to the PD SAM for the $NaClO_4$ electrolyte was also calculated. The values for all three scan rates are similar and relatively small for the 10-ferrocenyl alkanethiol. For the 8-ferrocenyl alkanethiol, high ratios are seen at the low concentrations whereas the at high concentrations we see a reduction in the ratio.

| Γ_{PD}/Γ_{PAD}	10-Ferrocenyl Alkanethiol		8-Ferrocenyl Alkanethiol	
	$HClO_4$	$NaClO_4$	$HClO_4$	$NaClO_4$
0.01 M	0.33	0.064	1.32	1.1
0.05M	0.36	0.082	1.67	1.34
0.1 M	0.39	0.07	1.64	1.02
0.5 M	0.4	0.103	1.85	0.74
1.0 M	0.41	0.14	1.75	0.48

Table 5.11: *Table of surface coverage ratios for the 8 and 10-ferrocenyl alkanethiol PDSAMs and PAD SAMs (Γ_P/Γ_{PA}) in $HClO_4$ and $NaClO_4$ at 100mVs^{-1}.*

5.5 Discussion

As noted from the results presented in sections 5.1 and 5.2, similar voltammetric behaviour is obtained irrespective of whether the SAM film is formed via PAD deposition or passive deposition. We observe that ΔE_p values increase, E^0 values become more positive, surface coverage values (Γ) increase and peak widths (ΔE_{fwhm}) broaden with increasing electrolyte solution concentration. These results do no alter if the nature of the electrolyte is changed ($HClO_4$ versus $NaClO_4$).

There are two main theories employed for the interpretation of our results. The first was proposed by Smith and White[12] and later refined by Ohtani[13]. These models develop a mathematical analysis of the potential distribution across the SAM film/solution interface. The second theory, proposed by Calvente[14], investigated the influence of a one-dimensional spatial dispersion of redox centers on the voltammetric features of electroactive SAMs, considering briefly the consequences of both ion-permeation and ion pairing formation.

The Smith-White and Ohtani analysis is based on classical electrostatic theory and involves assuming that the electrolyte and SAM can be viewed as dielectric continua. Smith and White analyzed the voltammetric behavior of metal electrodes coated with redox-active SAMs and showed that the broadening of voltammetric waves and shifts of their apparent formal potentials can be explained if the potential drop within the SAM is taken into account.
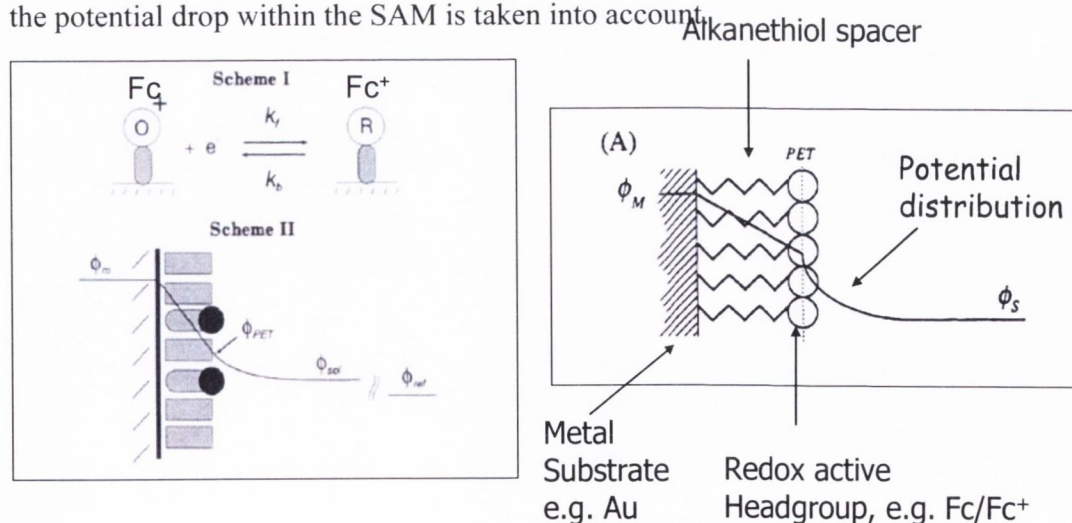
Figure 5.23: *Schematic drawing of irreversibly adsorbed SAMs in contact with an electrolyte solution. The interfacial potential profile (solid line) is linear across the dielectric region between the metal and the PET. The potential profile in the solution phase is non linear. Reproduced from reference 12.*

Only a fraction of the total interfacial drop occurs (φ_m-φ_s) occurs between the electrode and the plane of electron transfer (PET). The surface concentrations of Fc and Fc^+ will be governed by an equilibrium electrode potential (assuming that the Fc/Fc^+ reaction is Nernstian) that is a function of the electrostatic potential at the PET (φ_{PET}). In turn this potential will be a function of the molecular structure of the film and any parameter of the electrochemical cell that effects the potential distribution. e.g. dielectric constant of the SAM, surface concentration of electroactive adsorbate, electrolyte concentration.

Also the electrostatic charge of the redox couple will vary during the voltammetric sweep and therefore, φ_{PET} will be a function of oxidation state. Consequently the driving force for ET will vary throughout the voltammetric experiment. This complication has not been considered in simple approaches to understanding SAM voltammetry.
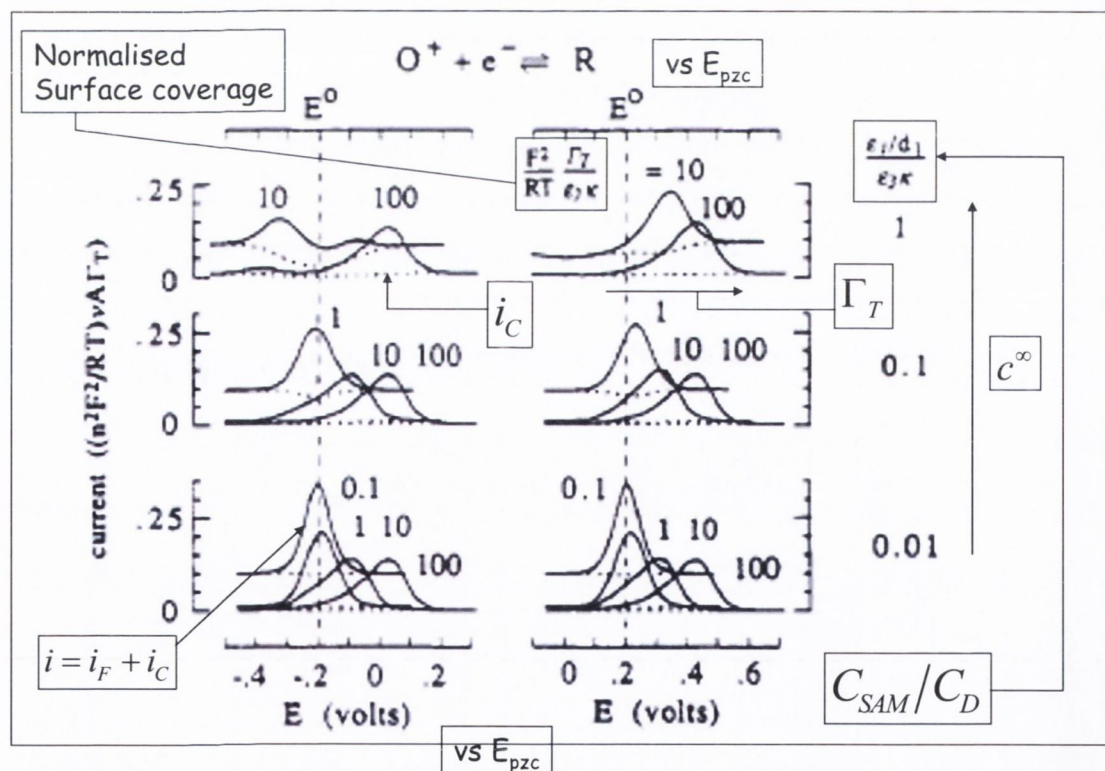
Figure 5.24: *Voltammetric behaviour for an electroactive film which undergoes the reaction $O^+ + e^- = R$. The six sets of voltammograms are arranged in two columns and three rows. The columns correspond to values of $E^0 = \pm0.2$ V (indicated by the vertical dashed lines). The rows correspond to C_{SAM}/C_D. The solid lines (-) correspond to the total voltammetric current (both Faradaic and charging components). The dashed lines (- - -) correspond to the charging current Both E and E^0 are reported with respect to E_{pzc}. Values of T= 298K and z=1 were used for each voltammogram. Reproduced from reference 12.*

The diagram presented in figure 5.24 illustrates results calculated from the Smith and White model. Qualitatively the latter voltammograms show behaviour similar to that observed experimentally i.e. peak potential shifts, peak widths vary and peak heights vary with changes in electrolyte concentration. Specifically, we note that if the electrolyte concentration increases the peaks are shifted in a positive direction, the current is reduced and the shape of the peak changes (broadened). These results are all similar to those observed in the work carried out for all n-ferrocenyl alkanethiols as illustrated in figure 5.1 and figure 5.2.

Ohtani made further refinements of the theoretical treatments of Smith and White in terms of formation of ion pairs and triple ions between the redox-active SAM and electrolyte ions[13]. The fact that Fc/Fc^+ transition is accompanied by ion transfer and pairing can be readily confirmed via EQCM analysis. The formation of an ion pair causes an increase in the mass of the monolayer.
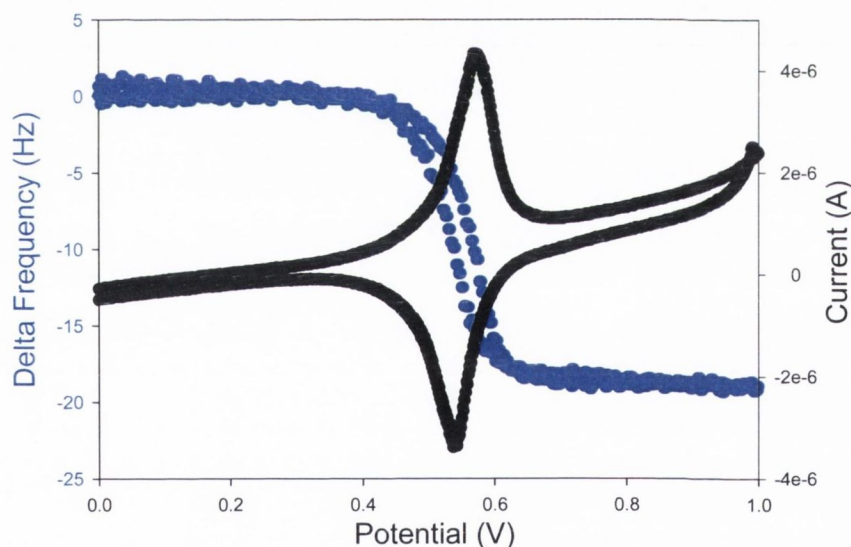
Figure 5.25: *CV (dark line) and frequency change (blue line) corresponding to the oxidation of the 12-ferrocenyl alkanethiol SAM. The ferrocene moiety is oxidised to ferricinium and there is subsequent formation of an ion pair at the surface of the SAM. Reproduced from reference 15.*

Figure 5.25 illustrates the typical EQCM recorded for a 12-ferrocenyl alkanethiol SAM as carried out by Michael Kinsella[15]. An increase in the mass loading on the surface of a quartz crystal corresponds to a damping in its resonance frequency. The formation of an ion pair at the SAM/solution interface will cause such a mass increase

and a consequent damping in resonant frequency. Michael Kinsella's work showed that ion pairing between electrolyte counter ions and oxidised ferrocene molecules occurs and that during oxidation a monolayer of anions is present at the SAM/solution interface. He also noted that during the reduction process the corresponding decrease in the mass change of the SAM is readily observed. This corresponds to the ferricinium cation returning to the neutral ferrocene and the ClO_4^- anions returning to solution.

Strong interaction between surface bound
cations and solution phase counterions.
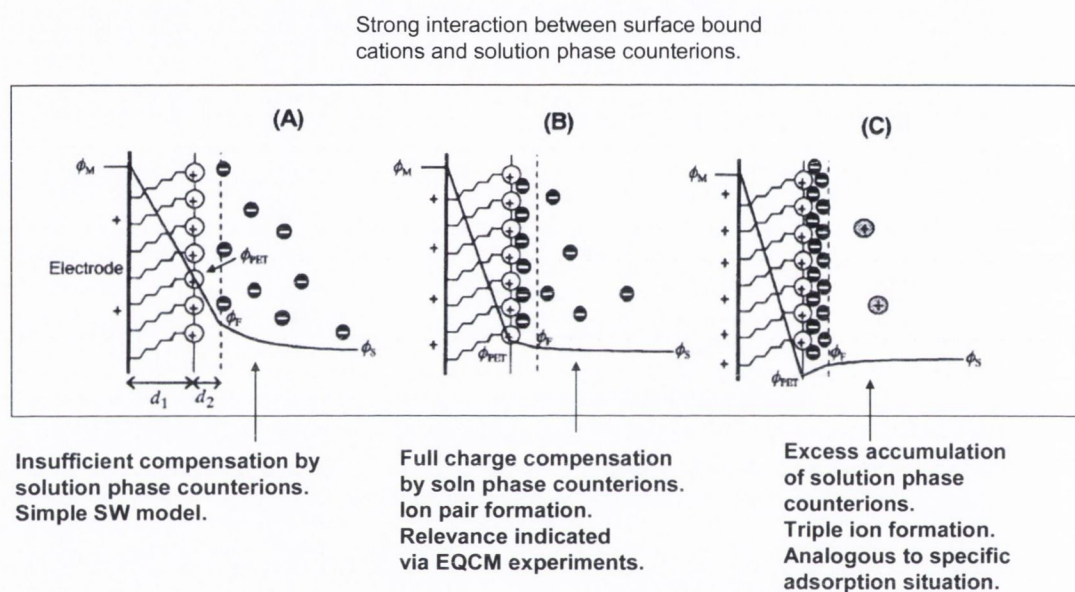
Figure 5.26: *Schematic illustration of potential distributions across solution/SAM/electrode substrate interface. The zig-zag line indicates a dielectric film like an alkyl chain of SAM, and the signs (+, -) denote charges of the electrode substrate surface, surface-confined species, and electrolyte ions: (A) for insufficient compensation of surface-confined positive charges with electrolyte anions; (B) for full neutralization; (C) for excessive accumulation of electrolyte anions. Reproduced from reference 13.*

We contend that the shape of the CV response will reflect the degree of charge compensation between oxidised Fc^+ sites and solution phase counterions affected via ion pair formation. The degree of the latter will in turn affect the potential distribution at the interface. Quantitative calculations have been performed by Ohtani. In the present discussion we provide a qualitative and largely illustrative overview of this work.

Figure 5.26 (A) presents a potential distribution profile in which insufficient charge compensation between Fc^+ and the electrolyte, ClO_4^-, is assumed for surface-

confined species. This model is similar to that employed in the original work by Smith and White; however, there is one marked difference in the point that the inner and outer Helmholtz planes are introduced in this model as was done by Fawcett for refinement of the treatments by Smith and White.

A potential distribution profile as shown in Figure 5.26 (B) is valid if the surface-confined cationic species (ferrocinium) interact strongly with the electrolyte counteranions. The potential drop between the electrode substrate and the solution bulk is almost concentrated in the SAM. Here there is complete charge compensation between Fc^+ and the electrolyte, ClO_4^-.

If the surface-confined cationic species are excessively compensated by the solution phase counterions the potential drop in the SAM is more increased, as shown in Figure 5.26 (C), which is also valid for metal electrodes having specific adsorption of electrolyte anions. As a result we get triple-ion formation. This scenario might be expected when the ClO_4^- concentration is high.

On analysis of the above picture one should expect a transition from case A through to case C as $[ClO_4^-]$ increases. If the changes seen in the potential distributions occur in the redox reactions of the surface-confined redox species the shape of voltammograms (ΔE_{fwhm}) will be changed, depending on the degree of interaction between the electroactive moieties of the SAM and the electrolyte ions. Figure 5.27 below is shown to aid in the interpretation of this feature.
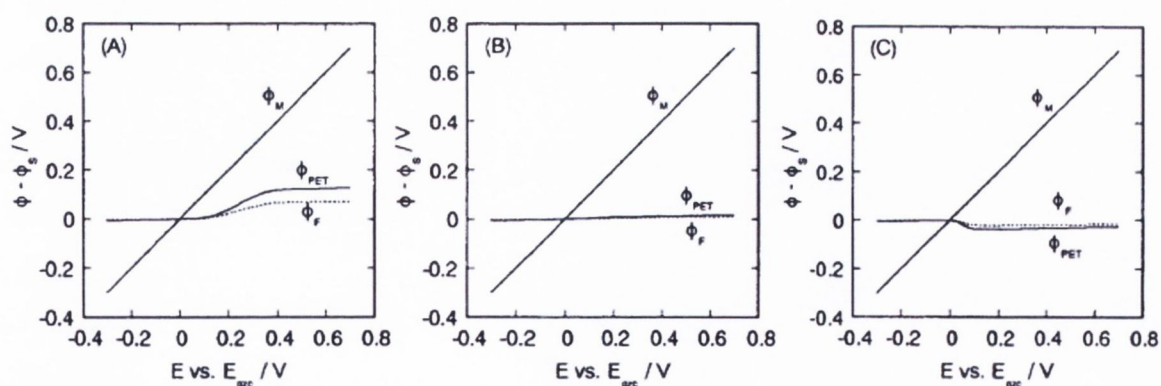
**Figure 5.27:** *Shows the electrostatic potentials of φ_M, φ_{PET}, and φ_F (vs φ_s) as a function of applied electrode potentials E (vs E_{pzc}) for conditions seen in figure 5.25. Reproduced from reference 13.*

At low concentrations, if the positive charges at the PET are insufficiently compensated, the value of φ_M-φ_{PET}, which determines the equilibrium state of surface-confined redox species is smaller than the applied electrode potential for E-E_{pzc}, where oxidation of the surface-confined redox species takes place, as shown in figure 5.25 (A). Then, an excessive polarization is necessary to complete the oxidation, resulting in enlargement of the width of the voltammetric wave (ΔE_{fwhm}> 90 mV). On increasing the concentration, positive charges generated at the PET will be almost neutralized by the ion pair formation, the magnitude of φ_M-φ_{PET} is close to the applied electrode potential (E - Epzc). Then, the shape of the voltammogram is almost the same as that of the ideal Nernstian voltammogram (ΔE_{fwhm} ≈ 90 mV), seen in figure 5.26 (B). Excess accumulation of the solution phase counterions results in the formation of triple ions. making the value of φ_M-φ_{PET} larger than the applied electrode potential as shown in Figure 5.26 (C). Therefore, the oxidation is accomplished with small polarization, resulting in decrease in the peak width of voltammetric waves from 90.6 mV to a lesser value. From section 5.3.2.4 our results are shown to follow a similar pattern for all n-ferrocenyl alkanethiol SAMs in both $HClO_4$ and $NaClO_4$ which is seen in figure 5.12. From this it is observed that the ΔE_{fwhm} values are greater than 90 mV at low concentrations and values decrease as the concentration increases. This result is seen for both self-assembly methods employed in the study.

Similarly, the peak potential (E^0) will alter if the changes seen in the potential distributions shown in figure 5.26 (A) occur in the redox reactions of the surface-confined redox species. As the concentration of the $HClO_4^-$ increases the E^0 values will become less positive. The highest E^0 value will occur for when there is insufficient compensation therefore excessive polarisation is required to complete the oxidation process. As the concentration of electrolyte increases, less polarisation is required for oxidation and E^0 values decrease. Looking at figure 5.9, it is observed that for the 8, 10 and 12-ferrocenyl alkanethiol SAMs in both $HClO_4$ and $NaClO_4$ electrolytes the E^0 values which are most positive at low concentrations become less and less positive on increasing the concentration. This result is seen for both self-assembly methods employed in the study.

On the basis of this result, the difference in peak potentials (ΔE_p) will also vary. At low concentrations excess polarisation is required for oxidation therefore there will also be an excess required for the reduction process and ΔE_p will be greater than 59 mV. On increasing the concentration there is less polarisation required to complete both oxidation and reduction, therefore, the ΔE_p will be closer to 59 mV. At the highest concentrations the least amount of polarisation will be required and the values will be less that 59 mV. This result is seen for both self-assembly methods employed in the study.

The second theory as described by Calvente, explored the electrochemical consequences of a discrete spatial distribution of redox centers by investigating the voltammetric response of electroactive SAMs[14]. Electrostatic modeling of the interfacial potential distribution by the aforementioned theoretical models (Smith-White and Ohtani) usually assumes that the redox centers are all located in the same plane at a given distance from the electrode surface.
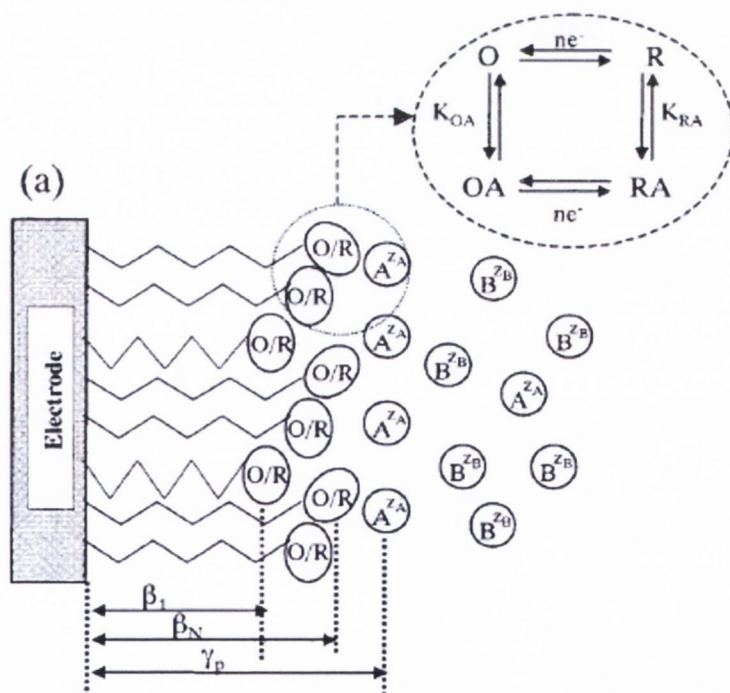
Figure 5.28: *Schematic representation of an electroactive self-assembled monolayer with spatial dispersion of the redox centers, which are located between two planes at distances β_1 and β_N from the electrode surface. Each redox center may undergo ion-pair formation with dissolved counterions, whose distance of closest approach to the electrode is γ_c. Symbols O and R stand for the oxidized and reduced forms of the redox couple, and A and B for counterions and co-ions in solution, respectively. Reproduced from reference 14.*

In this approach it was assumed that a single PET did not occur, rather one had a distribution of distances over which the Fc/Fc^+ electron transfer reaction operated. Again the analysis was based on classical electrostatic double layer theory and effectively was an extension of the Smith-White and Ohtani models. In chapter 6 we will see deviation from first order behaviour in the potential step chronoamperometry of the SAMs. This deviation is caused by the Gaussian spatial dispersion or by the potential drop within the SAM providing further evidence supporting these models.

Figure 5.28 illustrates the main qualitative features of the model for an electroactive self-assembled monolayer with spatial dispersion of the redox centers. All redox centers are assumed to be confined within a thin layer, which is delimited by two planes located at distances β_1 (inner redox plane) and β_N (outer redox plane) from the electrode surface.

As seen earlier, the φ_M-φ_{PET} potential drop governs the driving force for electron exchange between a redox center and the electrode. In the presence of spatial dispersion, different φ_{PET} potentials will be experienced by those redox planes that are located at different distances from the electrode surface and will change their oxidation state to a different extent at a given φ_M. Under these circumstances, the voltammetric wave will consist of a superposion of distinct electrochemical responses, each one being associated with those redox centers that are located at the same distance from the electrode surface, even when the formal potentials of all redox centers are identical. While real electroactive SAMs exhibit a continious spatial distribution of redox centers, Calvente adopted a discrete distribution. A series of voltammograms to illustrate the effect of a progressive spreading of the redox centers is shown in figure 5.29 (a). Their overall surface concentration was evenly distributed over a variable number of planes $(2< N_{PET}<6)$. Calvente observed that the increase in the redox spreading lead to a broadening of the voltammetric wave and the appearance of a shoulder at positive potentials. He noted that the spatial dispersion of the redox centers was only partly responsible for the voltammetric broadening. The potential drop across the diffuse layer as proposed by Smith-White constituted a second source for this broadening.
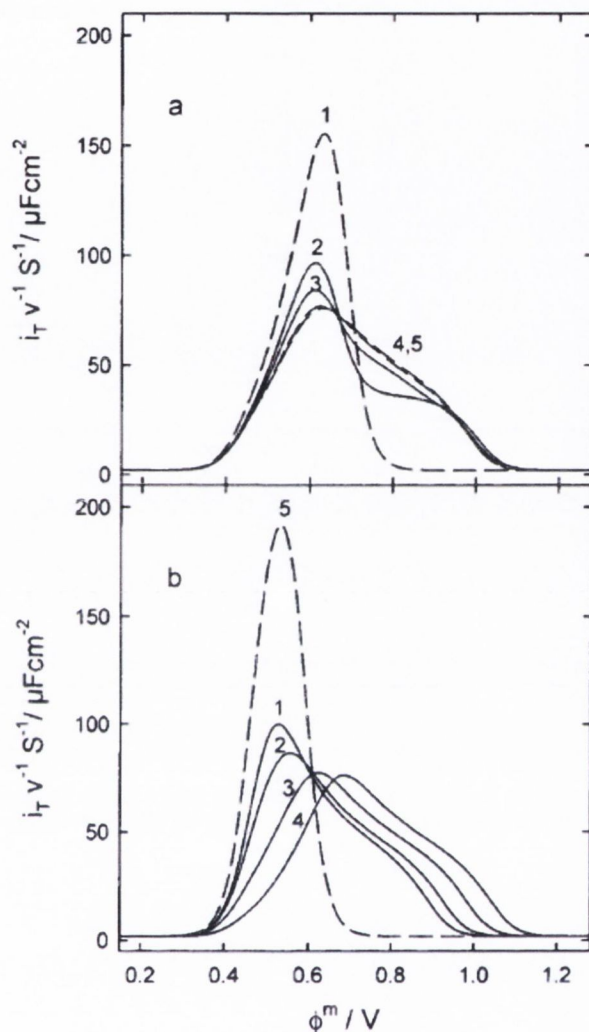
Figure 5.29: *(a) Influence of the linear density of redox planes on the voltammetric features: (1) $N_{PET} = 1$, $\beta_1 = 1.50$ nm; (2) $N_{PET} + 2$, $\beta_1 = 1.45$ nm, $\beta_2 = 1.50$ nm; (3) $N_{PET} = 3$, $\beta_1 = 1.45$ nm, $\beta_3 = 1.50$ nm, $\Delta\beta = 25$ pm; (4) $N_{PET} = 6$, $\beta_1 = 1.45$ nm, $\beta_6 = 1.50$ nm, $\Delta\beta = 10$ pm; (5) $N_{PET} = 11$, $\beta_1 = 1.45$ nm, $\beta_{12} = 1.50$ nm, $\Delta\beta = 5$ pm and $c_A^o = c_B^o = 0.1$ M. (b) Influence of the electrolyte concentration: (1) $c_A^o = c_B^o = 5$ M; (2) $c_A^o = c_B^o = 1$ M; (3) $\Delta\beta = 0.1$ M; (4) $c_A^o = c_B^o = 0.01$ M and $N_{PET} = 6$, $\beta_1 = 1.45$ nm, $\beta_6 = 1.50$ nm, $\Delta\beta = 10$ pm; (5) $c_A^o = c_B^o = 5$ M and $N_{PET} = 1$, $\beta_1 = 1.50$ nm. Other parameter values: $\gamma_A = \gamma_B = 1.50$ nm, $C_a = 3$, $C_s = 78.5$, $\Gamma_T = 3 \times 10^{-10}$ mol cm^{-2}, $z_o = +1$, $z_R = 0$, $z_A = -1$, $z_B = +1$, $K_{OA} = K_{RA} = 0$ and $\varphi^o{}_m = 0.5$ V. Reproduced from reference 14.*

To help to disentangle these two contributions, Figure 5.29 (b) the influence of the electrolyte concentration on the same electroactive SAM is illustrated. As the diffuse layer potential drop decreases, and the electrolyte concentration increases, voltammograms shift negatively along the potential axis and become narrower.

However, even in the most concentrated solution (curve 1), where the single plane model predicts a symmetrical voltammogram (curve 5) with a half-height width close to the ideal value (90.6 mV), the presence of redox spreading still leads to a broad and asymmetric wave. Whereas the diffuse layer potential drop causes essentially a wave broadening, redox dispersion can modify the wave shape, producing new voltammetric features, such as the wave shoulders depicted in figure 5.30, which is a blown up version of figure 5.1.
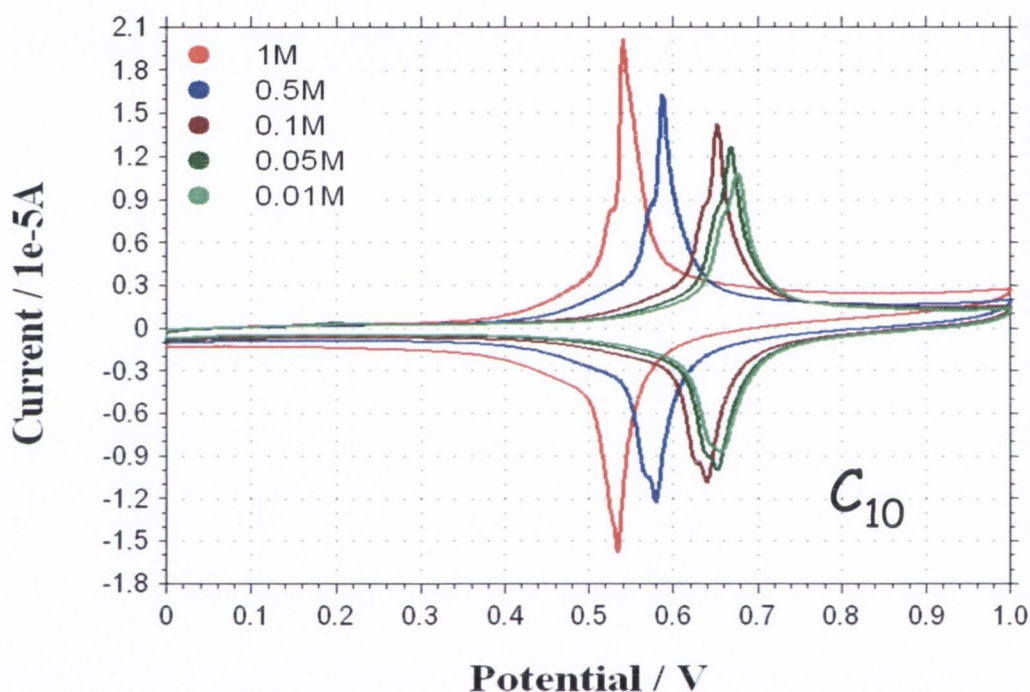
Figure 5.30: *Graph of the current (I_p/A) versus potential (E/mV) for an 10-ferrocenyl alkanethiol PAD SAM in varying concentrations of $HClO_4$ (1M →0.01M) at a scan rate of 100*

If a SAM has defect sites, electroactive centers are likely to be distributed within a range of distances from the electrode surface, and double-layer effects are expected to have a pronounced effect on the voltammetric features, due to the distinct variation of the local potential at each electron transfer plane. Calvente showed that the increase in the redox spreading leads to a broadening of the voltammetric wave. This broadening increases with the overall surface concentration of redox centers for a given relative spreading of the redox population.

References

1. Camillone, N.; Leung, T.Y.B.; Scoles, G., *Surf. Sci.* **1997**, 373, 333.

2. Badia, A.; Ph.D. Thesis, McGill University, **1996**.

3. Lennox, R.B.; Ma, F., *Langmuir*, **2000**, 16, 6188.

4. Finklea, H.O., *Electrochemistry of Organised Monolayers of Thiols and Related Molecules on Electrodes*, in *Electroanalytical Chemistry*, Marcel Dekker, NY, Vol.19, **1996**.

5. Stolberg, L.; Lipkowski, J.; Irish, D. E. *J. Electroanal. Chem.* **1987**, *238*, 333.

6. Sondag-Huethorst, J. A. M.; Fikkink, L. G. J. *Langmuir* **1992**, *8*, 2560.

7. Sondag-Huethorst, J. A. M.; Fikkink, L. G. J. *J. Electroanal. Chem.* **1994**, *367*, 49.

8. Sondag-Huethorst, J. A. M.; Fikkink, L. G. J. *Langmuir* **1995**, *11*, 2237.

9. Sondag-Huethorst, J. A. M.; Fikkink, L. G. J. *Langmuir* **1995**, *11*, 4823.

10. Popenoe, D. D.; Deinhammer, R. S.; Porter, M. D. *Langmuir* **1992**, 8, 2521.

11. Whitesides

12. Smith, C.P.; White, H.S. ***Anal. Chem.*** **1992, *64*,** 2398.

13. Ohtani, M.; Kuwabata, S.; Yoneyama, H. *Anal. Chem.* **1997,** 69,1045.

14. Calvente, J.J.; Andreu, R.; Molero, M.; Lopez-Perez, G.; Dominguez, M. *J. Phys. Chem. B* **2001,** 105, 9557.

15. Kinsella, M. *Ph.D Thesis* Dublin University, Trinity College **2007**.

CHAPTER 6

Magnetic Field Effects on Electroactive Alkanethiol SAMs

6.1 Introduction

In this chapter an investigation on the effect of an applied external magnetic field on electron transfer processes through self assembled monolayers was carried out. This area of work has never before been reported on prior to this. Before 1983, very little was known about the area of magnetoelectrochemistry until Fahidy[1] first reviewed it. Other studies carried out on magnetic fields have pertained to the effects on mass transport. These studies have shown that a magnetic field induces convection in the electrolyte solution, thereby reducing the diffusion layer thickness and hence increasing the rate of mass transport[2].

6.2 Electrochemical Characterization of Ferrocenyl Alkanethiol SAM in 0.5T Magnetic Field using varying orientations of the Magnet

The 12-ferrocenyl alkanethiol monolayer was fabricated via immersing in ethanol solution containing C_{12} ferrocenyl alkanethiol at 1mM concentration on a bare gold electrode for a period of 24 h. Cyclic voltammetry was subsequently carried out on the SAM in a 1 M concentration of $HClO_4$ at various scan rates. Following this, the cell containing the 1 M $HClO_4$ and 12-ferrocenyl alkanethiol SAM was placed in a 0.5 T Halbach bore magnet and the CV's were then repeated in various orientations of the magnet.
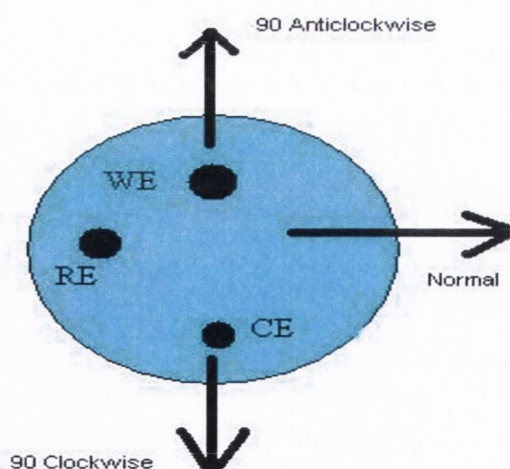
Figure 6.1: *Diagram of the varying orientations of the magnetic field employed in the experiment. The cell set-up is also included where WE denote the working electrode, RE is the reference electrode and CE represents the counter electrode.*

Finally, in order to find out whether the magnetic field effects are irreversible, the magnet was removed and a cyclic voltammogram recorded, again in the normal position. Figure 6.1 shows the varying orientations of the magnetic field employed.

Figure 6.2 shows the recorded CV's with the magnetic field absent and then with 0.5T magnetic field placed at various orientations with respect to monolayer film electrode. The cell was placed in the magnet with the electrode parallel to the field. The magnet was then turned 90° clockwise to the normal, then 90° anticlockwise to the normal. Finally, the monolayer was scanned in the absence of the magnet again. The scan rate for each run was 100 mVs^{-1}.
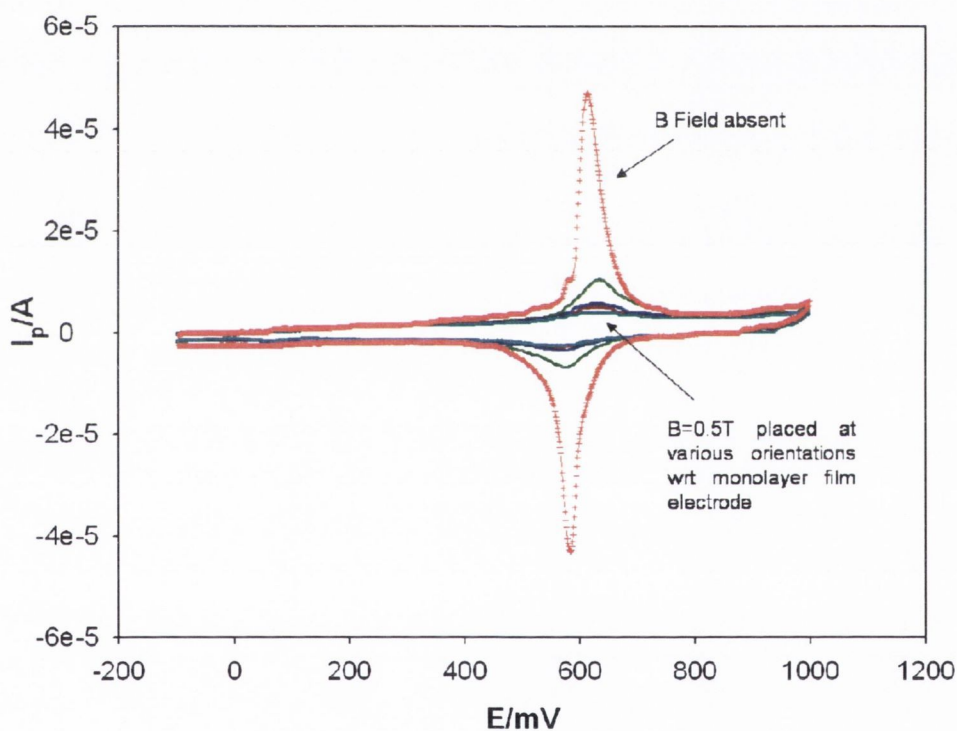
Figure 6.2: *CV of gold coated redox active 1mM C_{12} alkanethiol monolayer in 1M $HClO_4$, following immersion for 24 h in EtOH solution. Potential scanned from -0.2V to 1.2V.In absence of a magnetic field (—) and in the presence of magnetic field (0.5T) with various orientations, normal (—), 90° clockwise (—),90° anticlockwise (—), without magnetic field again (—). Scan rate 100 mVs^{-1} each time.*

There are some interesting conclusions to be made from this data. It can be seen that the presence of an external magnetic field (0.5T) causes a change in the redox activity of the immobilized ferrocene/ferricinium redox couple. These changes can be seen in

table 6.1 below. This effect is attributed to a field induced change in the structure of the monolayer which could decrease the electron tunneling probability between ferrocene moiety and the Au substrate.

Orientation	$E_{p,a}$	$I_{p,a}$	$E_{p,c}$	$I_{p,c}$	E^0
0T No Magnet	614	4.30×10^{-5}	584	-4.27×10^{-5}	599
0.5T Normal	634	7.99×10^{-6}	578	-6.11×10^{-6}	606
0.5T 90° Clockwise	631	3.67×10^{-6}	571	-2.79×10^{-6}	601
0.5T90° Anticlockwise	631	2.88×10^{-6}	558	-2.29×10^{-6}	594.5
0T after field use	634	2.46×10^{-6}	568	-1.8×10^{-6}	601

Table 6.1: *Comparison of the standard potentials (E/mV) and peak currents (i$_p$/A) for the 12-ferrocenyl alkanethiol SAM in 1M HClO$_4$ at the varying orientations used at 100 mVs^{-1}.*

There is however, a significant change in the potentials on applying the magnetic field. The potential for the voltammogram without the magnet is 614 mV, whereas the value obtained on applying a magnetic field is 631 mV. These values can be seen in the table above (table 6.1). Hence, typically a difference of ca. 20 mV in E^0 is observed between a field free and a field present experiment. Shifts in E^0 may reflect either change in interfacial potential distribution at the SAM/solution interface or a change in solvation of the redox active surface group. Both effects may simultaneously operate.

The surface coverage of the monolayer was also calculated as each orientation is applied and the results are shown below.

| Orientation	$\Gamma/10^{-10}$ mol cm^{-2}	Γ_B/Γ_0
0T No Magnet	3.09	1
0.5T Normal	1.32	0.43
0.5T 90° Clockwise	0.75	0.24
0.5T 90° Anticlockwise	0.62	0.19
0T after field use	0.56	0.18

Table 6.2: *Presents the surface coverage values (Γ_{Fc}) of the 24 hr 12-Ferrocenyl alkanethiol SAM in 1M HClO$_4$ at the varying orientations used at 100 mVs^{-1}.*

The surface coverage of the monolayer also decreases as each orientation is applied. From the CV in the absence of the magnetic field a surface coverage of 3.09×10^{-10} mol cm^{-2} is obtained. This value is not similar to the 4.5×10^{-10} surface coverage value obtained by Chidsey. On applying a magnetic field of 0.5 T perpendicular to the working electrode the surface coverage shows a marked decrease to a value of 1.32×10^{-10} mol cm^{-2}. This value equates to a ratio of 0.43 for the ratio of magnetic field surface coverage to zero field surface coverage. From this it clear that the addition of a magnetic field to a SAM monolayer formed after 24 h causes the surface coverage to decrease by over 50 %.

On rotating the magnet 90^0 clockwise to the normal, the surface coverage shows a further decrease to a value of 7.45×10^{-11} mol cm^{-2}. This is equivalent to a ratio of 0.24 when compared to the surface coverage of the zero field. The magnet was then rotated magnet 90^0 anticlockwise to the normal, which saw a further decrease to 6.02×10^{-11} mol cm^{-2} in the surface coverage value. As there is a decrease the ratio would also decrease to a value of 0.19. Finally, the magnet was removed from the solution and the surface coverage was again calculated. The surface coverage was again seen to slightly decrease from the value obtained for the last orientation with a ratio of 0.18 obtained. However, results obtained using an electrochemical quartz crystal microbalance have shown that surface coverage is dependent on time. It is seen that surface coverage decreases as time increases.

From these results it is seen that the redox behaviour of the monolayer is reversibly altered after being subjected to an external magnetic field for a period of time. When the external magnetic field was removed and the voltammetry repeated, the ferrocene peaks that showed on the first voltammetric run do not appear.

This experiment was repeated on a second monolayer immersed for 48 h in ethanol solution containing C_{12} ferrocenylalkane thiol at 1mM concentration on a bare gold electrode to see if a further 24 h immersion would cause any further change in the results. HClO$_4$ was again used in the measurements and the scan rate used was 100 mVs^{-1}. Figure 6.4 below is a representation of the voltammograms recorded.
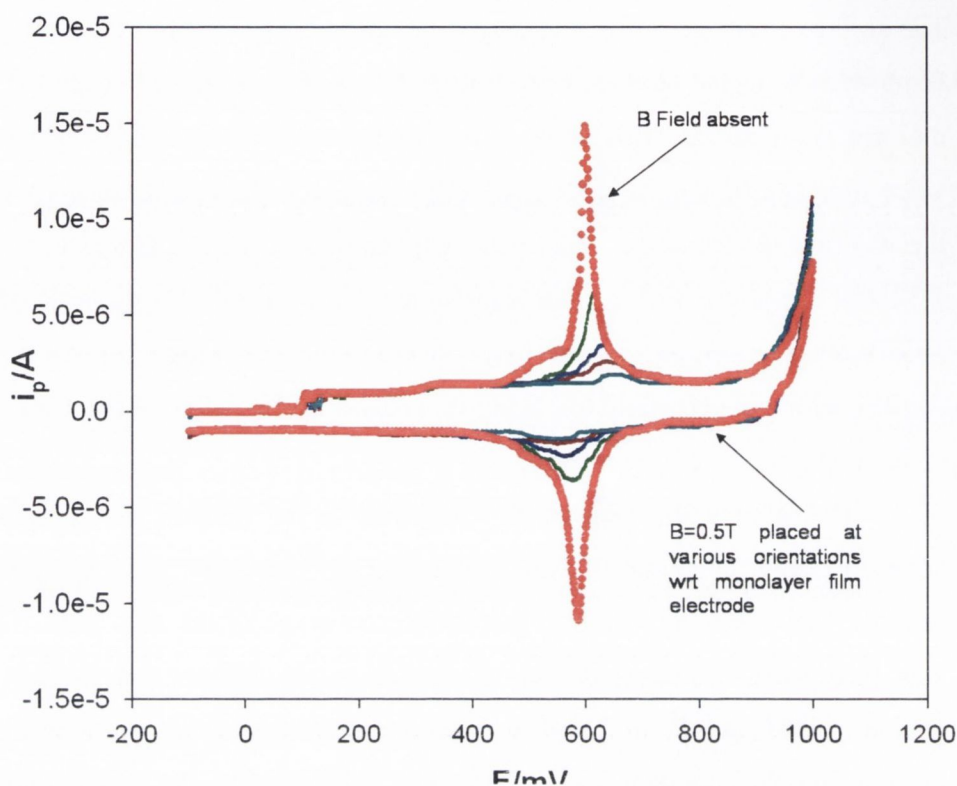
Figure 6.4: *CV of gold coated redox active 1mM C₁₂ alkanethiol monolayer in 1M HClO₄, following immersion for 48 hrs in EtOH solution. Potential scanned from -0.2V to 1.2V.In absence of a magnetic field (——) and in the presence of magnetic field (0.5T) with various orientations, normal (——), 90° clockwise (——),90° anticlockwise(——) , without magnetic field again (——) . Scan rate 100 mVs⁻¹ each time.*

There are both similarities and differences between the 24 h and the 48 h immersion voltammograms. The 48 h monolayer shows the same reduction in current as the 24 h monolayer. The values of these currents are tabulated in table 6.2. The currents also decrease in the same trend as the 24 h immersion.

Orientation	$E_{p,a}$	$I_{p,a}$	$E_{p,a}$	$I_{p,a}$	E^0
0T No Magnet	598	1.34×10^{-5}	587	-1.02×10^{-5}	592.5
0.5T Normal	614	4.69×10^{-6}	578	-3.02×10^{-6}	596
0.5T 90° Clockwise	629	1.95×10^{-6}	565	-1.78×10^{-6}	597
0.5T 90° Anticlockwise	636	1.14×10^{-6}	551	-1.059×10^{-6}	593.5
0T after field use	653	1.05×10^{-6}			

Table 6.3: *Comparison of the standard potentials (E/mV) and peak currents (iₚ/A) for the 12-ferrocenyl alkanethiol SAM in 1M HClO₄ at the varying orientations used at 100 mVs⁻¹.*

Unlike the 24 h immersion, there is a marked change in the potential values for the 48 h immersion. This is seen in the graph in that the peaks representing those for the magnet orientations are not directly under each other, but rather there is a shift. With no magnet present a potential of 598 mV is achieved, however, for the magnetic orientations the peak potentials vary from 614 mV to 653 mV. This range is far greater then the range of potentials in the 24 h immersion. The potentials actually increase with each particular orientation used. These data indicate that for more self-assembled films, the magnetic field and its orientations affects the interfacial properties and salvation state of the SAM to a marked degree.

Orientation	$\Gamma/10^{-10}$ mol cm^{-2}	Γ_B/Γ_0
0T No Magnet	1.63	1
0.5T Normal	0.75	0.46
0.5T 90° Clockwise	0.45	0.28
0.5T 90° Anticlockwise	0.38	0.17
0T after field use	0.13	0.08

Table 6.4: *Presents the surface coverage values (Γ_{Fc}) of the 48 hr 12-Ferrocenyl alkanethiol SAM in 1M HClO$_4$ at the varying orientations used at 100 mVs^{-1}.*

The surface coverage of the monolayer also decreases as each orientation is applied. From the CV in the absence of the magnetic field a surface coverage of 1.63 x10^{-10} mol cm^{-2} is obtained. On applying a magnetic field of 0.5 T perpendicular to the working electrode the surface coverage shows a marked decrease to a value of 7.5 x10^{-11} mol cm^{-2}. These surface coverages are sub-monolayer coverage values which assume cubic close packing. When the ratio of magnetic field surface coverage to zero field surface coverage is calculated, a value of 0.46 is obtained. From this it clear that the addition of a magnetic field to a SAM monolayer formed after 48 h causes the measured surface coverage to decrease by over 50 %.

On rotating the magnet 90^0 clockwise to the normal, the surface coverage shows a further decrease to a value of 4.53 x 10^{-11} mol cm^{-2}. This is equivalent to a ratio of 0.28 when compared to the surface coverage of the zero field. The magnet

was then rotated magnet 90^0 anticlockwise to the normal, which saw a further decrease to 2.77 x 10^{-11} mol cm^{-2} in the surface coverage value. As there is a decrease the ratio would also decrease to a value of 0.17. Finally, the magnet was removed from the solution and the surface coverage was again calculated. The surface coverage was seen to significantly decrease from the value obtained for the last orientation. When compared to the original surface coverage calculated in the zero field a ratio of 0.08 is obtained.

From the results it is clear that an external magnetic field has a similar effect on a 24 h growth SAM and a 48 h growth SAM. On addition of an external magnetic field, the ratio of surface coverages to the zero field coverage decrease.

We propose that the application of a magnetic field cause the alkane chains to become disordered and to possibly cause some of the pendant ferrocene redox sites to become buried in the surrounding alkane chain matrix. Sumner and Creager[4] investigated voltammetric studies on ferrocene moieties that were artificially buried in a surrounding alkane chain matrix. In order to achieve this they formed mixed monolayers comprised of a small percentage of alkanethiol molecules with pendant electroactive ferrocene groups coadsorbed with insulating, CH_3 terminated chains that were much longer. One of the main findings of this work was that when ferrocene groups were buried into the alkane chain matrix the redox potentials at which the oxidation/reduction occurred were shifted to much higher potentials relative to monolayers in which the ferrocene groups were exposed to the electrolyte. This would seem to agree with the results found in this work as seen in table 6.1 and 6.3.

Although it is possible to utilise well established theory to evaluate the electron transfer rate constant from this data, it is more accurate to obtain the latter fundamental parameter from a potential step chronoamperometry measurement, since extraction of kinetic parameters via the CV technique is prone to error from resistive effects.

6.3 Electrochemical Characterization of Ferrocenyl Alkanethiol Self-assembled Monolayers in 0.5T Magnetic Field

6.3.1 12-Ferrocenyl Alkanethiol SAM

The 12-ferrocenyl alkanethiol self-assembled monolayer was formed on gold support electrodes via adsorption from a dilute (1 mM) ethanolic solution of the alkanethiol for 48 h. The electron transfer dynamics across the alkanethiol monolayer were probed using cyclic voltammetry and potential step chronoamperometry using a BAS electrochemical workstation, in a standard three electrode electrochemical cell. Electrochemical experiments were performed in aqueous 1M $HClO_4$ solution at room temperature (293K). A three electrode electrochemical cell was placed in the bore of a permanent magnet with a fixed static field of 0.5T transverse to the bore. The magnetic field was applied parallel to the working electrode surface.
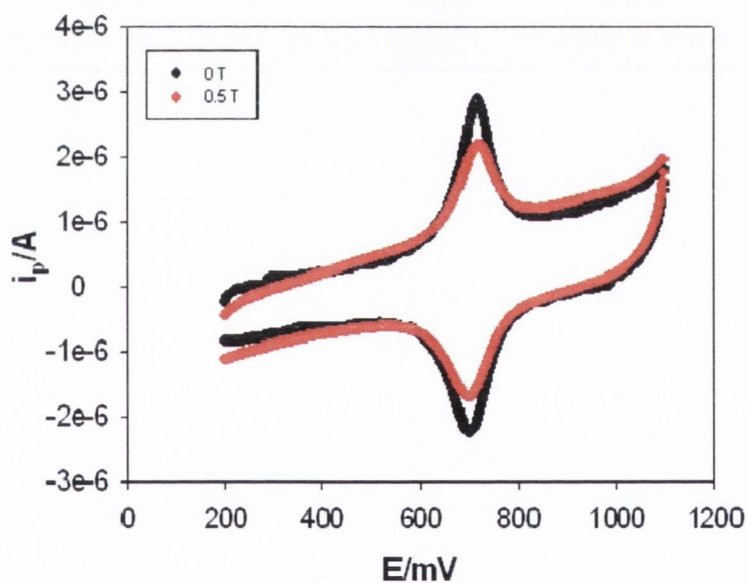

Figure 6.5: *Cyclic voltammetric response recorded for the 12-ferrocenyl alkanethiol self-assembled monolayer both in the presence of and in the absence of an external magnetic field in 1M $HClO_4$. Scan rate 100 mVs^{-1}.*

In figure 6.5 the voltammetric behaviour recorded at a sweep rate of 100 mVs^{-1} for the 12-ferrocenyl alkanethiol SAM in the absence and in the presence of an external magnetic field (B=0.5T) are shown. Redox peaks corresponding to the ferrocene/ferricinium surface redox transition are clearly discerned with E^0 having a

value of 709 mV (vs Ag/AgCl) at slow sweep rates. The latter does not change when an external magnetic field is applied (708 mV); hence the thermodynamics of the surface redox transformation is not field dependant. A significant decrease in surface coverage of attached electroactive ferrocene species was observed in the presence of the magnetic field ($\Gamma = 1.74 \times 10^{-10}$ mol cm^{-2} (B=0T) and $\Gamma = 1.15 \times 10^{-10}$ mol cm^{-2} (B=0.5T)).

Finally the surface coverage of the amount of electroactive ferrocene adsorbed on the surface of the electrode was calculated at each scan rate for both the zero and finite fields and the results are shown in figure 6.6. From figure 6.5 it was earlier seen that the surface coverage of the zero field was larger than the corresponding finite field at 100 mVs^{-1}.

It is clearly visible from the graph that the surface coverage of adsorbed ferrocene is larger in a zero field than in the corresponding finite field for each scan rate. The surface coverage of both the finite field and zero field decrease linearly as scan rate increases from 5 mVs^{-1} to 2000 mVs^{-1}. As the scan rate increases from 2000 mVs^{-1} the decrease in surface coverage is not as marked.
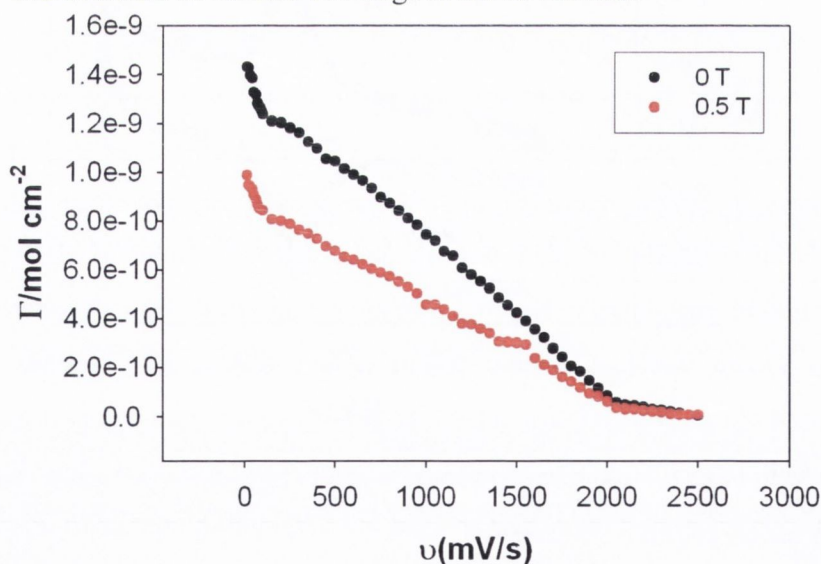
Figure 6.6: *Variation of surface coverage (Γ/mol cm^{-2}) with sweep rate recorded for a 12-ferrocenyl alkanethiol SAM film in 1 M HClO$_4$ with experimental sweep in the absence (black) and in the presence (red) of a static 0.5T magnetic field.*

In figure 6.7 (a) and figure 6.7 (b), the variation of the oxidative and reductive peak potentials as a function of sweep rate, both in zero and finite magnetic field is outlined. If the surface redox transformations i.e. oxidative ferrocene/ferricinium and reductive ferricinium/ferrocene) were Nernstian then the peak potentials should be invariant with sweep rate.

It is clear from figure 6.7 (b) that this pertains only when the experimental timescale is long and at low sweep rates. The peak potentials increase significantly with increasing sweep rate when the latter exceeds ca. 100 mVs^{-1}, thus signifying , according to the Laviron analysis[5], that the surface redox transformation is quasireversible i.e. peak potentials are proportional to the natural logarithm of υ (ln υ).
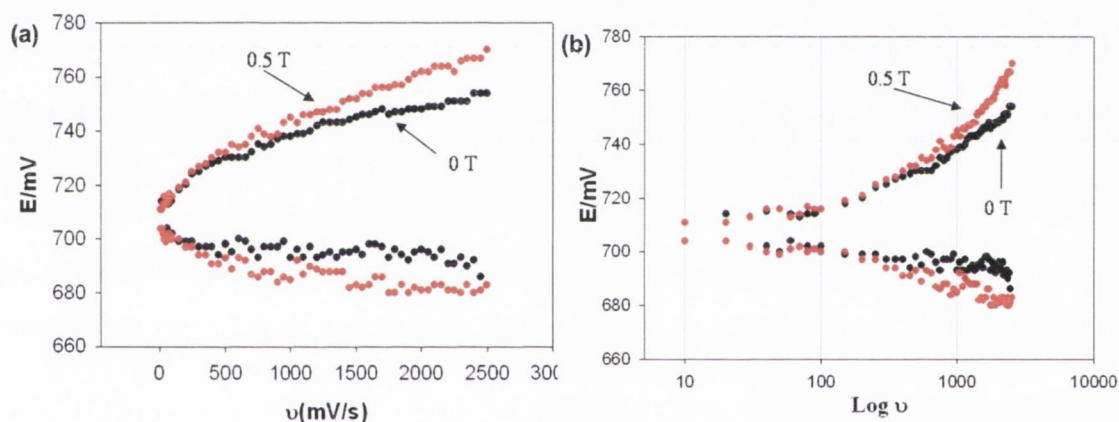
Figure 6.7: *Variation of oxidation and reduction voltammetric peak potentials recorded for a 12-ferrocenyl alkanethiol SAM film in 0.1M HClO$_4$ with experimental sweep rate in the absence (black) and in the presence (red) of a static 0.5T magnetic field. (a) graph of υ (mVs^{-1}) against E/mV (b) graph of Log υ against E/mV.*

From figure 6.7 (a) the surface redox transformation in the finite field is more irreversible than that in the zero field as the difference between the $E_{p, ox}$ and $E_{p,red}$ values in the finite field are larger than those in the zero field. The general trend in peak potential variation (ΔE_p/mV) is the same independent of magnetic field and the results are presented in figure 6.7. This result shows that the ΔE_p values of the finite field are larger than those of the zero field. Hence the potential drop across the SAM is affected by the presence of an external magnetic field (Smith-White model).
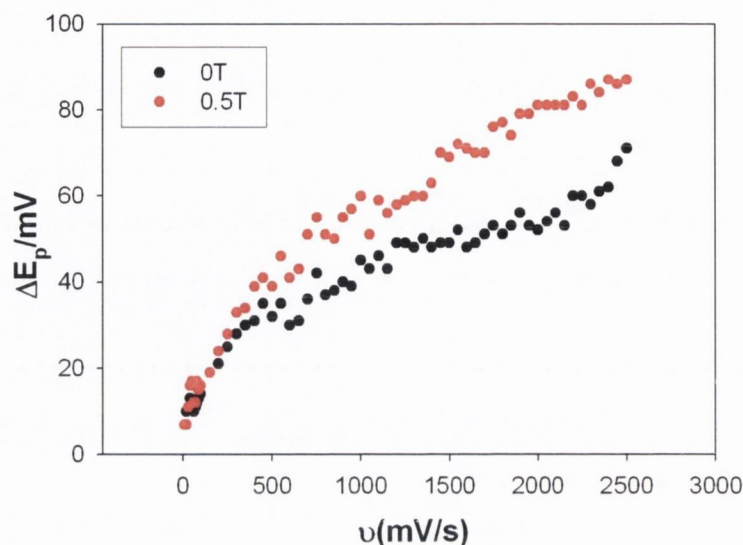
Figure 6.8: *Variation of voltammetric peak separation (ΔE$_p$/mV) with sweep rate recorded for a 12-ferrocenyl alkanethiol SAM film in 0.1 M HClO$_4$ with experimental sweep in the absence (black) and in the presence (red) of a static 0.5T magnetic field.*

The fact that the difference in voltammetric peak potential ΔE_p is non zero and varies with increasing scan rate both under zero and finite magnetic fields conditions signifies that neighbouring anchored ferrocene groups interact electrostatically.

By employing Laviron's analysis the standard rate constant for the surface reaction can be found. Laviron found that for a surface bound electrode reaction, the relationship between peak potential and scan rate is given by:

$$E_{pc} = E^0 + \frac{RT}{\alpha nF}\ln\frac{RTk^0}{\alpha nF} - \frac{RT}{\alpha nF}\ln v, \tag{6.1}$$

$$E_{pa} = E^0 + \frac{RT}{(1-\alpha)nF}\ln\frac{RTk^0}{(1-\alpha)nF} + \frac{RT}{(1-\alpha)nF}\ln v \tag{6.2}$$

where α is the electron transfer coefficient, k^0 is the standard rate constant for the surface reaction and E^0 is the standard redox potential. This potential is simply the midpoint of the cathodic and anodic peak potentials at low scan rates, which for this system was found to be 710 mV for both the finite field and zero field. If the two above expressions are combined we obtain

$$\Delta E_p = \frac{RT}{(1-\alpha)\alpha F}\left[\alpha\ln(1-\alpha) + (1-\alpha)\ln\alpha - \ln\left(\frac{RT}{F}\right) - \ln k^0\right] + \frac{RT}{(1-\alpha)\alpha nF}\ln v \tag{6.3}$$

Peak separations were plotted against natural logarithm of υ for high scan rates (at which the redox process exhibits quasi-reversible behaviour), as shown in figure 6.9. The slope of the graph was found to be 15.5 mV for the zero field and 26.7 mV for the finite field. This value along with the intercept for each plot was used to calculate a rate constant.
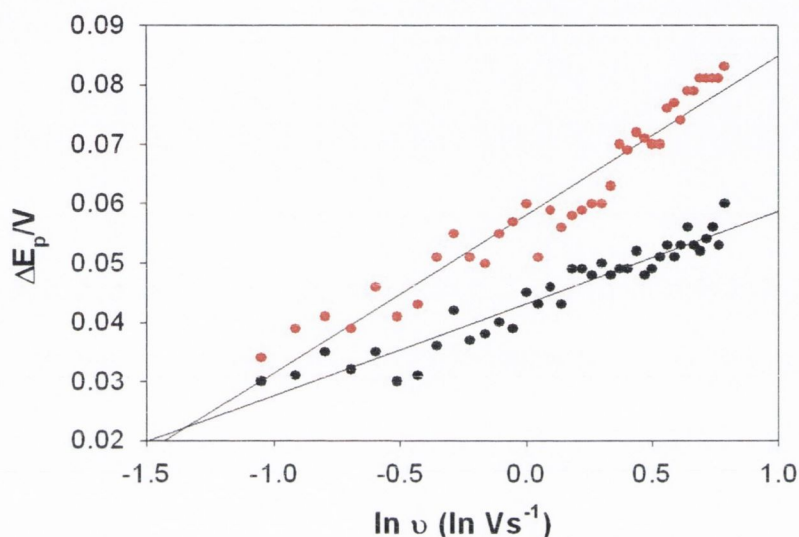

Figure 6.9: *Plot of peak separation against the natural logarithm of scan rate.*

However, we were unable to calculate the rate constant for the 12-ferrocenyl alkanethiol as an imaginary number was calculated for α. The reason for this is that the electron transfer process is quite fast (ΔE_p is only 0.09 V even at 2.2 Vs^{-1}). As a result, the Laviron approach, which is valid only when $\Delta E_p > 200/n$ mV, is not recommended for this system. Instead we suggest the use of potential step chronoamperometry to calculate rate constants (see section 6.3). In order for the Laviron method to provide a realistic view of such a kinetically facile reception, considerably higher scan rates must be employed. However, for this system, peaks are not discernable at these high scan rates and also film resistance effects become more important when the scan rate is larger.
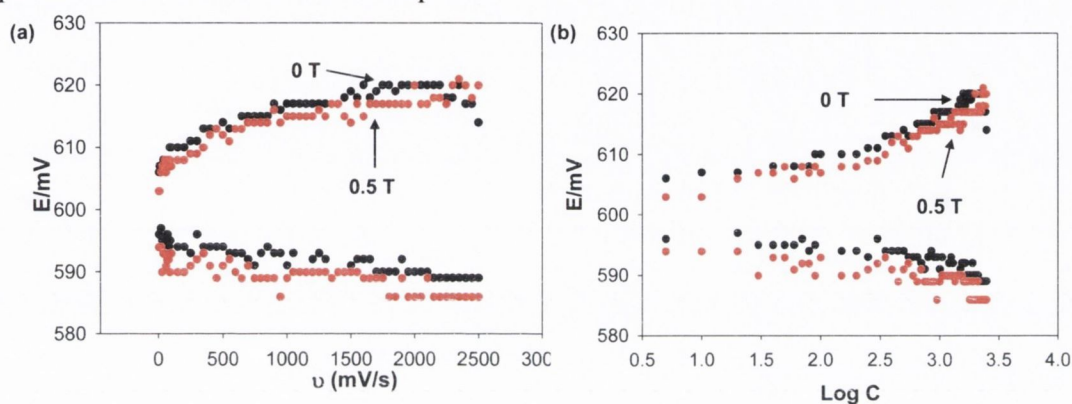
6.3.2 10-Ferrocenyl Alkanethiol SAM

The examination of magnetic field effects on the redox behaviour of a surface immobilized SAM film was repeated for the 10-ferrocenyl alkanethiol self-assembled monolayer. The latter was grown in the same manner as the 12-ferrocenyl alkanethiol. Figure 6.10 presents the voltammetric behaviour recorded at a sweep rate of 100 mVs^{-1} for the 10-ferrocenyl alkanethiol SAM in the absence and in the presence of an external magnetic field (B=0.5T).
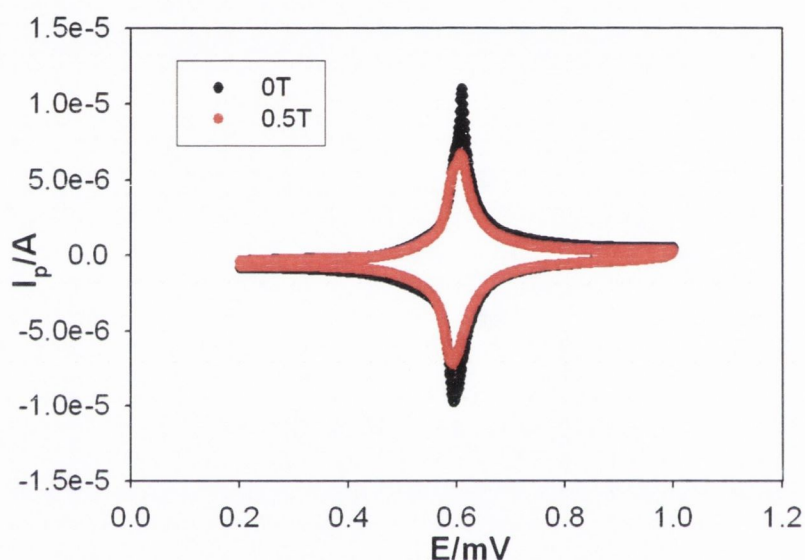
Figure 6.10: *Cyclic voltammetric response recorded for the 10-ferrocenyl alkanethiol self-assembled monolayer both in the presence of and in the absence of an external magnetic field in 1M HClO$_4$. Scan rate 100 mVs^{-1}.*

Redox peaks corresponding to the ferrocene/ferricinium surface redox transition are clearly discerned with E^0 having a value of 601.5 mV (vs Ag/AgCl) at slow sweep rates. The latter does not change when an external magnetic field is applied (600 mV); hence the thermodynamics of the surface redox transformation is not field dependant for the 10-ferrocenyl alkanethiol. The E^0 values of the 10-ferrocenyl alkanethiol are lower than those of the 12-ferrocenyl alkanethiol by around 100 mV. A slight decrease in surface coverage of attached electroactive ferrocene species was observed in the presence of the magnetic field (Γ = 2.049 nmol cm^{-2} (B=0T) and Γ= 1.686 nmol cm^{-2} (B=0.5T)).

The variation of the oxidative and reductive peak potentials as a function of sweep rate and the logarithm of scan rate, both in zero and finite magnetic field are shown in figure 6.11 (a) and figure 6.11 (b). Again the oxidative ferrocene/ferricinium and reductive ferricinium/ferrocene should show Nernstian behaviour if the peak potentials are invariant with sweep rate.

Figure 6.11: *Variation of oxidation and reduction voltammetric peak potentials recorded for a 10-ferrocenyl alkanethiol SAM film in 1M HClO₄ with experimental sweep rate in the absence (black) and in the presence (red) of a static 0.5T magnetic field. (a) graph of υ (mVs⁻¹) against E/mV (b) graph of Log υ against E/mV.*

From figure 6.11 (b) it is obvious that the oxidative and reductive peak potentials are invariant at low scan rates and thereby Nernstian behaviour i.e. reversible. However, on increasing the scan rate to larger values (> 100 mVs⁻¹) the peak potentials increase significantly with increasing sweep rate. From this it is concluded, according to the Laviron analysis[49], that the surface redox transformation is quasireversible. From figure 6.11 (a) the surface redox transformation in the finite and zero fields have the same irreversiblility as the difference between the $E_{p, ox}$ and $E_{p,red}$ values in the finite field and zero field are the same. This result is dissimilar to that obtained for the 12-ferrocenyl alkanethiol SAM.

For the difference between the $E_{p, ox}$ and $E_{p,red}$ values, it is seen that the ΔE_p values in the finite field are very similar to those in the zero field.
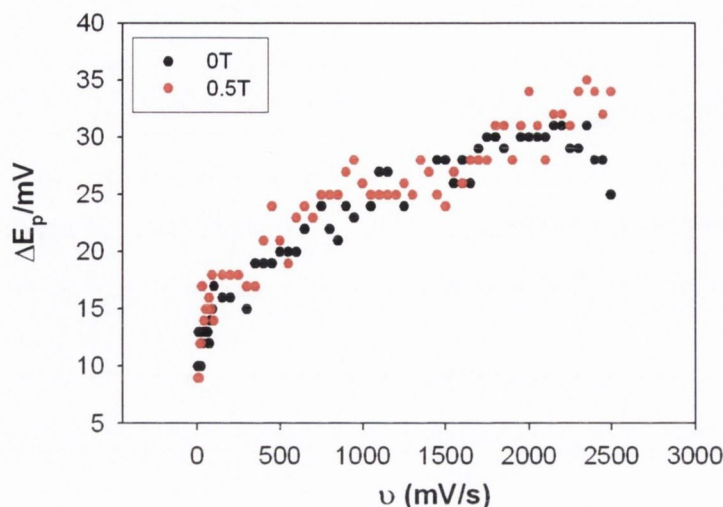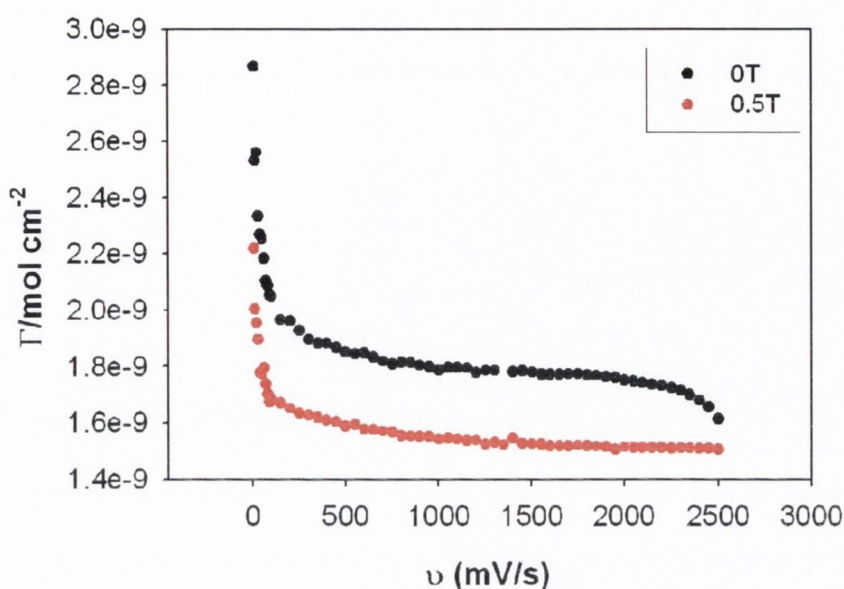
Figure 6.12: *Variation of voltammetric peak separation ($\Delta E_p/mV$) with sweep rate recorded for a 10-ferrocenyl alkanethiol SAM film in 1 M HClO$_4$ with experimental sweep in the absence (black) and in the presence (red) of a static 0.5T magnetic field.*

As also found for the 12-ferrocenyl alkanethiol the difference in voltammetric peak potential ΔE_p is non zero and varies with increasing scan rate both under zero and finite magnetic fields conditions for the 10-ferrocenyl alkanethiol SAM. Again this signifies that neighbouring anchored ferrocene groups interact electrostatically. One difference from the 10 and 12-ferrocenyl alkanethiols is that the ΔE_p values are lower for the 10-ferrocenyl alkanethiol SAM. The finite and zero field values of the 10-ferrocenyl alkanethiol SAM are also very similar to each other.

The surface coverage of the 10-ferrocenyl alkanethiol SAM at each scan rate was calculated for both the zero and finite fields and the results are shown in figure 6.13. It was earlier seen that the surface coverage of the zero field was larger than the corresponding finite field at 100 mVs^{-1}. From the graph it is seen that the surface coverage of adsorbed ferrocene is larger in a zero field than in the corresponding finite field for each scan rate. The surface coverage of both the finite field and zero field decrease at a fast rate at very low scan rates (5 mVs^{-1} to 100 mVs^{-1}). However, as the scan rates increase to higher values the surface coverage decrease becomes less marked. This result is in total opposition to that observed for the 12-ferrocenyl alkanethiol.

Figure 6.13: *Variation of surface coverage (Γ/mol cm⁻²) with sweep rate recorded for a 10-ferrocenyl alkanethiol SAM film in 1 M HClO₄ with experimental sweep in the absence (black) and in the presence (red) of a static 0.5T magnetic field.*

6.3.3 8-Ferrocenyl Alkanethiol SAM

Finally, the experiment was repeated for the 8-ferrocenyl alkanethiol self-assembled monolayer. Again the 8-ferrocenyl alkanethiol monolayer was grown in the same manner as the 10 and 12-ferrocenyl alkanethiol. Figure 6.14 presents the voltammetric behaviour recorded at a sweep rate of 100 mVs⁻¹ for the 8-ferrocenyl alkanethiol SAM in the absence and in the presence of an external magnetic field (B=0.5T).

Redox peaks corresponding to the ferrocene/ferricinium surface redox transition are clearly discerned with E^0 having a value of 601 mV (vs Ag/AgCl) at slow sweep rates. The latter does not change when an external magnetic field is applied (598 mV); hence the thermodynamics of the surface redox transformation is not field dependant for the 10-ferrocenyl alkanethiol. The E^0 values of the 8-ferrocenyl alkanethiol are lower than those of the 12-ferrocenyl alkanethiol by around 100 mV but very similar to the 10-ferrocenyl alkanethiol SAM. A slight decrease in surface coverage of attached electroactive ferrocene species was observed in the presence of the magnetic field (Γ = 3.28 nmol cm⁻² (B=0T) and Γ= 3.04 nmol cm⁻² (B=0.5T)).
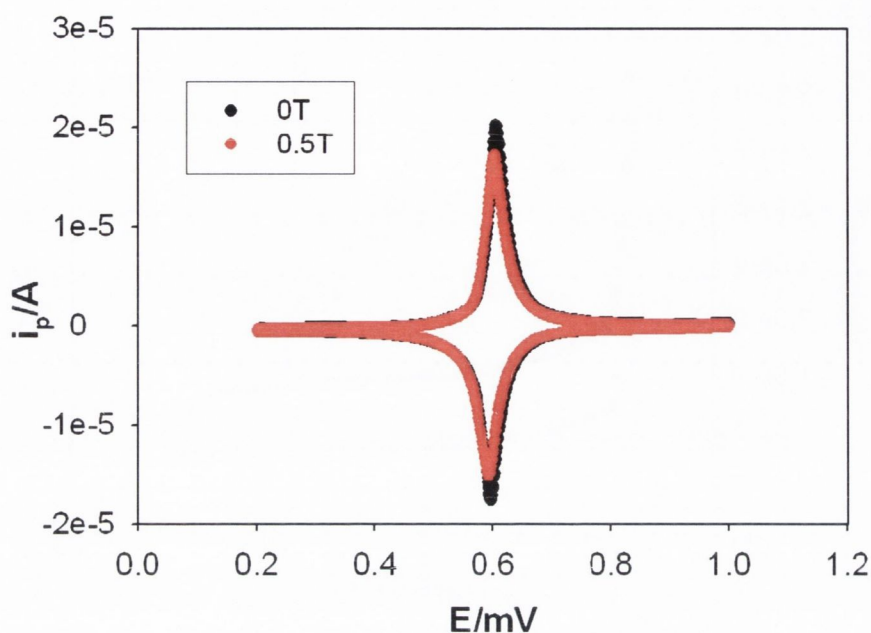
Figure 6.14: *Cyclic voltammetric response recorded for the 8-ferrocenyl alkanethiol self-assembled monolayer both in the presence of and in the absence of an external magnetic field in 1M HClO₄. Scan rate 100 mVs⁻¹.*

Similarly to the 10 and 12-ferrocenyl alkanethiols, the variation of the oxidative and reductive peak potentials as a function of sweep rate and the logarithm of scan rate, both in zero and finite magnetic field are shown in figure 6.15 (a) and figure 6.15 (b). Again the oxidative ferrocene/ferricinium and reductive ferricinium/ferrocene should show Nernstian behaviour if the peak potentials are invariant with sweep rate.

Similarly to the 10 and 12-ferrocenyl alkanethiol SAMs the difference in voltammetric peak potential ΔE_p is non zero and varies with increasing scan rate both under zero and finite magnetic fields conditions for the 8-ferrocenyl alkanethiol SAM (figure 6.15).

From figure 6.15 (b) it is obvious that the oxidative and reductive peak potentials are invariant at low scan rates and thereby Nernstian behaviour i.e. reversible. However, on increasing the scan rate to larger values (> 100 mVs⁻¹) the peak potentials increase significantly with increasing sweep rate. From this it is concluded, according to the Laviron analysis[49], that the surface redox transformation is quasireversible. From figure 6.15 (a) the surface redox transformation in the zero field is more irreversible than that in the finite field as the difference between the $E_{p,ox}$

and $E_{p,red}$ values in the zero field are slightly larger than those in the finite field. This result differs to those obtained for the 10 and 12-ferrocenyl alkanethiol SAMs.
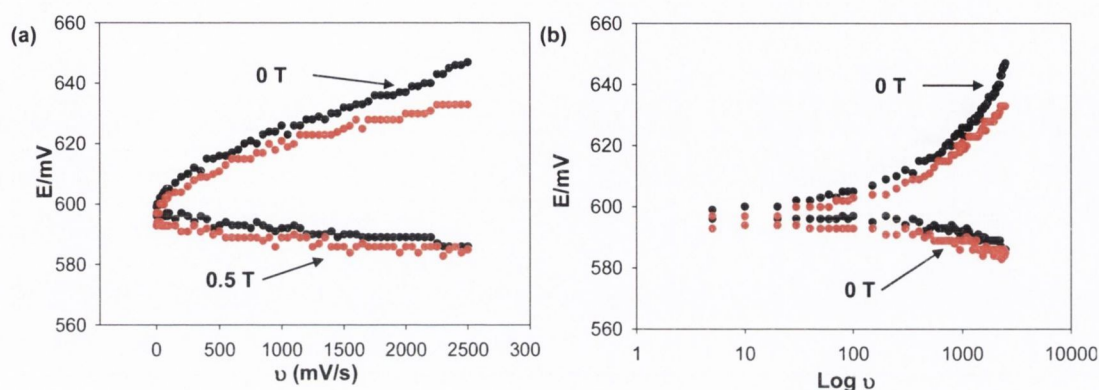
Figure 6.15: *Variation of oxidation and reduction voltammetric peak potentials recorded for a 8-ferrocenyl alkanethiol SAM film in 1M HClO₄ with experimental sweep rate in the absence (black) and in the presence (red) of a static 0.5T magnetic field. (a) graph of υ (mVs⁻¹) against E/mV (b) graph of Log υ against E/mV.*

Again this signifies that neighbouring anchored ferrocene groups interact electrostatically. One difference from the 10 and 12-ferrocenyl alkanethiols is that the ΔE_p values of the 8-ferrocenyl alkanethiol SAM are lower than the 12-ferrocenyl alkanethiol SAM but higher than the 10-ferrocenyl alkanethiol SAM. The finite and zero field values of the 10-ferrocenyl alkanethiol SAM are also very similar to each other.
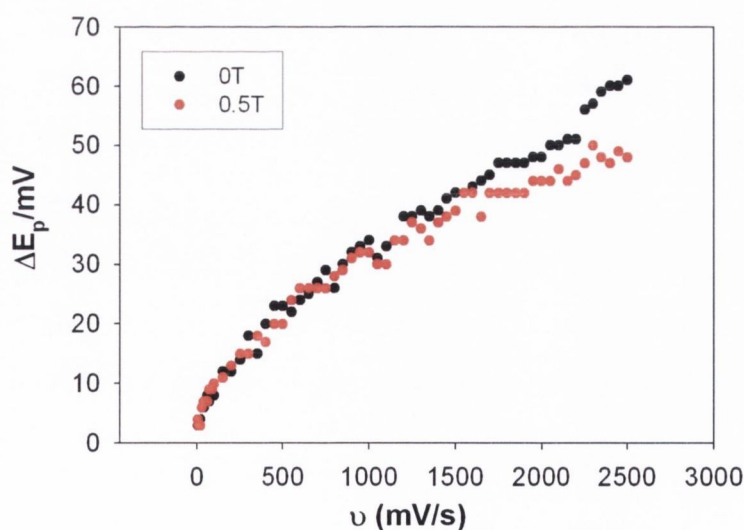
Figure 6.16: *Variation of voltammetric peak separation (ΔEₚ/mV) with sweep rate recorded for a 8-ferrocenyl alkanethiol SAM film in 1 M HClO₄ with experimental sweep in the absence (black) and in the presence (red) of a static 0.5T magnetic field.*

The surface coverage of the 8-ferrocenyl alkanethiol SAM at each scan rate was calculated for both the zero and finite fields and the results are shown in figure 6.17. From figure 6.14 it was earlier seen that the surface coverage of the zero field was larger than the corresponding finite field at 100 mVs^{-1}. From the graph it is seen that the surface coverage of adsorbed ferrocene is larger in a zero field than in the corresponding finite field for each scan rate. Similarly to the 10-ferrocenyl alkanethiol SAM the surface coverage of both the finite field and zero field decrease at a fast rate at very low scan rates (5 mVs^{-1} to 100 mVs^{-1}). However, as the scan rates increase to higher values the surface coverage decrease becomes less marked exhibiting result similar to the 10-ferrocenyl alkanethiol SAM.
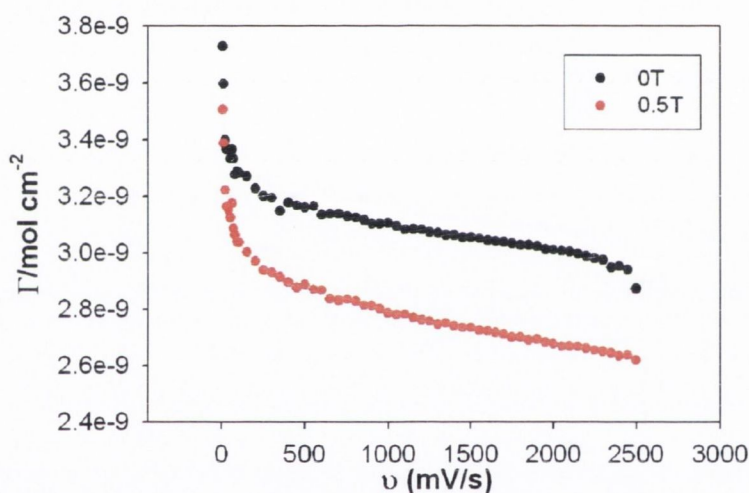
Figure 6.17: *Variation of surface coverage (Γ/mol cm^{-2}) with sweep rate recorded for a 8-ferrocenyl alkanethiol SAM film in 1 M HClO$_4$ with experimental sweep in the absence (black) and in the presence (red) of a static 0.5T magnetic field.*

The sections above (6.2.1-6.2.3) show that the application of a magnetic field has an effect on the SAMs. This confirms our earlier assumption that the application of a magnetic field causes the alkane chains to become disordered and to possibly cause some of the pendant ferrocene redox sites to become buried in the surrounding alkane chain matrix. In particular, this burying of ferrocene sites may cause their electroactivity to be limited and could be responsible for the observed decrease in the surface coverage on application of the magnetic field. The quality of the monolayer

formed will impact on the possibility of a pendant redox site being buried as a more ordered, densely packed alkane matrix will limit a headgroups ability to bury itself.

As seen with Sumner and Creager[4] work one of the main findings was that when ferrocene groups were buried into the alkane chain matrix the redox potentials at which the oxidation/reduction occurred were shifted to much higher potentials relative to monolayers in which the ferrocene groups were exposed to the electrolyte. In the work carried out here, the long chain 12-ferrocenyl alkanethiol is the only n-ferrocenyl alkanethiol SAM where there is a positive shift in the oxidative redox potential. The shorter 10 and 8 n-ferrocenyl alkanethiols see a drop in oxidative potentials on addition of a magnetic field.

6.4 Potential Step Chronoamperometry

As we have seen cyclic voltammetry does not always afford the optimal route to kinetic parameters. It can be difficult to distinguish between Ohmic drop and kinetic effects when investigating the variation of the voltammetric response with sweep rate. Instead potential step techniques can be employed to calculate electron transfer rate constants for redox systems immobilised on electrodes.
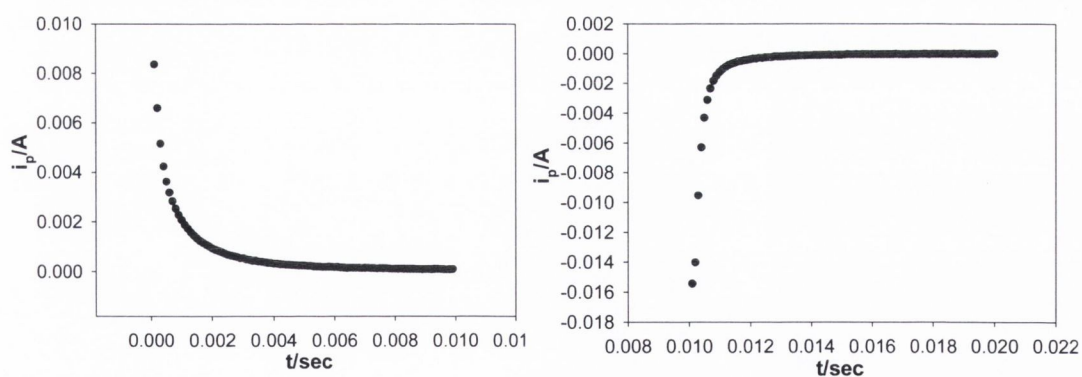
Figure 6.18: *Typical results from potential step experiments across the ferrocene oxidation and reduction potentials respectively of a 12-ferrocenyl alkanethiol SAM. The electrolyte employed was 1M HClO₄ and the pulse width is 10 msec.*

In this experiment the redox active ferrocenyl alkanethiol monolayer on gold in 1M $HClO_4$ is subjected to a potential step chronoamperometry measurement. This consists of the potential being stepped from an initial value of ca. 0.33 V to a final value some 0.55V more positive. In effect the potential is stepped across the redox peak, and an oxidative redox transformation ferrocene → ferrocinium is established.

The current flow arising from the latter is subsequently measured as a function of time. The time varying, chronoamperometric response expected by a surface immobilized redox group arising from a potential step is given by:

$$i = k^0 \Delta Q \exp(-kt) \tag{6.4}$$

Where k^0 denotes the potential dependent electron transfer rate constant and ΔQ represents the charge passed during the current transient. It is inferred from the latter expression that the ferrocene/ferricenium surface redox transformation should exhibit first order kinetics, and consequently, a plot of the natural logarithm of the current should vary linearly with elapsed time. The slope of the latter plot should then generate a value for the electron transfer rate constant k^0.

Figure 6.19 below shows a typical plot obtained for the oxidation of ferrocene at varying pulse widths (0.1 msec (a) and 1 msec (b)). The results obtained in such an experiment at the 12-ferrocenylalkanethiol SAM modified electrode under both zero and 0.5T magnetic field conditions are outlined.
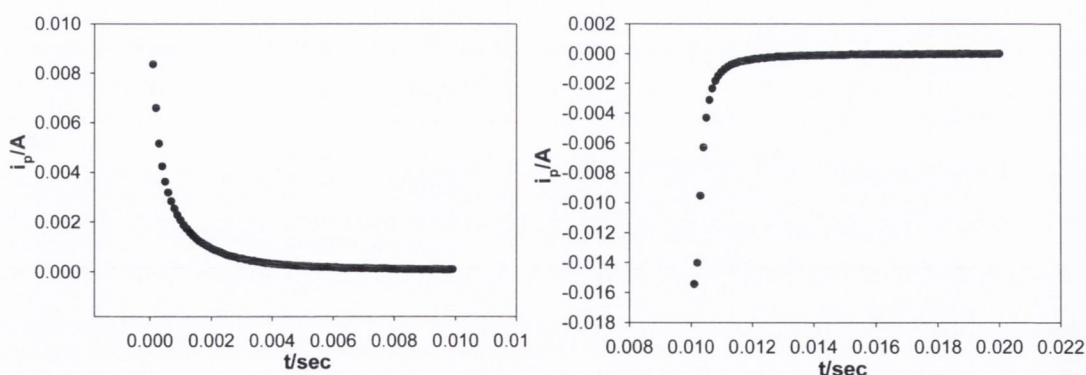
Figure 6.19: *Typical potential step chronamperograms across the ferrocene oxidation and reduction potentials respectively of a 12-ferrocenyl alkanethiol SAM both in the absence and presence of an external magnetic field. The electrolyte employed was 1M $HClO_4$ and the pulse width is $1e^{-4}$ sec (a) and 1 msec (b).*

From the figure 6.19 (b) it is obvious that there is some other process occurring in the initial stage of the chronoamperometry in the absence of the magnetic field. The current is seen to rise to a maximum and then decay as time increases. This type of "peaked" i versus t response is often characteristic of a nucleation-growth process at the electrode/SAM interface[6]. The reason for this is that some ferrocene sights could be buried and in order to be accessed by the ClO_4^- ion, the SAM needs to reorganise and open up. A similar situation has been seen in conducting polymers, where the current rise had been ascribed the polymer compacting when reduced and opening up and become porous, when subjected to an oxidative potential pulse. However, on applying an external magnetic field we see a change in the chronamperogram, the rise to a maximum is not observed but rather we see a straight current decay curve. From this it is concluded that the magnet has an immediate effect on the surface of the SAM and causes a reorganisation in the monolayer thereby allowing the SAM to open up and become porous.

We then carried out an ad hoc analysis of the chronamperograms, to see where the decay occurs after the maximum and hence investigate the dispersal kinetics. This analysis is carried out by plotting the natural logarithm of current versus time (ln i versus t) and from the slope the rate constant can be calculated. If there is no dispersion then the plots will be linear. However, when plots are non-linear it is because of one of two possible reasons. Firstly, there could be a kinetic dispersion in the rate constants i.e. the observed dependence of rate on potential will be perturbed. The second reason could be that the electrostatic potential drop that develops between the plane of electron transfer and the electrode surface. Figure 6.20 below shows a typical plot obtained for the oxidation of ferrocene. The results obtained in such an experiment at the 12-ferrocenylalkanethiol SAM modified electrode under both zero and 0.5T magnetic field conditions are outlined. It can be seen that the plots are not linear.
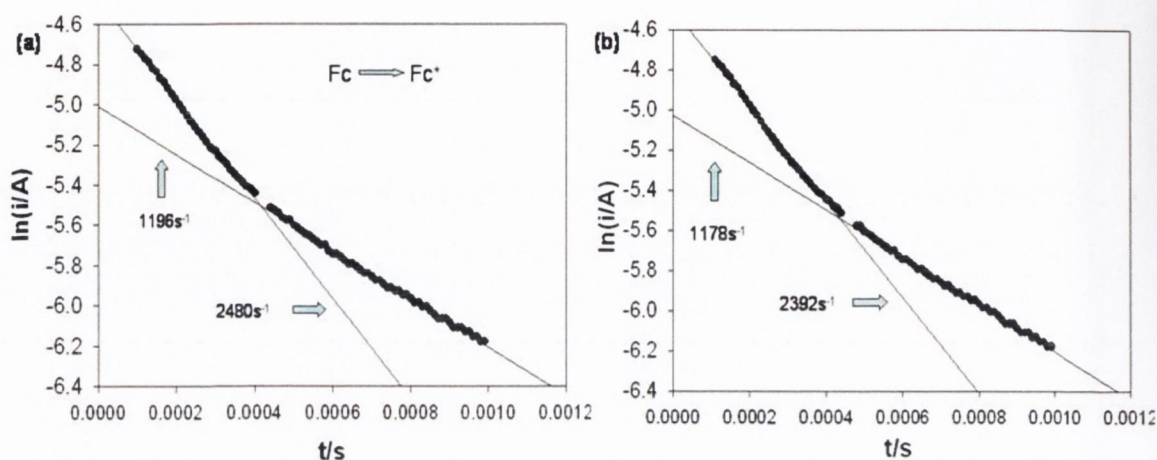
Figure 6.20: *PS chronoamperometric transients recorded in semi-logarithmic format for surface bound ferrocene/ferricinium redox transition in the absence and presence of an external magnetic field for a 12-Ferrocenyl alkanethiol SAM. Potential stepped from 300 - 880 mV with pulse width of 1 msec. The electrolyte used is 1 M HClO₄.*

As can be seen there is a spread in the observed rate constants for both the 0 T and 0.5 T potential steps. This spread maybe due to some ferrocene sites on the SAM being more active than other ferrocene sites. For each plot, oxidation and reduction, "fast" and "slow" rate constants were calculated, representing the ferrocene sites for which electron transfer is most and least facile. The table below presents rate constants calculated for both oxidation and reduction in the presence and absence of a magnetic field.

	"slow" k_{ox}	"fast" k_{ox}	"slow" k_{red}	"fast" k_{red}
0 T	1198	2480	2526	4929
0.5 T	1176	2392	2526	4929

Table 6.5: *Electron transfer rate constants of the 12-Ferrocenyl alkanethiol SAM calculated for both the oxidation and reduction of ferrocene. The k^0 values in the absence and presence of a 0.5 T magnetic field are calculated. The units of the rate constant are s^{-1} in each case.*

It can be readily seen that the semi – logarithmic curve corresponding to the oxidative ferrocene/ferricenium redox transformation decays more rapidly in the absence of a 0.5 T magnetic field than in the free field situation. The "slow" heterogeneous rate constant recorded for the ferrocene/ferricinium redox transformation across the alkanethiol monolayer to an underlying gold electrode was found to be 1198 s⁻¹ when

B = 0 T but was slightly decreased to 1176 s⁻¹ when B = 0.5T. A similar result is obtained for the "fast" rate constant with a value of 2480 s⁻¹ recorded when B = 0 T and 2392 s⁻¹ for B = 0.5T. In contrast, little effect of magnetic field could be found on the "slow" rate constant (k_{ET} 2526 s⁻¹ for B = 0 and B = 0.5 T) and the "fast" rate constant (k_{ET} 4929 s⁻¹ for B = 0 and B = 0.5 T) for the corresponding reductive ferricinium/ferrocene transformation (figure 6.21).
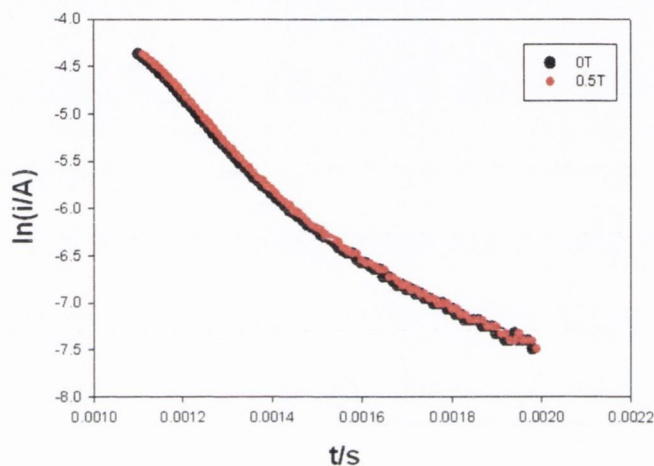
Figure 6.21: *PS chronoamperometric transients recorded in semi-logarithmic format for surface bound ferricinium/ferrocene redox transition in the absence and presence of an external magnetic field for a 12-Ferrocenyl alkanethiol SAM.*

The experiment was repeated for the 8 and 10-ferrocenyl alkanethiol Self assembled monolayers. The parameters of the experiment were unaltered for the remaining alkanethiols.
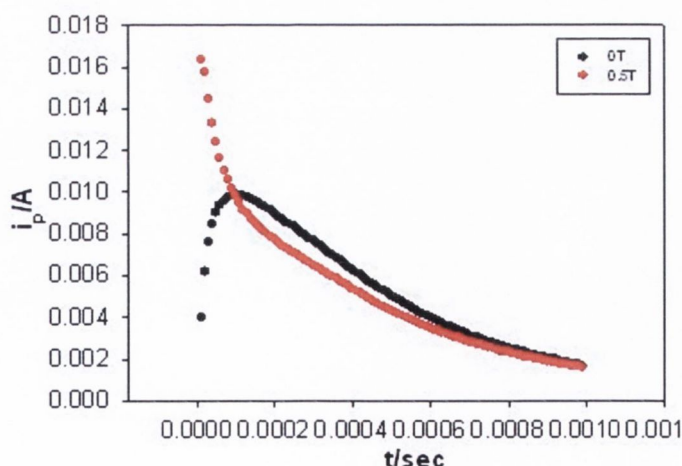
Figure 6.22: *Typical potential step chronamperograms across the ferrocene oxidation potentials of a 10-ferrocenyl alkanethiol SAM both in the absence and presence of an external magnetic field. The electrolyte employed was 1M HClO₄ and the pulse width is 1 msec.*

Similarly to the 12-ferrocenyl alkanethiol SAM, it is obvious that there is some other process occurring in the initial stage of the chronoamperometry for the 10-ferrocenyl alkanethiol SAM in the absence of the magnetic field (figure 6.22). Again the current is seen to rise to a maximum and then decay as time increases. The ferrocenyl alkanethiol SAM "peaked" i versus t response is characteristic of a nucleation-growth process at the electrode/SAM interface[6]. The reason for this is that some ferrocene sights could be buried and in order to be accessed by the ClO_4^- ion, the SAM needs to reorganise and open up. A similar situation has been seen in conducting polymers, where the current rise had been ascribed the polymer compacting when reduced and opening up and become porous, when subjected to an oxidative potential pulse. A similar result to the 12-ferrocenyl alkanethiol is obtained on applying an external magnetic field. Again a change in the chronamperogram is observed with the rise to a maximum not observed but rather we see a straight current decay curve. From this it is concluded that the magnet has an immediate effect on the surface of the SAM and causes a reorganisation in the monolayer thereby allowing the SAM to open up and become porous.
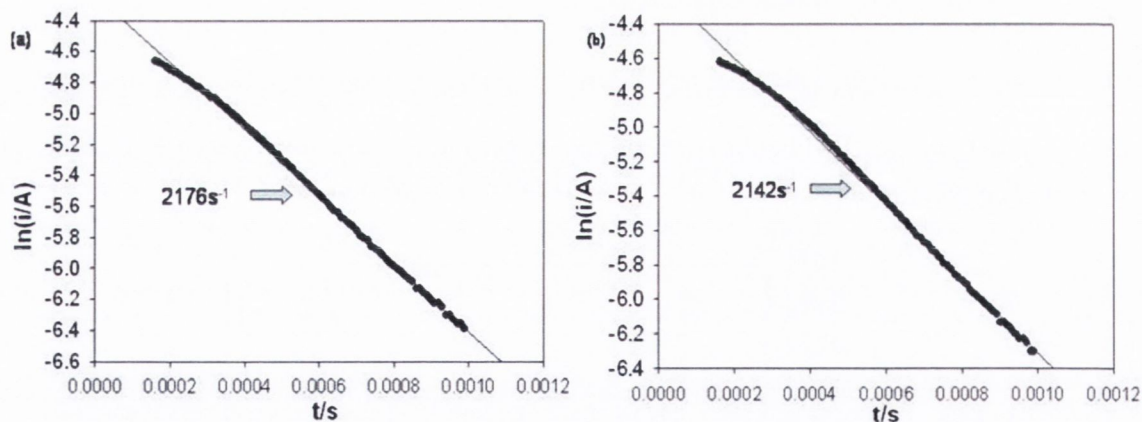

Figure 6.23: *PS chronoamperometric transients recorded in semi-logarithmic format for surface bound ferrocene/ferricinium redox transition in the absence (a) and presence of an external magnetic field (b) for a 10-Ferrocenyl alkanethiol SAM. Potential stepped from 300 - 880 mV with pulse width of 1 msec. The electrolyte used is 1 M $HClO_4$.*

We again carried out an analysis of the chronamperograms, to see where the decay occurs after the maximum and hence investigate the dispersal kinetics. Figure 6.23 below shows a typical plot obtained for the oxidation of ferrocene to ferricinium for a

10-ferrocenylalkanethiol SAM modified electrode under both zero and 0.5T magnetic field conditions.

It can be seen that the plots for the shorter 10-ferrocenyl alkanethiol are linear for the oxidation of ferrocene to ferricinium in both the absence and presence of magnetic field.

From these plots it is assumed that the linearity may indicate that all the ferrocene active sites are equal unlike in the 12-ferrcocenyl alkanethiol SAM. As the plot of ln(i/A) versus t is linear for the oxidation of the ferrocene in the absence and presence of the magnetic field only one electron transfer rate constant can be calculated for the oxidation plots. This indicates that the ferrocene sites all allow electron transfer to occur at the same time. However, for the reduction of ferricinium back to ferrocene (figure 6.24), there is a deviation in linearity in both cases. This again allows for "fast" and "slow" rate constants to be calculated, representing the ferrocene sites for which electron transfer is most and least facile. The table below presents rate constants calculated for both oxidation and reduction in the presence and absence of a magnetic field.

	k_{ox}	"slow" k_{red}	"fast" k_{red}
0 T	2176	2979	5265
0.5 T	2142	2815	5019

Table 6.6: *Electron transfer rate constants of the 10-Ferrocenyl alkanethiol SAM calculated for both the oxidation and reduction of ferrocene. The k^0 values in the absence and presence of a 0.5 T magnetic field are calculated. The units of the rate constant are s^{-1} in each case.*

As was seen in the 12-ferrocenyl alkanethiol SAM, the semi – logarithmic curve corresponding to the oxidative ferrocene/ferricenium redox transformation decays more rapidly in the absence of a 0.5 T magnetic field than in the free field situation for the 10-ferrocenyl alkanethiol SAM. The heterogeneous rate constant recorded for the ferrocene/ferricinium redox transformation across the alkanethiol monolayer to an underlying gold electrode was calculated as 2178 s^{-1} when B = 0 T. However, the rate constant decreased to 2142 s^{-1} on addition of the 0.5 T magnetic field.
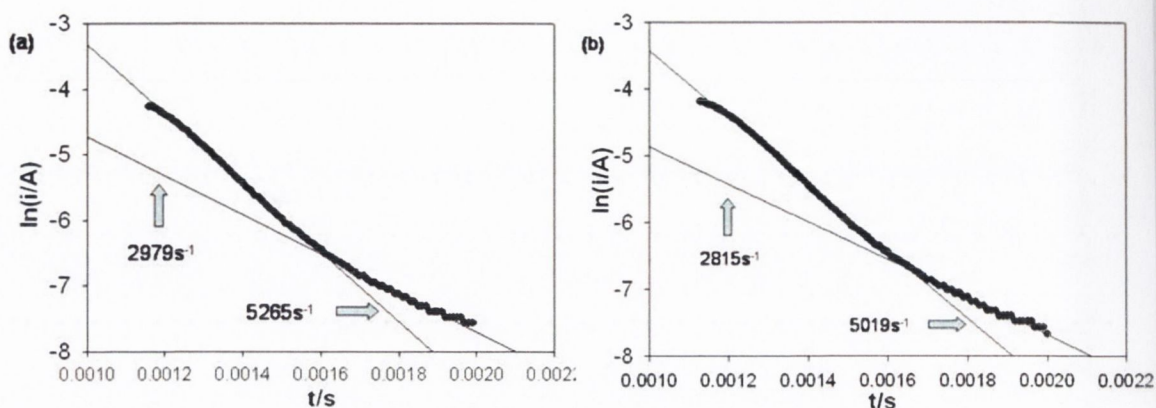
Figure 6.24: *PS chronoamperometric transients recorded in semi-logarithmic format for surface bound ferricinium/ferrocene redox transition in the absence and presence of an external magnetic field for a 10-Ferrocenyl alkanethiol SAM. Potential stepped from 300 - 880 mV with pulse width of 1 msec. The electrolyte used is 1 M $HClO_4$.*

Calculation of the "fast" and "slow" rate constants for the reduction of ferricinium to ferrocene sees a similar result to the 12-ferrocenyl alkanethiol SAM found (figure 6.22). Prior to the magnetic field being applied the "slow" rate constant was observed to have a value of 5265 s^{-1}. However addition of the 0.5 T magnetic field saw this value decrease to 5019 s^{-1}. Similarly for the "slow" rate constant the 2979 s^{-1} value obtained for the 0 T was seen to decrease to 2815 s^{-1} on applying the exterior magnetic field.

A typical potential step result obtained for the oxidation of ferrocene to ferricinium and reduction of ferricinium to ferrocene for the 8-ferrocenyl alkanethiol SAM in an experiment carried out under both zero and 0.5T magnetic field conditions are outlined below in figure 6.25.

Similarly to the longer chain ferrocenyl alkanethiol SAMs, there is some other process occurring in the initial stage of the chronoamperometry for the 8-ferrocenyl alkanethiol SAM in the absence of the magnetic field (figure 6.25) and can be attributed to a nucleation-growth process at the electrode/SAM interface, similar to the long chain alkanethiols.
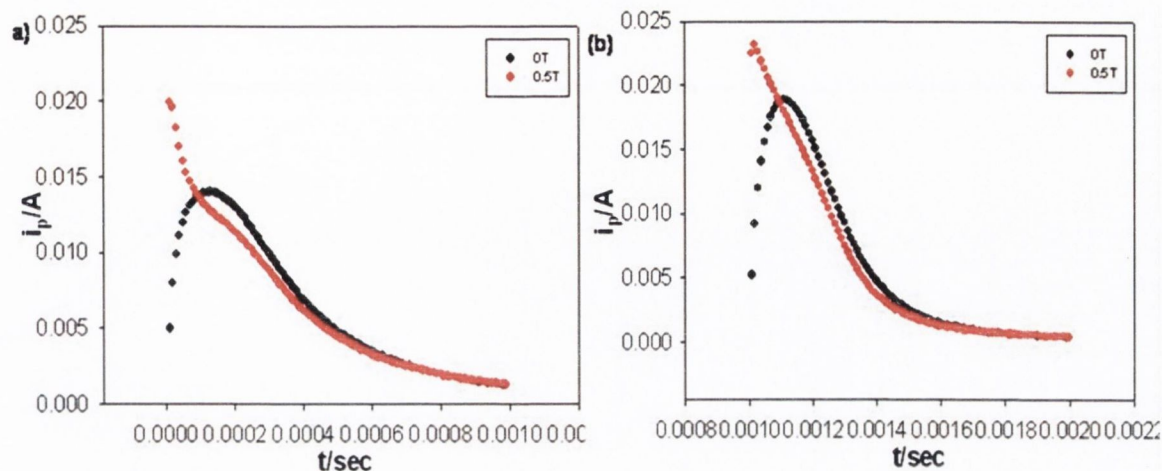
Figure 6.25: *Typical results from potential step experiments across the ferrocene oxidation and reduction potentials respectively of an 8-ferrocenyl alkanethiol SAM in the absence and presence of an external magnetic field. The electrolyte employed was 1M HClO₄.*

However, on applying an external magnetic field we see a change in the chronamperogram, the rise to a maximum is not observed but rather we see a straight current decay curve. From this it is concluded that the magnet has an immediate effect on the surface of the SAM and causes a reorganisation in the monolayer thereby allowing the SAM to open up and become porous.

We again carried out an analysis of the chronamperograms, to see where the decay occurs after the maximum and hence investigate the dispersal kinetics. From the results it is obvious that the addition of an external magnetic field has an effect on the 8-ferrocenyl alkanethiol SAM. In order to see the effect that the magnetic field has on the SAM, the plot of the natural logarithm of the current versus time for the oxidation of ferrocene to ferricinium and the reduction of ferricinium to ferrocene for a 8-ferrocenylalkanethiol SAM modified electrode under both zero and 0.5T magnetic field conditions was analysed.
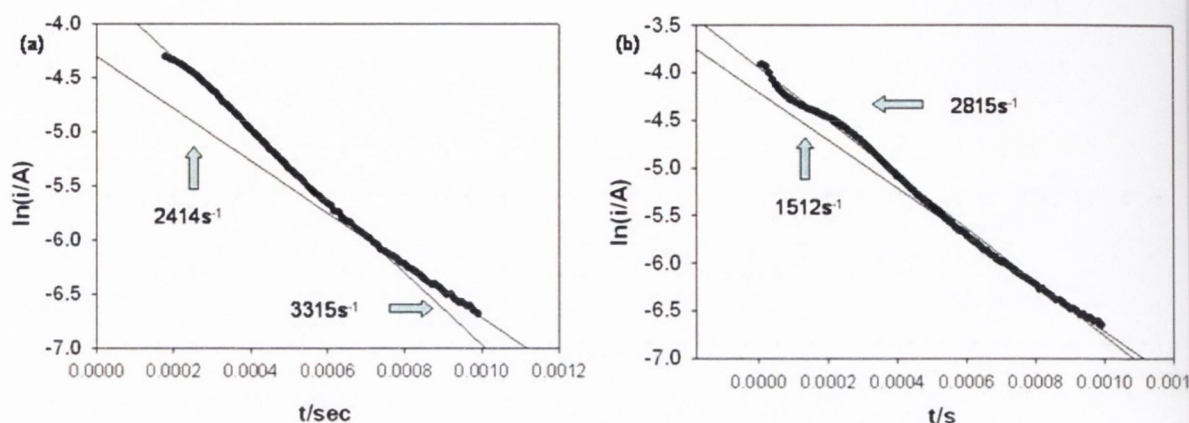
Figure 6.26: *PS chronoamperometric transients recorded in semi-logarithmic format for surface bound ferrocene/ferricinium redox transition in the absence (a) and presence of an external magnetic field (b) for a 8-Ferrocenyl alkanethiol SAM. Potential stepped from 300 - 880 mV with pulse width of 1 msec. The electrolyte used is 1 M $HClO_4$.*

From the plot it is obvious that they are not linear in either the absence or presence of the magnetic field. From this it is again assumed that there is a spread in the rate constants. This spread maybe due to some ferrocene sites on the SAM being more active than other ferrocene sites. For each plot, oxidation and reduction, "fast" and "slow" rate constants were calculated, representing the ferrocene sites for which electron transfer is most and least facile. The table below presents rate constants calculated for both oxidation and reduction in the presence and absence of a magnetic field.

	"slow" k_{ox}	"fast" k_{ox}	"slow" k_{red}	"fast" k_{red}
0 T	2414	3315	5795	3264
0.5 T	1512	2815	5402	3062

Table 6.7: *Electron transfer rate constants of the 8-Ferrocenyl alkanethiol SAM calculated for both the oxidation and reduction of ferrocene. The k^0 values in the absence and presence of a 0.5 T magnetic field are calculated. The units of the rate constant are s^{-1} in each case.*

It can be readily seen that the semi – logarithmic curve corresponding to the oxidative ferrocene/ferricenium redox transformation decays more rapidly in the absence of a 0.5 T magnetic field than in the free field situation. The "slow" heterogeneous rate constant recorded for the ferrocene/ferricinium redox transformation across the alkanethiol monolayer to an underlying gold electrode was found to be 2414 s^{-1} when

$B = 0$ T but was decreased to 1512 s^{-1} when $B = 0.5$T. A similar result is obtained for the "fast" rate constant with a value of 3315 s^{-1} recorded when $B = 0$ T and 2815 s^{-1} for $B = 0.5$T. In contrast to the 12-ferrocenyl alkanethiol, the corresponding reductive ferricinium/ferrocene transformation (figure 6.27) also shows that the magnetic field has an effect on the rate constants. The "slow" rate constant of the zero field was calculated as 3264 s^{-1} whereas the 0.5 T magnetic field saw a decrease in the rate constant to 3062 s^{-1}. The "fast" rate constant also saw a decrease in value on addition of a magnetic field with the values decreasing from 5795 s^{-1} to 5402 s^{-1}.

Figure 6.27: *PS chronoamperometric transients recorded in semi-logarithmic format for surface bound ferricinium/ferrocene redox transition in the absence and presence of an external magnetic field for a 8-Ferrocenyl alkanethiol SAM. Potential stepped from 300 - 880 mV with pulse width of 1 msec. The electrolyte used is 1 M HClO$_4$.*
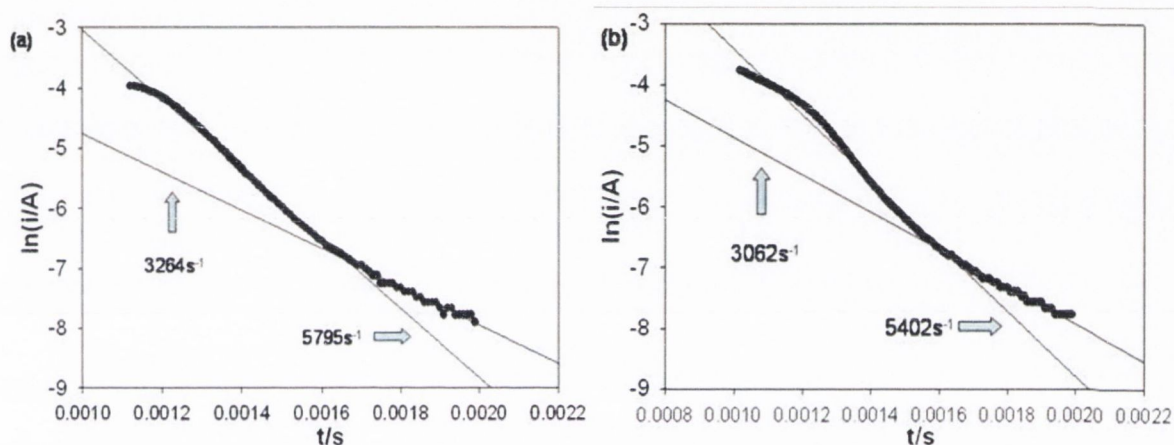
This result provides a firm confirmation for the first time that the rate of long range electron transfer across molecular barriers (the insulating hydrocarbon chains) is directly affected by the presence of a magnetic field. We have seen that the rate of ferrocene oxidation/reduction was dramatically slowed for ferrocene groups in the monolayer interior compared with the rates for ferrocene groups exposed to the electrolyte solution. Our work would seem to agree with Sumner and Creager's second observation which saw that burying of the pendant ferrocene redox group causes a decrease in the observed electron transfer rate constant.

6.5 Discussion

From the results presented here it is clear that the presence of an external magnetic field causes effects in the redox activity of n-ferrocenyl alkanethiol SAMs. From section 6.2 it is obvious that applying a magnetic field perpendicular to the Au/SAM electrode causes a reduction in the oxidative and reductive currents of the SAMs, grown for 24 hr and 48 h in a 1 mM ferrocenyl alkanethiol solution. Similarly, we see an increase in the oxidative peak potentials and a decrease in the reductive peak potentials and hence an increase in the ΔE_p values. The surface properties of the SAM also see a change. The surface coverage values of the SAM decrease on applying the magnetic field. On rotating the magnetic field parallel to the Au/SAM interface a further reduction in the properties are seen. From this we proposed that the application of a magnetic field causes the alkane chains to become disordered and to possibly cause some of the pendant ferrocene redox sites to become buried in the surrounding alkane chain matrix as our work concurred with that of Creager and Sumner[5].

Section 6.3 sees a comprehensive study of varying n-ferrocenyl alkanethiol SAMs and the effects caused by the application of an external magnetic field. From the results it is clear that the ferrocenyl alkanethiol SAMs qualitative results are affected in a similar manner. Both long-chain and short chain ferrocenyl alkanethiols sees marked changes in the redox properties of the SAM. All three varying chain lengths see a decrease in their respective surface coverage value on application of the magnet giving further claims to the proposal discussed above.

Sumner and Creager found that when ferrocene groups were buried into the alkane chain matrix the redox potentials at which the oxidation/reduction occurred were shifted to much higher potentials relative to monolayers in which the ferrocene groups were exposed to the electrolyte. In the work carried out here, the long chain 12-ferrocenyl alkanethiol is the only n-ferrocenyl alkanethiol SAM where there is a positive shift in the oxidative redox potential. The shorter 10 and 8 n-ferrocenyl alkanethiols see a drop in oxidative potentials on addition of a magnetic field.

It is stressed that the decrease in redox activity seen above is not expected to be caused by the loss of SAM molecules from the surface of the electrode. It must

also be stated that no decrease in redox activity occurs in the absence of the magnetic field. The cyclic voltammograms recorded prior to magnetic field application are very stable and can be reproduced several times.

From the potential step chronoamperometry (section 6.4) we obtained the quantitative results of the effects of the external magnetic field. It was observed that the effect of a magnetic field on is marked. The rise to a current maximum observed in the absence of a magnetic field is not observed but rather we see a straight current decay curve. From this it is concluded that the magnet has an immediate effect on the surface of the SAM and causes a reorganisation in the monolayer thereby allowing the SAM to open up and become porous. From the current decay curves we obtain rate constants for each of the ferrocenyl alkanethiol SAMs in the presence and absence of the magnetic field. For each n-ferrocenyl alkanethiol a decrease in the both the oxidative and reductive rate constants is observed on applying an external magnetic field. This result would seem to concur with Sumner and Creager's second observation which saw that burying of the pendant ferrocene redox group causes a decrease in the observed electron transfer rate constant. However, the decrease seen by Sumner and Creager was far more marked than observed by our work. Therefore the second main finding of Sumner and Creager work would appear to support the hypotheses that the burying of the ferrocene group could possibly occur upon application of an external magnetic field.

The Ohtani[6] model can also be employed to describe the processes occuring when a 12-ferrocenyl SAM is subjected to the presence of an external 0.5 T magnetic field. From our results an increase in ΔE_p values (figure 6.8) and a positive peak shift (figure 6.7) are obtained on addition of an external magnetic field. Hence, the potential drop across the SAM is affected by the presence of an external magnetic field.

Strong interaction between surface bound
cations and solution phase counterions.
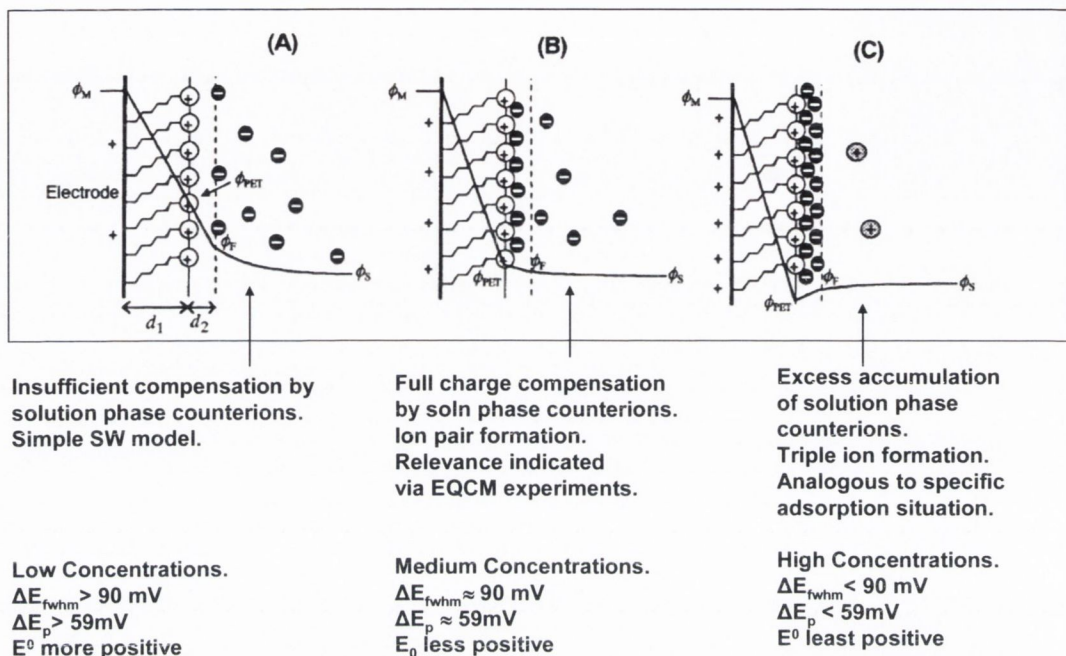
Figure 6.28: *Schematic illustration of potential distributions across solution/SAM/electrode substrate interface. The zig-zag line indicates a dielectric film like an alkyl chain of SAM, and the signs (+, -) denote charges of the electrode substrate surface, surface-confined species, and electrolyte ions: (A) for insufficient compensation of surface-confined positive charges with electrolyte anions; (B) for full neutralization; (C) for excessive accumulation of electrolyte anions .Reproduced from reference 6.*

Looking at figure 6.28 and from section 6.3.1, it is observed that the ΔE_p values increase and the E^0 values shift positively when either case c→b or case b→a occurs. Normally, either of these cases will occur when there is a reduction in the concentration. However, in this scenario in both the absence and presence of a magnetic field the concentrations are the same. Therefore it is assumed that the magnetic field must be responsible for these changes. From this it is concluded that the magnetic field causes "stirring" resulting in a reduction of charge compensation i.e. less solution phase ClO_4^- counterions interact with the surface bound cations. The ClO_4^- counterions are pulled away from the surface of the SAM.

The drop in peak current on addition of an external magnetic field as seen in figure 6.5 can be explained by the Smith-White model[7]:

$$i = \upsilon A \left(1 + \frac{d\phi_{pet}}{d\phi_M} \right) C_\Sigma \tag{6.5}$$

Where i is the peak current, υ is the sweep rate, A is the area of the electrode, $d\phi_M$ is the change in potential distribution of the SAM, $d\phi_{PET}$ is the change in the number of the counterions and C_Σ is the capacitance of the SAM.

In an ideal response:

$$i = \upsilon A C_\Sigma \tag{6.6}$$

i.e. there is full charge compensation by the solution phase counterions. Looking at the equation:

$$i = \frac{n^2 F^2 A \Gamma_\Sigma}{4RT} \upsilon \tag{6.7}$$

and then combining it with equation 6.2 we get:

$$C_\Sigma = \frac{n^2 F^2 \Gamma_\Sigma}{4RT} \tag{6.8}$$

As the values of n, F, R and T all remain constant it is shown that C_Σ is dependant on Γ_Σ. Therefore, we can assume that if Γ_Σ changes so too will C_Σ. From section 6.3.1, a decrease is seen in the Γ_Σ for the 12-ferrocenyl alkanethiol SAM on applying an 0.5 T external magnetic field ($\Gamma = 1.74 \times 10^{-10}$ mol cm^{-2} for B=0 T and $\Gamma = 1.15 \times 10^{-10}$ mol cm^{-2} for B=0.5 T). From this we can assume that C_Σ changes and therefore the slope $A \left(1 + \frac{d\varphi_{PET}}{d\varphi_M} \right) C_\Sigma$ will change on applying an external magnetic field. Hence the magnetic field causes two possible scenarios, (a) the potential distribution of the SAM changes ($d\phi_M$) or (b) number of counterions changes ($d\phi_{PET}$).

One last brief explanation that can be put forward to explain the effects of the external magnetic field on the various aspects of SAM redox activity relates to the effect of the magnetic field on solution ions. Previously, it was believed that the Lorentz force ($F_L = j \, x \, b$ where j is the current density) was the main force created on application of a magnetic field[8,9]. The Lorentz force arises from the motion of charge across lines of magnetic flux. The Lorentz force operates further into the diffuse layer. The Lorentz force caused convection in the solution which results in the diffusive movement of ions in solution. However, in our work the Lorentz force cannot be the only force working as the potential drop is near the PET which operates at distances very close to the electrode. In order to understand this reference has to be made to work recently published by Olivier[10]. He demonstrated that the effect of a magnetic field on the limiting current is equivalent to that produced by a tangential electric field close to the electrode surface. This electric field may be created by the application of a magnetic field parallel to the surface of the electrode. The electrokinetic stress or force on the charge density in the diffuse double layer induces a tangential flow which is transmitted by viscous forces to the bulk solution. The electrokinetic force operates only a few nanometers from the electrode surface. As stated earlier, the only other force due to the interaction of the magnetic field with the electric current is the Lorentz force. Both the Lorentz force and the electrokinetic force are similar in origin; the main difference between them is the scale on which they operate.

Lyons et al proposed that both forces play some role in the interplay between the two scales of flow, and that both must be considered in the quantitative analysis of field induced transport enhancement[11]. The magnetic field induces convection in the solution which is equivalent to rotating the electrode or stirring the solution thereby effecting the ability of perchlorate ions to form ion pairs and hence, reducing the number of counterions at the surface of the SAM. This results in the reduction of charge compensation causing a broadening of the peaks and a reduction in the current.

At this point in the study of magnetic field effects of electron transfer mechanisms in self assembled monolayers the postulation that an applied field causes pendant ferrocene groups to be buried in the surrounding alkane layer is a plausible one due to the comparisons with previous work carried out by Sumner and Creager. However, far more investigation needs to be conducted before it is assumed that this postulation can be taken as proven.

References

1. Fahidy, T.J.; *J. Appl. Electrochem.* **1983**, 13, 553.

2. Lyons, M.E.G.L.; Coey, J.M.D.; Hinds, G.; Spada, F.E.; Ni Mhiochain, T.R., *J. Phys. Chem. B.* **2001**, 105, 9487.

3. Chidsey, C.E.D.; Bertozzi, C.R.; Putvinski, T.M.' Mujsce, A.M., *J. Am. Chem. Soc.*, **1990**, 112, 4301.

4. Sumner, J.J.; Creager, S.E., *J. Phys. Chem. B,* **2001**, 105, 8739.

5. Laviron , E., *J. Electroanal. Chem.* **1979**, 100, 263.

6. Ohtani, M.; Kuwabata, S.; Yoneyama, H. *Anal. Chem.* **1997,** 69,1045.

7. Smith, C.P.; White, H.S. *Anal. Chem.* **1992,** *64,* 2398.

8. Fahidy, T.Z. *J. Appl. Electrochem.* **1983**, 13, 553.

9. Tacken, R.A.; Janssen, L.J.J. *J. Appl. Electrochem.* **1995**, 25, 1.

10. Olivier, A.; Chopart, J.P.; Amblard, J.; Merienne, E.; Aaboubi, O. *Models Chem.* **2000**, 133, 213.

11. Hinds, G.; Coey, J.M.D.; Lyons, M.E.G.L. *Electrochem. Commun,* **2001**, 3, 215.

CHAPTER 7

General Conclusions and Future Recommendations

7.1 General Conclusions

The majority of this work focused on the redox active properties of electroactive self assembled monolayers. The motivation for this work was to fully investigate the properties of the self assembled monolayers in order to allow the expansion of their applications. The most recent innovative application for these SAMs is at nanoscale level. It is thought that the area of nanotechnology could be worth upwards of €13 billion to the Irish economy by 2010, according to data from the Irish Council for Science, Technology and Innovation. They have also forecasted that worldwide the area could be worth in excess of $1 trillion by the same time.

The first results section (Chapter 4) characterized the electrochemistry of non redox active alkanethiol self assembled monolayers by employing cyclic voltammetry and electrochemical impedance spectroscopy. It is seen that non redox self assembled monolayers cause a change in the interfacial process which normally occurs for a bare gold electrode. This change or blocking effect has been described and the CV response of the SAM shows no trace of any direct ferrocyanide/ferricyanide redox activity at the underlying gold surface. Instead long range electron transfer between the solution phase redox couple and the underlying gold surface occurs via a tunneling mechanism through the hydrocarbon layer. This result is further reinforced by the results obtained for the electrochemical impedance spectroscopy. The effect of an external magnetic field on a non-redox active C_{12} alkanethiol SAM is shown. Experiments carried out on the addition of a known potential to a bare gold electrode immersed in a non redox active C_{12} alkanethiol found that there is a positive growth effect on the adsorption of the dodecanethiol on the gold electrode. From the results it was seen that the 0.4 V potential is the recommended value for use in the potential assisted adsorption of the SAM. This result is concluded as 0.4 V has a similar CV response to the CV response obtained for a SAM grown without the potential and confirmed by analysing the electron energy diagram of Au-SCH$_3$. From the result it is clear that the method of potential assisted growth does cause enhanced adsorption on a non-redox active alkanethiol and can therefore be employed to form SAMs of the redox active n-ferrocenyl alkanethiol.

The second results section (chapter 5) investigates the application of a 0.4 V potential to a bare gold electrode in a solution of 1 mM n-ferrocenyl alkanethiol for a 2 hr period. This method is found to produce self assembled monolayers of high quality with very high performance characteristics over a short time scale for n-ferrocenyl alkanethiols of varying chain lengths. On investigation of concentration studies several results were recorded which were reciprocated for all chain lengths: ΔE_p values increased, E^0 values became more positive, surface coverage values (Γ) increased and peak widths (ΔE_{fwhm}) broadened with increasing electrolyte solution concentration. These results do no alter if the nature of the electrolyte is changed ($HClO_4$ versus $NaClO_4$). By employing the Smith-White model and the Ohtani model which developed a mathematical analysis of the potential distribution across the SAM film/solution interface we were able to confirm that as the electrolyte concentration increased electrolyte counterion compensation with the electrode surface cations also increased leading to the formation on ion pairs at the electrode surface. This results in an increase in the potential drop across the SAM. If the changes seen in the potential distributions occur in the redox reactions of the surface-confined redox species the shape of voltammograms will be changed, depending on the degree of interaction between the electroactive moieties of the SAM and the electrolyte ions.

We also employed a theory by Calvente, who explored the electrochemical consequences of a discrete spatial distribution of redox centers by investigating the voltammetric response of electroactive SAMs. In this approach it was assumed that a single PET did not occur, rather one had a distribution of distances over which the Fc/Fc^+ electron transfer reaction operated. The potential drop (φ_M-φ_{PET}) governs the driving force for electron exchange between a redox center and the electrode. In the presence of spatial dispersion, different φ_{PET} potentials will be experienced by those redox planes that are located at different distances from the electrode surface and will change their oxidation state to a different extent at a given φ_M. Under these circumstances, the voltammetric wave will consist of a superposion of distinct electrochemical responses, each one being associated with those redox centers that are located at the same distance from the electrode surface, even when the formal potentials of all redox centers are identical.

From the results presented in the final results chapter (Chapter 6) it is clear that the presence of an external magnetic field causes affects in the redox activity of n-ferrocenyl alkanethiol SAMs. Application of a magnetic field perpendicular to the Au/SAM electrode causes a reduction in the oxidative and reductive currents of the SAMs, grown for 24 hr and 48 hrs in a 1 mM ferrocenyl alkanethiol solution. The surface coverage values of the SAM decrease on applying the magnetic field. On rotating the magnetic field parallel to the Au/SAM interface a further reduction in the properties are seen. From this we proposed that the application of a magnetic field causes the alkane chains to become disordered and to possibly cause some of the pendant ferrocene redox sites to become buried in the surrounding alkane chain matrix as our work concurred with that of Creager and Sumner.

The second part of the chapter features a comprehensive study of varying n-ferrocenyl alkanethiol SAMs and the effects caused by the application of an external magnetic field. It is clear that the ferrocenyl alkanethiol SAMs qualitative results are affected in a similar manner. Both long-chain and short chain ferrocenyl alkanethiols see marked changes in the redox properties of the SAM. All three varying chain lengths observe a decrease in their respective surface coverage value on application of the magnet giving further claims to our proposal. Sumner and Creager found that when ferrocene groups were buried into the alkane chain matrix the redox potentials at which the oxidation/reduction occurred were shifted to much higher potentials relative to monolayers in which the ferrocene groups were exposed to the electrolyte. In the work carried out here, the long chain 12-ferrocenyl alkanethiol is the only n-ferrocenyl alkanethiol SAM where there is a positive shift in the oxidative redox potential. The shorter 10 and 8 n-ferrocenyl alkanethiols see a drop in oxidative potentials on addition of a magnetic field.

The Ohtani model can also be employed to describe the processes occurring when a 12-ferrocenyl SAM is subjected to the presence of an external 0.5 T magnetic field. On application of a magnetic field a peak shift and shape change are obtained on addition of an external magnetic field. Hence, the potential drop across the SAM is affected by the presence of an external magnetic field. From this it is concluded that the magnetic field causes "stirring" resulting in a reduction of charge compensation

i.e. less solution phase ClO_4^- counterions interact with the surface bound cations. The ClO_4^- counterions are pulled away from the surface of the SAM.

We also looked at how magnetic forces (Lorentz force and electrokinetic force) play some role in the interplay between the two scales of flow, and that both must be considered in the quantitative analysis of field induced transport enhancement. The magnetic field induces convection in the solution which is equivalent to rotating the electrode or stirring the solution thereby effecting the ability of perchlorate ions to form ion pairs and hence, reducing the number of counterions at the surface of the SAM. This results in the reduction of charge compensation causing a broadening of the peaks and a reduction in the current.

From the potential step chronoamperometry (section 6.3) we obtained the quantitative results of the effects of the external magnetic field. It was observed that the effect of a magnetic field on is marked. The rise to a current maximum observed in the absence of a magnetic field is not observed but rather we see a straight current decay curve. From this it is concluded that the magnet has an immediate effect on the surface of the SAM and causes a reorganisation in the monolayer thereby allowing the SAM to open up and become porous. From these curves the rate constants are calculated and a decrease in the both the oxidative and reductive rate constants are observed on applying an external magnetic field. This would seem to agree with Sumner and Creager's second observation which saw that burying of the pendant ferrocene redox group causes a decrease in the observed electron transfer rate constant. However, the decrease seen by Sumner and Creager was far more dramatic than observed by our investigation. Therefore the second main finding of Sumner and Creager work would appear to support the hypotheses that the burying of the ferrocene group could possibly occur upon application of an external magnetic field.
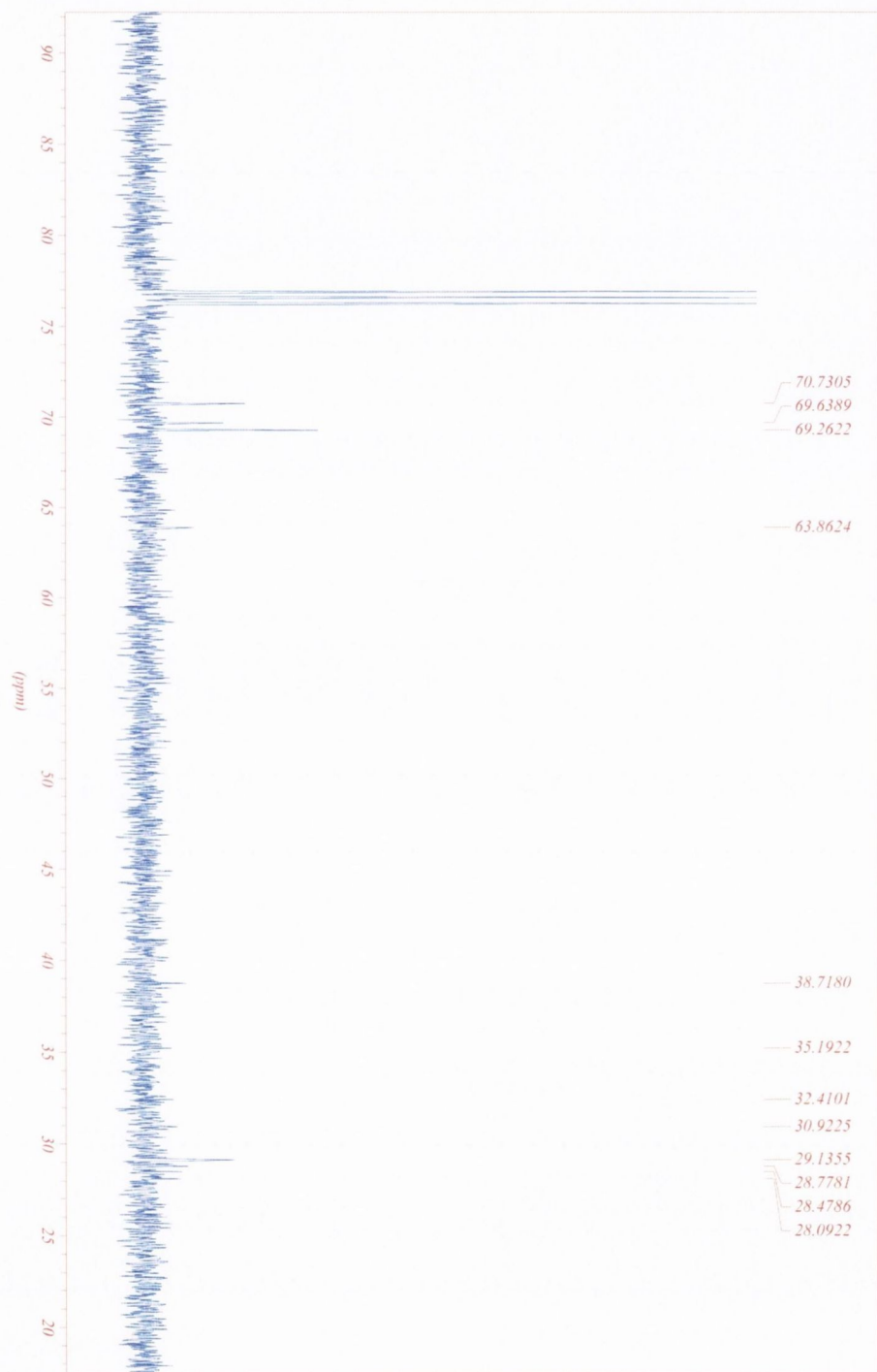
7.2 Future Recommendations

Recommendations regarding future work would focus on the magnetic field area. In particular, the development of theory regarding the effects of the magnetic field on the electron transfer properties of the ferrocenyl alkanethiol SAMs needs to be addressed. Our work has put forward the suggestion that an applied field causes pendant ferrocene groups to be buried in the surrounding alkane layer. However, far more investigation needs to be conducted before it is assumed that this postulation can be taken as proven.

Other recommendations would see more investigations on the potential assisted method especially as to how potential enhances the growth of SAMs and to investigate whether the method is ultimately reproducible.

Finally, a recommendation to develop the area of enzyme deposition atop self assembled monolayers is proposed. In this area particular attention should be given to the chemical and temporal stability of such systems particularly in the case of glucose oxidase system.

APPENDIX

NMR Characterisation of 12-Ferrocenyl Alkanethiol SAM